The mechanics of suspensions

Adam Kenneth Townsend

A dissertation submitted in partial fulfilment
of the requirements for the degree of
Doctor of Philosophy

Department of Mathematics
University College London

21 June 2017

Supervisor . . . . . Professor H. J. Wilson

Examiners . . . . . Professor E. J. Hinch
Professor E. R. Johnson

This work was supported in part by EPSRC grant EP/K502959/1.

I, Adam Townsend, confirm that the work presented in this thesis is my own. Where information has been derived from other sources, I confirm that this has been indicated in the thesis.

Adam Townsend, 21 June 2017

Abstract

Suspension mechanics—the flow of a fluid with small fragments of solid material suspended in it—is an area of wide applicability in both industry and nature. Examples include the transport of silt in rivers, the manufacture of toothpaste, and inkjet printing where pigments remain solid within the ink.

One widespread method to simulate these flows is Stokesian Dynamics, a truncated multipole expansion of the Stokes equations. It is computationally efficient while making a reasonable approximation to the hydrodynamic interactions between particles; however, all particles are identical spheres and the background matrix must be Newtonian.

This project extends Stokesian Dynamics to include differently-sized spheres. This allows us to study a variety of previously inaccessible suspension problems.

In many suspensions, e.g. toothpaste, the suspending fluid itself is non-Newtonian and exhibits viscoelastic properties. We have extended Stokesian Dynamics to incorporate a simple model of viscoelasticity by using the small spheres as 'beads' in bead–spring dumbbells. Different spring laws are then tested in shear, and their rheological behaviour is compared to continuum constitutive models.

Next, we replicate experiments in which a large sphere is dropped through a suspension of neutrally buoyant smaller spheres undergoing oscillatory shear flow. We qualitatively replicate the principal experimental observation—that at the moment of shear reversal, the suspension microstructure hinders the falling; while at the instant of fastest shear, it enhances the falling. We propose a physical mechanism explaining the observations.

Finally, we extend Stokesian Dynamics to properly implement interparticle frictional contact. Contact forces are a critical component of shear thickening in suspensions such as cornflour, yet are usually implemented in an ad hoc way, resulting in inaccurate predictions or high computational cost. The new method allows us to investigate contact models quickly and efficiently, and suggests an important factor in models of strongly shear-thickening fluids.

Acknowledgements

I am indebted, of course, to many people who have helped to make my PhD years such a wonderful time.

Firstly, to my supervisor, Professor Helen Wilson, who agreed to take me on as a PhD student five years ago despite being about to have her second child, and probably already being fed up of me after a year messing around with chocolate fountains. Since Helen's capitulation on that Circle line train we both happened to be on, I have been extremely grateful for her thoughtful guidance, her endless patience and her always-full teapot. Thank you for pointing me in the direction of interesting ideas, for trusting me to travel to exciting places to talk about them, and for believing that it was all going to work out. More than that, though, I am grateful for having been able to come for a chat whenever I needed it, both in the office and occasionally at home (even if Laura continues to show me up for how much it is possible to achieve in five years) and for Helen being a shining example that it is possible to be successful in academia and to be normal. Well... ish!

The Department of Mathematics at UCL has been a wonderful place to work. I'm not sure there is a friendlier place to do a PhD in the country. The opportunities to make a real contribution to the department, the university and its students are so great. Being allowed to write and run an undergraduate course over my time here has been really rewarding, personally and professionally, and I am grateful that the department trusts its postgraduate cohort to do such important work. I have been at UCL a long time—now almost nine years—and I have been lucky to enjoy conversation and advice from the many brilliant people here. Call it Stockholm syndrome, but I think I might even like the ubiquitous olive green paint.

In particular, I must thank Richard Hoyle for his endless work in accommodating my ridiculous requests when using the department computing facilities. Is there anything he can't do with a single terminal command?! I am also grateful for his good humour and the fact that he has forgiven me for breaking the nightly department-wide backups only half a dozen times. Also in the department, I must thank—in the way that tradition rightly dictates—Helen Higgins and Soheni for

Figure 0: A handsome group of talented mathematicians (with one probable exception) on the top of Snowdon

putting up with me.

My life here would have been much less interesting had I not met Luciano Rila, the greatest agent in London. All the fun ~~distractions~~ jobs I've had—teaching A-level, running maths competitions in schools, taking the Chocolate Fountain Talk™ around the country—have come about because Luciano thought I might do an alright job of them. For his confidence, and the huge amount of opportunities he has thrown my way, I am very grateful.

Speaking of teaching, I am grateful to Carl and Amanda at the BASc for letting me be an early part of their splendid programme. I am so pleased to see the successes of the smiling faces that came through my chalk-filled maths classes.

I have also been lucky to have such good friends here. A PhD can be lonely work and I may well have crumpled many years ago without the friendly chat, the outrageously long lunch breaks, and Dunkirk spirit of my fellow compatriots of the Kathleen Lonsdale Building Site. With special mention to Anna, $\widetilde{\mathrm{G}}$in, Ginbelg, Nurul Huda Binti Mohammad Ramli, Mart, Olly, Peter (who?), Sam and Scroggs: thank you for being great company and good people.

Closer to home, I am grateful for the good company and cooking of my friends in 28JH (with the exception of the mice), and for my family: Mum for making me love maths and for always being proud, Dad for those walks we had to the station every day and for reminding me to step back and look from other angles, and Clair for never forgetting to put me in my place.

It's been good fun.

Contents

Chapter 1

Introduction

This thesis concerns itself with the behaviour of *suspensions*: fluids with particles distributed within them. Suspensions can be found both in nature and as the basis of many products in industry. Blood, ceramics, paper pulp, paint and adhesives, to name just a few, can all be characterised as a background fluid in which small particles are distributed. Sometimes these background fluids can exhibit very simple behaviour—often it is just water—and sometimes they can be more complicated, such as the plasma surrounding blood cells. The submerged particles themselves—illustrated crudely in fig. 1.1—also alter the behaviour of the suspension. In some cases the submerged particles are mostly of the same size or shape: cornflour particles can be seen in fig. 1.2. But often, using the example of cells and proteins in blood again, they are widely varying in structure and number. Particle sizes can go from the order of nanometres in the case of proteins, to centimetres in the case of concretes. States of suspensions can vary from very low-viscosity gases to highly viscoelastic crystalline structures, so observations made of suspensions range wildly.

The key question, in both theory and practice, is how to predict and understand the macroscopic behaviour of these suspensions by considering their microscopic properties. The macroscopic behaviours we might be interested in include those both in equilibrium and in motion. For example, when pumping concrete (Hafid

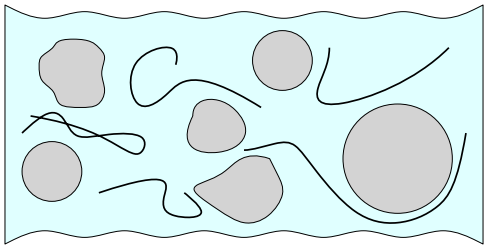

Figure 1.1: Suspensions can consist of all sorts of particle shapes: big, small; smooth, rough; ball-like particles, string-like molecules.

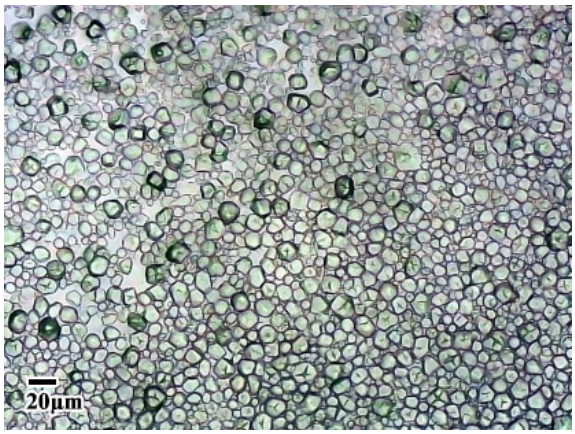

Figure 1.2: Cornflour in suspension, where the polymer has formed into particles. Image shows approximately 0.7 mm on the horizontal. Micrograph courtesy of Peter Kilbride at Asymptote.

et al., 2010), it is observed that the stones in the concrete aggregate form clusters and chains. These clusters can cause blockages in pipes, and so understanding the impact of an imposed shear rate on particle aggregation rate could prove useful. Similarly, being able to predict the effective viscosity of this mixture would allow on-site engineers to set the pumping pressure to its most efficient. More technological implementations may wish to learn about the thermal conductivity of a suspension.

On the microscopic scale, we could consider hydrodynamic and lubrication forces: loosely, how the particles interact with each other. As well as considering forces on the particles, we would also want to track the positions of the particles—either at an individual level, or as some form of average. With a complete set of microscopic information for a material, determining the macroscopic behaviour reduces to having to solve a well-posed boundary-value problem (in theory).

Suspensions of very small particles (orders of nanometres) are known as *colloids*. At this scale, the particles additionally bounce around randomly in the fluid continuously. This distinction applies to how we model the particles: at very small, molecular scales, colloids require the inclusion of Brownian motion, modelling the random vibrations of molecules at this level. The simulation approach we introduce in chapter 2 can be used with colloidal suspensions, but this thesis otherwise concerns itself with suspensions of larger particles, i.e. non-colloidial suspensions.

The investigation of suspensions fits naturally in the field of *rheology*: the branch of fluid mechanics studying deformation and flow. Understanding how a fluid behaves when it is subjected to an imposed stress—for example, being pumped through a pipe or streaming down a surface—is key to determining its flow. In turn, the flow of a fluid can directly affect the final outcome of the flow: think of a smooth paint coating on an aeroplane wing. To this end, a wide range of rheological experiments have been developed to describe the reactions of a fluid to various stresses. To understand

these reactions, however, requires coupling these measurements to theory. Often the reaction is governed by the internal structure of the fluid, and it is with the theory of the structure that rheologists are able to predict the behaviour of classes of fluid. Suspensions can provide a great deal of structure to a fluid, not just by their presence but also by how they aggregate and disperse, which makes it a natural problem for rheologists to investigate.

Practical studies of particle suspensions can often be difficult and expensive, due to the small length and time scales involved, as well as multiple interactions in difficult geometries under imposed external factors (forces, velocities, temperatures, etc.). On the lengthscales we are examining (generally order nanometres to micrometres), interactions are both physical and chemical, and extracting the physics we want (typically the influence of a certain factor) can be complicated by the influence of these on each other. As such, a move to a numerical simulation can increase the understanding we have about these suspensions and allow us a greater degree of control. We can try different interaction models or combine imposed conditions, as examples, with little time or expense penalty.

The addition of particles to a flowing liquid unsurprisingly causes the flow to become significantly more complicated, and since they are ubiquitous in the aforementioned fields, considerable work has been done in modelling these suspensions. Indeed, chapters 3 and 5 are concerned quite heavily with taking rheological measurements of suspensions. The first rheological question asked of suspensions was how the addition of particles affects the *viscosity* of a fluid. The viscosity of a fluid, μ, is a measure of its resistance to deformation.

The conventional way to measure a fluid's viscosity is to place it between parallel plates, shear it, and measure the forces it exerts on the plates. This gives a measure of the internal forces in the fluid, represented as the stress. In the simplest case, we may find that there is a linear relationship between the stress, σ (also τ in some literature), and the strain rate it is experiencing, $\dot{\gamma}$, representing the movement of the fluid,

$$\sigma = \mu\dot{\gamma}. \tag{1.1}$$

The viscosity term, μ, is the scalar factor in this linear relationship, and if this relationship holds, we say that the fluid is Newtonian. This class of fluids includes water and air.

Many fluids, however, do not behave in this way, and have stresses which depend on not just the shear rate but the current amount of shear, temperature, electric fields, time, or historical values of these quantities. Indeed, the addition of particles makes the fluid inhomogeneous and so the stress–shear rate relation may no longer be given

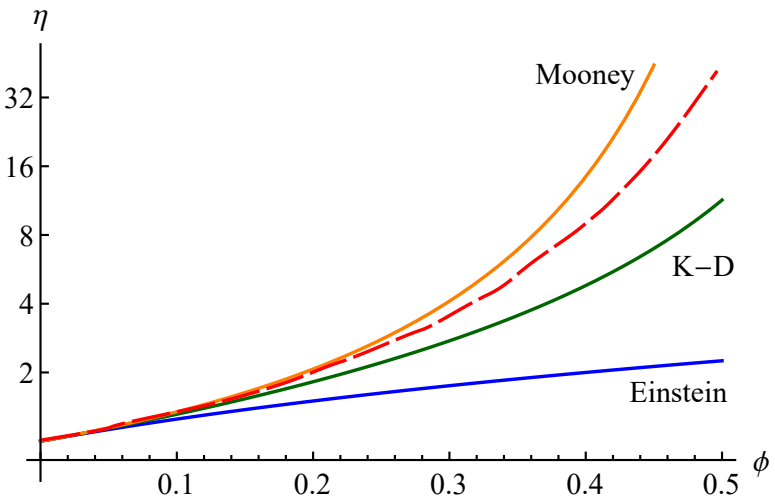

Figure 1.3: Comparison of viscosity models from Einstein (1906) (eq. (1.3)), Krieger & Dougherty (1959) (eq. (1.4)) and Mooney (1951) with dashed best-fit curve through data from experiments with noncolloidal glass spheres of sizes 5–105 µm (Lewis & Nielsen, 1968).

by the Newtonian linear relationship. We therefore define the *effective viscosity*, η, to be the viscosity of the Newtonian fluid which gives the same stress at the same shear rate.

The first answer to the question of how the addition of a suspension affects the effective viscosity was given by Einstein (1906). In his paper he derives theoretically an expression for the effective viscosity of a dilute suspension of spheres in terms of the volume fraction, or packing fraction, ϕ,

$$\phi = \frac{V_{\text{particles}}}{V_{\text{particles}} + V_{\text{fluid}}}, \tag{1.2}$$

where $V_{\text{particles}}$ and V_{fluid} are the volumes of the particles and fluid respectively. His expression, valid for a dilute concentration of spheres in a Newtonian suspending medium of viscosity μ, gives the effective viscosity, η, of the suspension as

$$\eta = \left(1 + \frac{5}{2}\phi\right)\mu. \tag{1.3}$$

Since this expression can be considered as the first two terms in an expansion in ϕ, it is only valid for concentrations where ϕ^2 is very small. This small volume concentration, or dilute, limit also insists that the particles are sufficiently separated so that they only interact with the flow, not each other.

Figure 1.3 shows the validity of this approximation when compared with experimental results from Lewis & Nielsen (1968). To better capture the effective viscosity at higher volume fractions, other models have since been proposed. A common choice, also plotted in fig. 1.3 is the Krieger–Dougherty equation (Krieger &

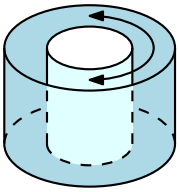

Figure 1.4: The Couette rheometer is a standard piece of rheological equipment. The test fluid is placed in between concentric cylinders and the inner cylinder is rotated.

Dougherty, 1959), which is given for spheres as

$$\eta = \left(1 - \frac{\phi}{\phi_m}\right)^{-5\phi_m/2} \mu. \tag{1.4}$$

Here, ϕ_m is the maximum packing fraction, empirically normally chosen to be 0.64, which corresponds to random close packing in 3D. Many other models of the form $\eta = \mu f(\phi, \phi_m)$ exist (see Table I in Dörr *et al.* (2013)), all of which are designed for use with small and large values of ϕ, and most of which reduce to Einstein's formulation for low volume fractions. Differences between the models emerge at larger values of ϕ, where the effect of particle structure, ignored in this formulation, is more noticeable.

From these very simple models of suspensions, more advanced methods have been designed to tackle different complications. A current area of research is the effect of suspended particles of difference sizes, or polydispersity. It is noticeable that at high concentrations, having just two sets of differently-sized particles can substantially reduce the viscosity of the system (Chong *et al.*, 1971).

No first-principles theory currently exists for polydisperse concentrated systems. A typical simplification is to reduce to n-disperse systems, for small n. That is to say, systems are considered with particles of only a few different classes of size. Having done this, one recent approach to determining the effective viscosity of the suspension by Mwasame *et al.* (2016) is to weight these size classes appropriately. Going from small to large, each new large particle class is considered to be in a Newtonian solution with an effective viscosity already calculated from the previous particle class.

In our simulations we are able to model n-disperse systems. In theory, n can be as large as necessary, but—as will be discussed in chapter 2—resistance data needs to be computed for each size ratio, and in practice this is too time-consuming. However, this represents an improvement over existing codes that use our method. For the purposes of the cases we are interested in, we only show experiments with up to two particle sizes.

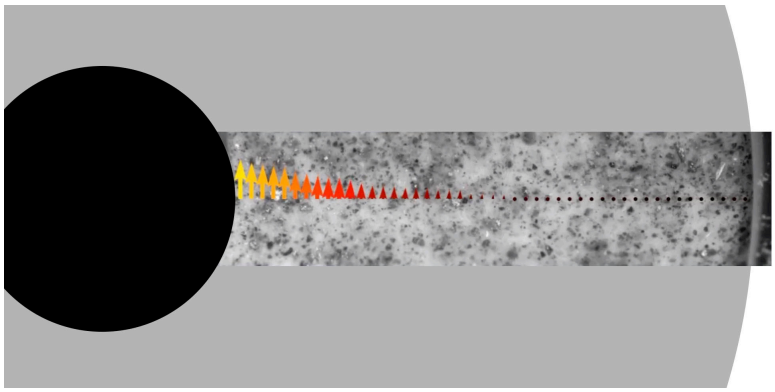

Figure 1.5: With concentrated suspensions in Couette rheometer, sometimes we observe jamming. Here, we look down on a Couette rheometer. The inner cylinder is rotated, driving flow near to it. However, the suspension near the outer cylinder has jammed and does not move. Central image reproduced from the second supplementary video to Peters *et al.* (2016).

Performing rheometry—for example, trying to measure viscosity—on suspensions has its challenges with conventional equipment. In a Couette rheometer, illustrated in fig. 1.4, the test fluid is placed in between concentric cylinders and the inner cylinder is set to rotate. The resulting force on the outer cylinder walls is measured, and, as is discussed in chapter 3, this allows us to measure the viscosity of the fluid, among other things. However, suspensions are not guaranteed to have the same behaviour throughout the sample. Under applied shear, particles can begin to cluster, particularly in concentrated systems. Figure 1.5 shows one such problem in a concentrated suspension placed in a Couette rheometer. The inner cylinder is rotating, driving flow near to it; notated here by the arrows. However, the suspension near the outer cylinder has jammed and does not move. The force recorded by the rheometer as a response to the applied shear is therefore an inaccurate measurement if we have made the standard assumption that the shear has transmitted through the sample. For this reason, other methods are sometimes required to perform rheometry on suspensions, such as suspension imaging.

This thesis concerns the simulation of particles moving through fluid. Returning to the microscale, the simplest such problem is a single particle sedimenting through an otherwise still, viscous, Newtonian liquid. The first work on this problem was by Stokes in 1851, when the now-named Stokes' law was published for the velocity of a small single sphere sedimenting in such a fluid. As will be discussed at the beginning of chapter 2, the simulation method used in the work that follows is ultimately an extension of this law.

As we have seen, real-life particles are rarely completely spherical, and theory has been developed since 1851 for sedimenting particles of different shapes. Not long after, Oberbeck (1876) calculated analytically a solution for a sedimenting spheroid, and, more recently, Batchelor (1970) used slender-body theory to find the velocity

of a sedimenting rod or fibre. The appetite for analytically finding the flow around particles of prescribed shapes has waned in the literature as studies have become more interested in multiple-particle systems. Given the development of theory for spherical particles, common approaches for particles of other shapes tend to be variations on spherical particles. Roughening up the sides of spherical particles, for example, is considered in chapter 5.

As we have already seen, work on modelling multiple-particle systems started with Einstein (1906). The development of work with dilute suspensions is nicely summarised (although a little outdated now) in the review by Davis & Acrivos (1985), and the theory derived in this area forms the basis of that for more concentrated suspensions, in which we are interested.

Modelling the behaviour of particles in more concentrated solutions presents some difficulties, perhaps the most significant of which comes from the many-body interactions of the particles. In the dilute limit, particles only act with the flow, and not each other. In concentrated suspensions we see that particles act on each other in two ways: with *long-range hydrodynamic* interactions and *lubrication* interactions. Particles suspended in a fluid create long-ranged flows as they move, and in turn move according to the motion of the suspending fluid. In this way, particles that can be quite separate move according to the motion of all other particles in the fluid (which could be reflected by any walls): this is the long-range hydrodynamic interaction. As particles get very close, they experience a force resulting from the pressure in the thin viscous layer of fluid which is squeezed out from between them: this is the lubrication interaction. Accurately describing both of these interactions, ideally with an efficient method, is key to modelling the overall behaviour of the fluid.

The importance of many-body hydrodynamic interactions was shown by Beenakker (1984) and others in the early 1980s, when calculations showed that these many-body effects were significant in determining the effective viscosity of the fluid. Since the disturbance to fluid velocity caused by a force acting on a particle decays away from that particle as $1/r$ (where r is distance), in a many-body system, we have a large sum of terms that does not converge. Fortunately, thanks to slightly earlier work by Batchelor (1972), this non-convergence was interpreted and understood, leading to an absolutely convergent form of velocity disturbance. This was then extended, with further problems resolved, by Brady & Bossis (1988), giving us the form that we use in this thesis, and which is described fully in chapter 2.

Several methods for simulating dynamic suspensions in general have been developed over the years. Brady & Bossis (1988) breaks them into five different length scales:

1. Molecular scale: Classical mechanics governs molecular dynamics as particles interact in vacuum through interparticle forces from electrostatic or Lennard-Jones potentials, for example.

2. Single large molecules (e.g. proteins, polymer chains): The chemistry/geometry of the molecule dictates the macromolecular properties, such as elasticity of polymers. Questions asked here include how polymers fold.

3. Entire protein/polymer molecules or fibres and glass beads: Particles interact through hydrodynamic forces and interparticle forces.

4. Granular scale: Now in the domain of grains of sand up to billiard balls, still in a continuum model, we are assuming that the fluid between the particles (often air) plays no role in the dynamics of the grains. Behaviour is mostly governed by particle interactions and gravity, where we have to include macroscopic concepts such as friction and elasticity.

5. Gravitational/stellar scale: Here we consider whole planets, stars or even galaxies as point particles, interacting in vacuum under classical mechanics (back to the molecular scale!). Questions asked here involve the stability of the solar system and the evolution of galaxies.

The third scale is the one we are interested in, but it has the disadvantage of being also the scale where the continuum nature of the problem is most important. Being unable to disregard it, any approach has to tackle this issue directly, which makes it difficult. Admittedly, the problem could be much harder: glass beads in water, for example, suffers from being a macroscopic particle problem with moderate Reynolds number and a background fluid through which particles interact. Fortunately, in our scale, the Reynolds number is small—that is to say, viscous forces are stronger than inertial forces, or more simply that the flow is slow and the fluid is thick—and this gives us our way into the problem.

Chapter 2 introduces the method we use: *Stokesian Dynamics*. It is a relatively popular choice for multiple-particle simulations as it considers both long-range hydrodynamics and lubrication, as well as allowing for any additional particle force laws. It is well-suited to three-dimensional simulation, both in finite and periodic domains, with relatively low calculation and time penalty. Other approaches exist, of course. One contemporary choice, found in Yeo & Maxey (2010), is the Force-Coupling Method. This is similar to Stokesian Dynamics in that it also uses a truncated multipole expansion of the Stokes equations. Another choice, employed in Gallier *et al.* (2014*a*), is to use a fictitious domain approach, combined with Stokesian Dynamics for lubrication forces. This approach allows them to get over the typical constraints of multipole expansion methods: namely that the particles

have to be spherical and the background fluid has to be Newtonian. Other methods of overcoming the spherical constraint exist: there are equivalent sphere models with various levels of success. We overcome the latter problem in a different way in chapter 3.

The structure of this thesis is as follows. A full introduction to each study is included in each chapter.

Chapter 2 We introduce Stokesian Dynamics thoroughly and derive the appropriate equations. We develop Stokesian Dynamics to take in both spherical particles and bead-and-spring dumbbells, which allows for non-Newtonian background fluids. A full recipe is given for creating one's own implementation of Stokesian Dynamics, both non-periodic and periodic. This fixes many typographical errors in the original papers and provides a collated reference. There is a discussion on the computational choices to make. We discuss an anomaly in a popular approximation to the Stokesian Dynamics method which can lead to unstable simulations in some circumstances.

Chapter 3 Simulations are made of non-Newtonian fluids by performing rheological tests on bead-and-spring dumbbell suspensions. We demonstrate that our adaption to Stokesian Dynamics in the previous chapter makes switching dumbbell laws very easy. We establish the validity of this approach by confirming that various dumbbell laws correspond to viscoelastic fluid models under certain regimes. We show how parameters in the models lead to the suspension exhibiting certain properties. We also discuss how best to perform rheological tests in the simulation.

Chapter 4 We simulate a large spherical particle sedimenting through a suspension of many smaller particles that is undergoing oscillatory shear. This follows a recent experimental paper where at some parts of the shear, the sedimenting particle is found to fall 'upwards'. We examine the structure of the small particles formed by the imposed oscillatory shear and the heavy sedimenting particle under various conditions and offer some explanations and a mechanism for the peculiar experimental observation.

Chapter 5 We simulate shear-thickening suspensions by adding friction to our particles. We implement this in Stokesian Dynamics with a new, more accurate method. We demonstrate the level of shear-thickening achieved under shear given certain properties of the suspension. Finally, we suggest a condition on the frictional model for discontinuous shear thickening to be exhibited.

Chapter 6 Conclusions are offered from the studies in the preceding chapters, and further work is suggested.

Chapter 2

Stokesian Dynamics

2.1 Introduction

Here we use *Stokesian Dynamics*: a microhydrodynamic, low Reynolds number approach to modelling suspensions which considers the interaction of particles with each other against a Newtonian background solvent (Brady & Bossis, 1988). We choose it for its suitability for three-dimensional simulation with low calculation and time penalty.

In the most basic case, Stokes' law (Stokes, 1851), states that a single sphere of radius a, such as in fig. 2.1, travelling with a velocity $\boldsymbol{U}$ in an unbounded Newtonian fluid of viscosity μ, in a low Reynolds number regime, experiences a drag force $\boldsymbol{F}$ of

$$\boldsymbol{F} = -6\pi\mu a\boldsymbol{U}. \tag{2.1}$$

Stokesian Dynamics, at its heart, is an extension of this linear relationship between the force acting on a particle and the velocity at which it travels. As a method, it is adaptable and continues to be used by others in the field, providing some interesting insight into the behaviour of particle suspensions. Validations with experiments (Dratler & Schowalter, 1996) have shown it to provide results within acceptable error.

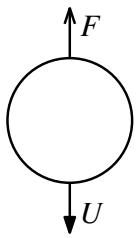

Figure 2.1: Stokesian Dynamics is essentially a multiparticle extension of Stokes' law.

Stokesian Dynamics considers particles suspended in Newtonian fluids—fluids such as air and water whose viscosities, now thinking macroscopically, remain constant under changes in local shear rate. However, it is observable that particles suspended in viscoelastic, non-Newtonian fluids behave differently to those in Newtonian fluids. In these fluids, such as whipped cream, quicksand or printer ink, the relationship between viscosity and shear rate (or indeed history of shear rate, time, or many other things) is more complicated, and we may see elastic effects. Rather than relating viscosity to shear rate, it is more convenient to relate shear stress to shear rate (and other things) and the form of this relationship forms the constitutive equation. There are several well-used models for non-Newtonian fluids, including the Bingham and Oldroyd-B models, each with constitutive equations of varying complication.

The observations of particles in viscoelastic fluids here mentioned are summarised, starting from investigations in 1946, in Chhabra (2006, table 4.1). Some early observations include recognising that in a Bingham plastic, the region of fluid flow caused by a falling sphere is bounded, with only elastic deformation rather than shear occurring outside of the yielded region, which moves with the sphere. Many calculations have been made to find the drag coefficient of a falling sphere, which differs in different models. Later work examined time-dependence of sphere settling velocities, again different from Newtonian background fluids.

Here, then, we adapt Stokesian Dynamics for non-Newtonian fluids, by creating a framework in which we can introduce polymer chains. Polymers are large, stringy molecules which either arise naturally (such as DNA or proteins), or are synthesised and added to fluids (such as polystyrene) for their useful physical properties: these might include toughness or viscoelasticity. We model the polymers here as bead-and-spring dumbbells: two smaller spherical particles ('beads') with a force between the two.

The validity of modelling polymers through dumbbells is well-established. The constitutive equations of the Oldroyd-B model for viscoelastic fluids, at least, can be derived directly from considering a suspension of dumbbells (Bird & Hassager, 1987, eq. 13.4–5). Each dumbbell has an internal force and in our formulation, the force law given to the dumbbell springs is left open to alteration, allowing for simulations of a variety of models for the background fluid.

This adaptation of Stokesian Dynamics was first seen in Binous & Phillips (1999), where a relationship was formulated between the particles' and dumbbells' velocities and angular velocities, and the forces and torques exerted on them. In this study we refine this formulation and go a step further, considering the dumbbells as a whole with an internal velocity difference, allowing larger particles of different sizes, and introducing a background shear rate to our fluid. This increases the number

of scenarios we can set our simulation working on, as well as allowing us to easily switch between different fluid models. A fuller description of the improvements is found in section 2.3.2.

The predictions of our dumbbell model can be seen in chapter 3.

This motivation has also allowed us to investigate bidisperse Newtonian suspensions by turning the dumbbell forces off, allowing the smaller beads to move freely. Such a study can be seen in chapter 4.

2.2 Mathematical setup

Consider a finite system of N rigid spheres suspended in an unbounded Newtonian fluid. The spheres are small enough such that the particle Reynolds number $Re = \rho U a/\mu$ is much less than one, where ρ is the density of the fluid. The fluid may be undergoing an imposed linear flow,

$$\boldsymbol{u}^{\infty}(\boldsymbol{x}) = \boldsymbol{U}^{\infty} + \boldsymbol{\Omega}^{\infty}\times\boldsymbol{x} + \boldsymbol{E}^{\infty}\cdot\boldsymbol{x}. \tag{2.2}$$

Such a flow is illustrated in fig. 2.2, where a shear flow at the top of the figure is composed from a constant background velocity, $\boldsymbol{U}^{\infty}$, a background angular velocity, $\boldsymbol{\Omega}^{\infty}$, and a background strain rate, $\boldsymbol{E}^{\infty}$. Since the Reynolds number is small, inertia is negligible. Furthermore, we do not consider external forces acting on the fluid, which means we are looking to solve the Stokes equations,

$$\boldsymbol{\nabla}\cdot\boldsymbol{\sigma} = \boldsymbol{0}, \qquad \boldsymbol{\nabla}\cdot\boldsymbol{u} = 0. \tag{2.3}$$

For a Newtonian fluid, the stress tensor, $\boldsymbol{\sigma}$, is given by

$$\boldsymbol{\sigma} = -p\boldsymbol{I} + 2\mu\boldsymbol{E} = -p\boldsymbol{I} + 2\mu\left(\boldsymbol{\nabla}\boldsymbol{u} + (\boldsymbol{\nabla}\boldsymbol{u})^{\mathrm{T}}\right). \tag{2.4}$$

A key property of the Stokes equations is that they have no explicit time dependence: the fluid flow is determined instantaneously by the imposed boundary conditions. In particle suspensions, these conditions are the forces applied to the boundaries of the particles, therefore the flow depends entirely on the configuration of the suspending particles, along with the imposed forces. The goal of the Stokesian Dynamics method is to take this configuration and these forces as inputs, and to generate the flow velocities.

The linearity of the Stokes equations allows us to use Green's functions to solve them. This, as discussed fully in section 2.3.1, leads to a linear relationship between

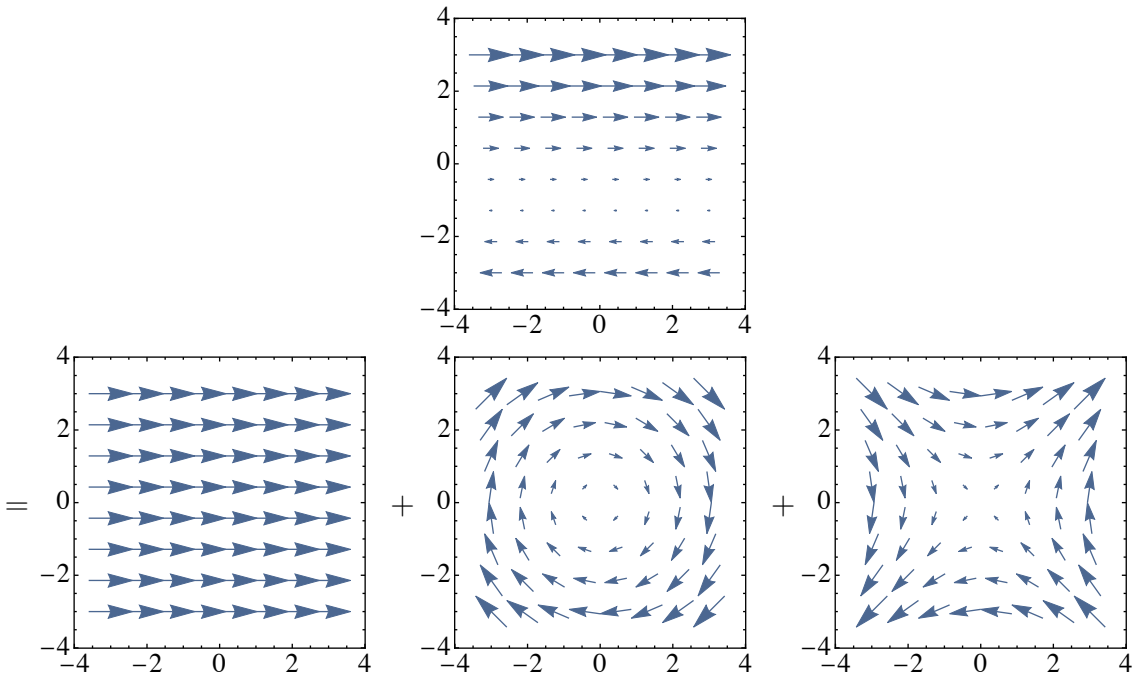

Figure 2.2: The linear flow at the top, $\boldsymbol{u}^\infty(\boldsymbol{x})$, is composed of $\boldsymbol{U}^\infty + \boldsymbol{\Omega}^\infty \times \boldsymbol{x} + \boldsymbol{E}^\infty \cdot \boldsymbol{x}$. The values here, typical of a shear flow in the xz-plane, are $\boldsymbol{U}^\infty = (1,0,0)$, $\boldsymbol{\Omega}^\infty = \frac{1}{2}(0,1,0)$, $\boldsymbol{E}^\infty = \frac{1}{2}\left(\begin{smallmatrix} 0 & 0 & 1 \\ 0 & 0 & 0 \\ 1 & 0 & 0 \end{smallmatrix}\right)$.

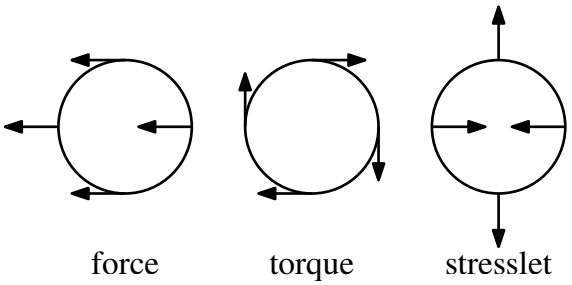

Figure 2.3: The first force moments: force, torque and stresslet, illustrated diagrammatically.

the velocity of suspended particles and the distribution of point forces applied to them. We consolidate the point force distributions into the total forces on each particle by expanding the force and velocity terms into moments. This expansion, again discussed in section 2.3.1, keeps this linear relationship between the force and velocity moments (given that the background velocity is also linear), and hence we can relate these moments by a matrix.

The basic Stokesian Dynamics problem is therefore to formulate the Stokes equations in order to generate an N-particle *grand resistance matrix*, $\mathcal{R}$, (Brenner & O'Neill, 1972) which relates force moments exerted by the fluid on the particles, with particle velocity moments.

Having said that we expand the force and velocity in moments, these moments have physical meaning. The zeroth force moment is the net force, $\boldsymbol{F}^\alpha$, acting on

particle α. The first-order moment is split into an antisymmetric part, the torque $\boldsymbol{T}^\alpha$; and the symmetric part, the stresslet $\boldsymbol{S}^\alpha$. These are shown diagrammatically in fig. 2.3. In most problems, the force and torque will be prescribed, but the stresslet represents particle rigidity, or resistance to compression, so is calculated as part of the method. The stresslet is so-named because the sum of all the particle stresslets in a system gives the total stress of the system. The trace of the first moment is the pressure. Typically, Stokesian Dynamics simulations do no more than calculate the pressure in the system as the particle dynamics in an unbounded system is not considered to be pressure-driven. Should we want to, however, it is possible to simulate pressure-driven flow with Stokesian Dynamics (Nott & Brady, 1994).

The respective velocity moments are the particle velocity against the background flow, $\boldsymbol{U}^\alpha - \boldsymbol{u}^\infty(\boldsymbol{x}^\alpha)$ (where $\boldsymbol{x}^\alpha$ is the position of the particle), the angular velocity against the background flow, $\boldsymbol{\Omega}^\alpha - \boldsymbol{\Omega}^\infty$, and (minus) the rate of strain of the background flow, $-\boldsymbol{E}^\infty$. Note that since the particles are rigid, there is no rate of strain inside the particle, hence we have just the background term. These moments are the minimum amount required, and we choose to not include higher-order moments. There are problems where higher-order moments are significant (Ladd, 1990), but ours is not one of them, and hence we save computational effort (Sierou & Brady, 2001).

The resistance formulation, then, is

$$\begin{pmatrix} \boldsymbol{F}^\alpha \\ \boldsymbol{T}^\alpha \\ \boldsymbol{S}^\alpha \end{pmatrix} = \mathcal{R} \begin{pmatrix} \boldsymbol{U}^\alpha - \boldsymbol{u}^\infty(\boldsymbol{x}^\alpha) \\ \boldsymbol{\Omega}^\alpha - \boldsymbol{\Omega}^\infty \\ -\boldsymbol{E}^\infty \end{pmatrix}. \tag{2.5}$$

The inverse problem is to calculate the velocity moments from the force moments:

$$\begin{pmatrix} \boldsymbol{U}^\alpha - \boldsymbol{u}^\infty(\boldsymbol{x}^\alpha) \\ \boldsymbol{\Omega}^\alpha - \boldsymbol{\Omega}^\infty \\ -\boldsymbol{E}^\infty \end{pmatrix} = \mathcal{M} \begin{pmatrix} \boldsymbol{F}^\alpha \\ \boldsymbol{T}^\alpha \\ \boldsymbol{S}^\alpha \end{pmatrix}. \tag{2.6}$$

The matrix $\mathcal{M}$ is the *grand mobility matrix*, and is given by $\mathcal{M} = \mathcal{R}^{-1}$. Detailed construction of these matrices, in particular how we manipulate rank 2 tensors $\boldsymbol{S}$ and $\boldsymbol{E}$ to fit into the two column vectors, comes in sections 2.3 and 2.4.

The grand matrices $\mathcal{M}$ and $\mathcal{R}$ possess important properties:

- They are symmetric, as shown in section 2.4.5,
- They are positive definite, due to the dissipative nature of the system (Kim & Karrila, 2005, sec. 5.2.1),

- They depend only on the instantaneous positions of the particles, as discussed in sections 2.3 and 2.4.

The symmetry and positive definiteness of the matrices allows for quicker inversion routines.

In this thesis we consider suspensions of spheres and dumbbells (in chapter 3) or large spheres and small spheres (in chapter 4). The aim in this section is to construct the grand mobility and resistance matrices for a suspension of spheres and dumbbells, or large spheres and small spheres, in a convenient and computationally cheap way, while still preserving the matrix symmetry.

Dumbbells are formed from two small particles a vector distance $\Delta\boldsymbol{x}$ apart, with a force $\Delta\boldsymbol{F}$ between them. In theory, there is no reason why we cannot include these pairs of two small particles in the resistance and mobility formulations, eqs. (2.5) and (2.6). However, it is advantageous to list the dumbbells separately for two reasons. Firstly, because their force differences, $\Delta\boldsymbol{F}$, are given by our choice of spring law, which in turn is a direct consequence of the choice of non-Newtonian model that we are trying to simulate in chapter 3. Leaving this term exposed, then, allows us to impose different spring laws easily. Secondly, we choose to only impose the zeroth force and velocity moments of the dumbbells, and let the higher moments be free. This gives us a considerable computational advantage, while only losing information (such as rotation) about the system's smallest particles which we are not interested in.

Force laws investigated in chapter 3 include those in the following models:

- Hookean,
$$\Delta\boldsymbol{F} = -k\Delta\boldsymbol{x}, \tag{2.7}$$

- FENE (finitely extensible nonlinear elastic) (Bird & Hassager, 1987, eq. 13.5-1),
$$\Delta\boldsymbol{F} = \frac{-k\Delta\boldsymbol{x}}{1-(\Delta x)^2/\ell^2}, \tag{2.8}$$

(for parameters k, ℓ), at least, as these are common model choices in other simulations. The Hookean models enjoys simplicity, while the FENE model is a closer approximation to polymer deformation (Flory, 1953, p. 428, eq. B-4). If we are performing simulations, as in chapter 4, with large spheres and small spheres, it suffices to set the force law to be zero.

The form of the resistance formulation that we settle on, including dumbbells, is

then

$$\begin{pmatrix} \boldsymbol{F}^{\alpha} \\ \boldsymbol{T}^{\alpha} \\ \boldsymbol{S}^{\alpha} \\ \boldsymbol{F}^{\beta} \\ \Delta\boldsymbol{F}^{\beta} \end{pmatrix} = \mathcal{R} \begin{pmatrix} \boldsymbol{U}^{\alpha} - \boldsymbol{u}^{\infty}(\boldsymbol{x}^{\alpha}) \\ \boldsymbol{\Omega}^{\alpha} - \boldsymbol{\Omega}^{\infty} \\ -\boldsymbol{E}^{\infty} \\ \boldsymbol{U}^{\beta} - \boldsymbol{u}^{\infty}(\overline{\boldsymbol{x}}^{\beta}) \\ \frac{1}{2}\left[\Delta\boldsymbol{U}^{\beta} - \Delta\boldsymbol{u}^{\infty}(\overline{\boldsymbol{x}}^{\beta}; \Delta\boldsymbol{x}^{\beta})\right] \end{pmatrix}, \tag{2.9}$$

where we have adopted the notation α to represent spheres, and β to represent dumbbells (or pairs of small spheres). The mobility form is the same as eq. (2.9), but inverted. The detail in the construction of the vectors and the motivation behind their form can be found in section 2.3.3.

Throughout this section, we adopt the common convention of labelling the elements of the resistance and mobility matrix using the letters $\boldsymbol{A}, \boldsymbol{B}, \boldsymbol{C}, \boldsymbol{G}, \boldsymbol{H}, \boldsymbol{M}$, and extending to $\boldsymbol{R}$ for the dumbbell elements:

$$\mathcal{R} = \begin{pmatrix} \boldsymbol{A} & \widetilde{\boldsymbol{B}} & \widetilde{\boldsymbol{G}} & \boldsymbol{R}^{14} & \boldsymbol{R}^{15} \\ \boldsymbol{B} & \boldsymbol{C} & \widetilde{\boldsymbol{H}} & \boldsymbol{R}^{24} & \boldsymbol{R}^{25} \\ \boldsymbol{G} & \boldsymbol{H} & \boldsymbol{M} & \boldsymbol{R}^{34} & \boldsymbol{R}^{35} \\ \boldsymbol{R}^{41} & \boldsymbol{R}^{42} & \boldsymbol{R}^{43} & \boldsymbol{R}^{44} & \boldsymbol{R}^{45} \\ \boldsymbol{R}^{51} & \boldsymbol{R}^{52} & \boldsymbol{R}^{53} & \boldsymbol{R}^{54} & \boldsymbol{R}^{55} \end{pmatrix}. \tag{2.10}$$

The mobility matrix uses the same six letters but in lowercase, and we label the dumbbell elements $\boldsymbol{m}^{44}$, etc.,

$$\mathcal{M} = \begin{pmatrix} \boldsymbol{a} & \tilde{\boldsymbol{b}} & \tilde{\boldsymbol{g}} & \boldsymbol{m}^{14} & \boldsymbol{m}^{15} \\ \boldsymbol{b} & \boldsymbol{c} & \tilde{\boldsymbol{h}} & \boldsymbol{m}^{24} & \boldsymbol{m}^{25} \\ \boldsymbol{g} & \boldsymbol{h} & \boldsymbol{m} & \boldsymbol{m}^{34} & \boldsymbol{m}^{35} \\ \boldsymbol{m}^{41} & \boldsymbol{m}^{42} & \boldsymbol{m}^{43} & \boldsymbol{m}^{44} & \boldsymbol{m}^{45} \\ \boldsymbol{m}^{51} & \boldsymbol{m}^{52} & \boldsymbol{m}^{53} & \boldsymbol{m}^{54} & \boldsymbol{m}^{55} \end{pmatrix}. \tag{2.11}$$

As the number of particles in a system increases, the computational cost of working out the fluid velocity around them using an exact method (such as a boundary integral method) becomes prohibitively large. Stokesian Dynamics reduces this cost by taking advantage of the nature of the hydrodynamic interaction of particles. For particles at large separation distances, we have asymptotic expressions for the velocity of the surrounding fluid. At short separation distances, the majority of the hydrodynamic force on a particle comes from the strong pressure gradients required to squeeze fluid out from between it and its neighbour. For interacting spheres we have full expressions for this lubrication-dominated fluid motion. Stokesian Dynamics combines these two regimes to provide expressions which work well at all separation distances.

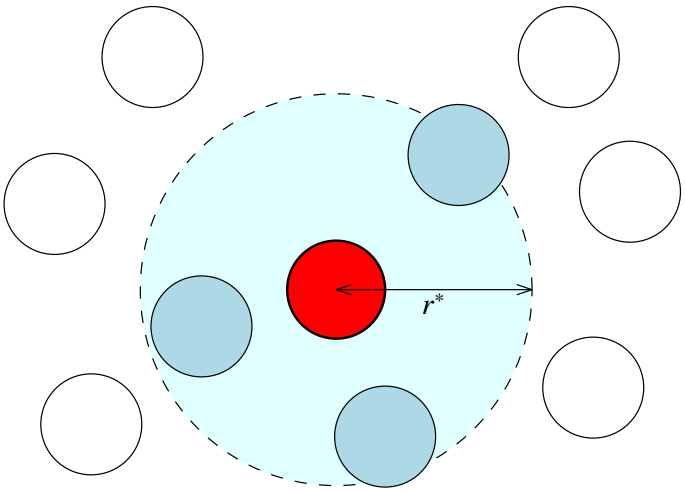

Figure 2.4: All particle pairs have their far-field mobility interactions included in $\mathcal{M}^{\infty}$, but only particle pairs closer than the critical radius, r^*, have lubrication forces included in the resistance matrices $\mathcal{R}^{2\mathrm{B,exact}}$ and $\mathcal{R}^{2\mathrm{B},\infty}$.

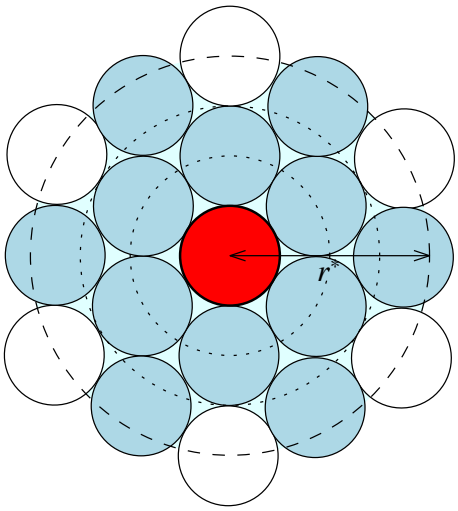

Figure 2.5: The choice of $r^* = 4$ sets particles to interact under lubrication forces with particles in a 'shell' of neighbours (dark blue).

The far-field asymptotic expressions concern all pairs of particles, whereas the lubrication expressions only concern close pairs. For two spherical particles with radius a_α and $a_{\widetilde{\alpha}}$, the lubrication force scales as $(r - a_\alpha - a_{\widetilde{\alpha}})^{-1}$, so we define 'close' by choosing a threshold value of r,

$$r^* = 2(a_\alpha + a_{\widetilde{\alpha}}), \tag{2.12}$$

where for particles closer than this, we include lubrication forces on top of the mobility forces. A typical choice for r^* is 4 (Banchio & Brady, 2003). Figures 2.4 and 2.5 illustrate this setup.

The Stokesian Dynamics method of combining the two regimes is made slightly complicated by the fact that the far-field expressions come as asymptotic expansions in the mobility form, eq. (2.6), while the near-field lubrication expressions come in

the resistance, i.e. the inverse, form, eq. (2.5). The far-field, asymptotic expressions are linear equations known as *Faxén's laws*, and the construction of the mobility matrix, called $\mathcal{M}^\infty$, from them is given in section 2.3. The lubrication expressions are known exactly for pairs of particles, so by summing these relations for all pairs of close particles, ignoring three-body effects (discussed briefly in section 2.8 and in more detail in Wilson (2013)), we construct a resistance matrix, $\mathcal{R}^{\text{2B,exact}}$. This construction is detailed in section 2.4.

Combining the two forms requires inverting the far-field mobility expressions, $\mathcal{M}^\infty$, into a far-field resistance matrix, $(\mathcal{M}^\infty)^{-1}$. In doing so, we calculate infinite reflections among all particles and moments to find a true many-body, far-field interaction (Durlofsky *et al.*, 1987). We only include the first two moments of the asymptotic mobility expansion in the method, but note that had we included all of them, lubrication would have been included in the inversion of the mobility matrix.

We then add the inverted far-field mobility matrix to the lubrication matrix. We have to be careful about double-counting, however, since the lubrication expressions already include mobility interactions, and hence we need to remove a mobility interaction. This is done by finding $\mathcal{M}^\infty$ for each 'close' particle pair, inverting it; and calling the sum of that over all pairs $\mathcal{R}^{\text{2B},\infty}$. This is then subtracted from the sum of $(\mathcal{M}^\infty)^{-1}$ and $\mathcal{R}^{\text{2B,exact}}$.

In summary, then, the Stokesian Dynamics method is:

1. **Find mobility interaction:** Find the mobility matrix $\mathcal{M}$, up to $\boldsymbol{S}$ and $\boldsymbol{E}$ levels, for all pairs of particles, using Faxén's laws. Call it $\mathcal{M}^\infty$. Invert it to get $(\mathcal{M}^\infty)^{-1}$,

2. **Include lubrication interaction:** Find $\mathcal{R}$ using lubrication techniques for each particle pair with centre distance $r < r^*$. Sum over all pairs and call that $\mathcal{R}^{\text{2B,exact}}$ (the two-body, exact resistance matrix).

3. **Remove double-counting:** When we find $\mathcal{R}^{\text{2B,exact}}$, this inadvertently includes mobility interactions. Since we have already included mobility interactions in step 1, we have double-counted and need to remove a mobility interaction. Hence we find $\mathcal{M}^\infty$ for each particle pair $r < r^*$, invert it; and call the sum of that over all pairs $\mathcal{R}^{\text{2B},\infty}$, with a view to subtracting it.

Finally we construct our grand resistance matrix $\mathcal{R}$ by putting these three matrices together:

$$\mathcal{R} = (\mathcal{M}^\infty)^{-1} + (\mathcal{R}^{\text{2B,exact}} - \mathcal{R}^{\text{2B},\infty}). \tag{2.13}$$

The details of this construction from a programmatic perspective can be found in section 2.6.1.

Stokesian Dynamics considers a finite number of particles in an unbounded fluid. The construction presented here does not natively allow for an infinite number of particles. If the suspension can be considered as existing in a periodic domain (which is not always possible, for example under three-dimensional uniaxial strain (Sami, 1996)), the method can be applied to this periodic domain using Ewald summation (Brady *et al.*, 1988). This is developed in section 2.5, and used in chapter 5.

2.3 Construction of far-field mobility matrix $\mathcal{M}^\infty$

2.3.1 Mobility matrix for spheres only

We have already said that the linearity of the Stokes equations allows us to use Green's functions to solve them. Stokesian Dynamics works by considering each particle in the suspension as a distribution of point forces over the surface of the particle. The Green's function for Stokes flow, sometimes called the Oseen tensor $\boldsymbol{J}(\boldsymbol{r})$,

$$J_{ij}(\boldsymbol{r}) = \frac{\delta_{ij}}{r} + \frac{r_i r_j}{r^3} \tag{2.14}$$

$$= (\nabla^2 \delta_{ij} - \nabla_i \nabla_j) r, \tag{2.15}$$

where $r = |\boldsymbol{r}|$, gives us the response of the (viscous) fluid, $\boldsymbol{u}(\boldsymbol{x})$, to a single point force, $\boldsymbol{f}$:

$$u_i(\boldsymbol{x}) = \frac{1}{8\pi\mu} J_{ij}(\boldsymbol{x}) f_j. \tag{2.16}$$

(Note that here, and throughout the thesis, we use the Einstein summation convention.) Since the linearity of the Stokes equations allows us to superimpose these responses, we are able to find a linear expression for the response of the fluid—its velocity—by summing over the point forces which have been distributed over all the particles. This gives us the following integral representation for the velocity field in Stokes flow.

The velocity field, $\boldsymbol{u}(\boldsymbol{x})$, due to N particles at zero Reynolds number in an otherwise unbounded and quiescent fluid is given by the boundary integral equation for Stokes flow (Ladyzhenskaya, 1964; Durlofsky *et al.*, 1987, eqs. 19 and 2.4 respectively):

$$u_i(\boldsymbol{x}) = u_i^\infty(\boldsymbol{x}) + \frac{1}{8\pi\mu} \sum_{\widetilde{\alpha}=1}^{N} \int_{S^{\widetilde{\alpha}}} \left[J_{ij}(\boldsymbol{x} - \boldsymbol{y}) f_j(\boldsymbol{y}) \right] \mathrm{d}S_{\boldsymbol{y}}, \tag{2.17}$$

where

- $u_i^\infty(\boldsymbol{x})$ is the linear velocity field in the absence of the particles, eq. (2.2),
- $S^{\widetilde{\alpha}}$ is the surface of particle $\widetilde{\alpha}$;
- $\boldsymbol{y}$ is the location on the particle surface;
- $f_j(\boldsymbol{y})$ is the force density at the point $\boldsymbol{y}$ on the surface of the particle, expressible in terms of the stress tensor σ_{jk} by

$$f_j(\boldsymbol{y}) = \sigma_{jk}(\boldsymbol{y}) n_k(\boldsymbol{y}); \tag{2.18}$$

- $n_i(\boldsymbol{y})$ is the surface normal vector pointing from the fluid into the particle (note that this is the opposite direction to Durlofsky *et al.* (1987), and hence their boundary integral equation has a minus sign before the summation).

We avoid evaluating the Green's function in eq. (2.17) over the surfaces of the particles by instead taking a Taylor series—called a multipole expansion—about the centre, $\boldsymbol{x}^{\widetilde{\alpha}}$, of each particle. Expanding the J_{ij} term alone,

$$\begin{aligned} J_{ij}(\boldsymbol{x}-\boldsymbol{y}) &= J_{ij}(\boldsymbol{x}-\boldsymbol{x}^{\widetilde{\alpha}}) + (x_k^{\widetilde{\alpha}} - y_k)\nabla_k J_{ij}(\boldsymbol{x}-\boldsymbol{x}^{\widetilde{\alpha}}) + \cdots, & (2.19)\\ &= J_{ij}(\boldsymbol{x}-\boldsymbol{x}^{\widetilde{\alpha}}) - (y_k - x_k^{\widetilde{\alpha}})\nabla_k J_{ij}(\boldsymbol{x}-\boldsymbol{x}^{\widetilde{\alpha}}) + \cdots, & (2.20) \end{aligned}$$

then the integral in eq. (2.17) becomes

$$\int_{S^{\widetilde{\alpha}}} \left[J_{ij}(\boldsymbol{x}-\boldsymbol{x}^{\widetilde{\alpha}}) f_j(\boldsymbol{y}) - (y_k - x_k^{\widetilde{\alpha}})\nabla_k J_{ij}(\boldsymbol{x}-\boldsymbol{x}^{\widetilde{\alpha}}) f_j(\boldsymbol{y}) \right] \mathrm{d}S_{\boldsymbol{y}}. \tag{2.21}$$

or, dropping the dependencies,

$$\int_{S^{\widetilde{\alpha}}} \left[J_{ij} f_j - (y_k - x_k^{\widetilde{\alpha}})\nabla_k J_{ij} f_j \right] \mathrm{d}S_{\boldsymbol{y}}. \tag{2.22}$$

Claim: I now make the claim that, looking at the second term,[1]

$$\int_{S^{\widetilde{\alpha}}} -(y_k - x_k^{\widetilde{\alpha}})\nabla_k J_{ij} f_j \,\mathrm{d}S_{\boldsymbol{y}} = R_{ij} T_j - K_{ijk} S_{jk} \tag{2.23}$$

where

$$R_{ij} = \frac{1}{4}\varepsilon_{\ell kj}(\nabla_k J_{i\ell} - \nabla_\ell J_{ik}) = -\frac{1}{2}\varepsilon_{jk\ell}\nabla_k J_{i\ell}, \tag{2.24}$$

[1]The minus sign in the right-hand side contradicts Durlofsky *et al.* (1987), which in its corresponding expression (2.13) uses a plus sign. Here, our $\boldsymbol{R}$, $\boldsymbol{T}$, $\boldsymbol{K}$, $\boldsymbol{S}$ and later $\boldsymbol{F}$ (eq. (2.42)) all match Durlofsky (2.14), (2.7b), (2.12b), (2.10), (2.7a) respectively. $\boldsymbol{R}$ and $\boldsymbol{K}$ match explicitly. $\boldsymbol{F}$, $\boldsymbol{T}$ and $\boldsymbol{S}$ match because they are defined here with different sign *and* with different signed normal. The hope is that the following working serves to show an error in Durlofsky *et al.* (1987), which we believe comes from confusion over the direction of the surface normal.

$$K_{ijk} = \frac{1}{2}(\nabla_k J_{ij} + \nabla_j J_{ik}), \tag{2.25}$$

and

$$T_i = \int_{S^{\widetilde{\alpha}}} \varepsilon_{ijk}(y_j - x_j^{\widetilde{\alpha}}) f_k(\boldsymbol{y}) \,\mathrm{d}S_{\boldsymbol{y}}, \tag{2.26}$$

$$S_{ij} = \frac{1}{2}\int_{S^{\widetilde{\alpha}}} \left[(y_i - x_i^{\widetilde{\alpha}})f_j + (y_j - x_j^{\widetilde{\alpha}})f_i - \frac{2}{3}\delta_{ij}(y_k - x_k^{\widetilde{\alpha}})f_k\right] \mathrm{d}S_{\boldsymbol{y}}. \tag{2.27}$$

The term T_i is the total torque (or couple) exerted by the particle on the fluid, and S_{ij} is the stresslet exerted by the fluid on the particle. The propagator for the torque, R_{ij}, is sometimes called the *rotlet*.

We choose, for now, to simplify the algebra by introducing $X_i = (y_i - x_i^{\widetilde{\alpha}})$. Then

$$\begin{aligned}
R_{ij}T_j &= \int_{S^{\widetilde{\alpha}}} -\frac{1}{2}\varepsilon_{jk\ell}\nabla_k J_{i\ell}\varepsilon_{jmn}X_m f_n \,\mathrm{d}S && (2.28)\\
&= \int_{S^{\widetilde{\alpha}}} -\frac{1}{2}(\varepsilon_{k\ell j}\varepsilon_{jmn})\nabla_k J_{i\ell}X_m f_n \,\mathrm{d}S && (2.29)\\
&= \int_{S^{\widetilde{\alpha}}} -\frac{1}{2}(\delta_{km}\delta_{\ell n} - \delta_{kn}\delta_{\ell m})\nabla_k J_{i\ell}X_m f_n \,\mathrm{d}S && (2.30)\\
&= \int_{S^{\widetilde{\alpha}}} -\frac{1}{2}\left[\nabla_k J_{i\ell}X_k f_\ell - \nabla_k J_{i\ell}X_\ell f_k\right] \mathrm{d}S && (2.31)\\
&= \int_{S^{\widetilde{\alpha}}} -\frac{1}{2}\nabla_k J_{i\ell}\left[X_k f_\ell - X_\ell f_k\right] \mathrm{d}S && (2.32)\\
&= \int_{S^{\widetilde{\alpha}}} -\frac{1}{2}\nabla_k J_{ij}\left[X_k f_j - X_j f_k\right] \mathrm{d}S. && (2.33)
\end{aligned}$$

Also observe that

$$\begin{aligned}
K_{ijk}S_{jk} &= \int_{S^{\widetilde{\alpha}}} \frac{1}{4}(\nabla_k J_{ij} + \nabla_j J_{ik})\left(X_j f_k + X_k f_j - \frac{2}{3}X_\ell f_\ell \delta_{jk}\right) \mathrm{d}S && (2.34)\\
&= \int_{S^{\widetilde{\alpha}}} \frac{1}{4}\left[J_{ij}\left(\nabla_k X_j f_k + \nabla_k X_k f_j - \frac{2}{3}\nabla_j X_\ell f_\ell\right)\right.\\
&\qquad \left. + J_{ik}\left(\nabla_j X_j f_k + \nabla_j X_k f_j - \frac{2}{3}\nabla_k X_\ell f_\ell\right)\right] \mathrm{d}S. && (2.35)
\end{aligned}$$

Now since

$$\nabla_j J_{ij} = 0, \tag{2.36}$$

(by the definition of J_{ij}, eq. (2.15)), this reduces to

$$\begin{aligned}
K_{ijk}S_{jk} &= \int_{S^{\widetilde{\alpha}}} \frac{1}{4}\left[J_{ij}(\nabla_k X_j f_k + \nabla_k X_k f_j) + J_{ik}(\nabla_j X_j f_k + \nabla_j X_k f_j)\right] \mathrm{d}S && (2.37)\\
&= \int_{S^{\widetilde{\alpha}}} \frac{1}{4}J_{ij}\left[\nabla_k X_j f_k + \nabla_k X_k f_j + \nabla_k X_k f_j + \nabla_k X_j f_k\right] \mathrm{d}S && (2.38)
\end{aligned}$$

$$= \int_{S^{\widetilde{\alpha}}} \frac{1}{2} \nabla_k J_{ij} \left[X_j f_k + X_k f_j \right] \mathrm{d}S. \tag{2.39}$$

Hence

$$\begin{aligned} R_{ij} T_j - K_{ijk} S_{jk} &= \int_{S^{\widetilde{\alpha}}} -\frac{1}{2} \nabla_k J_{ij} \left[X_k f_j - X_j f_k \right] \mathrm{d}S \\ &\qquad - \int_{S^{\widetilde{\alpha}}} \frac{1}{2} \nabla_k J_{ij} \left[X_j f_k + X_k f_j \right] \mathrm{d}S \qquad (2.40) \\ &= \int_{S^{\widetilde{\alpha}}} -\nabla_k J_{ij} X_k f_j \, \mathrm{d}S, \qquad (2.41) \end{aligned}$$

as claimed. □

Now, defining

$$F_i = \int_{S^{\widetilde{\alpha}}} f_i(\boldsymbol{y}) \, \mathrm{d}S_{\boldsymbol{y}}, \tag{2.42}$$

the total force exerted by the particle on the fluid, we have, from eq. (2.22),

$$u_i(\boldsymbol{x}) = u_i^\infty(\boldsymbol{x}) + \frac{1}{8\pi\mu} \sum_{\widetilde{\alpha}=1}^{N} \left[J_{ij}(\boldsymbol{x} - \boldsymbol{x}^{\widetilde{\alpha}}) F_j + R_{ij}(\boldsymbol{x} - \boldsymbol{x}^{\widetilde{\alpha}}) T_j - K_{ijk}(\boldsymbol{x} - \boldsymbol{x}^{\widetilde{\alpha}}) S_{jk} + \cdots \right]. \tag{2.43}$$

The ellipsis represents the summation over higher-order moments, with error terms of $O\left(a_{\widetilde{\alpha}}/|\boldsymbol{x} - \boldsymbol{x}^{\widetilde{\alpha}}|^3\right)$, where $a_{\widetilde{\alpha}}$ is the particle radius (Rallison, 2014, p. 172, top). For spherical particles, we can reduce the error term to $O\left(a_{\widetilde{\alpha}}/|\boldsymbol{x} - \boldsymbol{x}^{\widetilde{\alpha}}|^5\right)$ by replacing the Green's function for a point force, J_{ij}, with the Green's function for a sphere, $(1 + a^2\nabla^2/6)J_{ij}$, (and similarly for K_{ijk}), giving

$$\begin{aligned} u_i(\boldsymbol{x}) = u_i^\infty(\boldsymbol{x}) + \frac{1}{8\pi\mu} \sum_{\widetilde{\alpha}=1}^{N} \Bigg[&\left(1 + \frac{1}{6} a^2 \nabla^2\right) J_{ij}(\boldsymbol{x} - \boldsymbol{x}^{\widetilde{\alpha}}) F_j + R_{ij}(\boldsymbol{x} - \boldsymbol{x}^{\widetilde{\alpha}}) T_j \\ &- \left(1 + \frac{1}{10} a^2 \nabla^2\right) K_{ijk}(\boldsymbol{x} - \boldsymbol{x}^{\widetilde{\alpha}}) S_{jk} + \cdots \Bigg]. \end{aligned} \tag{2.44}$$

The motion of a particle, α, immersed in the flow field, eq. (2.44), can be described by *Faxén's laws* for spheres. If we have the same imposed background linear flow of $\boldsymbol{u}^\infty$ as in eq. (2.2), and we have N spherical particles immersed in this flow, then the motion of particle α is given by (Durlofsky *et al.*, 1987, eq. 2.15):

$$U_i^\alpha - u_i^\infty(\boldsymbol{x}^\alpha) = \frac{F_i^\alpha}{6\pi\mu a_\alpha} + \left(1 + \frac{a_\alpha^2}{6} \nabla^2\right) u_i'(\boldsymbol{x}^\alpha), \tag{2.45a}$$

$$\Omega_i^\alpha - \Omega_i^\infty = \frac{T_i^\alpha}{8\pi\mu a_\alpha^3} + \frac{1}{2} \varepsilon_{ijk} \nabla_j u_k'(\boldsymbol{x}^\alpha), \tag{2.45b}$$

$$-E_{ij}^\infty = \frac{1}{2} \left[\frac{S_{ij}^\alpha}{\frac{10}{3}\pi\mu a_\alpha^3} + \left(1 + \frac{a_\alpha^2}{10} \nabla^2\right) \left(\nabla_j u_i'(\boldsymbol{x}^\alpha) + \nabla_i u_j'(\boldsymbol{x}^\alpha) \right) \right], \tag{2.45c}$$

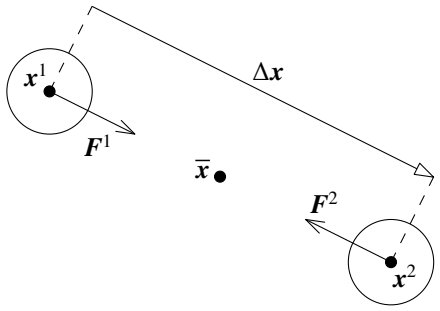

Figure 2.6: Treating the dumbbell as two beads with forces

where a_α is the radius of particle α; μ is the Newtonian viscosity of the suspending fluid; $\nabla_i = \frac{\partial}{\partial x_i}$; $\boldsymbol{x}^\alpha$ is the centre of particle α; and $u_i'(\boldsymbol{x}^\alpha)$ is the disturbance in the velocity field caused by all the particles which are not particle α, and not by the imposed background flow $u_i^\infty(\boldsymbol{x}^\alpha)$,

$$u_i'(\boldsymbol{x}^\alpha) = \frac{1}{8\pi\mu} \sum_{\substack{\widetilde{\alpha}=1 \\ \widetilde{\alpha}\neq\alpha}}^{N} \left[\left(1 + \frac{a_{\widetilde{\alpha}}^2}{6}\nabla^2\right) J_{ij}(\boldsymbol{x}^\alpha - \boldsymbol{x}^{\widetilde{\alpha}}) F_j^{\widetilde{\alpha}} + R_{ij}(\boldsymbol{x}^\alpha - \boldsymbol{x}^{\widetilde{\alpha}}) T_j^{\widetilde{\alpha}} + \left(1 + \frac{a_{\widetilde{\alpha}}^2}{10}\nabla^2\right) K_{ijk}(\boldsymbol{x}^\alpha - \boldsymbol{x}^{\widetilde{\alpha}}) S_{jk}^{\widetilde{\alpha}} + \cdots \right]. \tag{2.46}$$

That we can then write $\boldsymbol{U} - \boldsymbol{u}^\infty$, $\boldsymbol{\Omega} - \boldsymbol{\Omega}^\infty$ and $-\boldsymbol{E}^\infty$, through Faxén's laws, eq. (2.45), as linear combinations of $\boldsymbol{F}$, $\boldsymbol{T}$ and $\boldsymbol{S}$, allows us to relate these six quantities using a matrix $\mathcal{M}$, as in eq. (2.6), or its inverse, $\mathcal{R}$. We will now extend this formulation for a mixture of spheres and dumbbells.

2.3.2 Addition of dumbbells

The first addition of dumbbells to Stokesian Dynamics, as previously mentioned, was performed by Binous & Phillips (1999), whom considered their dumbbells as separate beads. Their mobility form, eq. (2.6)—their eq. (7)—was

$$\begin{pmatrix} \boldsymbol{U}^\alpha \\ \boldsymbol{\Omega}^\alpha \\ \boldsymbol{U}^b \end{pmatrix} = \begin{pmatrix} \boldsymbol{a}^{\alpha\alpha} & \tilde{\boldsymbol{b}}^{\alpha\alpha} & \boldsymbol{a}^{\alpha b} \\ \boldsymbol{b}^{\alpha\alpha} & \boldsymbol{c}^{\alpha\alpha} & \boldsymbol{b}^{\alpha b} \\ \boldsymbol{a}^{b\alpha} & \tilde{\boldsymbol{b}}^{b\alpha} & \boldsymbol{I} \end{pmatrix} \begin{pmatrix} \boldsymbol{F}^\alpha \\ \boldsymbol{T}^\alpha \\ \boldsymbol{F}^b \end{pmatrix}, \tag{2.47}$$

with α marking spheres and b marking beads. In their simulations, they found it convenient to ignore bead–bead interactions, hence the appearance of the identity matrix, $\boldsymbol{I}$. We improve on this formulation in a few ways.

Firstly, by including a background linear flow, i.e., including $\boldsymbol{E}^\infty$ and $\boldsymbol{S}^\alpha$ terms, we are able to perform shear tests on suspensions in chapters 3 and 5 directly through the background flow, a method we find to be better than the alternative of imposing

opposing velocities on walls of spheres. Secondly, we find that in dense suspensions as in chapter 4, the bead–bead interactions are important, so we keep this term. Thirdly, by explicitly pairing the beads as dumbbells, we expose terms that appear in dumbbell models (such as internal force difference), making it easy to apply and switch between these models.

Finally, our code allows for spheres and dumbbells of multiple sizes. Since we only include the zeroth moment for dumbbells—the same as Binous & Phillips (1999)—but include the symmetric and antisymmetric first moments for spheres, this effectively allows us to choose the level of accuracy we want in our simulations, independent of particle size. Although this is at the expense of the third advantage above, we find this useful in discussions such as in section 2.8, where we analyse the accuracy of the method.

In order to expose the useful dumbbell force and velocity terms, we first treat the dumbbells as separate beads, but then perform some simple row and column operations. We find these to be not computationally expensive. Suppose, as in fig. 2.6, the two beads are positioned at $\boldsymbol{x}^1$ and $\boldsymbol{x}^2$, and are exerting forces $\boldsymbol{F}^1$ and $\boldsymbol{F}^2$ (respectively) on each other. We denote:

- the vector distance between them $\Delta\boldsymbol{x} = \boldsymbol{x}^2 - \boldsymbol{x}^1$,
- their midpoint $\overline{\boldsymbol{x}} = \frac{1}{2}(\boldsymbol{x}^1 + \boldsymbol{x}^2)$,
- the difference in forces $\Delta\boldsymbol{F} = \boldsymbol{F}^2 - \boldsymbol{F}^1$,
- the total force $\boldsymbol{F} = \boldsymbol{F}^1 + \boldsymbol{F}^2$,
- the difference in velocities $\Delta\boldsymbol{U} = \boldsymbol{U}^2 - \boldsymbol{U}^1$,
- the average velocity $\boldsymbol{U} = \frac{1}{2}(\boldsymbol{U}^1 + \boldsymbol{U}^2)$,
- the background velocity at the midpoint $\boldsymbol{u}^\infty(\overline{\boldsymbol{x}}) = \frac{1}{2}[\boldsymbol{u}^\infty(\boldsymbol{x}^1) + \boldsymbol{u}^\infty(\boldsymbol{x}^2)]$,
- the difference in background velocity between the beads $\Delta\boldsymbol{u}^\infty(\overline{\boldsymbol{x}}; \Delta\boldsymbol{x}) = \boldsymbol{u}^\infty(\boldsymbol{x}^2) - \boldsymbol{u}^\infty(\boldsymbol{x}^1)$.

The form of the force–velocity part of the mobility matrix, then, is

$$\begin{pmatrix} \boldsymbol{U}^1 - \boldsymbol{u}^\infty(\boldsymbol{x}^1) \\ \boldsymbol{U}^2 - \boldsymbol{u}^\infty(\boldsymbol{x}^2) \end{pmatrix} = \begin{pmatrix} \boldsymbol{a}^{11} & \boldsymbol{a}^{12} \\ \boldsymbol{a}^{21} & \boldsymbol{a}^{22} \end{pmatrix} \begin{pmatrix} \boldsymbol{F}^1 \\ \boldsymbol{F}^2 \end{pmatrix}. \tag{2.48}$$

Row and column operations give us

$$\begin{pmatrix} \boldsymbol{U} - \boldsymbol{u}^\infty(\overline{\boldsymbol{x}}) \\ \frac{1}{2}[\Delta\boldsymbol{U} - \Delta\boldsymbol{u}^\infty(\overline{\boldsymbol{x}}; \Delta\boldsymbol{x})] \end{pmatrix} = \frac{1}{4}\begin{pmatrix} 1 & 1 \\ -1 & 1 \end{pmatrix}\begin{pmatrix} \boldsymbol{a}^{11} & \boldsymbol{a}^{12} \\ \boldsymbol{a}^{21} & \boldsymbol{a}^{22} \end{pmatrix}\begin{pmatrix} 1 & -1 \\ 1 & 1 \end{pmatrix}\begin{pmatrix} \boldsymbol{F} \\ \Delta\boldsymbol{F} \end{pmatrix} \tag{2.49}$$

$$= \frac{1}{4}\begin{pmatrix} \boldsymbol{a}^{11} + \boldsymbol{a}^{12} + \boldsymbol{a}^{21} + \boldsymbol{a}^{22} & -\boldsymbol{a}^{11} + \boldsymbol{a}^{12} - \boldsymbol{a}^{21} + \boldsymbol{a}^{22} \\ -\boldsymbol{a}^{11} - \boldsymbol{a}^{12} + \boldsymbol{a}^{21} + \boldsymbol{a}^{22} & \boldsymbol{a}^{11} - \boldsymbol{a}^{12} - \boldsymbol{a}^{21} + \boldsymbol{a}^{22} \end{pmatrix}\begin{pmatrix} \boldsymbol{F} \\ \Delta\boldsymbol{F} \end{pmatrix}. \tag{2.50}$$

This has allowed us to expose the dumbbell spring force, $\Delta\boldsymbol{F}$, and the internal velocity difference $\Delta\boldsymbol{U}$, as separate from the force and velocities of the dumbbells as wholes. It is this procedure which we use to fill the dumbbell section of the mobility and resistance matrices.

Note the appearance of the factor of 1/4, reflecting the fact that the velocity of a dumbbell is the *average* of its bead velocities, but the force on a dumbbell is the *sum* of the bead forces.

2.3.3 Construction of velocity and force vectors, including dumbbells

We have already established in eq. (2.6) that for a suspension of spheres, we can write

$$\begin{pmatrix} \boldsymbol{U}^\alpha - \boldsymbol{u}^\infty \\ \boldsymbol{\Omega}^\alpha - \boldsymbol{\Omega}^\infty \\ -\boldsymbol{E}^\infty \end{pmatrix} = \mathcal{M}\begin{pmatrix} \boldsymbol{F}^\alpha \\ \boldsymbol{T}^\alpha \\ \boldsymbol{S}^\alpha \end{pmatrix}. \tag{2.51}$$

We now consider in detail the construction of the two vectors and the matrix.

For a system of N particles, in three dimensions, the vectors $\boldsymbol{U}$, $\boldsymbol{\Omega}$, $\boldsymbol{F}$ and $\boldsymbol{T}$ all represent

$$(U_1^1, U_2^1, U_3^1, U_1^2, U_2^2, U_3^2, \ldots, U_1^N, U_2^N, U_3^N), \text{ etc.} \tag{2.52}$$

For our tensors $\boldsymbol{E}$ and $\boldsymbol{S}$, we need to represent their terms as a vector in an efficient manner. Since both $\boldsymbol{E}$ and $\boldsymbol{S}$ are symmetric and traceless ($\boldsymbol{S}$ by its definition in eq. (2.27), and $\boldsymbol{E}$ symmetric by definition and traceless because $\mathrm{tr}(\boldsymbol{E}) = \boldsymbol{\nabla}\cdot\boldsymbol{u} = 0$), in the three dimensions we are working in, they are composed of only five independent terms. We choose to represent these terms in the following way, where $\boldsymbol{E} = E_{ij}$ becomes 'contracted' into $\boldsymbol{E}_{[\,]} = E_{[i]}$:

$$E_{[1]} = \frac{\sqrt{3}+1}{2}E_{11} + \frac{\sqrt{3}-1}{2}E_{22}, \tag{2.53a}$$

$$E_{[2]} = \sqrt{2}E_{12}, \tag{2.53b}$$

$$E_{[3]} = \frac{\sqrt{3}-1}{2}E_{11} + \frac{\sqrt{3}+1}{2}E_{22}, \tag{2.53c}$$

$$E_{[4]} = \sqrt{2}E_{13}, \tag{2.53d}$$

$$E_{[5]} = \sqrt{2}E_{23}. \tag{2.53e}$$

Equivalently we can say

$$E_{[i]} = \mathcal{E}_{ijk}E_{jk}, \tag{2.54}$$

where

$$\mathcal{E}_{1ij} = \begin{pmatrix} \frac{\sqrt{3}+1}{2} & 0 & 0 \\ 0 & \frac{\sqrt{3}-1}{2} & 0 \\ 0 & 0 & 0 \end{pmatrix}_{ij}, \qquad \mathcal{E}_{2ij} = \begin{pmatrix} 0 & \sqrt{2} & 0 \\ 0 & 0 & 0 \\ 0 & 0 & 0 \end{pmatrix}_{ij}, \qquad \text{etc.} \tag{2.55}$$

This choice of representation has the useful property that for any symmetric and traceless tensors A_{ij} and B_{ij},

$$A_{[i]}B_{[i]} = A_{ij}B_{ij}, \tag{2.56}$$

the usefulness of which will become apparent shortly.

From the linearity observed in eqs. (2.45), (2.46) and (2.49), we choose to add our dumbbells to eq. (2.51) as

$$\begin{pmatrix} \boldsymbol{U}^\alpha - \boldsymbol{u}^\infty(\boldsymbol{x}^\alpha) \\ \boldsymbol{\Omega}^\alpha - \boldsymbol{\Omega}^\infty \\ -\boldsymbol{E}^\infty_{[\,]} \\ \boldsymbol{U}^\beta - \boldsymbol{u}^\infty(\overline{\boldsymbol{x}}^\beta) \\ \frac{1}{2}\left[\Delta\boldsymbol{U}^\beta - \Delta\boldsymbol{u}^\infty(\overline{\boldsymbol{x}}^\beta; \Delta\boldsymbol{x}^\beta)\right] \end{pmatrix} = \mathcal{M} \begin{pmatrix} \boldsymbol{F}^\alpha \\ \boldsymbol{T}^\alpha \\ \boldsymbol{S}^\alpha_{[\,]} \\ \boldsymbol{F}^\beta \\ \Delta\boldsymbol{F}^\beta \end{pmatrix}, \tag{2.57}$$

where the half in the $\Delta\boldsymbol{U}^\beta$ term makes $\mathcal{M}$ symmetric, as shown in section 2.4.5.

Recall that we are taking the dumbbell beads to be freely rotating, so they are free of any applied torque: hence we do not include a dumbbell torque or angular velocity term.

If N^α is the number of spheres we have, and N^β is the number of dumbbells, then the dimensions of each element in both vectors are

$$(3N^\alpha, 3N^\alpha, 5N^\alpha, 3N^\beta, 3N^\beta), \tag{2.58}$$

giving $\mathcal{M}^\infty$ the size $(11N^\alpha + 6N^\beta) \times (11N^\alpha + 6N^\beta)$.

2.3.4 Symmetry of $\mathcal{M}^\infty$

The entries in $\mathcal{M}^\infty$ are given by the Faxén laws, eq. (2.45), with velocity disturbance eq. (2.46). From these definitions, we can see that the matrix for spheres-only is symmetric, i.e. $a_{ij}^{(\alpha\widetilde{\alpha})} = a_{ji}^{(\widetilde{\alpha}\alpha)}$, $b_{ij}^{(\alpha\widetilde{\alpha})} = \tilde{b}_{ji}^{(\widetilde{\alpha}\alpha)}$, etc., in the notation of eq. (2.11).

For example, considering $\tilde{\boldsymbol{b}}$, this is formed from Faxén's first law eq. (2.45a) and the velocity disturbance term for $\boldsymbol{T}^\alpha$ in eq. (2.46):

$$\tilde{b}_{ij}^{(\alpha\widetilde{\alpha})} = \frac{1}{8\pi\mu}\left(1 + \frac{a_\alpha^2}{6}\nabla^2\right) R_{ij}(\boldsymbol{x}^\alpha - \boldsymbol{x}^{\widetilde{\alpha}}), \tag{2.59}$$

while $\boldsymbol{b}$ is formed from Faxén's second law eq. (2.45b) and the velocity disturbance term for $\boldsymbol{F}^\alpha$ in eq. (2.46):

$$\begin{aligned} b_{ij}^{(\alpha\widetilde{\alpha})} &= \frac{1}{8\pi\mu}\left(1 + \frac{a_{\widetilde{\alpha}}^2}{6}\nabla^2\right)\frac{1}{2}\varepsilon_{ik\ell}\nabla_k J_{\ell j}(\boldsymbol{x}^\alpha - \boldsymbol{x}^{\widetilde{\alpha}}) && (2.60)\\ &= -\frac{1}{8\pi\mu}\left(1 + \frac{a_{\widetilde{\alpha}}^2}{6}\nabla^2\right)\frac{1}{2}\varepsilon_{ik\ell}\nabla_k J_{\ell j}(\boldsymbol{x}^{\widetilde{\alpha}} - \boldsymbol{x}^\alpha) && (2.61)\\ &= \frac{1}{8\pi\mu}\left(1 + \frac{a_{\widetilde{\alpha}}^2}{6}\nabla^2\right) R_{ji}(\boldsymbol{x}^{\widetilde{\alpha}} - \boldsymbol{x}^\alpha) && (2.62)\\ &= \tilde{b}_{ji}^{(\widetilde{\alpha}\alpha)}, && (2.63) \end{aligned}$$

where we have used the definition of the rotlet R_{ij} from eq. (2.24), and used that $\nabla_k J_{ij}(\boldsymbol{r}) = -\nabla_k J_{ij}(-\boldsymbol{r})$.

We still have symmetry in the sphere–dumbbell and dumbbell–dumbbell parts of the matrix, since these are derived from the force–velocity relationships of $\boldsymbol{a}$, which are already symmetric, and are then transformed by symmetric row and column operations.

Since $\mathcal{M}^\infty$ is symmetric, we need only compute the upper-half triangle, the elements of which are written out explicitly in table 2.1.

2.4 Construction of resistance matrix $\mathcal{R}^{\mathrm{2B,exact}}$

The resistance matrix $\mathcal{R}^{\mathrm{2B,exact}}$ is formed as the sum of the two-body resistance matrices of pairs of particles less than a critical distance apart:

$$\mathcal{R}^{\mathrm{2B,exact}} = \sum_{(\alpha,\widetilde{\alpha}):|\boldsymbol{x}^\alpha - \boldsymbol{x}^{\widetilde{\alpha}}|<r^*} (\mathcal{R}^{\mathrm{2B,exact}})^{(\alpha\widetilde{\alpha})}, \tag{2.65}$$

In the following table, $\delta_{ijk\ell}$ is the fourth-rank deviatoric unit tensor as defined in eq. (A.4), such that it contracts under eq. (2.79) to the rank 2 identity tensor δ_{ij}.

$$a_{ij}^{(\alpha\widetilde{\alpha})} = \frac{\delta_{ij}^{(\alpha\widetilde{\alpha})}}{6\pi\mu a_\alpha} + \frac{1}{8\pi\mu}\left(1 + \frac{a_\alpha^2 + a_{\widetilde{\alpha}}^2}{6}\nabla^2\right) J_{ij}(\boldsymbol{x}^\alpha - \boldsymbol{x}^{\widetilde{\alpha}}), \tag{2.64a}$$

$$\tilde{b}_{ij}^{(\alpha\widetilde{\alpha})} = \frac{1}{8\pi\mu}\left(1 + \frac{a_\alpha^2}{6}\nabla^2\right) R_{ij}(\boldsymbol{x}^\alpha - \boldsymbol{x}^{\widetilde{\alpha}}), \tag{2.64b}$$

$$\tilde{g}_{ijk}^{(\alpha\widetilde{\alpha})} = -\frac{1}{8\pi\mu}\left(1 + \left(\frac{a_\alpha^2}{6} + \frac{a_{\widetilde{\alpha}}^2}{10}\right)\nabla^2\right) K_{ijk}(\boldsymbol{x}^\alpha - \boldsymbol{x}^{\widetilde{\alpha}}), \tag{2.64c}$$

$$c_{ij}^{(\alpha\widetilde{\alpha})} = \frac{\delta_{ij}^{(\alpha\widetilde{\alpha})}}{8\pi\mu a_\alpha^3} + \frac{1}{2}\varepsilon_{ik\ell}\frac{1}{8\pi\mu}\nabla_k R_{\ell j}(\boldsymbol{x}^\alpha - \boldsymbol{x}^{\widetilde{\alpha}}), \tag{2.64d}$$

$$\tilde{h}_{ijk}^{(\alpha\widetilde{\alpha})} = -\frac{1}{2}\varepsilon_{i\ell m}\frac{1}{8\pi\mu}\left(1 + \frac{a_{\widetilde{\alpha}}^2}{10}\nabla^2\right)\nabla_\ell K_{mjk}(\boldsymbol{x}^\alpha - \boldsymbol{x}^{\widetilde{\alpha}}), \tag{2.64e}$$

$$m_{ijk\ell}^{(\alpha\widetilde{\alpha})} = \frac{\delta_{ijk\ell}^{(\alpha\widetilde{\alpha})}}{\frac{20}{3}\pi\mu a_\alpha^3} - \frac{1}{8\pi\mu}\left(1 + \frac{a_\alpha^2 + a_{\widetilde{\alpha}}^2}{10}\nabla^2\right) \times \frac{1}{2}\left(\nabla_j K_{ik\ell}(\boldsymbol{x}^\alpha - \boldsymbol{x}^{\widetilde{\alpha}}) + \nabla_i K_{jk\ell}(\boldsymbol{x}^\alpha - \boldsymbol{x}^{\widetilde{\alpha}})\right). \tag{2.64f}$$

Table 2.1: Elements of $\mathcal{M}^\infty$, explicitly written out.

where the dimensions of the two-body matrix $(\mathcal{R}^{\mathrm{2B,exact}})^{(\alpha\widetilde{\alpha})}$ are the same as the full matrix $\mathcal{R}^{\mathrm{2B,exact}}$, so the two-body matrix has rows and columns of zeros corresponding to particles not in the pair. We can, however, generate the full matrix directly.

2.4.1 Resistance matrix for spheres only

For Stokesian Dynamics with N^α spheres, we have an established form of $\mathcal{R}^{\mathrm{2B,exact}}$ given by

$$\begin{pmatrix} \boldsymbol{F}^\alpha \\ \boldsymbol{T}^\alpha \\ \boldsymbol{S}^\alpha \end{pmatrix} = \begin{pmatrix} \boldsymbol{A} & \widetilde{\boldsymbol{B}} & \widetilde{\boldsymbol{G}} \\ \boldsymbol{B} & \boldsymbol{C} & \widetilde{\boldsymbol{H}} \\ \boldsymbol{G} & \boldsymbol{H} & \boldsymbol{M} \end{pmatrix} \begin{pmatrix} \boldsymbol{U}^\alpha - \boldsymbol{u}^\infty \\ \boldsymbol{\Omega}^\alpha - \boldsymbol{\Omega}^\infty \\ -\boldsymbol{E}^\infty \end{pmatrix}, \tag{2.66}$$

where, for any tensor $\boldsymbol{P}$ in the resistance matrix,

$$\boldsymbol{P} = \begin{pmatrix} \boldsymbol{P}^{(11)} & \boldsymbol{P}^{(12)} & \dots & \boldsymbol{P}^{(1N^\alpha)} \\ \boldsymbol{P}^{(21)} & \boldsymbol{P}^{(22)} & \dots & \boldsymbol{P}^{(2N^\alpha)} \\ \vdots & \vdots & \ddots & \vdots \\ \boldsymbol{P}^{(N^\alpha 1)} & \boldsymbol{P}^{(N^\alpha 2)} & \dots & \boldsymbol{P}^{(N^\alpha N^\alpha)} \end{pmatrix}, \text{ etc.} \tag{2.67}$$

The component resistance tensors $\boldsymbol{P}^{(\alpha\widetilde{\alpha})}$ represent the relationship between a force moment on α and a velocity moment on $\tilde{\alpha}$.

We will standardise vocabulary here:

- $\mathcal{R}^{\mathrm{2B,exact}}$ is the *resistance matrix*,
- $\boldsymbol{P}$ is a *tensor*, and its matrix form (as described in section 2.4.4) a *submatrix* of the resistance matrix,
- $\boldsymbol{P}^{(\alpha\widetilde{\alpha})}$ is a *component tensor*, and its matrix form a *component matrix*.

2.4.2 Definitions of component tensors

The component tensors are defined below, in terms of the following two classes of functions:

- Scalar resistance functions $X^P_\gamma(s',\lambda), Y^P_\gamma(s',\lambda), Z^P_\gamma(s',\lambda)$, where $\boldsymbol{P}$ is the relevant component tensor. Note:
  - The X, Y, Z notation follows that introduced by Jeffrey & Onishi (1984), where X-functions relate to terms that are parallel to the line of centres, and Y- and Z-functions relate to perpendicular terms.
  - The parameter γ is either 1 or 2, depending on whether $\tilde{\alpha} = \alpha$ or $\tilde{\alpha} \neq \alpha$, respectively.
  - The separation distance of the particles is $s = |\boldsymbol{x}^{\widetilde{\alpha}} - \boldsymbol{x}^{\alpha}|$, which is scaled on the average particle size to form $s' = 2s/(a_\alpha + a_{\widetilde{\alpha}})$.
  - The size ratio of the particles is $\lambda = a_{\widetilde{\alpha}}/a_\alpha$.

  (See appendix A.2.1 regarding differences in notation here from that of the literature.)
- Unit displacement tensors $L^E_{ij(k\ell)}$, of ranks 2 to 4, for $1 \leqslant E \leqslant 9$. These are all functions of the unit displacement vector between the two particles, $\boldsymbol{d} = (\boldsymbol{x}^{\widetilde{\alpha}} - \boldsymbol{x}^{\alpha})/s$.

For any component tensor $\boldsymbol{P}^{(\alpha\widetilde{\alpha})}$,

$$\boldsymbol{P}^{(\alpha\widetilde{\alpha})} = \begin{cases} \displaystyle\sum_{\alpha'\neq\alpha} \boldsymbol{P}_1^{(\alpha\alpha')} & \text{if } \tilde{\alpha} = \alpha \\ \boldsymbol{P}_2^{(\alpha\widetilde{\alpha})} & \text{if } \tilde{\alpha} \neq \alpha \end{cases}, \tag{2.68}$$

where the summation on the $\tilde{\alpha} = \alpha$ case is derived from the summation in eq. (2.65).

The component tensors, in this notation, adapted from Kim & Karrila (2005, table

7.1), are then given by

$$(A_\gamma^{(\alpha\widetilde{\alpha})})_{ij} = X_\gamma^A L_{ij}^1 + Y_\gamma^A L_{ij}^2, \tag{2.69a}$$
$$(B_\gamma^{(\alpha\widetilde{\alpha})})_{ij} = Y_\gamma^B L_{ij}^3, \tag{2.69b}$$
$$(C_\gamma^{(\alpha\widetilde{\alpha})})_{ij} = X_\gamma^C L_{ij}^1 + Y_\gamma^C L_{ij}^2, \tag{2.69c}$$
$$(G_\gamma^{(\alpha\widetilde{\alpha})})_{ijk} = X_\gamma^G L_{ijk}^4 + Y_\gamma^G L_{ijk}^5, \tag{2.69d}$$
$$(H_\gamma^{(\alpha\widetilde{\alpha})})_{ijk} = Y_\gamma^H L_{ijk}^6, \tag{2.69e}$$
$$(M_\gamma^{(\alpha\widetilde{\alpha})})_{ijk\ell} = X_\gamma^M L_{ijk\ell}^7 + Y_\gamma^M L_{ijk\ell}^8 + Z_\gamma^M L_{ijk\ell}^9, \tag{2.69f}$$

and the unit displacement tensors by

$$L_{ij}^1 = d_i d_j, \tag{2.70a}$$
$$L_{ij}^2 = \delta_{ij} - d_i d_j, \tag{2.70b}$$
$$L_{ij}^3 = \varepsilon_{ijk} d_k, \tag{2.70c}$$
$$L_{ijk}^4 = \left(d_i d_j - \frac{1}{3}\delta_{ij} \right) d_k, \tag{2.70d}$$
$$L_{ijk}^5 = d_i \delta_{jk} + d_j \delta_{ik} - 2 d_i d_j d_k, \tag{2.70e}$$
$$L_{ijk}^6 = \varepsilon_{ik\ell} d_\ell d_j + \varepsilon_{jk\ell} d_\ell d_i, \tag{2.70f}$$
$$L_{ijk\ell}^7 = \frac{3}{2} \left(d_i d_j - \frac{1}{3}\delta_{ij} \right) \left(d_k d_\ell - \frac{1}{3}\delta_{k\ell} \right), \tag{2.70g}$$
$$L_{ijk\ell}^8 = \frac{1}{2}(d_i \delta_{j\ell} d_k + d_j \delta_{i\ell} d_k + d_i \delta_{jk} d_\ell + d_j \delta_{ik} d_\ell - 4 d_i d_j d_k d_\ell), \tag{2.70h}$$
$$\begin{aligned} L_{ijk\ell}^9 = \frac{1}{2}(&\delta_{ik}\delta_{j\ell} + \delta_{jk}\delta_{i\ell} - \delta_{ij}\delta_{k\ell} + d_i d_j \delta_{k\ell} + \delta_{ij} d_k d_\ell \\ &- d_i \delta_{j\ell} d_k - d_j \delta_{i\ell} d_k - d_i \delta_{jk} d_\ell - d_j \delta_{ik} d_\ell + d_i d_j d_k d_\ell). \end{aligned} \tag{2.70i}$$

2.4.3 Values of scalar resistance functions

The scalar resistance functions

$$X_\gamma^P(s', \lambda), \quad Y_\gamma^P(s', \lambda), \quad Z_\gamma^P(s', \lambda), \tag{2.71}$$

where $\boldsymbol{P}$ is the relevant component tensor, are found for $s' \gtrsim 2.014$ numerically using the two-sphere method of Wilson (2013), based on Lamb's solution to Stokes flow (Lamb, 1932).

If we write the resistance formulation for spheres alone, eq. (2.66), in more compact form,

$$\mathcal{F} = \mathcal{R}\mathcal{U}, \tag{2.72}$$

the code published with the two-sphere method takes the inputs s, λ and $\mathcal{F}$, and

Choice for $\mathcal{F}$	Mobility scalars it produces
$\boldsymbol{F}^1 = (1,0,0)$	$x^a_{11}, x^a_{21}, x^g_{11}, x^g_{21}$
$\boldsymbol{F}^1 = (0,1,0)$	$y^a_{11}, y^a_{21}, y^b_{11}, y^b_{21}, y^g_{11}, y^g_{21}$
$\boldsymbol{F}^2 = (1,0,0)$	$x^a_{12}, x^a_{22}, x^g_{12}, x^g_{22}$
$\boldsymbol{F}^2 = (0,1,0)$	$y^a_{12}, y^a_{22}, y^b_{12}, y^b_{22}, y^g_{12}, y^g_{22}$
$\boldsymbol{T}^1 = (1,0,0)$	x^c_{11}, x^c_{21}
$\boldsymbol{T}^1 = (0,1,0)$	y^c_{11}, y^c_{21}
$\boldsymbol{T}^2 = (1,0,0)$	x^c_{12}, x^c_{22}
$\boldsymbol{T}^2 = (0,1,0)$	y^c_{12}, y^c_{22}
$\boldsymbol{S}^1 = \begin{pmatrix} 1 & 0 & 0 \\ 0 & -1/2 & 0 \\ 0 & 0 & -1/2 \end{pmatrix}$	x^m_{11}, x^m_{21}
$\boldsymbol{S}^1 = \begin{pmatrix} 0 & 0 & 0 \\ 0 & 0 & 1 \\ 0 & 1 & 0 \end{pmatrix}$	z^m_{11}, z^m_{21}
$\boldsymbol{S}^1 = \begin{pmatrix} 0 & 1 & 0 \\ 1 & 0 & 0 \\ 0 & 0 & 0 \end{pmatrix}$	$y^h_{11}, y^h_{12}, y^m_{11}, y^m_{21}$
$\boldsymbol{S}^2 = \begin{pmatrix} 1 & 0 & 0 \\ 0 & -1/2 & 0 \\ 0 & 0 & -1/2 \end{pmatrix}$	x^m_{12}, x^m_{22}
$\boldsymbol{S}^2 = \begin{pmatrix} 0 & 0 & 0 \\ 0 & 0 & 1 \\ 0 & 1 & 0 \end{pmatrix}$	z^m_{12}, z^m_{22}
$\boldsymbol{S}^2 = \begin{pmatrix} 0 & 1 & 0 \\ 1 & 0 & 0 \\ 0 & 0 & 0 \end{pmatrix}$	$y^h_{21}, y^h_{22}, y^m_{12}, y^m_{22}$

Table 2.2: Convenient choices for $\mathcal{F}$ when $\boldsymbol{d} = (1,0,0)$. All other elements of $\mathcal{F}$ are set to zero.

gives the output $\mathcal{U}$. From here, we invert $\mathcal{R}$ to give $\mathcal{M}$, the form of which is found in appendix A.1.1, and which is filled with mobility scalar functions.

We then choose some convenient input of $\mathcal{F}$ (see table 2.2), apply $\mathcal{M}$ to it, and compare directly against the outputted $\mathcal{U}$ to find the mobility scalars. We can then invert the scalars back to find the resistance scalar functions.

The two-sphere code fails below values of $s' \approx 2.014$, so we need another approach for closer spheres. For values of $s' - 2 \ll 1$ and $s' - 2 \ll \lambda$ (so in our simulations for $s' < 2.001$), we use asymptotic forms from Jeffrey & Onishi (1984) and Jeffrey (1992), compiled in appendix A.2.2, with a full set of corrections. For values of s' between 2.001 and 2.014, we interpolate across the gap. Figure 2.7 shows a smooth transition between the two regimes, indicated either side of a central red column, inside which both techniques perform poorly.

We are therefore able to generate a large table of values of the resistance scalar functions for many values of s' and λ. For intermediate values, we use linear interpolation, which is validated by the smooth plots in fig. 2.7.

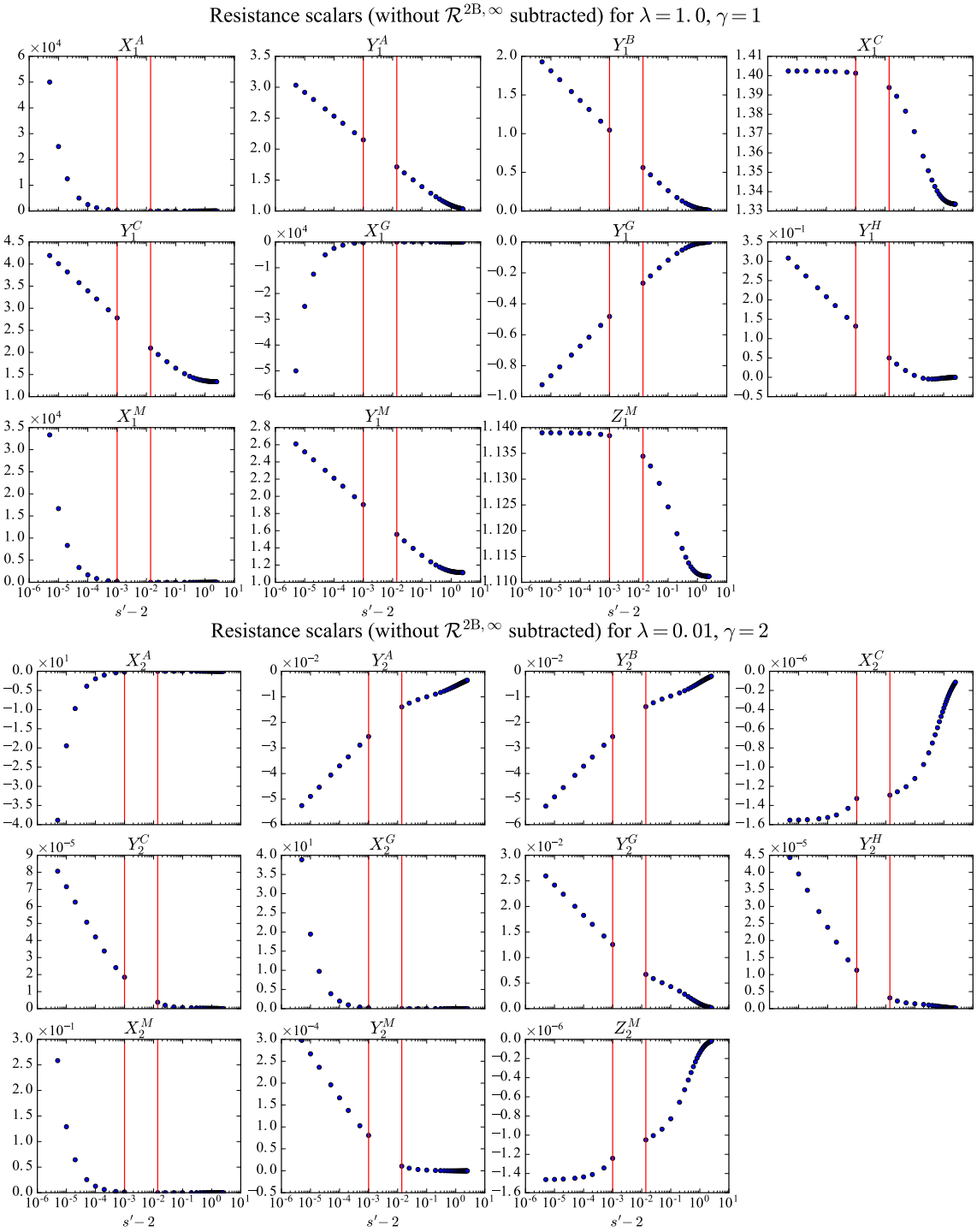

Figure 2.7: Values of some of the scalar resistance functions over scaled separation distance, s', for two different values of size ratio, λ. Values on the left of the first red vertical line are computed asymptotically from Jeffrey & Onishi (1984) and Jeffrey (1992) (corrected), and those to the right of the second red vertical line are computed with the two-sphere code from Wilson (2013). These plots show a smooth transition between the regimes.

2.4.4 Contracting component tensors into component matrices

It is important to note that:

- $\boldsymbol{A}^{(\alpha\widetilde{\alpha})}$, $\boldsymbol{B}^{(\alpha\widetilde{\alpha})}$, $\widetilde{\boldsymbol{B}}^{(\alpha\widetilde{\alpha})}$ and $\boldsymbol{G}^{(\alpha\widetilde{\alpha})}$ are rank 2 tensors,
- $\boldsymbol{G}^{(\alpha\widetilde{\alpha})}$, $\widetilde{\boldsymbol{G}}^{(\alpha\widetilde{\alpha})}$, $\boldsymbol{H}^{(\alpha\widetilde{\alpha})}$ and $\widetilde{\boldsymbol{H}}^{(\alpha\widetilde{\alpha})}$ are rank 3 tensors,
- $\boldsymbol{M}^{(\alpha\widetilde{\alpha})}$ is a rank 4 tensor.

Such a mix of tensors does not compile nicely into a large matrix, so we contract all the tensors to be rank 2. The contraction is as follows, using the contraction tensor, $\mathcal{E}$, from eq. (2.54).

Consider $\widetilde{\boldsymbol{G}}^{(\alpha\widetilde{\alpha})} = \widetilde{G}^{(\alpha\widetilde{\alpha})}_{ijk}$. Observe that $\boldsymbol{F}^{\alpha} = \widetilde{\boldsymbol{G}}^{(\alpha\widetilde{\alpha})} : \boldsymbol{E}^{\widetilde{\alpha}}$, i.e.

$$F^{\alpha}_{i} = \widetilde{G}^{(\alpha\widetilde{\alpha})}_{ijk} E^{\widetilde{\alpha}}_{jk} = \widetilde{G}^{(\alpha\widetilde{\alpha})}_{i[m]} E^{\widetilde{\alpha}}_{[m]} = \mathcal{E}_{mjk} \widetilde{G}^{(\alpha\widetilde{\alpha})}_{ijk} E^{\widetilde{\alpha}}_{[m]}. \tag{2.73}$$

Hence, after contraction,

$$\widetilde{\boldsymbol{G}}^{(\alpha\widetilde{\alpha})} = \widetilde{G}^{(\alpha\widetilde{\alpha})}_{i[m]} = \mathcal{E}_{mjk} \widetilde{G}^{(\alpha\widetilde{\alpha})}_{ijk}. \tag{2.74}$$

Considering $\boldsymbol{G}^{(\alpha\widetilde{\alpha})}$, we see that $S^{\alpha}_{ij} = G^{(\alpha\widetilde{\alpha})}_{ijk} U^{\widetilde{\alpha}}_{k}$ and hence

$$S^{\alpha}_{[m]} = G^{(\alpha\widetilde{\alpha})}_{[m]k} U^{\widetilde{\alpha}}_{k} = \mathcal{E}_{mij} G^{(\alpha\widetilde{\alpha})}_{ijk} U^{\widetilde{\alpha}}_{k}, \tag{2.75}$$

and hence, after contraction,

$$\boldsymbol{G}^{(\alpha\widetilde{\alpha})} = G^{(\alpha\widetilde{\alpha})}_{[m]i} = \mathcal{E}_{mjk} G^{(\alpha\widetilde{\alpha})}_{jki}. \tag{2.76}$$

The tensors $\boldsymbol{H}^{(\alpha\widetilde{\alpha})}$ and $\widetilde{\boldsymbol{H}}^{(\alpha\widetilde{\alpha})}$ are contracted in the same way.

Then considering $\boldsymbol{M}^{(\alpha\widetilde{\alpha})} = M^{(\alpha\widetilde{\alpha})}_{ijk\ell}$, see that

$$S^{\alpha}_{ij} = M^{(\alpha\widetilde{\alpha})}_{ijk\ell} E^{\widetilde{\alpha}}_{k\ell} = M^{(\alpha\widetilde{\alpha})}_{ij[m]} E^{\widetilde{\alpha}}_{[m]} \tag{2.77}$$

$$\implies S^{\alpha}_{[n]} = M^{(\alpha\widetilde{\alpha})}_{[n][m]} E^{\widetilde{\alpha}}_{[m]} \tag{2.78}$$

and hence, after contraction,

$$\boldsymbol{M}^{(\alpha\widetilde{\alpha})} = M^{(\alpha\widetilde{\alpha})}_{[n][m]} = \mathcal{E}_{nij} \mathcal{E}_{mk\ell} M^{(\alpha\widetilde{\alpha})}_{ijk\ell}. \tag{2.79}$$

Having set up our matrix with the expressions for spheres, we now expand it to include our dumbbells, in the form of eq. (2.57), using row and column operations

as discussed in section 2.3.2.

$$\begin{pmatrix} \boldsymbol{F}^\alpha \\ \boldsymbol{T}^\alpha \\ \boldsymbol{S}^\alpha_{[\,]} \\ \boldsymbol{F}^\beta \\ \Delta\boldsymbol{F}^\beta \end{pmatrix} = \begin{pmatrix} \boldsymbol{A} & \widetilde{\boldsymbol{B}} & \widetilde{\boldsymbol{G}} & \boldsymbol{R}^{14} & \boldsymbol{R}^{15} \\ \boldsymbol{B} & \boldsymbol{C} & \widetilde{\boldsymbol{H}} & \boldsymbol{R}^{24} & \boldsymbol{R}^{25} \\ \boldsymbol{G} & \boldsymbol{H} & \boldsymbol{M} & \boldsymbol{R}^{34} & \boldsymbol{R}^{35} \\ \boldsymbol{R}^{41} & \boldsymbol{R}^{42} & \boldsymbol{R}^{43} & \boldsymbol{R}^{44} & \boldsymbol{R}^{45} \\ \boldsymbol{R}^{51} & \boldsymbol{R}^{52} & \boldsymbol{R}^{53} & \boldsymbol{R}^{54} & \boldsymbol{R}^{55} \end{pmatrix} \begin{pmatrix} \boldsymbol{U}^\alpha - \boldsymbol{u}^\infty(\boldsymbol{x}^\alpha) \\ \boldsymbol{\Omega}^\alpha - \boldsymbol{\Omega}^\infty \\ -\boldsymbol{E}^\infty_{[\,]} \\ \boldsymbol{U}^\beta - \boldsymbol{u}^\infty(\overline{\boldsymbol{x}}^\beta) \\ \frac{1}{2}\left[\Delta\boldsymbol{U}^\beta - \Delta\boldsymbol{u}^\infty(\overline{\boldsymbol{x}}^\beta; \Delta\boldsymbol{x}^\beta\cdot)\right] \end{pmatrix}. \quad (2.80)$$

Note that again in this expansion, the sizes of each of the component vectors are

$$(3N^\alpha, 3N^\alpha, 5N^\alpha, 3N^\beta, 3N^\beta), \quad (2.81)$$

giving us a resistance matrix with dimension $(11N^\alpha + 6N^\beta) \times (11N^\alpha + 6N^\beta)$.

2.4.5 Symmetry of $\mathcal{R}^{\mathbf{2B,exact}}$

The symmetry of $\mathcal{R}^{\mathrm{2B,exact}}$, as well as validation of our setup of force and velocity vectors, can be shown with the Lorentz reciprocal theorem (Lorentz, 1896), using the method of Hinch (1972) as generalised to more than one particle by Brenner & O'Neill (1972).

Consider a closed region of fluid V bounded by a surface S. Suppose that the velocity fields $\boldsymbol{u}_1$ and $\boldsymbol{u}_2$ both satisfy the Stokes equations. Denote their respective stress fields by $\boldsymbol{\sigma}_1$ and $\boldsymbol{\sigma}_2$. Then the theorem states that

$$\int_S \boldsymbol{u}_1 \cdot (\boldsymbol{\sigma}_2 \cdot \boldsymbol{n})\,\mathrm{d}S = \int_S \boldsymbol{u}_2 \cdot (\boldsymbol{\sigma}_1 \cdot \boldsymbol{n})\,\mathrm{d}S. \quad (2.82)$$

The theorem can be thought of as an analogue to Green's second identity for two harmonic functions u_1, u_2 on a domain with boundary S, which says

$$\int_S u_1 \frac{\partial u_2}{\partial \boldsymbol{n}}\,\mathrm{d}S = \int_S u_2 \frac{\partial u_1}{\partial \boldsymbol{n}}\,\mathrm{d}S, \quad (2.83)$$

where $\partial u_i/\partial \boldsymbol{n} = \boldsymbol{\nabla} u_i \cdot \boldsymbol{n}$ is the directional derivative of u_i in the direction of the outward pointing normal $\boldsymbol{n}$ to the surface S. (For more discussion on the theorem and its applications, see Zapryanov & Tabakova (1998), sections 2.1 and 2.4, and Kim & Karrila (2005), section 6.3.)

Symmetry of component matrices on the diagonal

Before we use the reciprocal theorem, there are some easier observations to make. See that by their definitions, eqs. (2.69a) and (2.69c),

$$(A_\gamma^{(\alpha\widetilde{\alpha})})_{ij} = (A_\gamma^{(\widetilde{\alpha}\alpha)})_{ji}, \qquad (C_\gamma^{(\alpha\widetilde{\alpha})})_{ij} = (C_\gamma^{(\widetilde{\alpha}\alpha)})_{ji}. \tag{2.84}$$

Hence

$$A_{ij}^{(\alpha\widetilde{\alpha})} = A_{ji}^{(\widetilde{\alpha}\alpha)}, \qquad C_{ij}^{(\alpha\widetilde{\alpha})} = C_{ji}^{(\widetilde{\alpha}\alpha)}, \tag{2.85}$$

and so $\boldsymbol{A} = \boldsymbol{A}^{\mathrm{T}}$ and $\boldsymbol{C} = \boldsymbol{C}^{\mathrm{T}}$.

For $\boldsymbol{M}$ to have the same symmetry, this requires

$$M_{[n][m]}^{(\alpha\widetilde{\alpha})} = M_{[m][n]}^{(\widetilde{\alpha}\alpha)}, \tag{2.86}$$

the contraction of which as in eq. (2.79) requires

$$M_{ijk\ell}^{(\alpha\widetilde{\alpha})} = M_{k\ell ij}^{(\widetilde{\alpha}\alpha)}. \tag{2.87}$$

Fortunately the definition of $\boldsymbol{M}$, eq. (2.69f), treated in the same manner as above, shows this to be true.

Since the dumbbell–dumbbell terms are derived from symmetric row and column operations on the $\boldsymbol{A}$ terms, these are also symmetric.

Relationship between $\boldsymbol{B}$ and $\widetilde{\boldsymbol{B}}$

We set up two hydrodynamics problems on which to apply the reciprocal theorem.

Consider two spheres, α and $\tilde{\alpha}$, in suspension with surfaces S^α and $S^{\widetilde{\alpha}}$ respectively. Let $S = S^\alpha + S^{\widetilde{\alpha}}$ be the combined surfaces. Then consider velocity fields

$$\boldsymbol{u}_1 = \begin{cases} \boldsymbol{U}^\alpha & \text{on } S^\alpha \\ 0 & \text{on } S^{\widetilde{\alpha}} \end{cases}, \tag{2.88}$$

$$\boldsymbol{u}_2 = \begin{cases} 0 & \text{on } S^\alpha \\ \boldsymbol{\Omega}^{\widetilde{\alpha}} \times \boldsymbol{x} & \text{on } S^{\widetilde{\alpha}} \end{cases}. \tag{2.89}$$

It follows that

$$\boldsymbol{T}^{\widetilde{\alpha}} = \boldsymbol{B}^{(\widetilde{\alpha}\alpha)} \cdot \boldsymbol{U}^\alpha, \tag{2.90}$$

$$\boldsymbol{F}^{\alpha} = \widetilde{\boldsymbol{B}}^{(\alpha\widetilde{\alpha})} \cdot \boldsymbol{\Omega}^{\widetilde{\alpha}}. \tag{2.91}$$

Then the reciprocal theorem gives us

$$\int_S \boldsymbol{u}_1 \cdot (\boldsymbol{\sigma}_2 \cdot \boldsymbol{n}) \, \mathrm{d}S = \int_S \boldsymbol{u}_2 \cdot (\boldsymbol{\sigma}_1 \cdot \boldsymbol{n}) \, \mathrm{d}S \tag{2.92}$$

$$\implies \boldsymbol{U}^{\alpha} \cdot \int_{S^{\alpha}} (\boldsymbol{\sigma}_2 \cdot \boldsymbol{n}) \, \mathrm{d}S = \boldsymbol{\Omega}^{\widetilde{\alpha}} \cdot \int_{S^{\widetilde{\alpha}}} \boldsymbol{x} \times (\boldsymbol{\sigma}_1 \cdot \boldsymbol{n}) \, \mathrm{d}S \tag{2.93}$$

$$\implies \boldsymbol{U}^{\alpha} \cdot \boldsymbol{F}^{\alpha} = \boldsymbol{\Omega}^{\widetilde{\alpha}} \cdot \boldsymbol{T}^{\widetilde{\alpha}} \tag{2.94}$$

$$\implies \boldsymbol{U}^{\alpha} \cdot \widetilde{\boldsymbol{B}}^{(\alpha\widetilde{\alpha})} \cdot \boldsymbol{\Omega}^{\widetilde{\alpha}} = \boldsymbol{\Omega}^{\widetilde{\alpha}} \cdot \boldsymbol{B}^{(\widetilde{\alpha}\alpha)} \cdot \boldsymbol{U}^{\alpha} \tag{2.95}$$

$$\implies B_{ij}^{(\widetilde{\alpha}\alpha)} = \widetilde{B}_{ji}^{(\alpha\widetilde{\alpha})}, \tag{2.96}$$

where we have used the definitions of $\boldsymbol{F}^{\alpha}$ and $\boldsymbol{T}^{\alpha}$ from eqs. (2.26) and (2.42).

Relationship between $\boldsymbol{H}$ and $\widetilde{\boldsymbol{H}}$

This time consider velocity fields

$$\boldsymbol{u}_1 = \begin{cases} \boldsymbol{\Omega}^{\alpha} \times \boldsymbol{x} & \text{on } S^{\alpha} \\ 0 & \text{on } S^{\widetilde{\alpha}} \end{cases}, \tag{2.97}$$

$$\boldsymbol{u}_2 = \begin{cases} 0 & \text{on } S^{\alpha} \\ -\boldsymbol{E}^{\infty} \cdot \boldsymbol{x} & \text{on } S^{\widetilde{\alpha}} \end{cases}. \tag{2.98}$$

It follows, then, that

$$\boldsymbol{S}^{\widetilde{\alpha}} = \boldsymbol{H}^{(\widetilde{\alpha}\alpha)} \cdot \boldsymbol{\Omega}^{\alpha}, \tag{2.99}$$

$$\boldsymbol{T}^{\alpha} = -\widetilde{\boldsymbol{H}}^{(\alpha\widetilde{\alpha})} : \boldsymbol{E}^{\infty}. \tag{2.100}$$

Then the reciprocal theorem gives us

$$\int_S \boldsymbol{u}_1 \cdot (\boldsymbol{\sigma}_2 \cdot \boldsymbol{n}) \, \mathrm{d}S = \int_S \boldsymbol{u}_2 \cdot (\boldsymbol{\sigma}_1 \cdot \boldsymbol{n}) \, \mathrm{d}S \tag{2.101}$$

$$\implies \boldsymbol{\Omega}^{\alpha} \cdot \int_{S^{\alpha}} \boldsymbol{x} \times (\boldsymbol{\sigma}_2 \cdot \boldsymbol{n}) \, \mathrm{d}S = -\boldsymbol{E}^{\infty} : \int_{S^{\widetilde{\alpha}}} \boldsymbol{x} (\boldsymbol{\sigma}_1 \cdot \boldsymbol{n}) \, \mathrm{d}S \tag{2.102}$$

$$\implies \boldsymbol{\Omega}^{\alpha} \cdot \boldsymbol{T}^{\alpha} = -\boldsymbol{E}^{\infty} : \boldsymbol{S}^{\widetilde{\alpha}} \tag{2.103}$$

$$\implies \boldsymbol{\Omega}^{\alpha} \cdot \widetilde{\boldsymbol{H}}^{(\alpha\widetilde{\alpha})} : (-\boldsymbol{E}^{\infty}) = -\boldsymbol{E}^{\infty} : \boldsymbol{H}^{(\widetilde{\alpha}\alpha)} \cdot \boldsymbol{\Omega}^{\alpha} \tag{2.104}$$

$$\implies H_{ijk}^{(\widetilde{\alpha}\alpha)} = \widetilde{H}_{kij}^{(\alpha\widetilde{\alpha})}. \tag{2.105}$$

Here we have used the definition $\boldsymbol{T}^{\alpha}$ from eq. (2.26), and made use of the following observation for $\boldsymbol{S}^{\widetilde{\alpha}}$. Since $\boldsymbol{S}$ and $\boldsymbol{E}$ are symmetric and traceless, we use the definition

of $\boldsymbol{S}$ given in eq. (2.27) to see that (temporarily using $\boldsymbol{\sigma}$ to stand for $\boldsymbol{\sigma}_1$),

$$\boldsymbol{E} : \boldsymbol{S} = \frac{1}{2}\int_S \left[E_{ij}x_i\sigma_{jk}n_k + E_{ij}\sigma_{jk}n_k x_j - \frac{2}{3}E_{ij}\delta_{ij}x_k\sigma_{k\ell}n_\ell\right] \mathrm{d}S \tag{2.106}$$

$$= \frac{1}{2}\int_S \left[E_{ij}x_i\sigma_{jk}n_k + E_{ji}\sigma_{ik}n_k x_i - \frac{2}{3}E_{ii}x_k\sigma_{k\ell}n_\ell\right] \mathrm{d}S \tag{2.107}$$

$$= \frac{1}{2}\int_S \left[E_{ij}x_i\sigma_{jk}n_k + E_{ij}\sigma_{ik}n_k x_i - 0\right] \mathrm{d}S \tag{2.108}$$

$$= E_{ij}\int_S \left[x_i\sigma_{jk}n_k\right] \mathrm{d}S \tag{2.109}$$

$$= \boldsymbol{E} : \int_S \boldsymbol{x}(\boldsymbol{\sigma}\cdot\boldsymbol{n})\,\mathrm{d}S. \tag{2.110}$$

Relationship between $\boldsymbol{G}$ and $\widetilde{\boldsymbol{G}}$

The relationship

$$G_{ijk}^{(\widetilde{\alpha}\alpha)} = \widetilde{G}_{kij}^{(\alpha\widetilde{\alpha})} \tag{2.111}$$

is derived in exactly the same way as above.

Relationship between $\boldsymbol{R}^{14}$ and $\boldsymbol{R}^{41}$

This time we consider one sphere with surface S^α and one dumbbell with surface S^β suspended in the fluid. We turn the background velocity off and let $S = S^\alpha + S^\beta$ be the combined surface.

Consider velocity fields

$$\boldsymbol{u}_1 = \begin{cases} 0 & \text{on } S^\alpha \\ \boldsymbol{U}^\beta & \text{on } S^\beta \end{cases}, \tag{2.112}$$

$$\boldsymbol{u}_2 = \begin{cases} \boldsymbol{U}^\alpha & \text{on } S^\alpha \\ 0 & \text{on } S^\beta \end{cases}. \tag{2.113}$$

It follows that

$$\boldsymbol{F}^\alpha = (\boldsymbol{R}^{14})^{(\alpha\beta)}\cdot(\boldsymbol{U}^\beta), \tag{2.114}$$

$$\boldsymbol{F}^\beta = (\boldsymbol{R}^{41})^{(\beta\alpha)}\cdot(\boldsymbol{U}^\alpha). \tag{2.115}$$

The reciprocal theorem gives us

$$\int_S \boldsymbol{u}_1\cdot(\boldsymbol{\sigma}_2\cdot\boldsymbol{n})\,\mathrm{d}S = \int_S \boldsymbol{u}_2\cdot(\boldsymbol{\sigma}_1\cdot\boldsymbol{n})\,\mathrm{d}S \tag{2.116}$$

$$\implies \boldsymbol{U}^{\beta} \cdot \int_{S^{\beta}} (\boldsymbol{\sigma}_2 \cdot \boldsymbol{n}) \, \mathrm{d}S = \boldsymbol{U}^{\alpha} \cdot \int_{S^{\alpha}} (\boldsymbol{\sigma}_1 \cdot \boldsymbol{n}) \, \mathrm{d}S \tag{2.117}$$

$$\implies \boldsymbol{U}^{\beta} \cdot \boldsymbol{F}^{\beta} = \boldsymbol{U}^{\alpha} \cdot \boldsymbol{F}^{\alpha} \tag{2.118}$$

$$\implies \boldsymbol{U}^{\beta} \cdot (\boldsymbol{R}^{41})^{(\beta\alpha)} \cdot \boldsymbol{U}^{\alpha} = \boldsymbol{U}^{\alpha} \cdot (\boldsymbol{R}^{14})^{(\alpha\beta)} \cdot \boldsymbol{U}^{\beta} \tag{2.119}$$

$$\implies (R^{14})_{ij}^{(\alpha\beta)} = (R^{41})_{ji}^{(\beta\alpha)}. \tag{2.120}$$

Relationship between $\boldsymbol{R}^{15}$ and $\boldsymbol{R}^{51}$

We continue to consider one sphere with surface S^{α} and one dumbbell with surface S^{β} suspended in the fluid, but this time we say $S^{\beta} = S^{\beta 1} + S^{\beta 2}$, the surfaces of the two beads at the end of the dumbbell. We still have $S = S^{\alpha} + S^{\beta}$. If we keep background flow off and set up the velocity fields

$$\boldsymbol{u}_1 = \begin{cases} 0 & \text{on } S^{\alpha} \\ -\frac{1}{2}\Delta\boldsymbol{U}^{\beta} & \text{on } S^{\beta 1} \\ \frac{1}{2}\Delta\boldsymbol{U}^{\beta} & \text{on } S^{\beta 2} \end{cases}, \tag{2.121}$$

$$\boldsymbol{u}_2 = \begin{cases} \boldsymbol{U}^{\alpha} & \text{on } S^{\alpha} \\ 0 & \text{on } S^{\beta} \end{cases}, \tag{2.122}$$

it follows that

$$\boldsymbol{F}^{\alpha} = (\boldsymbol{R}^{15})^{(\alpha\beta)} \cdot \frac{1}{2}\Delta\boldsymbol{U}^{\beta}, \tag{2.123}$$

$$\Delta\boldsymbol{F}^{\beta} = (\boldsymbol{R}^{51})^{(\beta\alpha)} \cdot \boldsymbol{U}^{\alpha}. \tag{2.124}$$

Applying the reciprocal theorem gives us

$$\int_{S} \boldsymbol{u}_1 \cdot (\boldsymbol{\sigma}_2 \cdot \boldsymbol{n}) \mathrm{d}S = \int_{S} \boldsymbol{u}_2 \cdot (\boldsymbol{\sigma}_1 \cdot \boldsymbol{n}) \, \mathrm{d}S \tag{2.125}$$

$$\begin{aligned} \implies -\frac{1}{2}\Delta\boldsymbol{U}^{\beta} \cdot \int_{S^{\beta 1}} (\boldsymbol{\sigma}_2 \cdot \boldsymbol{n}) \, \mathrm{d}S \\ + \frac{1}{2}\Delta\boldsymbol{U}^{\beta} \cdot \int_{S^{\beta 2}} (\boldsymbol{\sigma}_2 \cdot \boldsymbol{n}) \, \mathrm{d}S = \boldsymbol{U}^{\alpha} \cdot \int_{S^{\alpha}} (\boldsymbol{\sigma}_1 \cdot \boldsymbol{n}) \, \mathrm{d}S \end{aligned} \tag{2.126}$$

$$\implies -\frac{1}{2}\Delta\boldsymbol{U}^{\beta} \cdot \boldsymbol{F}^{\beta 1} + \frac{1}{2}\Delta\boldsymbol{U}^{\beta} \cdot \boldsymbol{F}^{\beta 2} = \boldsymbol{U}^{\alpha} \cdot \boldsymbol{F}^{\alpha} \tag{2.127}$$

$$\implies \frac{1}{2}\Delta\boldsymbol{U}^{\beta} \cdot \Delta\boldsymbol{F}^{\beta} = \boldsymbol{U}^{\alpha} \cdot \boldsymbol{F}^{\alpha} \tag{2.128}$$

$$\implies \frac{1}{2}\Delta\boldsymbol{U}^{\beta} \cdot (\boldsymbol{R}^{51})^{(\beta\alpha)} \cdot \boldsymbol{U}^{\alpha} = \boldsymbol{U}^{\alpha} \cdot (\boldsymbol{R}^{15})^{(\alpha\beta)} \cdot \frac{1}{2}\Delta\boldsymbol{U}^{\beta} \tag{2.129}$$

$$\implies (R^{15})_{ij}^{(\alpha\beta)} = (R^{51})_{ji}^{(\beta\alpha)}. \tag{2.130}$$

Summary of results

Similar calculations give us the following relationships:

$$\begin{aligned} B_{ij}^{(\alpha\widetilde{\alpha})} &= \widetilde{B}_{ji}^{(\widetilde{\alpha}\alpha)}, & G_{ijk}^{(\alpha\widetilde{\alpha})} &= \widetilde{G}_{kij}^{(\widetilde{\alpha}\alpha)}, & H_{ijk}^{(\alpha\widetilde{\alpha})} &= \widetilde{H}_{kij}^{(\widetilde{\alpha}\alpha)}, \\ (R^{41})_{ij}^{(\beta\alpha)} &= (R^{14})_{ji}^{(\alpha\beta)}, & (R^{51})_{ij}^{(\beta\alpha)} &= (R^{15})_{ji}^{(\alpha\beta)}, & (R^{43})_{ijk}^{(\beta\alpha)} &= (R^{34})_{kij}^{(\alpha\beta)}, \\ (R^{42})_{ij}^{(\beta\alpha)} &= (R^{24})_{ji}^{(\alpha\beta)}, & (R^{52})_{ij}^{(\beta\alpha)} &= (R^{25})_{ji}^{(\alpha\beta)}, & (R^{53})_{ijk}^{(\beta\alpha)} &= (R^{35})_{kij}^{(\alpha\beta)}. \end{aligned} \tag{2.131}$$

Notice that with the contractions,

$$G_{[m]i}^{(\alpha\widetilde{\alpha})} = \mathcal{E}_{mjk} G_{jki}^{(\alpha\widetilde{\alpha})} = \mathcal{E}_{mjk} \widetilde{G}_{ijk}^{(\widetilde{\alpha}\alpha)} = \widetilde{G}_{i[m]}^{(\widetilde{\alpha}\alpha)}, \tag{2.132}$$

and by the same method,

$$\begin{aligned} H_{[m]i}^{(\alpha\widetilde{\alpha})} &= \widetilde{H}_{i[m]}^{(\widetilde{\alpha}\alpha)}, \\ (R^{34})_{[m]i}^{(\alpha\beta)} &= (R^{43})_{i[m]}^{(\beta\alpha)}, \\ (R^{35})_{[m]i}^{(\alpha\beta)} &= (R^{53})_{i[m]}^{(\beta\alpha)}. \end{aligned} \tag{2.133}$$

Hence the contracted tensors have the same symmetry as the uncontracted tensors.

We can conclude that all the off-diagonal component matrices have the symmetry we need for the grand resistance matrix to be symmetric. Furthermore, since we saw in section 2.4.5 that the on-diagonal component matrices are symmetric, we can see that the grand resistance matrix, $\mathcal{R}$, is indeed symmetric.

Note again that the symmetry of $\mathcal{R}$ is reliant on the factor of 1/2 in the $\Delta \boldsymbol{U}^{\beta}$ term in our velocity vector. This should not surprise us, as there is a natural factor-of-2 imbalance in the force on a whole dumbbell and the velocity of the dumbbell: whereas the force on a dumbbell is the *sum* of the individual forces on its beads, the velocity of a dumbbell is the *average* of the individual velocities of the beads.

Lastly, we can also verify that since the inverse of a symmetric matrix is also symmetric, the grand mobility matrix, $\mathcal{M}$, is symmetric as well.

2.5 Periodic domains

Large-amplitude shears in Stokesian Dynamics require samples which are wide enough to not be 'flattened' under large shear. These samples therefore require large numbers of particles. Indeed, the large-amplitude *oscillatory* shear tests, as in chapter 3, are performed with a large, finite, number of particles for this reason. However,

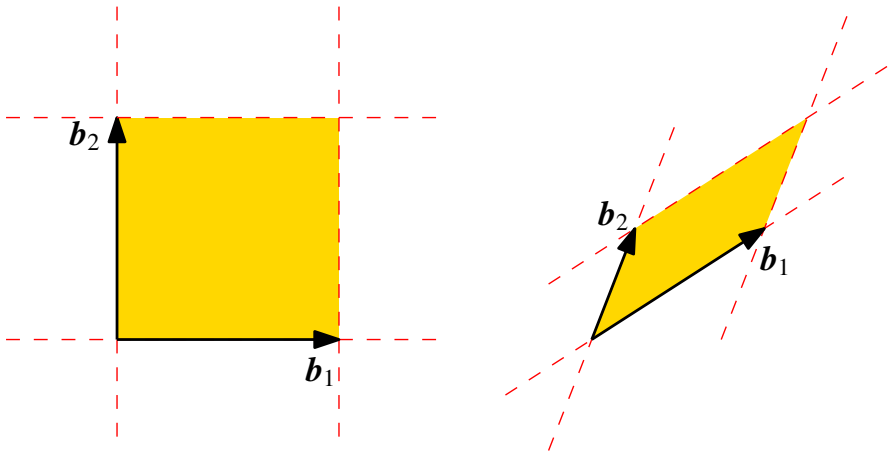

Figure 2.8: The periodic domain (yellow shaded area) is defined as having basis vectors $\boldsymbol{b}_1, \boldsymbol{b}_2, \boldsymbol{b}_3$. This notation also allows the domain to be sheared, as in the right-hand figure. (Here, $\boldsymbol{b}_3$ is omitted for clarity.)

continuous shear, as used in chapter 5, presents problems, as the amplitude of shear only increases. As the grand mobility/resistance matrix scales as $O(N^2)$, for N particles, adding extra particles leads us to hitting large time penalties very quickly. The problem is fixed by adapting Stokesian Dynamics for use in periodic domains. Then, continuous shear can be applied to much smaller domains, but with the condition that particles that disappear from one side of the domain reappear on the other. The details of this process are collated and explained in this section.

Consider the domain to be a box with a basis $\mathcal{B}$ of vectors $\boldsymbol{b}_1, \boldsymbol{b}_2, \boldsymbol{b}_3$, as shown in fig. 2.8. We set up periodicity by repeating the box as a lattice. The basis is such that a particle at a point, $\boldsymbol{r}$, has copies at

$$\boldsymbol{r} + \ell\boldsymbol{b}_1 + m\boldsymbol{b}_2 + n\boldsymbol{b}_3, \quad \ell, m, n \in \mathbb{Z}. \tag{2.134}$$

When $\ell = m = n = 0$, we have the original particle.

If the box is simply a cuboid with dimension $L_x \times L_y \times L_z$, as in the left-hand figure of fig. 2.8, then

$$\boldsymbol{b}_1 = L_x\hat{\boldsymbol{i}}, \quad \boldsymbol{b}_2 = L_y\hat{\boldsymbol{j}}, \quad \boldsymbol{b}_3 = L_z\hat{\boldsymbol{k}}, \tag{2.135}$$

where $\hat{\boldsymbol{i}}$, $\hat{\boldsymbol{j}}$ and $\hat{\boldsymbol{k}}$ are the canonical 3D unit vectors.

2.5.1 Periodic exact resistance matrix

Making the two-body resistance matrix, $\mathcal{R}^{\mathrm{2B,exact}}$, periodic does not take very much work, as the only change is that particles near the boundary of the periodic box may have particles in their critical radius, r^*, which are on the other side of the boundary. For example, in fig. 2.9, the white and black particle now feel each other. There are

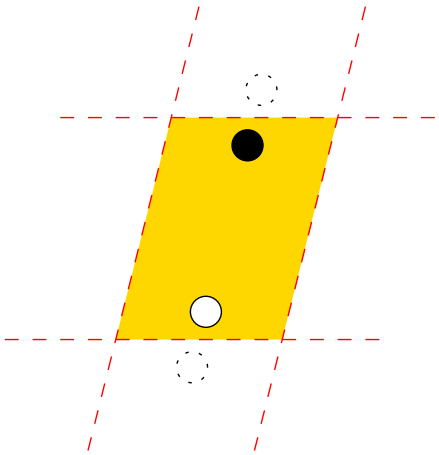

Figure 2.9: The only change needed to $\mathcal{R}^{\mathrm{2B,exact}}$ is that, in this figure, the black and white particles are now in each other's critical radius.

many options for the method of finding particles in another's critical radius with periodic domains. One such implementation is, for each particle, to

1. unshear the box by multiplying all particle positions by the matrix $\mathcal{B}^{-1} = (\boldsymbol{b}_1, \boldsymbol{b}_2, \boldsymbol{b}_3)^{-1}$, making the box a unit cube,
2. move all particles so that the focus particle is at $(\frac{1}{2}, \frac{1}{2}, \frac{1}{2})$, using arithmetic modulo 1,
3. reshear the box with $\mathcal{B}$,
4. find the particles within the critical radius of the focus particle in the usual way.

So long as the sphere described by the critical radius is smaller than the periodic box, then this method works.

2.5.2 Periodic mobility matrix

Adapting the mobility matrix $\mathcal{M}^{\infty}$ for periodic domains requires more work, as now every particle must interact hydrodynamically with all periodic images of all other particles.

Particles at a point $\boldsymbol{r}$ have, from eq. (2.134), copies a vector $\boldsymbol{r}_{\ell mn}$ away, where

$$\boldsymbol{r}_{\ell mn} = \ell \boldsymbol{b}_1 + m\boldsymbol{b}_2 + n\boldsymbol{b}_3, \qquad \ell, m, n \in \mathbb{Z}. \tag{2.136}$$

Therefore the replacement that appears to be required, using the mobility tensor $\boldsymbol{a}$ as an example, is

$$\boldsymbol{a}(\boldsymbol{r}) \longrightarrow \sum_{\ell mn} \boldsymbol{a}(\boldsymbol{r} + \boldsymbol{r}_{\ell mn}), \tag{2.137}$$

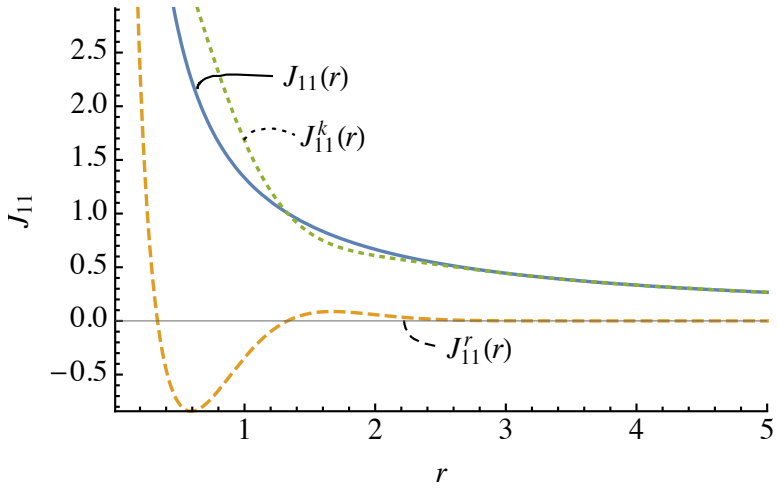

Figure 2.10: The xx-component of $\boldsymbol{J}(r)$, the first-order term of $\boldsymbol{a}$, decays as $1/r$—i.e. slowly—away from zero. Splitting this term into $\boldsymbol{J}^r(r)$ and $\boldsymbol{J}^k(r)$ gives us a term that decays quickly (the former), and a term that initially appears to still decay slowly (the latter): these terms are shown on the figure. In this illustration, we move away from zero on the trajectory $\boldsymbol{r} = (r/\sqrt{3}, r/\sqrt{3}, r/\sqrt{3})$, and $\lambda = 1$.

i.e. we sum over all ℓ, m and n. This sum decays slowly, however, as we go away from the original particle. This is demonstrated in fig. 2.10, where $J_{11}(r)$—the xx-component of the leading-order term in $\boldsymbol{a}$—can be seen to decay as $1/r$. Such slow decay requires many copies of each particle before the sum starts to converge.

Convergence can be sped up by using Ewald summation (Ewald, 1921). Following the technique of Brady *et al.* (1988), it is first noted that

$$J_{ij}(\boldsymbol{r}) = [\delta_{ij}\nabla^2 - \nabla_i\nabla_j](r). \tag{2.138}$$

Defining

$$J^r_{ij}(\boldsymbol{r}) = [\delta_{ij}\nabla^2 - \nabla_i\nabla_j](r\,\mathrm{erfc}(\lambda r)), \tag{2.139}$$
$$J^k_{ij}(\boldsymbol{r}) = [\delta_{ij}\nabla^2 - \nabla_i\nabla_j](r\,\mathrm{erf}(\lambda r)), \tag{2.140}$$

this term is split into two:

$$J_{ij}(\boldsymbol{r}) = J^r_{ij}(\boldsymbol{r}) + J^k_{ij}(\boldsymbol{r}). \tag{2.141}$$

Here, $\mathrm{erf}(x)$ is the error function and $\mathrm{erfc}(x)$ is the complementary error function,

$$\mathrm{erf}(x) = \frac{2}{\sqrt{\pi}}\int_0^x \mathrm{e}^{-t^2}\mathrm{d}t, \qquad \mathrm{erfc}(x) = 1 - \mathrm{erf}(x). \tag{2.142}$$

The key property of the error function, and the reason for its use here, is its quick convergence. The parameter λ allows us to tune the convergence, effectively setting

the radius at which the main contribution switches from $\boldsymbol{J}^r$ to $\boldsymbol{J}^k$: Beenakker (1986) suggests a value of

$$\lambda = \frac{\sqrt{\pi}}{V^{1/3}}, \tag{2.143}$$

where V is the volume of the box, $V = |(\boldsymbol{b}_1 \times \boldsymbol{b}_2) \cdot \boldsymbol{b}_3|$.

Given that we have

$$J_{ij}(\boldsymbol{r}) = J^r_{ij}(\boldsymbol{r}) + J^k_{ij}(\boldsymbol{r}), \tag{2.144}$$

we now see in fig. 2.10 that $\boldsymbol{J}^r$ decays quickly, whereas $\boldsymbol{J}^k$ still decays slowly. The observation of Ewald summation is that while $\boldsymbol{J}^k(\boldsymbol{r})$ decays slowly, its Fourier transform decays *quickly*.

We can exploit this by using the Poisson summation formula, which for a function f on a lattice, says

$$\sum_{\ell mn} f(\boldsymbol{r}_{\ell mn}) = \frac{1}{V} \sum_{\ell mn} \hat{f}(\boldsymbol{k}_{\ell mn}), \tag{2.145}$$

or in its shifted version,

$$\sum_{\ell mn} f(\boldsymbol{r} + \boldsymbol{r}_{\ell mn}) = \frac{1}{V} \sum_{\ell mn} \exp(\mathrm{i}\boldsymbol{k}_{\ell mn} \cdot \boldsymbol{r}) \hat{f}(\boldsymbol{k}_{\ell mn}). \tag{2.146}$$

There are equivalent definitions of the Fourier transform, but following Beenakker (1986) we give the Fourier transform of a function $f(\boldsymbol{r})$ as

$$\hat{f}(\boldsymbol{r}) = \int f(\boldsymbol{r}) \exp(\mathrm{i}\boldsymbol{k} \cdot \boldsymbol{r}) \, \mathrm{d}\boldsymbol{r}. \tag{2.147}$$

We convert from realspace $\boldsymbol{r}$ to wavespace $\boldsymbol{k}$ by using

$$\boldsymbol{r}_{\ell mn} = (\ell\boldsymbol{b}_1 + m\boldsymbol{b}_2 + n\boldsymbol{b}_3) \implies \boldsymbol{k}_{\ell mn} = \frac{2\pi}{V}(\ell\boldsymbol{b}_1 \times \boldsymbol{b}_3 + m\boldsymbol{b}_3 \times \boldsymbol{b}_2 + n\boldsymbol{b}_1 \times \boldsymbol{b}_2). \tag{2.148}$$

For a cuboidal lattice with the canonical $(\hat{\boldsymbol{i}}, \hat{\boldsymbol{j}}, \hat{\boldsymbol{k}})$ 3D basis, this is equivalent to

$$\boldsymbol{r}_{\ell mn} = \begin{pmatrix} \ell L_x \\ m L_y \\ n L_z \end{pmatrix} \implies \boldsymbol{k}_{\ell mn} = 2\pi \begin{pmatrix} -m/L_x \\ -\ell/L_y \\ n/L_z \end{pmatrix}. \tag{2.149}$$

Note that this ensures that $\boldsymbol{r} \cdot \boldsymbol{k}$ is a multiple of 2π, which accounts for the lack of a factor of 2π in our definition of the Fourier transform. Note also that in the shifted Poisson summation formula, eq. (2.146), that so long as the lattice indices are symmetric about zero (e.g. we sum over ℓ from -2 to 2, not -1 to 2), that since

$\exp(\mathrm{i}x) = \cos x + \mathrm{i}\sin x$, the imaginary parts cancel and

$$\sum_{\ell mn} \exp(\mathrm{i}\boldsymbol{k}_{\ell mn} \cdot \boldsymbol{r}) = \sum_{\ell mn} \cos(\boldsymbol{k}_{\ell mn} \cdot \boldsymbol{r}). \tag{2.150}$$

It therefore seems, then, the replacement required for a tensor in a periodic box is

$$\boldsymbol{a}(\boldsymbol{r}) \longrightarrow \sum_{\ell mn} \boldsymbol{a}^r(\boldsymbol{r} + \boldsymbol{r}_{\ell mn}) + \frac{1}{V} \sum_{\ell mn} \cos(\boldsymbol{k}_{\ell mn} \cdot \boldsymbol{r}) \widehat{\boldsymbol{a}^k}(\boldsymbol{k}_{\ell mn}). \tag{2.151}$$

These sums converge quickly, typically needing only two or three terms in each direction away from the focus particle.

There is a final subtlety, however, involving *backflow*: if a single particle is placed in a periodic domain and given a force to the right (for example), it will continue to accelerate in that direction as its periodic images reinforce this motion. To stop unbounded acceleration, we apply backflow to the box, i.e. we apply a force to the whole box which equals the total particle forces in magnitude, but is opposite in direction. Again using the tensor $\boldsymbol{a}$ as an example, we should subtract off

$$\frac{1}{V} \int \boldsymbol{a}(\boldsymbol{r}') \, \mathrm{d}\boldsymbol{r}', \tag{2.152}$$

where the integral is over all space. As it happens, however, it can be shown (Brady *et al.*, 1988, eq. 2.40) that

$$\widehat{\boldsymbol{a}^k}(\boldsymbol{0}) = \int \boldsymbol{a}(\boldsymbol{r}') \, \mathrm{d}\boldsymbol{r}'. \tag{2.153}$$

The replacement can therefore be written as

$$\boldsymbol{a}(\boldsymbol{r}) \longrightarrow \sum_{\ell mn} \boldsymbol{a}^r(\boldsymbol{r} + \boldsymbol{r}_{\ell mn}) + \frac{1}{V} {\sum_{\ell mn}}' \cos(\boldsymbol{k}_{\ell mn} \cdot \boldsymbol{r}) \widehat{\boldsymbol{a}^k}(\boldsymbol{k}_{\ell mn}), \tag{2.154}$$

where the dash on the summation indicates summing over all ℓ, m, n but not $\ell = m = n = 0$.

In the case where $\boldsymbol{r} = \boldsymbol{0}$ (i.e. self-terms), we can remove $\boldsymbol{a}^r(\boldsymbol{0})$ from the first sum and write it as $\boldsymbol{a} - \boldsymbol{a}^k(\boldsymbol{0})$, giving us the expressions which follow in the summarised recipe.

In summary, we can replace the mobility tensors in the following way. For terms relating a particle to itself, $\boldsymbol{a}^{\alpha\alpha}$, and terms relating a particle to a particle a distance

$\boldsymbol{r}$ away, $\boldsymbol{a}^{\alpha\widetilde{\alpha}}(\boldsymbol{r})$, these terms become

$$\boldsymbol{a}^{\alpha\alpha,\mathrm{rep}} = \boldsymbol{a}^{\alpha\alpha} + \sum_{\ell mn}{}' \boldsymbol{a}^r(\boldsymbol{r}_{\ell mn}) + \frac{1}{V}\sum_{\ell mn}{}' \widehat{\boldsymbol{a}^k}(\boldsymbol{k}_{\ell mn}) - \boldsymbol{a}^k(\boldsymbol{0}), \tag{2.155}$$

$$\boldsymbol{a}^{\alpha\widetilde{\alpha},\mathrm{rep}}(\boldsymbol{r}) = \sum_{\ell mn}\boldsymbol{a}^r(\boldsymbol{r}+\boldsymbol{r}_{\ell mn}) + \frac{1}{V}\sum_{\ell mn}{}' \cos(\boldsymbol{k}_{\ell mn}\cdot\boldsymbol{r})\widehat{\boldsymbol{a}^k}(\boldsymbol{k}_{\ell mn}). \tag{2.156}$$

The summations with a dash, $\sum'$, indicate summing over all ℓ, m, n apart from $\ell = m = n = 0$, and V is the volume of the periodic box.

Term-by-term, these are computed thus:

- $\boldsymbol{a}^{\alpha\alpha}$: the usual, non-periodic value of this tensor.

- $\boldsymbol{a}^r$: the realspace periodic version of $\boldsymbol{a}$,

  $$a^r_{ij}(\boldsymbol{r}) = \frac{1}{8\pi\mu}\left(J^r_{ij}(\boldsymbol{r}) + \frac{a_1^2+a_2^2}{6}\nabla^2 J^r_{ij}(\boldsymbol{r})\right), \tag{2.157}$$

  which is the same as the non-periodic definition of $\boldsymbol{a}$, but with $\boldsymbol{J}$ replaced with $\boldsymbol{J}^r$. The derivatives of $\boldsymbol{J}^r$ are computed in appendix A.2.4

- $\widehat{\boldsymbol{a}^k}$: the Fourier transform of the wavespace periodic version of $\boldsymbol{a}$,

  $$\widehat{a^k_{ij}}(\boldsymbol{k}) = \frac{1}{8\pi\mu}\left(\widehat{J^k_{ij}}(\boldsymbol{k}) + \frac{a_1^2+a_2^2}{6}\widehat{\nabla^2 J^k_{ij}}(\boldsymbol{k})\right), \tag{2.158}$$

  which is the same as the non-periodic definition of $\boldsymbol{a}$, but with $\boldsymbol{J}$ replaced with $\widehat{\boldsymbol{J}^k}$. The Fourier-transformed derivatives of $\boldsymbol{J}^k$ are computed in appendix A.2.7.

- $\boldsymbol{a}^k(\boldsymbol{0})$: the wavespace periodic version of $\boldsymbol{a}$, evaluated at $\boldsymbol{r} = \boldsymbol{0}$,

  $$a^k_{ij}(\boldsymbol{0}) = \frac{1}{8\pi\mu}\left(J^k_{ij}(\boldsymbol{0}) + \frac{a_1^2+a_2^2}{6}\nabla^2 J^k_{ij}(\boldsymbol{0})\right). \tag{2.159}$$

  These are computed in appendix A.2.8.

The other periodic mobility tensors have the the same forms with the following special observations:

- $\boldsymbol{b}^{\alpha\alpha,\mathrm{rep}} = \boldsymbol{g}^{\alpha\alpha,\mathrm{rep}} = \boldsymbol{0}$, since these terms are odd and cancel out over the sums,

- $\sum'_{\ell mn}\cos(\boldsymbol{k}_{\ell mn}\cdot\boldsymbol{r})\widehat{\boldsymbol{b}^k}(\boldsymbol{k}_{\ell mn}) = \boldsymbol{0}$, and the same for $\widehat{\boldsymbol{g}^k}$, since the Fourier-transformed tensors are imaginary and cancel out over the sum.

2.6 Computational approach

Our simulation software is written in Python 2.7.6. For the matrix computation, we use the NumPy 1.12.1 and SciPy 0.17.1 packages, and for the graphical output, we use Matplotlib 1.5.1 or 2.0.2.

Python is increasingly popular for scientific computing, being open source, well-supported in the number of libraries, and being generally well-documented online. It is therefore filling the role typically taken by Matlab, with the advantage of also being used outside of academia. Its easy-to-read syntax makes it a good choice for scientific projects which may be developed and used by multiple people on different machines. Two major drawbacks to using Python for scientific computing are that there are often multiple ways of performing an operation, without it being clear which is the optimal choice; and that since Python is untyped, unoptimised code can be quite slow. For-loops, in particular, are much slower than in C or Fortran. Often these are avoidable by using library methods (for example, in matrix multiplication), but sometimes they are not. Part of the aim of this project is to replace old Fortran code, so we pre-compile basic functions which are called a large order of times (for example, the Oseen tensor J_{ij}) using *Cython*. This operates as a Python extension which takes code mostly written in Python syntax (but with typing), and compiles it into C functions. These optimised functions are then called from Python and give fast, C-like performance.

All the Stokesian Dynamics code is written in this way. Resistance and mobility scalars are generated by the slightly adapted 2-sphere code of Wilson (2013), which is written in Fortran 95.

A novel feature of the software is that it admits particles of theoretically any mix of sizes. In practicality, the dispersity of the suspension is dictated by the requirement to generate resistance scalars for all size ratios prior to running the simulation, reducing it to 'n-dispersity'. In this thesis, we restrict our attention to bidisperse suspensions.

An independent novel feature is the ability to compute the motion of some particles through full $\boldsymbol{F}$-$\boldsymbol{T}$-$\boldsymbol{S}$ simulations (the 'spheres'), and some through reduced $\boldsymbol{F}$ simulations (the dumbbells). This couples well with the bidispersity as it allows us to speed up computation with particles—typically the smaller ones—whose angular behaviour we are not interested in.

2.6.1 Program to generate matrix formulation

Recall that the aim of this approach is to construct the grand resistance matrix eq. (2.13),

$$\mathcal{R} = (\mathcal{M}^{\infty})^{-1} + \mathcal{R}^{\mathrm{2B,exact}} - \mathcal{R}^{\mathrm{2B},\infty}. \tag{2.160}$$

For this we need to input

- the positions of the particles,
- the sizes of the particles.

Having done this, we construct the component matrices in the following ways:

Far-field mobility matrix, $\mathcal{M}^{\infty}$

As shown in section 2.3, Faxén's laws allow for an analytic derivation of the elements of the far-field mobility matrix, which have been explicitly displayed in table 2.1. Pre-calculated, explicit forms of the Oseen tensor ($\boldsymbol{J}$) and its derivatives from appendix A.2.3 are used in these calculations.

Two-body resistance matrix, $\mathcal{R}^{\mathrm{2B,exact}} - \mathcal{R}^{\mathrm{2B},\infty}$

The combined two-body resistance matrix $\mathcal{R}^{\mathrm{2B}} = \mathcal{R}^{\mathrm{2B,exact}} - \mathcal{R}^{\mathrm{2B},\infty}$ is constructed from scalar resistance functions, section 2.4.2, which have been altered to include the effect of subtracting $\mathcal{R}^{\mathrm{2B},\infty}$.

Following the description in section 2.4, we fill the upper-triangular half of the $\mathcal{R}^{\mathrm{2B}}$ matrix according to the expressions in eq. (2.69), using row and column operations to fill the dumbbell sections, and then use the symmetry of $\mathcal{R}^{\mathrm{2B,exact}}$ shown in section 2.4.5 to complete the matrix.

We need now to subtract off the $\mathcal{R}^{\mathrm{2B},\infty}$ contribution to the scalars. For each value of s' and λ, we generate a two-body far-field mobility matrix, using the method described in section 2.3. We invert it and subtract it from the exact resistance matrix found using the above method,

$$(\mathcal{R}^{\mathrm{2B}})^{(\alpha\widetilde{\alpha})} = (\mathcal{R}^{\mathrm{2B,exact}})^{(\alpha\widetilde{\alpha})} - ((\mathcal{M}^{\infty})^{(\alpha\widetilde{\alpha})})^{-1}. \tag{2.161}$$

By choosing the same convenient input choices in table 2.2, we can extract the value of the $\mathcal{R}^{\mathrm{2B}}$ scalars. Choosing to store these scalars gives a significant time saving when computing the combined resistance matrix $\mathcal{R}^{\mathrm{2B}}$.

2.6.2 Composition and timestepping

Finally, we add the inverted far-field mobility matrix to the two-body resistance matrix for each timestep, and solve the matrix equation

$$\mathcal{F} = \left[(\mathcal{M}^{\infty})^{-1} + \mathcal{R}^{\mathrm{2B}}\right]\mathcal{U}, \tag{2.162}$$

for the velocity vector, $\mathcal{U}$, in order to determine the positions and orientations of the particles at the next timestep.

Inverting matrices is a slow, unparallelisable procedure which can cause bottlenecks in the code. Rather than inverting the grand resistance matrix above to solve the equation, we call the matrix equation solve function from the Numpy library. This in turn calls the matrix equation solver from the LAPACK library, which uses LU decomposition for both a speed and accuracy increase.

Even avoiding inverting the grand resistance matrix, it still appears that we have to invert the dense far-field mobility matrix, $\mathcal{M}^{\infty}$. However, this can be avoided by multiplying eq. (2.162) through by $\mathcal{M}^{\infty}$ and rewriting:

$$\mathcal{M}^{\infty}\mathcal{F} = (\boldsymbol{I} + \mathcal{M}^{\infty}\mathcal{R}^{\mathrm{2B}})\mathcal{U}. \tag{2.163}$$

We instead solve this equation using the matrix equation solve function. It appears that we have simply switched inverting $\mathcal{M}^{\infty}$ with computing $\mathcal{M}^{\infty}\mathcal{R}^{\mathrm{2B}}$, and same-sized matrix multiplication has the same computational complexity as matrix inversion. However, $\mathcal{R}^{\mathrm{2B}}$ is sparse, and computing $\mathcal{M}^{\infty}\mathcal{R}^{\mathrm{2B}}\mathcal{U}$ is performed in the Numpy solver as $\mathcal{M}^{\infty}(\mathcal{R}^{\mathrm{2B}}\mathcal{U})$, i.e. two quick matrix-vector multiplications.

Whether to use this method has to be weighed up against simply generating $\mathcal{M}^{\infty}$ explicitly every m timesteps. We timestep using the fourth-order Runge–Kutta 'RK4' numerical integration scheme, so one explicit generation of $(\mathcal{M}^{\infty})^{-1}$ can be used (given the particles do not move sufficiently) $4m$ times. The speed difference versus the above method we find to depend on the system, and so we leave both methods as options.

2.6.3 Representing the geometry

A nice feature of this simulation approach is that interesting geometries are quickly and easily constructed. Walls are formed by placing rows of nearly-touching spheres with a fixed zero velocity, allowing for the free formation of many boundaries. We can simulate pipe flow or shear flow, for example, by constructing parallel walls

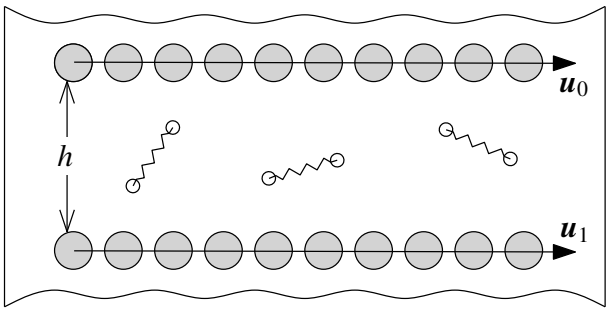

Figure 2.11: We can create flow in a channel of width h by setting up nearly-touching spheres as walls with fixed velocities $\boldsymbol{u}_0$ and $\boldsymbol{u}_1$.

a distance apart, and fixing constant parallel velocities upon them as boundary conditions. Figure 2.11 shows such a construction, where we have dumbbells alone in the bulk of the flow.

2.7 Test cases

We now verify that the Stokesian Dynamics method has been implemented correctly by reproducing some results from the literature. We pick two original test cases from Durlofsky *et al.* (1987) for finite domains, and a test case from Brady *et al.* (1988) for periodic domains.

The first test case, fig. 1 in their paper, concerns a horizontal chain of n spheres, with their centres spaced 4 radii apart, sedimenting perpendicular to their line of centres. For 5, 9 and 15 spheres, the drag $\lambda = F/6\pi\mu aU$ on each particle is measured and plotted (since the forces on the chain are symmetric, only half the chain is shown). Our results, in fig. 2.12, match exactly.

The second test case from this paper is their fig. 5, where three identical spheres are dropped with x-coordinates -5, 0 and 7 in particle radius units. Figure 2.13 shows our falling profiles for the spheres, which matches well with the full ***F*-*T*-*S*** simulations from the paper. At heights $z \lesssim -600$, we begin to see slightly different behaviour, due to the sensitivity to specific configuration, which in turn is determined by the manner of interpolation between resistance scalars at close approaches. Interestingly, setups of this kind are known to be chaotic, and Jánosi *et al.* (1997) give a thorough review of the long-term behaviour of triplets of particles falling from an initial horizontal configuration.

The third test case involves periodic domains. Brady *et al.* (1988, fig. 1) considers the sedimentation of a simple cubic array, although this figure contains errors which are fixed in Sierou & Brady (2001, fig. 9). In these figures, the velocity of the sedimenting

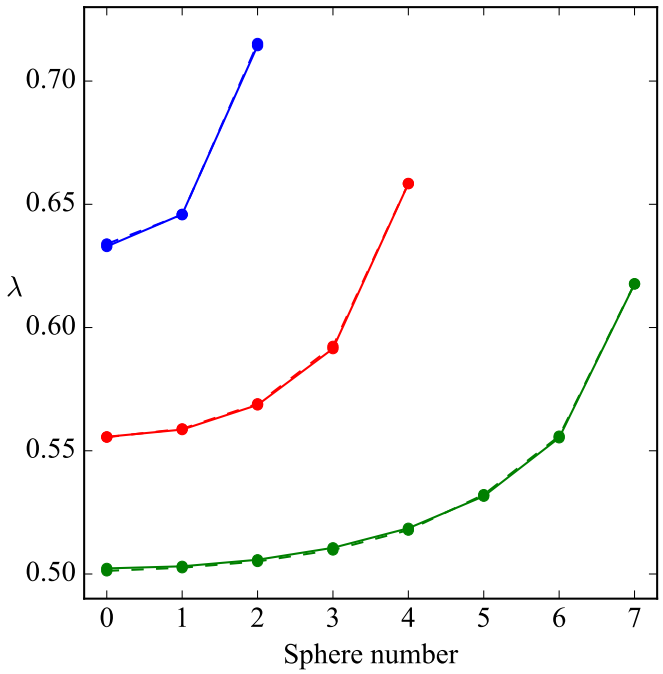

Figure 2.12: Our simulation of the test case from fig. 1 of Durlofsky *et al.* (1987). Horizontal chains of length 5, 9 and 15 spheres drop vertically and the drag coefficient on each particle is measured. Our results (—) are in complete agreement with the paper's (– –).

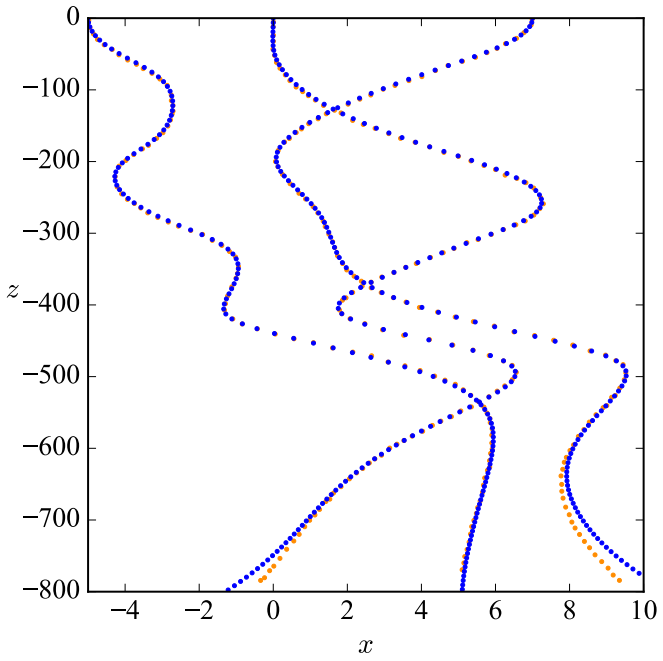

Figure 2.13: Our simulation of the test case from fig. 5 of Durlofsky *et al.* (1987). Three identical balls are dropped with x-coordinates -5, 0 and 7 in particle radius units. Positions are plotted every 10 dimensionless time units. Our profile (blue) matches their full ***F*-*T*-*S*** simulation (orange) very well.

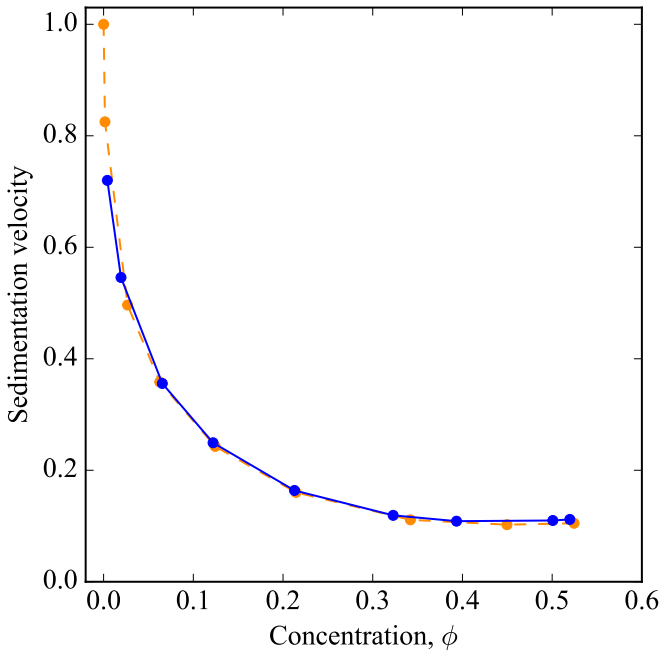

Figure 2.14: Our simulation of the test case from fig. 9 of Sierou & Brady (2001) (which corrects fig. 1 of Brady *et al.* (1988)). The velocity of a sedimenting, simple cubic array is measured for different particle concentrations. Our results (blue, —) match theirs exactly (orange, – –).

array under a unit force is measured for different particle concentrations. Our results are shown in fig. 2.14, where it can be seen that they match the published results exactly.

2.8 Anomalous effect of 'turning off' $\mathcal{M}^\infty$

The two-body lubrication resistance matrices, $\mathcal{R}^{\text{2B,exact}}$ and $\mathcal{R}^{\text{2B},\infty}$, are sparse, as they are calculated only for pairs of particles which are sufficiently close together, normally with a scaled separation distance less than a critical value, r^* (eq. (2.12)). A typical value (Banchio & Brady, 2003) for r^* is 4. Meanwhile, the long-range mobility matrix, $\mathcal{M}^\infty$, considers the motion of each particle as a result of all other particles, so is always dense.

A common approach to speeding up Stokesian Dynamics is to avoid the creation and inversion of this dense matrix. Indeed, the original Stokesian Dynamics method suggested creating and inverting this slowly-changing matrix only every 10 timesteps (Bossis & Brady, 1987).

One such approach, Accelerated Stokesian Dynamics (Sierou & Brady, 2001), works by taking the resistance formulation of Stokesian Dynamics, eq. (2.5), writing out

the matrix in full, eq. (2.13),

$$\boldsymbol{F} = \underbrace{(\mathcal{M}^\infty)^{-1} \cdot \boldsymbol{U}}_{\boldsymbol{F}_{\text{ff}}} + (\mathcal{R}^{\text{2B,exact}} - \mathcal{R}^{\text{2B},\infty}) \cdot \boldsymbol{U}, \tag{2.164}$$

and trying to generate the first term—the far-field force $\boldsymbol{F}_{\text{ff}}$—separately. It does this using an iterative convergence scheme, balancing a real-space contribution (explicit terms for close pairs) and a wave-space contribution (the forces in the system distributed over a grid) to calculate the far-field force. Initially the convergence can be quite slow—slower than normal Stokesian Dynamics in our implementation—so considerations over time savings have to be made.

An easier avoidance technique, common in concentrated suspensions of Brownian particles (Ball & Melrose, 1997; Bybee, 2009; Kumar, 2010; Banchio & Brady, 2003; Ando *et al.*, 2013) but also seen with non-Brownian particles (Torres & Gilbert, 1996), is for simulators to assert that although the long-range hydrodynamic interactions decay slowly (like $1/r$), they are screened by the many-body effects in the dense suspension. The effective motion of the particles is governed predominantly by their neighbours rather than the hydrodynamics of the system as a whole. In other words, the large number and strength of near-field lubrication forces exceeds the effect of the far-field hydrodynamic forces. This theory was first established—for entangled polymer solutions—by De Gennes (1976), who gave a cutoff distance for a given polymer concentration, after which long-range hydrodynamic interactions can be ignored.

In this case, researchers 'turn off' the dense $\mathcal{M}^\infty$, instead replacing it (in both the first and third terms in the right-hand side of eq. (2.13)) with its far-field limit: a 'lubrication hydrodynamics' (LH) approximation. This limit, which can be seen from table 2.1 as $r \to \infty$, consists solely of self-terms on the leading diagonal of the matrix. In particular, for identical particles of radius a, it is given by

$$\mathcal{M}^\infty_{\text{far-field limit}} = \begin{pmatrix} \dfrac{\boldsymbol{I}}{6\pi\mu a} & \boldsymbol{0} & \boldsymbol{0} \\ \boldsymbol{0} & \dfrac{\boldsymbol{I}}{8\pi\mu a^3} & \boldsymbol{0} \\ \boldsymbol{0} & \boldsymbol{0} & \dfrac{\boldsymbol{I}}{\frac{20}{3}\pi\mu a^3} \end{pmatrix}, \tag{2.165}$$

where $\boldsymbol{I}$ is the appropriately-sized identity matrix. The viscosity term, μ, is often replaced with an effective viscosity, $\eta(\phi)$, dependent on suspension concentration. For monodisperse suspensions, this may be chosen to be the dilute Einstein (1906) limit, $\eta(\phi) = \mu(1 + 5\phi/2)$ (Ando *et al.*, 2013): effective viscosities are discussed more in chapter 5.

Replacing $\mathcal{M}^\infty$ with this far-field limit gives a considerable time-saving (in our calculations, up to 50%) as the remaining grand resistance matrix,

$$\mathcal{R}_{\text{LH}} = (\mathcal{M}^\infty_{\text{far-field limit}})^{-1} + \mathcal{R}^{\text{2B,exact}} - \mathcal{R}^{\text{2B},\infty}_{\text{far-field limit}}, \tag{2.166}$$

is sparse, but at the expense of accuracy.

Note that in eq. (2.166), the first and third terms do not cancel for systems of more than two spheres, even if the viscosity term in the first matrix is not ϕ-dependent. To see this, recall that the purpose of $\mathcal{R}^{\text{2B},\infty}$ is to remove inadvertently-included mobility interactions from $\mathcal{R}^{\text{2B,exact}}$. The elements of $\mathcal{R}^{\text{2B},\infty}$ depend on the number of close pairs of particles, whereas $\mathcal{M}^\infty$ simply consists of a self-term for each particle. Thus we are left with the first term representing unbounded Stokes flow for each particle, and the following two terms representing pairwise lubrication.

The accuracy of the LH approximation for some n-disperse non-Brownian systems will be tested here. The accuracy of the approximation for modelling diffusion in dense, polydisperse, Brownian suspensions was examined in Ando *et al.* (2013). They found that particle diffusion constants were broadly accurate but that intermolecular dynamical correlations were significantly underestimated.

In this section, we first show that viscosity measurements taken in monodisperse, periodic systems under continuous shear, are qualitatively unaffected by switching from SD to the LH approximation. There is a systematic error in the stresses which results in reduced measurements (up to 20%) at higher concentrations, but otherwise the system behaviour broadly matches the full SD readings.

In systems where the particles are given external forces, rather than simply moving due to an imposed shear, we begin to find anomalous results for the LH approximation. In particular, we find that we have to be careful about the application of the lubrication forces for bidisperse suspensions. We will show how the default application leads to unphysical results.

To do this, we examine the motion produced by the LH method of up to five close spheres in simple test cases, both monodisperse and bidisperse. These simple test cases demonstrate the mechanism by which these unphysical results are predicted by the LH approximation for much larger bidisperse suspensions.

In particular, we find that under an external force on a large particle, small particles 'bunch up' behind the large particle. In an adaptive timestepping regime, the resultant decrease in particle separations requires reducing the timestep at every timestep. In the test cases, as we will see for viscosity measurements in larger suspensions, we find motion driven by an applied shear to be mostly unaffected, with a small ac-

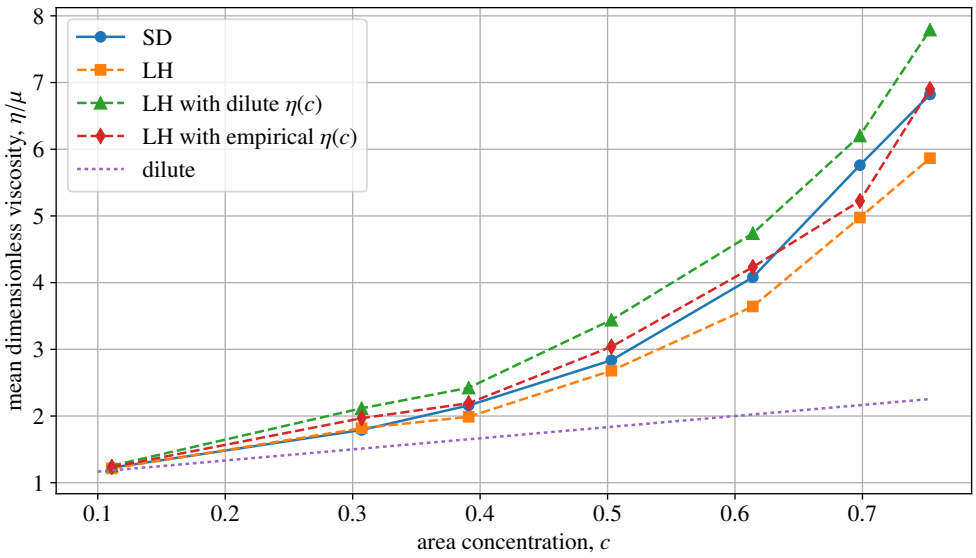

Figure 2.15: The viscosity of a monodisperse monolayer suspension of varying concentration in a periodic system is measured with a full SD simulation (—) and with the LH approximation (- -). The LH approximation is performed with the standard background viscosity, $\eta = \mu$ (squares); with an effective viscosity given by the dilute limit, $\eta = \mu(1 + 5c/3)$ (triangles); and with an empirical effective viscosity, chosen to match the SD data, $\eta = \mu(1 + 5c/6)$ (diamonds). The dilute limit is also shown (···). The periodic box has side length 15 particle radii.

curacy loss. In the finite test cases, the concentration is effectively zero, so we use the unaltered solvent viscosity, μ. The lubrication critical radius, r^*, is set to be as large as necessary so that all particle pairs are included.

It is first worth noting that for two spheres, SD and LH methods will produce the same result, since the true $\mathcal{M}^\infty$ matrix (term 1 in the right-hand side of eq. (2.13)) will match the sum over all pairwise mobility matrices (term 3 in the same equation). At higher numbers of spheres, a discrepancy grows.

2.8.1 Viscosity measurements

We first measure the viscosity of a periodic monodisperse monolayer undergoing continuous shear, using full SD and using the LH approximation. The viscosity is measured using the method detailed in section 5.4, and particles are given a contact force as described in section 5.2. For pairs of approaching particles, this contact force acts in the direction normal to the particle surfaces to exactly stop the approach once the particle surfaces become sufficiently close (here, $10^{-2}a$). No other forces, such as tangential friction forces or repulsion forces, are imposed on the particles. The system is then placed under continuous shear, $\dot{\gamma} = 1$, and the viscosity is taken from the average of three shear cycles, measured after two shear units have passed.

This gives time for the system to equilibrate and this approach is discussed fully in chapter 5.

Figure 2.15 shows the recorded viscosity at different concentrations for SD and LH. We see very good agreement at low concentrations, but find that at higher concentrations, the viscosity readings are underestimated with the LH approximation, up to 20%. The graph shape is qualitatively right, however. In the dilute limit, the effective viscosity of a monolayer suspension with area concentration c is

$$\eta(c) = \mu\left(1 + \frac{5c}{3}\right), \tag{2.167}$$

as derived in section 5.4 (this differs from the fully 3D case where the second term is $5\phi/2$, for a volume fraction ϕ). This is shown on the graph for comparison.

The suggestion in Ando *et al.* (2013) (for fully 3D suspensions) of changing the viscosity term, μ, in eq. (2.165), to the dilute effective viscosity, is also shown on the graph. We find that it overestimates the viscosity by about 20%, suggesting that perhaps this effective viscosity switch does not work particularly well in monolayers. Instead, we find that an empirical effective viscosity of $\eta(c) = \mu(1 + 5c/6)$ gives better agreement. The $5c/3$ term in eq. (2.167) is derived in section 5.4 from an effective volume of the monolayer, which is taken to have depth $2a$. The empirical effective viscosity therefore suggests an 'effective depth' of a monolayer to be $4a$, in order that it scales in the same way as the fully 3D solution, i.e., that the dilute limit is an appropriate effective viscosity.

A very similar comparison experiment for a fully 3D suspension is found in Bybee (2009, fig. 2.16)—where their 'fast lubrication dynamics' is the same as our LH but with a further approximation to $\mathcal{R}^{\mathrm{2B,exact}}$—and draws the same conclusion.

2.8.2 Monodisperse test cases

We illustrate the discrepancy between using the full SD grand resistance matrix, eq. (2.13), ('$\mathcal{M}^\infty$ on') and the simplified far-field LH form, eq. (2.166), ('$\mathcal{M}^\infty$ off') with a setup from Wilson (2013): three identical spheres of radius a, arranged in an equilateral triangle with a given side length (see fig. 2.16). All three spheres are then given a force of $6\pi\mu a$ perpendicular to the plane of the spheres. Figure 2.17 shows the resultant sphere velocities for both cases, and compares it with the true three-sphere velocity.

In agreement with fig. 2 in Wilson (2013), our SD code (with $\mathcal{M}^\infty$ turned on) matches the exact 3-sphere solution for all separations well, with the largest error

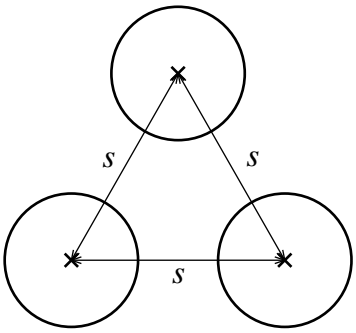

Figure 2.16: Three identical spheres are arranged in an equilateral triangle with side length s, and are given a force perpendicular to the plane in which they lie.

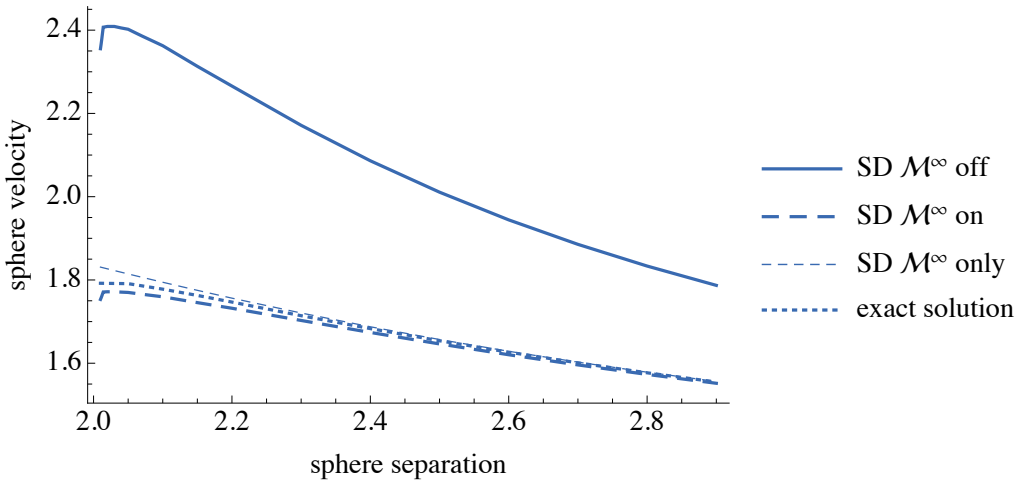

Figure 2.17: Velocity of an equilateral triangle of spheres given identical forces perpendicular to their plane. The Stokesian Dynamics code with $\mathcal{M}^\infty$ turned on matches the exact solution from the Wilson (2013) 3-sphere code well apart from at values very close to $s = 2$, but the lubrication hydrodynamics method with $\mathcal{M}^\infty$ turned off overestimates the velocity by up to 30%.

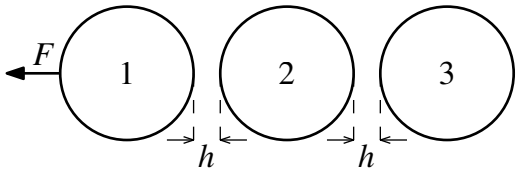

Figure 2.18: Three spheres are aligned in a row, with their surfaces separated by an equal distance h. The first sphere is then given a force directly away from the other spheres.

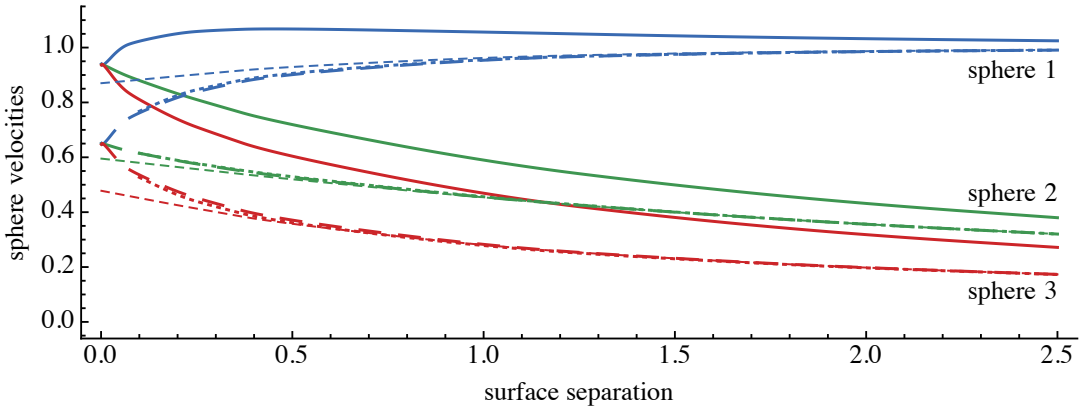

Figure 2.19: Velocities of three identical particles, aligned in a row with a given, equal surface separation. The first particle is given a force directly away from the other particles and the velocities are measured with $\mathcal{M}^\infty$ off (—) and $\mathcal{M}^\infty$ on (– –). The exact solution from Wilson (2013) (···) is also shown, as well as with $\mathcal{M}^\infty$ alone (- - -).

(2%) at very close sphere separations. However, the LH code (with $\mathcal{M}^\infty$ turned off) shows much worse results, overestimating the velocity by up to 30% at the smallest separations. The results are considerably worse than those from a run with the long-range mobility matrix $\mathcal{M}^\infty$ enabled but the lubrication matrices $\mathcal{R}^{\mathrm{2B,exact}}$ and $\mathcal{R}^{\mathrm{2B},\infty}$ disabled ('$\mathcal{M}^\infty$ only'): this has an error of at most 5%. Finally, at high separations, all solutions converge.

We are now going to consider a setup of three identical, linearly aligned particles of radius a, as illustrated in fig. 2.18. The first particle is given a force of $6\pi\mu a$ directly away from the other particles, and the velocities produced with $\mathcal{M}^\infty$ both on and off are recorded in fig. 2.19. We see a similar phenomenon as before: turning $\mathcal{M}^\infty$ off results in velocities for all three particles which have a similar profile shape, but whereas they converge to the exact result at high separations, at the smallest separations the readings are up to 45% larger. Once again this is worse than ignoring lubrication completely ('$\mathcal{M}^\infty$ only'), which has a maximum error of 34%.

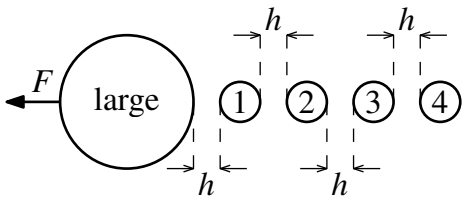

Figure 2.20: A large sphere and a tail of smaller spheres are aligned in a row, with their surfaces separated by an equal distance h. The large sphere is then given a force directly away from the smaller spheres in our test cases.

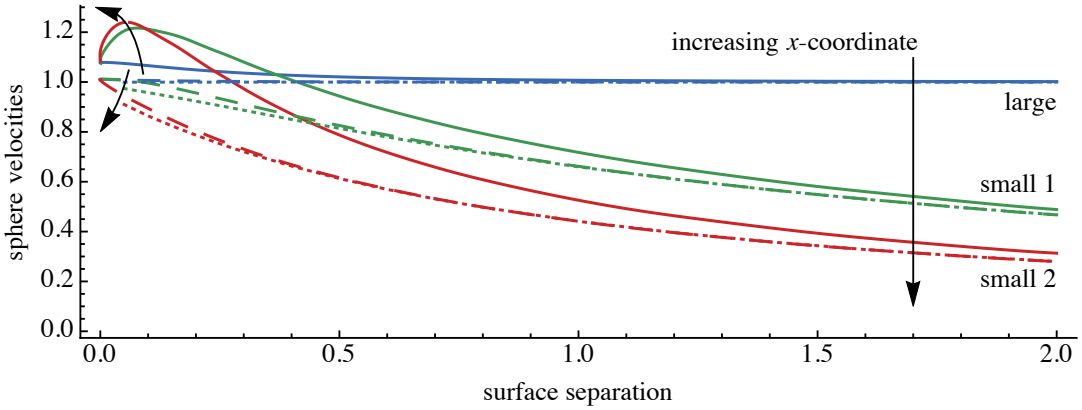

Figure 2.21: Velocities of one large and two small particles, aligned in a row with a given, equal surface separation. The large particle is given a force directly away from the smaller particles and the velocities are measured with $\mathcal{M}^\infty$ off (—) and $\mathcal{M}^\infty$ on (– –). The exact solution from Wilson (2013) (···) is also shown. The arrows point towards the tail of the row of spheres, i.e. in the increasing x-direction.

2.8.3 Bidisperse linear test cases

Although inaccurate, the 30%–45% increase in velocity seen in the monodisperse test cases is still qualitatively feasible. Since the shapes of the velocity profiles are similar, in a concentrated suspension, having many more lubrication forces, it can be argued that such local effects might 'average out' and would be mitigated in a concentrated suspension by use of the modified effective viscosity, $\mu(\phi)$. With bidisperse suspensions, however, we begin to see unphysical behaviour with $\mathcal{M}^\infty$ turned off.

This time consider a setup of linearly aligned particles, similar to the last one, but with one large particle (of radius a) and two small (of radius $a/10$) particles, as illustrated in fig. 2.20 but with a shorter tail. The large particle is given a force of $6\pi\mu a$ directly away from the smaller particles and the velocities produced by SD, with $\mathcal{M}^\infty$ on, and LH, with $\mathcal{M}^\infty$ off, are shown in fig. 2.21.

For this setup, the velocity profiles for $\mathcal{M}^\infty$ on and off no longer have the same shape. Still, at large surface separations we find convergence of the LH $\mathcal{M}^\infty$-off velocities to the exact result (provided by Wilson (2013)). Full SD ($\mathcal{M}^\infty$ on) agrees well

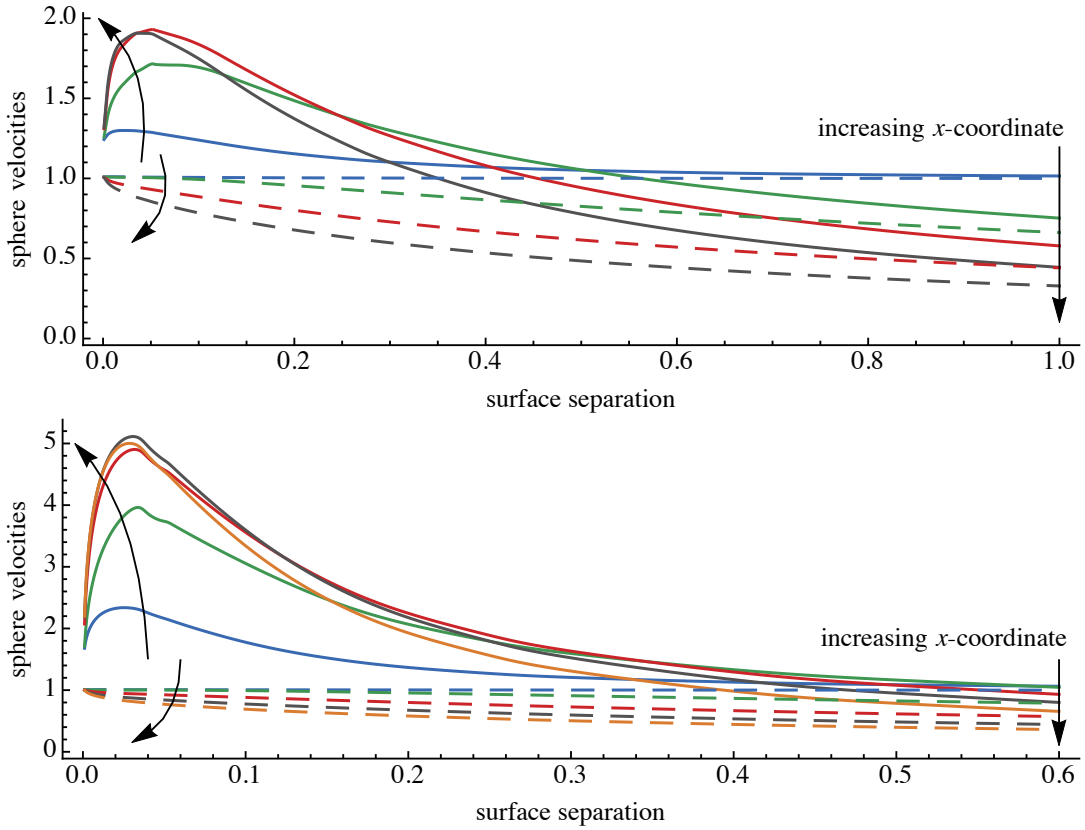

Figure 2.22: **Top:** Velocities of one large and three small particles, aligned in a row with a given, equal surface separation. The large particle is given a force directly away from the smaller particles and the velocities are measured with $\mathcal{M}^\infty$ off (—) and $\mathcal{M}^\infty$ on (– –). The arrows point towards the tail of the row of spheres, i.e. in the increasing x-direction. **Bottom:** Same but with one large and four small particles.

throughout with the exact result, with errors of no more than 4% for the furthest sphere at small surface separations. However, at these close surface separations, we find the unphysical result of the small particles travelling *faster* than the sphere with the force on it. Furthermore, the small particles travel even faster the further away from the large particle they are, leading to 'bunching'. This effect gives rise to particles approaching each other unphysically at the end of the tail, as they 'chase' the lead particle too quickly, causing potential numerical instabilities at small timesteps. In an adaptive timestepping regime, this requires reducing the timestep at every timestep in order to prevent the particles from overlapping in the simulation.

This result is amplified as the tail length increases. Figure 2.22 shows velocities for tails with three and four small particles. In the latter case, we find velocities of the small particles which are measured to be over five times larger with $\mathcal{M}^\infty$ off than with $\mathcal{M}^\infty$ on.

We only find this bunching effect with applied external forces. Placing the same system in an external shear produces an acceptable error between full SD and the reduced LH simulation, similar to the monodisperse case.

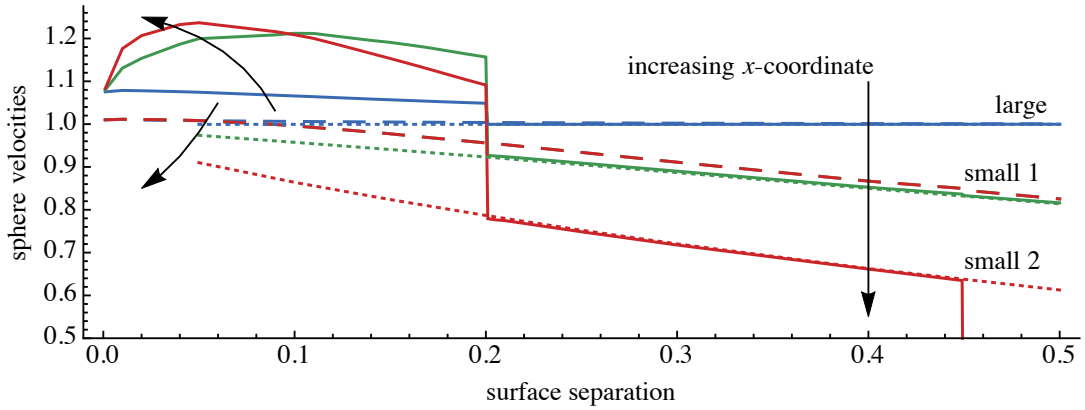

Figure 2.23: The same configuration as in fig. 2.21, but with a reduced critical radius of $r^* = 4$. Velocities of one large and two small particles, aligned in a row with a given, equal surface separation. The large particle is given a force directly away from the smaller particles and the velocities are measured with $\mathcal{M}^\infty$ off (—) and $\mathcal{M}^\infty$ on (– –). The exact solution from Wilson (2013) (···) is also shown. The arrows point towards the tail of the row of spheres, i.e. in the increasing x-direction.

2.8.4 Mechanism

The mechanism we propose for the bunching behaviour described in this section comes from the reach of the lubrication forces. These forces have a stronger effect on the small spheres than on the large one, and the setting of a critical radius, eq. (2.12), means that we can find multiple sets of lubrication interactions on the small spheres. In particular, the last small sphere in the tail feels all of these forces pulling it in the same direction, giving it a larger velocity than the others. In reality, the small spheres in between provide screening against this effect; but this is exactly what the full long-range mobility matrix $\mathcal{M}^\infty$ captures (Brady & Bossis, 1988), which is what is lost.

In the test cases above, the critical radius has been made sufficiently large to capture all pairwise lubrication interactions. Setting it to the previously-mentioned typical value of $r^* = 4$ and reproducing the first test case in section 2.8.3 (the results of which are in fig. 2.21), fig. 2.23 shows us three distinct regions. At closest separations, all particles are within each others' critical radius, and we see the same bunching problem as before. For separations between 0.2 and 0.45, the large particle and the furthest small particle are no longer in each other's critical radius, and we see much better agreement with full SD simulations. At separations above 0.45, the furthest small particle is no longer in any other particle's critical radius and hence feels no force at all, giving it zero velocity.

The best agreement with full SD is in the central region of fig. 2.23. We suggest therefore, that to avoid the bunching effect while still allowing particles to feel lubrication, the LH method should be adapted to turn on lubrication only for a

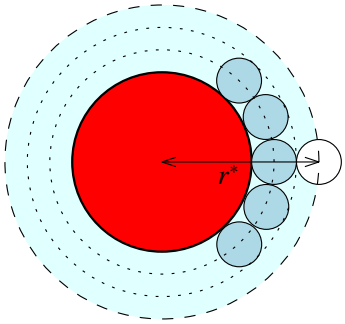

Figure 2.24: The choice of $r^* = a_1 + 3a_2$ sets particles to interact under lubrication forces with particles in a 'shell' of neighbours (dark blue).

shell of actual nearest neighbours. Recalling the shell of nearest neighbours given by setting $r^* = 4$ in fig. 2.5, for bidisperse suspensions with sizes a_1 and a_2, this is typically interpreted as 4 average particle radii,

$$\frac{2r^*}{a_1 + a_2} = 4. \tag{2.168}$$

Instead, we propose keeping this for equal-sized particles, but for distinct-sized particles where $a_1 > a_2$, we propose using, as in fig. 2.24,

$$r^* = a_1 + 3a_2. \tag{2.169}$$

2.8.5 Conclusion

The efficacy of replacing the long-range mobility matrix $\mathcal{M}^\infty$ in Stokesian Dynamics with its far-field form has been tested. We find it to be appropriate in shear-driven, periodic suspensions, but for bidisperse suspensions where the particles are exposed to an external force, it can produce errors if we are not careful about how we apply the lubrication forces.

For monodisperse suspensions under applied force or bidisperse suspensions under applied shear, these errors are large for small separations but affect all the particles equally. However, for bidisperse particles under applied force, the error disproportionately affects the smaller particles, giving them unphysical velocities which, over even small timesteps, can lead to particles approaching each other too quickly for any chosen timestep. That the effect is greater with increasing numbers of particles is particularly concerning. We suggest, therefore, that methods involving this lubrication hydrodynamics simplification should therefore be used with caution when applying external forces to bidisperse suspensions. This effect should be mitigated by enabling lubrication with a critical radius which represents a shell of actual nearest neighbours.

Chapter 3

Oscillatory rheometry

In this chapter we add small bead-and-spring dumbbells to our suspension to mimic a viscoelastic background fluid. We establish the validity of this approach by showing that Newtonian suspensions with dumbbells exhibit the rheological behaviour of viscoelastic fluids.

3.1 Linear rheological measurements

3.1.1 Theory

Most rheometrical measurements are taken in simple shear, or viscometric, flow. Illustrated in fig. 3.1, in simple shear flow, the fluid travels unidirectionally in the (say) x-direction, with velocity gradient in the y-direction, and is neutral in the z-direction. This is often depicted as flow between two infinite plates, where the top plate is moving, but good, realisable approximations are often used in rheometrical equipment, such as flow between concentric cylinders (a Couette rheometer) or flow between a cone and a plate (see fig. 3.2).

In simple shear flow, the only nonzero shear rate component is $\dot{\gamma}_{xy} = \mathrm{d}u/\mathrm{d}y$ and

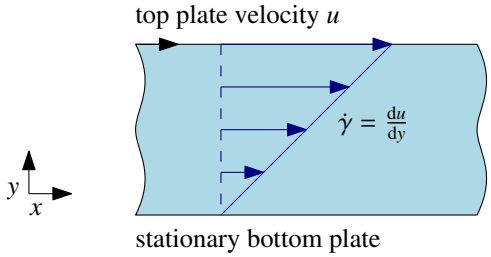

Figure 3.1: A simple shear flow

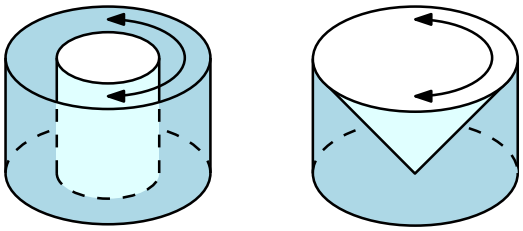

Figure 3.2: Rheometers making good approximations to shear flow. **Left:** a Couette rheometer; **Right:** a cone and plate rheometer

the flow is given by

$$\boldsymbol{u} = (\dot{\gamma}_{xy} y, 0, 0). \tag{3.1}$$

The stress response, $\boldsymbol{\sigma}$, of a Newtonian fluid to this simple shear is simply proportional,

$$\sigma_{xy} = \eta \dot{\gamma}_{xy}, \tag{3.2}$$

a relationship which is described by the fluid's constitutive equation, eq. (1.1). For the remainder of this chapter, we will only be considering stresses and shear rates in the xy-direction, and as such will label them σ and $\dot{\gamma}$ respectively.

In a linear viscoelastic fluid, the stress is dictated not just by the current rate of strain, but also by historical rate of strain,

$$\sigma(t) = \int_{-\infty}^{t} G(t - t') \dot{\gamma}(t') \, \mathrm{d}t'. \tag{3.3}$$

Here, the function $G(t)$ is called the relaxation modulus of the fluid, and represents the importance of the rate of strain from a time t ago on the current stress in the system. Since more recent rates of strain should be more important, $G(t)$ is a decreasing function. Determining the form of the relaxation modulus is the goal of linear rheology, as it allows us to classify viscoelastic fluids.

For example, a purely viscous fluid will have a relaxation modulus of $G(t) = \eta \delta(t)$, where $\delta(t)$ is the Dirac delta function: this reduces eq. (3.3) to eq. (3.2). A linearly elastic solid will have a constant relaxation modulus: $G(t) = G_0$. This reduces eq. (3.3) to

$$\sigma(t) = G_0 \int_{-\infty}^{t} \dot{\gamma}(t') \, \mathrm{d}t', \tag{3.4}$$

where the integral is the total strain the material has undergone.

The test often performed by rheologists to determine the relaxation modulus of a fluid is one of oscillatory shear, where the shear, γ, is given by

$$\gamma(t) = \alpha \sin(\omega t), \tag{3.5}$$

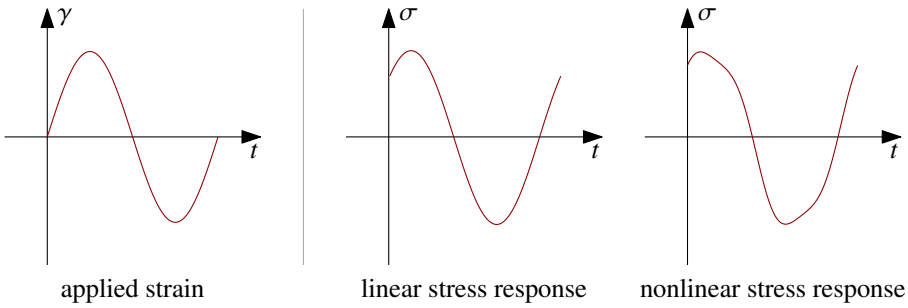

Figure 3.3: A linear and nonlinear stress response to an oscillatory shear over time. For SAOS, we expect the former, but for LAOS, we expect the latter.

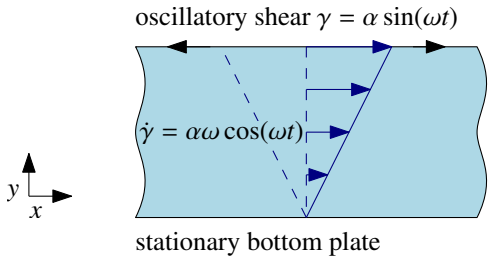

Figure 3.4: Oscillatory shear flow

for an amplitude α and frequency ω. The shear rate is therefore

$$\dot{\gamma}(t) = \alpha\omega\cos(\omega t). \tag{3.6}$$

Experimentally, a sample is placed in a Couette cell and the inner cylinder is rotated to impose a shear on the fluid. So long as the gap is narrow compared to the cylinder radii, and there are no instabilities or shear inhomogeneities, this is equivalent to simple shear flow (fig. 3.4). In practice, the amplitude of the oscillation must be small enough so that the stress response of the fluid is also sinusoidal, i.e. the fluid must remain in its linear regime. At these amplitudes the stress is linear in the amplitude (Hyun *et al.*, 2011). These tests are called small-amplitude oscillatory shear (SAOS).

If the amplitude is increased, the stress response of a fluid may no longer be sinusoidal. For these large-amplitude oscillatory shear (LAOS) tests, a typical nonlinear response is demonstrated in fig. 3.3. Although the following definitions are only defined for small-amplitude oscillatory shear, their large-amplitude analogues provide useful rheological data (Hyun *et al.*, 2011), as discussed in section 3.3.

Imposing an oscillatory shear, then, eq. (3.5), if we stay in the linear regime the stress is given by

$$\sigma(t) = \int_{-\infty}^{t} G(t-t')\alpha\omega\cos(\omega t')\,\mathrm{d}t'. \tag{3.7}$$

With a change of variable $s = t - t'$ and writing $\cos(\omega(t-s)) = \Re[\mathrm{e}^{\mathrm{i}\omega(t-s)}]$, this

becomes (Wilson, 2006)

$$\sigma(t) = \alpha\omega\,\Re\left[\mathrm{e}^{\mathrm{i}\omega t}\int_0^\infty G(s)\mathrm{e}^{-\mathrm{i}\omega s}\,\mathrm{d}s\right]. \tag{3.8}$$

The integral on the right-hand side is not a function of t and is, in fact, just a complex number. We thus define the *complex shear modulus* G^* as

$$G^* = \mathrm{i}\omega\int_0^\infty G(s)\mathrm{e}^{-\mathrm{i}\omega s}\,\mathrm{d}s. \tag{3.9}$$

Its real and imaginary parts,

$$G^* = G' + \mathrm{i}G'', \tag{3.10}$$

are called the *storage modulus* G' and the *loss modulus* G''.

The stress can therefore be written, in this linear regime, as

$$\sigma(t) = G'\gamma(t) + \frac{G''}{\omega}\dot{\gamma}(t). \tag{3.11}$$

This form is powerful because it splits the viscous and elastic contributions. The storage modulus, G', is associated with the total shear γ, and thus represents elasticity. The loss modulus, G'', is associated with the instantaneous shear rate $\dot{\gamma}$, and thus represents viscosity.

The two moduli, G' and G'', are measured by rheologists as a function of frequency, ω, for a wide range of viscoelastic fluids. A typical example looks like fig. 3.12. The inverse of the frequency where the two curves intersect, $\tau = 1/\omega_{\text{intersect}}$, is described as the typical relaxation time of the fluid.

This parameter allows us to nondimensionalise eq. (3.5) (Giacomin *et al.*, 2011), writing the imposed shear as

$$\gamma(t) = \frac{Wi}{De}\sin\left(De\,\frac{t}{\tau}\right), \tag{3.12}$$

where the Deborah number, $De = \tau\omega$, is the ratio of the relaxation time to the oscillation period, and the Weissenberg number, $Wi = \tau\alpha\omega$, is the ratio of viscous forces to elastic forces. However, since determining τ requires us to have already determined G' and G'', we choose not to nondimensionalise the equations in this chapter.

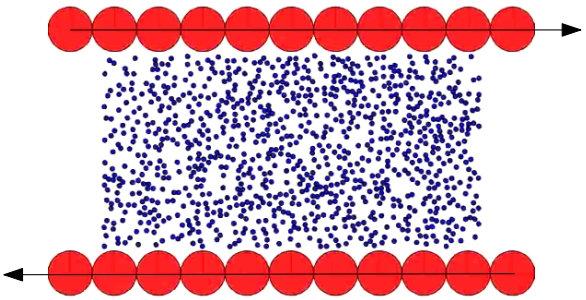

Figure 3.5: A dumbbell suspension between two walls. The dumbbells are each represented by two small beads at their ends. Lines connecting the dumbbells have been omitted for clarity, but the dumbbells are of various lengths and the connecting springs can overlap.

3.1.2 Extraction of rheological measurements from simulations

In this chapter we perform oscillatory simulations on a sample of Newtonian fluid with dumbbells suspended in it. To measure the moduli, G' and G'', we need to be able to extract the fluid stress from the simulation. In this section, we compare different methods of extracting the rheological information from our simulations.

In laboratory rheometrical tests, the fluid stress is extracted from the force experienced by the walls of the rheometer, so this provides a starting place to obtain our measurements.

Method I: Force on two wall rows of spheres; walls driving the motion
We implement a sea of dumbbells as a 3D monolayer, 17 units across and 9 units high. Dumbbells are represented by two beads, of radius 0.1 units, various lengths apart, connected by a spring with a given force law. As we discuss on page 79 ('effect of wall separation'), we find this sample size to be large enough to probe the suspension for its rheological properties without feeling wall or edge effects, but small enough so that simulations are not too computationally expensive.

To model the walls of the rheometer, we can create walls with fixed velocities. When desired, we create these out of larger particles, of radius 1 unit, and create the walls sufficiently long so as not to see edge effects. A typical medium concentration simulation is shown in fig. 3.5. The flow is then driven by the oscillatory velocity imposed on the walls.

In a rheometer, as the walls move, the tangential force applied to the walls by the fluid is measured. For small-amplitude oscillatory shear of the form $\gamma = \alpha \sin(\omega t)$, the force response is also sinusoidal, but delayed by a phase shift, δ. The stress response is given by the force divided by the cross-sectional area of the walls, so we

can write

$$\sigma(t) = \sigma_0 \sin(\omega t + \delta). \tag{3.13}$$

We can extract G' and G'' from this by using the sine sum identity:

$$\sigma(t) = \sigma_0 \sin(\omega t)\cos\delta + \sigma_0 \cos(\omega t)\sin\delta \tag{3.14}$$

$$= \frac{\sigma_0 \cos\delta}{\alpha}\gamma(t) + \frac{\sigma_0 \sin\delta}{\alpha\omega}\dot{\gamma}(t). \tag{3.15}$$

Comparison with eq. (3.11) gives

$$G' = \frac{\sigma_0}{\alpha}\cos\delta; \qquad G'' = \frac{\sigma_0}{\alpha}\sin\delta. \tag{3.16}$$

The phase shift, δ, and amplitude of the stress response, σ_0, are easily measured by plotting the stress response against the strain of the system. These plots are *Lissajous curves* (sometimes Lissajous–Bowditch curves) (Ewoldt *et al.*, 2009), and they provide a useful way of describing the viscoelasticity of a fluid. In a linearly elastic solid, $\sigma = G_0\gamma$, i.e.

$$\sigma = G_0\alpha \sin(\omega t). \tag{3.17}$$

This corresponds, as can be seen in fig. 3.6, to a straight-line Lissajous curve. Meanwhile, in a purely viscous fluid, $\sigma = \eta\dot{\gamma}$, i.e.

$$\sigma = \eta\alpha\omega\cos(\omega t) = \eta\alpha\omega \sin\left(\omega t + \frac{\pi}{2}\right). \tag{3.18}$$

This corresponds to a circular (or elliptical where $\delta = \pi/2$) curve. Fluids that exhibit both viscous and elastic effects have a slanted elliptical orbit somewhere in between these two extremes. In our simulations, plotting the Lissajous curve is useful because we can fit an ellipse to the data, allowing us to take accurate measures of σ_0 and δ.

For SAOS, Lissajous curves are always ellipses, possibly tilted, centred at the origin. This can be verified by substituting $\dot{\gamma} = \alpha\omega\sqrt{1-\gamma^2/\alpha^2}$ into eq. (3.11) and rearranging, giving

$$\frac{1}{G''^2\alpha^2}\sigma^2 - \frac{2G'}{G''^2\alpha^2}\gamma\sigma + \frac{G'^2 + G''^2}{G''^2\alpha^2}\gamma^2 = 1: \tag{3.19}$$

the form of a tilted ellipse.

The measurements of G' and G'' over a frequency sweep as described above for a suspension of Hookean dumbbells are shown in fig. 3.7 (solid lines). Comparing with the Newtonian sweep in the same figure (dashed), we can see no difference in G'': the effect of the dumbbells is masked by the dominating Newtonian viscous contribution, as discussed later in section 3.2.2. Furthermore, we established in section 3.1.1 that

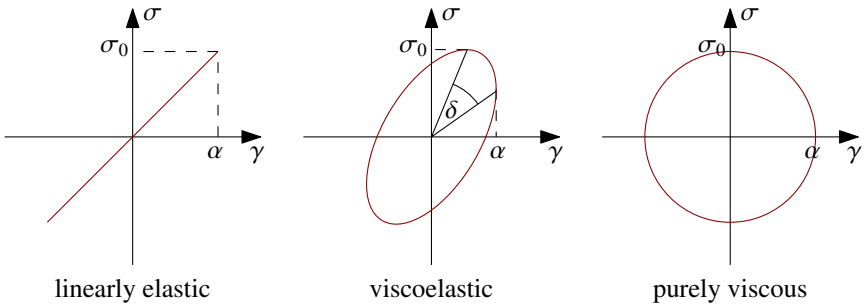

Figure 3.6: Lissajous curves for a linearly elastic solid, viscoelastic fluid, and purely viscous fluid. The eccentricity of the orbit gives an indication as to the balance between viscous and elastic effects. By fitting an ellipse to the data, accurate measures of σ_0 and δ can be found.

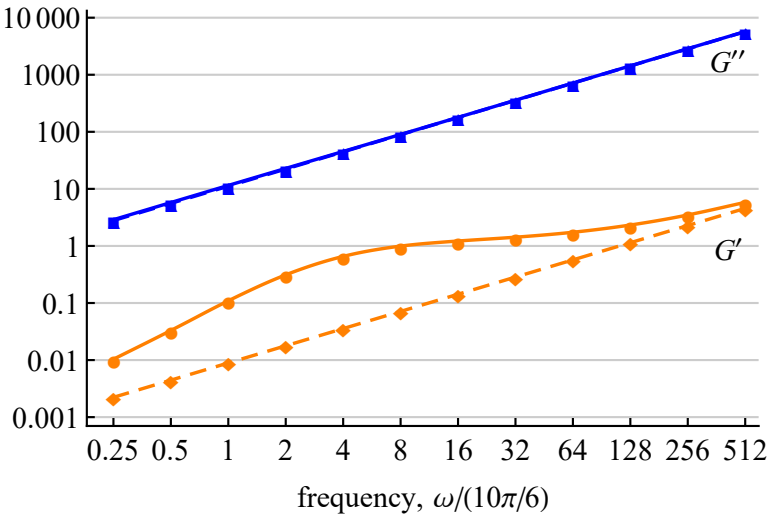

Figure 3.7: Method I: Measurements of G' and G'' for a Hookean dumbbell suspension (—) and a Newtonian fluid (– –). The force measured is the average of the forces on the two walls. The motion is driven by the oscillating walls. The Hookean and Newtonian results for G'' are impossible to distinguish. The Newtonian G' is a systematic error, based on timestep.

for a purely viscous fluid, $G' = 0$, so we know that the measured G' Newtonian result should be very small. At three orders of magnitude smaller than G'', we can see from the figure that it is small, but there appears to be a linear dependence on frequency. This, however, is a reflection of the timestepping procedure in our simulations. Since we generate the inverse mobility matrix $(\mathcal{M}^{\infty})^{-1}$ every 10 timesteps, this generates a very small bias towards past measurements, which manifests in removing the perfect symmetry of the Lissajous curve ever so slightly. With a very small phase shift of $\delta = 0.05°$ clockwise, this bias is enough to produce the positive measurements of G' seen in the figure.

Overall, due to the domination of the viscous contribution, we need another method in order to extract the dumbbell contribution to the force on the walls.

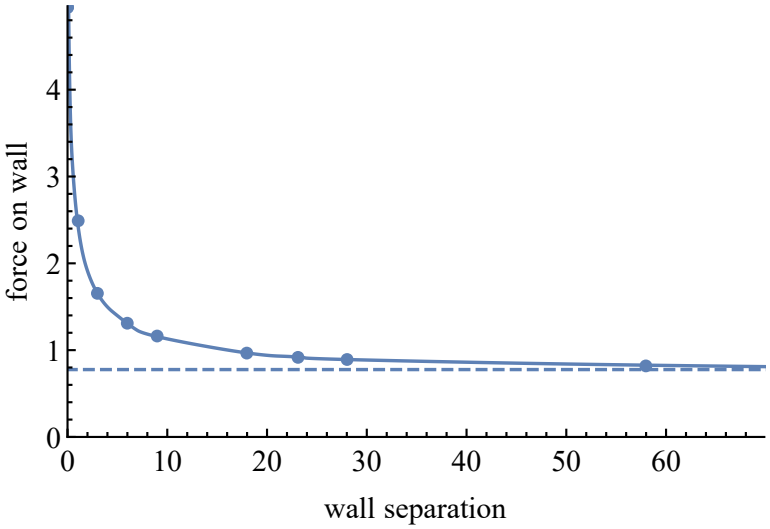

Figure 3.8: The force on the lower wall from an empty Newtonian fluid, as the upper wall is moved further away. The dashed line represents the force on the lower wall in the absence of any upper wall.

Effect of wall separation When we measure the force on the walls, we want this to be the force from the fluid, not an interaction from the other wall. In commercial rheometers (TA Instruments, 2000), the gap size between the plates is recommended to be at least 10 times larger than the diameter of the largest particle. In our simulation we test the force experienced on the lower wall for an empty suspension: only the Newtonian background fluid is present. Figure 3.8 shows the magnitude of this force as we move the upper plate away, which reduces to the limit where we remove the upper wall entirely. At this point, the remaining force on the plate comes entirely from the imposed velocity on each particle, and the resultant interaction between the particles in the wall. The force on the wall behaves like a shifted $1/r$, which is to be expected as the hydrodynamic force between two particles has this form (see eq. (2.14)).

We settle on the sample height of 9 units, as mentioned already, as a compromise between wall effects and computational expense. At the end of this subsection (Method V), we remove the walls entirely and show that the effect of removing them on G' and G'' is small.

Method II: Force on two wall rows of spheres from dumbbells only; walls driving the motion To find the effect of the dumbbells on the storage and loss moduli, we need to remove the dominating viscous behaviour. One option is to simply subtract the measurements of G' and G'' in the empty Newtonian case from the Hookean dumbbell case: the dotted lines in fig. 3.9. In theory this method should isolate the force contribution from the dumbbells, but as can be seen in the figure, this method performs badly, since a viscous contribution remains to G''.

We can improve the method by taking into account the increased viscosity of the solution due to the dumbbells: the 20% dumbbell concentration is found to increase the effective viscosity of the solution by 2.8%. In order to subtract off the viscosity contribution to the moduli, we need to perform a simulation with inactive (passive) dumbbells. As shown in fig. 3.9 (dashed lines), without the viscosity contribution to G'', the curves now cross, which allow us to extract a relaxation time for the dumbbells, as discussed in section 3.2.2. However, at the highest frequency, the difference in measurements for G'' between the inactive and Hookean dumbbell solutions is $3 \times 10^{-6}\%$, well within the regime of numerical errors. As such, it is difficult to extract reliable measurements for G'' at high frequencies. At low frequencies for G'' and for all frequencies of G', the viscosity contribution is much lower proportionally, and hence the results are more reliable in this region.

A better method, and one that does not require two simulations, is to make good use of the Stokesian Dynamics system, which allows us to extract the forces on the walls which come solely from the dumbbells, and not the other wall particles. In the mobility formulation,

$$\begin{pmatrix} \boldsymbol{F}^{\alpha}_{\text{wall}} \\ \boldsymbol{U}^{\alpha}_{\text{free}} \\ \boldsymbol{\Omega}^{\alpha} \\ \boldsymbol{S}^{\alpha} \\ \boldsymbol{U}^{\beta} \\ \frac{1}{2}\Delta\boldsymbol{U}^{\beta} \end{pmatrix} = \begin{pmatrix} \cdot & \cdot & \cdot & \cdot & * & * \\ \cdot & \cdot & \cdot & \cdot & \cdot & \cdot \\ \cdot & \cdot & \cdot & \cdot & \cdot & \cdot \\ \cdot & \cdot & \cdot & \cdot & \cdot & \cdot \\ \cdot & \cdot & \cdot & \cdot & \cdot & \cdot \\ \cdot & \cdot & \cdot & \cdot & \cdot & \cdot \end{pmatrix} \begin{pmatrix} \boldsymbol{U}^{\alpha}_{\text{wall}} \\ \boldsymbol{F}^{\alpha}_{\text{free}} \\ \boldsymbol{T}^{\alpha} \\ \boldsymbol{E}^{\infty} \\ \boldsymbol{F}^{\beta} \\ \Delta\boldsymbol{F}^{\beta} \end{pmatrix}, \tag{3.20}$$

this corresponds to measuring the contribution to $\boldsymbol{F}^{\alpha}_{\text{wall}}$ from the terms marked $*$.

The downside to this approach is that it requires calculating the mobility matrix above explicitly. The Stokesian Dynamics procedure, as discussed in chapter 2, creates its inverse, the resistance matrix $\mathcal{R}$, explicitly and then solves the above equation,

$$\begin{pmatrix} \boldsymbol{F}^{\alpha}_{\text{wall}} \\ \boldsymbol{U}^{\alpha}_{\text{free}} \\ \boldsymbol{\Omega}^{\alpha} \\ \boldsymbol{S}^{\alpha} \\ \boldsymbol{U}^{\beta} \\ \frac{1}{2}\Delta\boldsymbol{U}^{\beta} \end{pmatrix} = \mathcal{R}^{-1} \begin{pmatrix} \boldsymbol{U}^{\alpha}_{\text{wall}} \\ \boldsymbol{F}^{\alpha}_{\text{free}} \\ \boldsymbol{T}^{\alpha} \\ \boldsymbol{E}^{\infty} \\ \boldsymbol{F}^{\beta} \\ \Delta\boldsymbol{F}^{\beta} \end{pmatrix}, \tag{3.21}$$

using linear algebra solving methods. This is computationally quicker than inverting $\mathcal{R}$ explicitly (Golub & Van Loan, 2012), so we lose some speed with this method of extracting the dumbbell contribution to the force on the walls.

The results of the frequency sweep for G' and G'', measuring solely the forces from

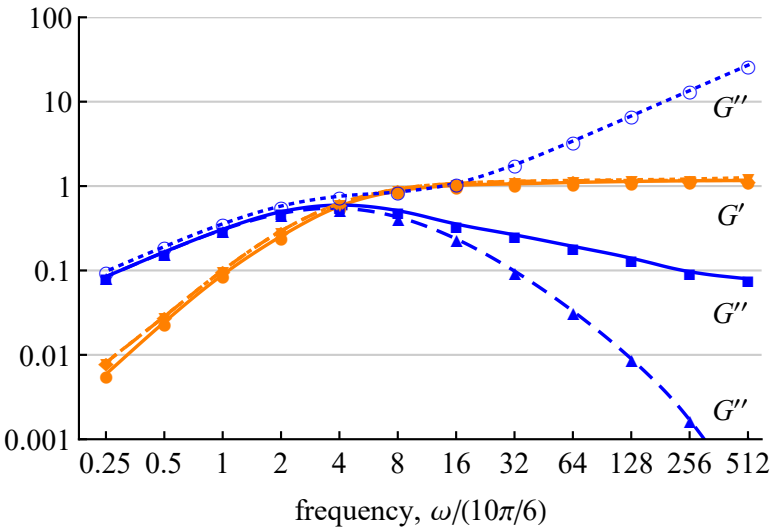

Figure 3.9: Method II: Measurements of G' and G'' for a Hookean dumbbell suspension. The force measured is the dumbbell contribution to each wall, averaged. The motion is driven by the oscillating walls. Measuring directly (—) gives a better result than subtracting the inactive dumbbell forces from the full solution forces (– –), or than subtracting the Newtonian forces from the full solution forces (···). The G' and G'' curves now cross, allowing us to extract a relaxation time, as discussed in section 3.2.2.

the dumbbells, is also displayed (solid lines) in fig. 3.9. This process is shown to be more reliable and we continue to refine this method for extracting the contribution to the moduli from the dumbbells.

Method III: Force on two deeper wall rows of spheres from dumbbells only; walls driving the motion We can capture more forces on the walls by making the walls deeper. Although the simulations are in a 3D monolayer, by making the walls deeper in the third dimension, the central wall particles feel less resistance from the fluid. It also improves the shear: fig. 3.10 shows the amplitude of the shear across the sample. It can be seen that the deeper walls (dark green) provide a more constant shear across the sample than the shallower walls, where the shear is stronger near the walls.

Figure 3.11 compares the readings of G' and G'' against Method II (dashed lines), showing a very slight increase, indicative of capturing slightly more force on the walls. Choosing to align the wall particles in the depth direction in square-packing or hex-packing was shown to produce an indistinguishable difference.

Method IV: Force on two deeper wall rows of spheres from dumbbells only; background fluid driving the motion We have seen in fig. 3.10 that applying motion through the walls creates an uneven shear in the fluid. For a perfectly sharp shear, we can apply it through the background shear rate, $\boldsymbol{E}^{\infty}$. This

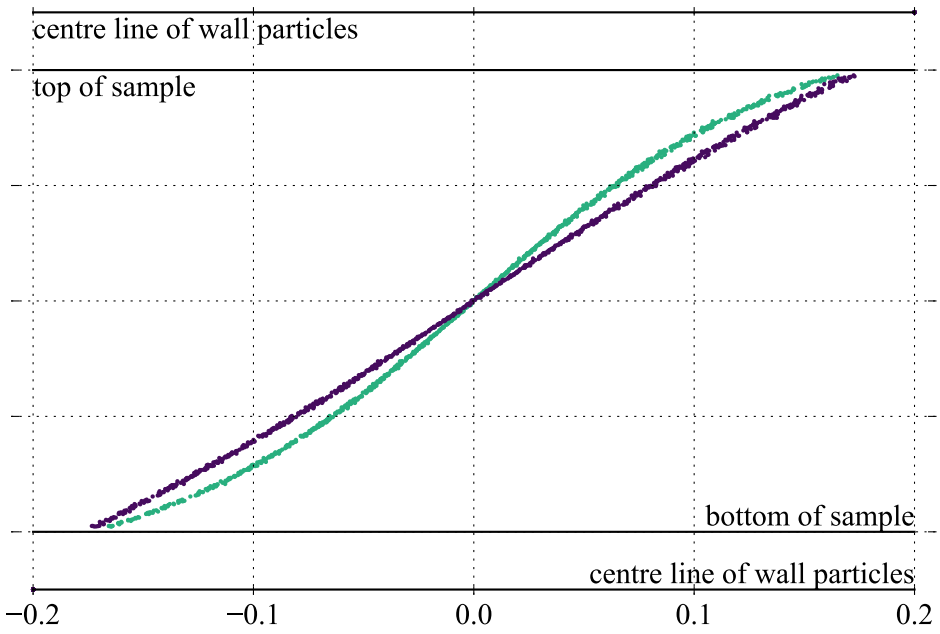

Figure 3.10: Shear amplitude across the sample for all particles. Light green: Method I, shallower walls. Dark purple: Method III, deeper walls. The deeper walls provide a more consistent shear.

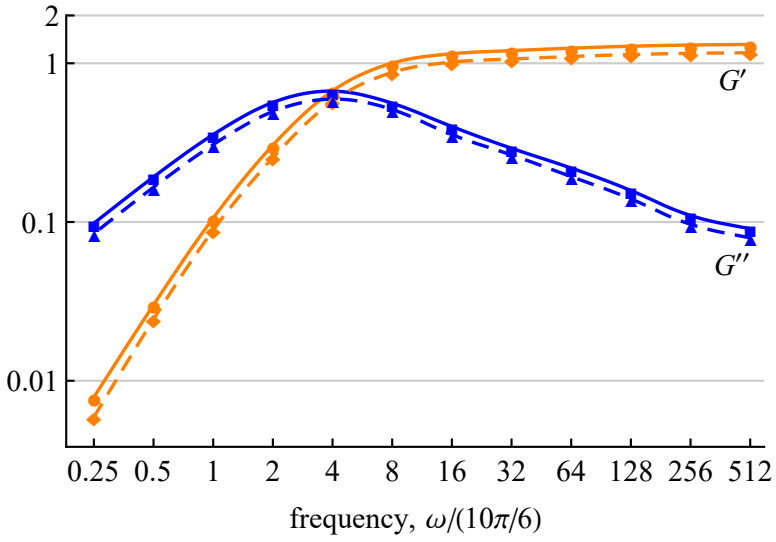

Figure 3.11: Method III: Measurements of G' and G'' for a Hookean dumbbell suspension. The force measured is the dumbbell contribution to each wall, averaged. The motion is driven by the oscillating walls. Walls are now three times as deep. The measurements (—) are shown to be slightly higher than in Method II (– –).

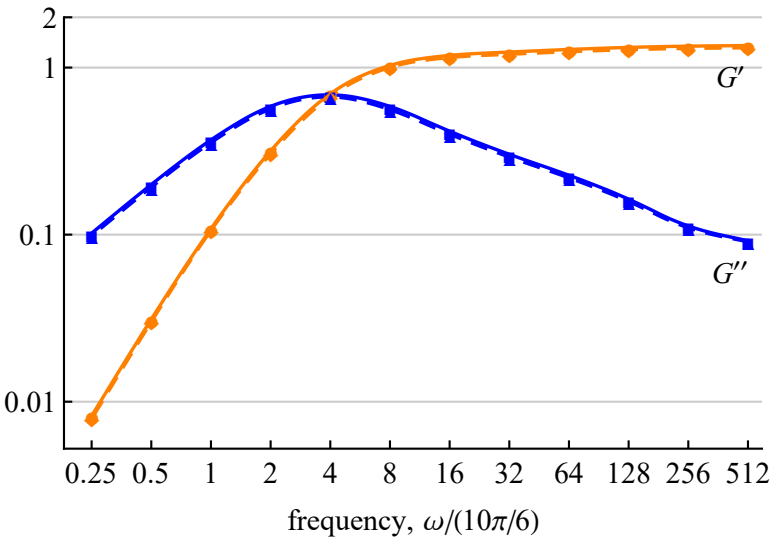

Figure 3.12: Method IV: Measurements of G' and G'' for a Hookean dumbbell suspension. The force measured is the dumbbell contribution to each wall, averaged. The motion is driven by background shear. The measurements from this method (—) match very well those from Method III (– –) when the walls were driving the flow.

method is only available to us because we are performing shear tests; Poiseuille flow, for example, could not be imposed in this way. This method has the advantage of not having to impose velocities on the wall particles, saving us computational effort in moving elements around in the mobility equation.

The imposed background strain rate $\boldsymbol{E}^{\infty}$ felt by the particles is the simple shear

$$\boldsymbol{E}^{\infty} = \frac{1}{2}\begin{pmatrix} 0 & 0 & \dot{\gamma} \\ 0 & 0 & 0 \\ \dot{\gamma} & 0 & 0 \end{pmatrix}, \tag{3.22}$$

where

$$\dot{\gamma} = A\omega\cos(\omega t). \tag{3.23}$$

To make the wall spheres oscillate with amplitude α, the strain rate amplitude A should be

$$A = \frac{2\alpha}{H_W}, \tag{3.24}$$

where H_W is the centre-to-centre wall separation.

Although the walls no longer drive the motion, we can fix them in the background oscillatory flow and extract the force on them in the same way as the previous method. A frequency sweep comparing the G' and G'' measurements in this method to the previous method, where we imposed the shear using the walls, is shown in fig. 3.12. This background-shear method (solid lines) gives equivalent results to when the flow was driven by the walls (dashed lines). The difference in shear amplitude using this

background-forced method and the walls-driven method is shown in fig. 3.14. The walls-driven method (dark green) and the background-forced (mid green) have the same amplitude, but the shear is shown to be a straight line in the latter. The difference, however, is small.

Method V: No walls; background fluid driving the motion We can avoid having to use wall particles at all by imposing shear flow on a sea of dumbbells through the background shear, $\boldsymbol{E}^\infty$, and measuring the total force in the system through the stresslets imposed on the fluid from the dumbbells.

The total force on a volume, V, of fluid, with boundary ∂V, is given by

$$\boldsymbol{F}_V = \iint_{\partial V} \boldsymbol{\sigma} \cdot \boldsymbol{n} \, \mathrm{d}S, \tag{3.25}$$

where $\boldsymbol{\sigma}$ is the stress in the fluid. We want to measure the force on an imaginary upper wall, which for a 3D monolayer makes this equation

$$(F_V)_i = \sigma_{i3} 2 a_\beta L_W, \tag{3.26}$$

where L_W is the box width and $a_\beta = 0.1$ is the radius of the dumbbell beads.

The total stress (per unit monolayer volume), $\boldsymbol{\sigma}$, in a Newtonian fluid with N suspended particles of area fraction c is (Wilson & Davis, 2002)

$$\sigma_{ij} = -p\delta_{ij} + 2\eta E^\infty_{ij} + \frac{c}{2\pi a_\beta^3 N} \sum_\alpha S^\alpha_{ij}, \tag{3.27}$$

where we are summing over the stresslets, $\boldsymbol{S}$, in the fluid. Note that $c/2\pi a_\beta^3 N$ is the reciprocal of the fluid volume.

The stresslet on the fluid by a dumbbell with length $\Delta\boldsymbol{x}$ and force difference $\Delta\boldsymbol{F}$ can be derived from the definition of the stresslet, eq. (2.27). Summing the stresslets of two particles with positions $\boldsymbol{x}^1$ and $\boldsymbol{x}^2$, where $\Delta\boldsymbol{x} = \boldsymbol{x}^2 - \boldsymbol{x}^1$, and with forces $-\frac{1}{2}\Delta\boldsymbol{f}$ and $\frac{1}{2}\Delta\boldsymbol{f}$, and recalling from eq. (2.42),

$$\Delta F_i = \int_S \Delta f_i(\boldsymbol{y}) \, \mathrm{d}S_{\boldsymbol{y}}, \tag{3.28}$$

gives us the dumbbell stresslet contribution

$$S_{ij} = -\frac{1}{4}\left[\Delta x_i \Delta F_j + \Delta x_j \Delta F_i - \frac{2}{3}\delta_{ij}\Delta x_k \Delta F_k\right]. \tag{3.29}$$

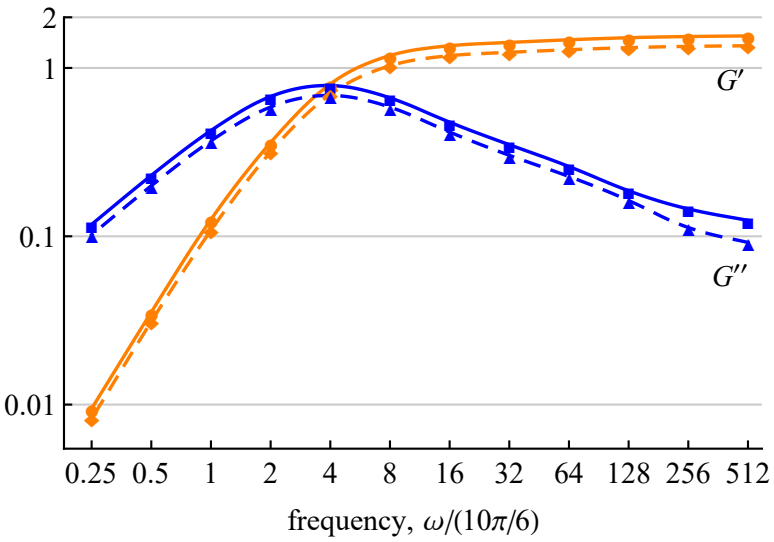

Figure 3.13: Method V: Measurements of G' and G'' for a Hookean dumbbell suspension. The motion is driven by background shear. The force calculated from the dumbbells (—) is slightly higher, but otherwise in good agreement with, the force on the walls (– –), calculated using Method IV.

This method still works with the walls in, of course, and fig. 3.13 shows that this stresslet method gives similar results to those we have just found in Method IV. That the measurements with this method are slightly higher than in Method IV—by consistently about 15%—suggests that the stresslet method captures more of the internal fluid forces.

Removing the walls entirely reduces the computational intensity of the problem on two fronts: we no longer have to extract the dumbbell contribution to the walls, so we can solve the mobility equation using fast linear algebra methods; and we can remove large particles from the problem, each of which contributes an extra 11 terms to the force moment and velocity moment vectors.

The wall removal, however, as can be seen in fig. 3.14, also affects the strain rate amplitude A. With walls, $A = 2\alpha/H_W$ sets the walls oscillating with the required amplitude (α), which forces the fluid beneath the walls to oscillate at that amplitude, in effect moving the oscillating wall toward the fluid sample. The figure shows, by continuing the mid-green line to an amplitude of 0.2, that this effective wall is almost exactly half a large particle radius beneath the centre line of the wall particles.

A frequency sweep for Method V with different wall configurations is shown in fig. 3.15. The walls case (dotted lines) gives higher readings than the no-walls case with the same strain rate amplitude, $A = 2\alpha/H_W$ (solid lines). Changing this to be $A = 2\alpha/H_S$, where H_S is the distance between the aforementioned effective walls, produces a shear which matches that given by the walls, and hence gives readings of the shear and loss moduli (dashed lines) which match the walls case better.

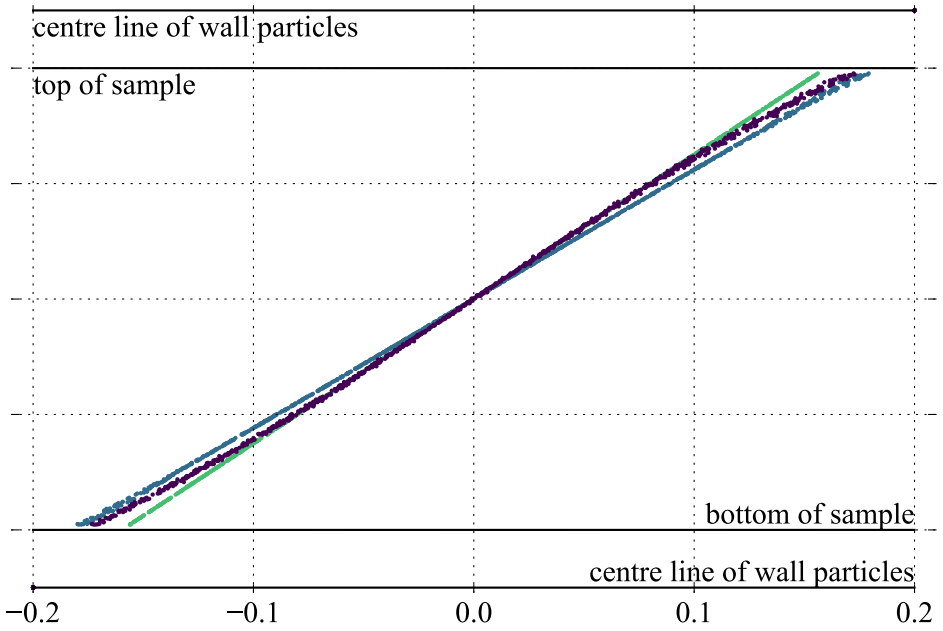

Figure 3.14: Shear amplitude across the sample for all particles using different methods. Dark purple: Method III, deep walls, walls driving motion. Mid blue: Method IV, deep walls, background shear driving motion. Light green: Method V, no walls, background shear driving motion. Background shear gives consistent shear, but removing the wall changes the amplitude of oscillation.

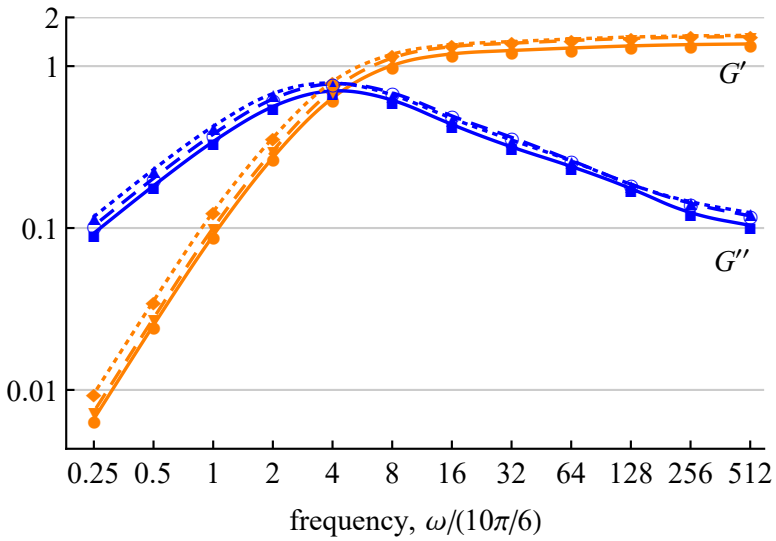

Figure 3.15: Method V: Measurements of G' and G'' for a Hookean dumbbell suspension. The force is calculated from the dumbbells. The motion is driven by background shear. There is good agreement between the walls (···) and same amplitude no-walls (—) cases, but better agreement between the walls and effective amplitude no-walls (– –) cases.

Since the stresslet calculation is faster and captures the physics convincingly, we use this method to perform rheometry with our Stokesian Dynamics simulations. In the next section, we show the results of these tests for various spring laws to validate this method as a way to simulate viscoelastic background fluids.

3.2 Spring forces corresponding to fluid models

As we perform oscillatory simulations, we show here that different force laws on the dumbbells correspond to different fluid models: some by design, and some by observation.

3.2.1 Newtonian: no dumbbells

The trivial case we should check is the empty Newtonian fluid. As can be seen from eq. (3.11), for a Newtonian fluid, $G' = 0$ and $G'' = \omega\eta$. Calculations of these moduli using the stresslet method will certainly agree with these figures, as it follows algebraically from eqs. (3.27) to (3.29). To demonstrate with G'': since a purely viscous fluid will give a Lissajous curve with a phase difference of $\delta = \pi/2$, eq. (3.16) gives us

$$G'' = \frac{\sigma_0}{\alpha}. \tag{3.30}$$

Then by eq. (3.27),

$$G'' = \frac{\sigma_0}{\alpha} = \frac{\eta\dot{\gamma}_{\max}}{\alpha} = \frac{\eta\alpha\omega}{\alpha} = \eta\omega. \tag{3.31}$$

So we can use this to check how much of this we are capturing with rows of spheres on the walls. Figure 3.7 showed that G'' followed this linear relationship. Of course, the walls are contributing to the viscosity here: fig. 3.16 shows the measurements of G' and G'' at the highest frequency we test, $\omega/(10\pi/6) = 512$, for different wall lengths. As expected, the linear relationships show that viscosity is proportional to the wall length.

3.2.2 Oldroyd-B model: Hooke's law

The simplest force law we can apply to our dumbbells is Hooke's law:

$$\boldsymbol{F} = -k\boldsymbol{x}, \tag{3.32}$$

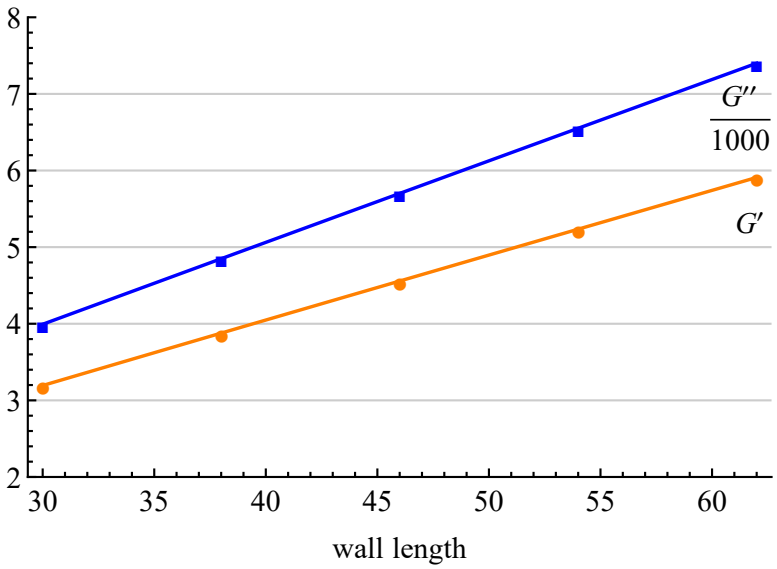

Figure 3.16: Measurements of G' and G'' at $\omega/(10\pi/6) = 512$ in a no-dumbbell solution for different wall lengths. The linear relationships show, as expected, that viscosity is proportional to the wall length.

for an extension $\boldsymbol{x}$ and spring constant k.[1]

The Oldroyd-B model (Oldroyd, 1950) of a viscoelastic fluid is typically represented by a system of equations which govern the evolution of the constitutive equation in time. As it is, in fact, derived from a system of a Newtonian background fluid with bead-and-spring dumbbells, it should provide a theoretical validation of our rheological measurements.

It can be derived from the model (Wilson, 2006) that its storage and loss moduli are

$$G' = \frac{G\omega^2\tau^2}{1+\omega^2\tau^2}, \qquad G'' = \eta\omega + \frac{G\omega\tau}{1+\omega^2\tau^2}. \tag{3.33}$$

Here, G is a constant proportional to the spring constant, $G = km$, where m is the number of dumbbells per unit volume, and τ is the relaxation time of the dumbbell, $\tau = 3\pi a\eta/2k$.

Since we are interested in the contribution from the dumbbells, rather than the solute, we choose to plot G'' without the viscosity component. Along with the shape of the graphs of G' and G'', then, this also allows us to compare some extracted constants: G is the asymptote of G' and $\tau = 1/\omega$ is the crossover point of G' and G''.

These curves are plotted in fig. 3.17 (dashed lines) with the constants G and τ extracted from the simulation in fig. 3.13 (solid lines). There is excellent shape

[1]Note: in the next chapter, we use k as the strength of the *repulsive* force between particles, instead of any spring force. No repulsive force is applied to particles in this chapter, nor do we consider in the entire thesis particles with both spring forces and repulsive forces applied to them.

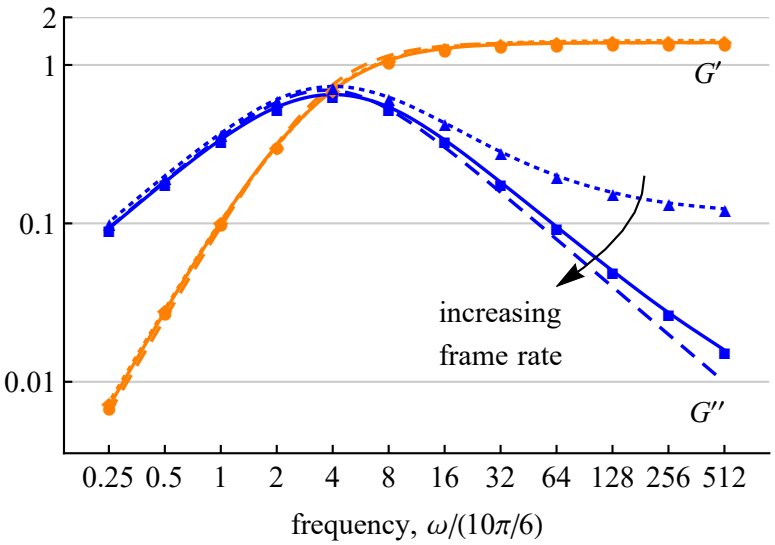

Figure 3.17: The storage and loss moduli, G' and G'', for an Oldroyd-B fluid. There is good agreement between the theoretical (– –) and experimental values. At high frequencies, measurements of G'' at low frame rates (···) diverge from the theoretical values, but increasing the frame rate (—) solves this. In this example, τ and G have been extracted from the simulation in fig. 3.13.

agreement throughout, which is as we would expect. However, to attain this agreement requires very fine timestep resolution in the simulation. At relatively large timesteps (40 frames per oscillation, dotted lines), we see good agreement for all G' and at low frequencies in G''. However, high frequencies give higher readings of G'' than expected. To match the theoretical readings requires much smaller timesteps (1000 frames per oscillation in fig. 3.17, solid lines). The dependency of the higher frequency reading of G'' on frame rate is shown in fig. 3.18, which shows the reduction of the difference between the measurements of G'' and its theoretical value as we increase the frame rate, up to 4000 frames per oscillation.

This sensitivity at high frequencies is because the sample acts almost entirely elastically in this region: the Lissajous plot is almost a (diagonal) straight line. Determining the phase difference between the maximum stress and maximum strain therefore requires very high resolution, even when using the Fourier transform method of finding the moduli, as discussed later in section 3.3.

Effect of concentration Figure 3.19 shows plots of G' and G'' for dumbbell concentrations of 10%, 20% and 40%. Doubling the concentration leads to readings for G' and G'' which are, on average, twice as large. At low concentrations, this is in line with what we expect from eq. (3.33), since G is proportional to the concentration of dumbbells. At higher concentrations, we might expect that the dumbbell beads would interact in a way so as to not lead to a proportional increase in G' and G''. This complication does not appear to happen, at least up to $c = 40\%$.

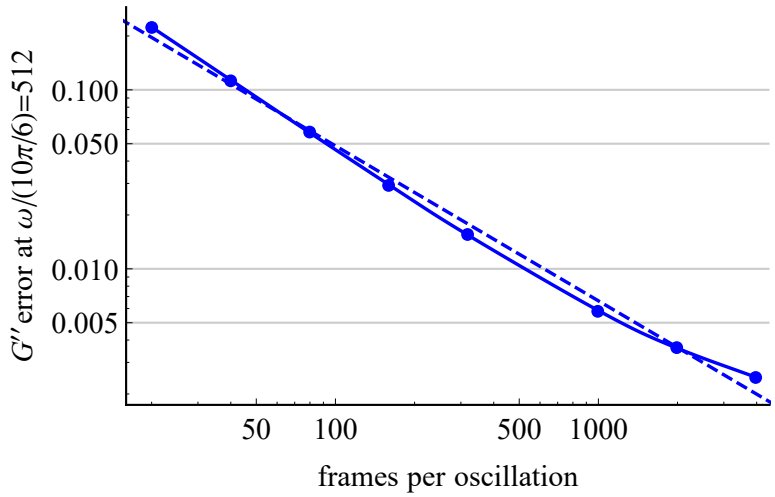

Figure 3.18: Error between the measurements of G'' at the highest frequency in fig. 3.17 and the theoretical value for an Oldroyd-B fluid at the same frame rate. Error term follows the line $E(f) = 2.62f^{-0.866}$ (– –), for f frames per oscillation.

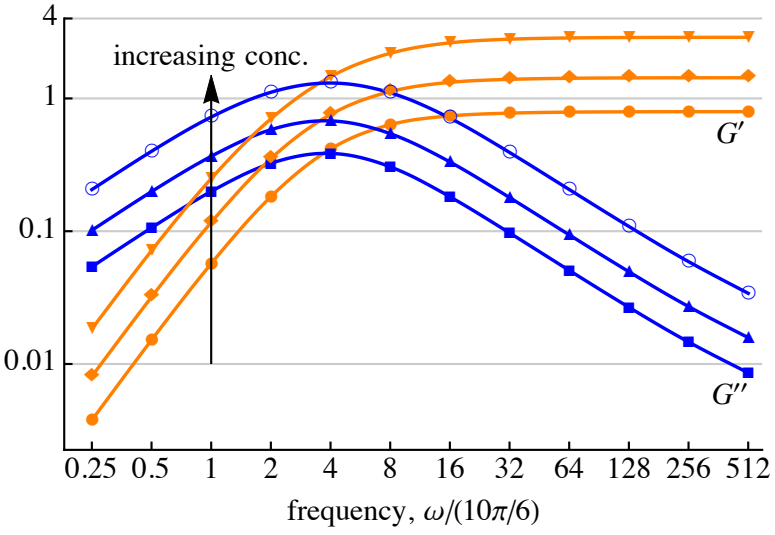

Figure 3.19: The storage and loss moduli, G' and G'', for Hookean dumbbells at concentrations of 10%, 20% and 40%. Higher concentrations lead to proportionally higher readings.

Effect of natural length of dumbbell In the Oldroyd-B model, the idealised dumbbells have a natural length set by the strength of the Brownian motion, which we are not including. To stop the dumbbells contracting to zero length, then, we specify a natural length, L, for our dumbbells. Hooke's law then applies to the *extension*, $\boldsymbol{x}$, from the natural length,

$$\boldsymbol{x} = \Delta\boldsymbol{x} - \frac{L\Delta\boldsymbol{x}}{|\Delta\boldsymbol{x}|}, \tag{3.34}$$

for a dumbbell with end-to-end vector $\Delta\boldsymbol{x}$.

The impact of this imposed natural dumbbell length on G' and G'' is therefore less clear. Figure 3.20 shows the measurements of G' and G'' for three natural lengths: 1, 2, and 4 units. At high frequencies, both G' and G'' show that doubling the natural length leads to approximately a quadrupling of the moduli; whereas at low frequencies, this leads to much lower proportional increases (on average, doubling). This is not altogether surprising: eq. (3.29) shows that the dumbbell stresslet contribution, from which the total fluid stress is calculated, behaves as

$$S \sim \Delta x \Delta F. \tag{3.35}$$

The dumbbell length Δx is dominated in the small-amplitude oscillatory regime by the natural dumbbell length L, and the force is proportional to the extension x, so S behaves as

$$S \sim Lx. \tag{3.36}$$

At large frequencies, the dumbbells have little time to respond to the background motion, which dominates the extension. The extension due to the background flow also scales as L, since dumbbells beads which are further apart feel a greater velocity gradient. Hence the stresslet behaves as L^2 for large frequencies, which is what we observe. At lower frequencies, the spring force plays a larger role, and we have to return to stating $S \sim Lx$, with an unclear scaling for x.

Effect of spring constant Figure 3.21 shows plots of G' and G'' for spring constants of $k = 1$, 2 and 4. The dependency on k agrees with what we expect from the theoretical values in eq. (3.33), as a playoff between $G \sim k$ and $\tau \sim 1/k$. Summarised:

	low ω	high ω
$G' \sim$	$1/k$	k
$G'' \sim$	independent	k

At high frequencies, then, increasing the absolute value of the spring constant leads

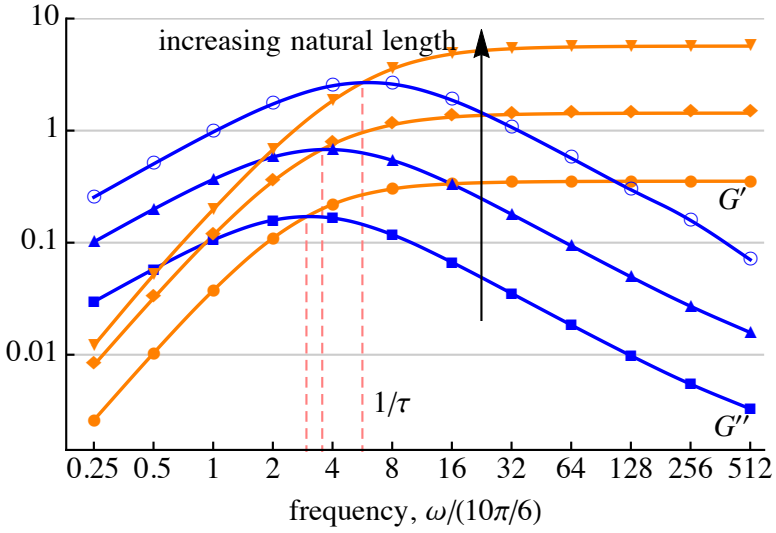

Figure 3.20: The storage and loss moduli, G' and G'', for Hookean dumbbells show a strong dependence on the natural dumbbell length. Increasing the dumbbell length leads to increases in the measurements.

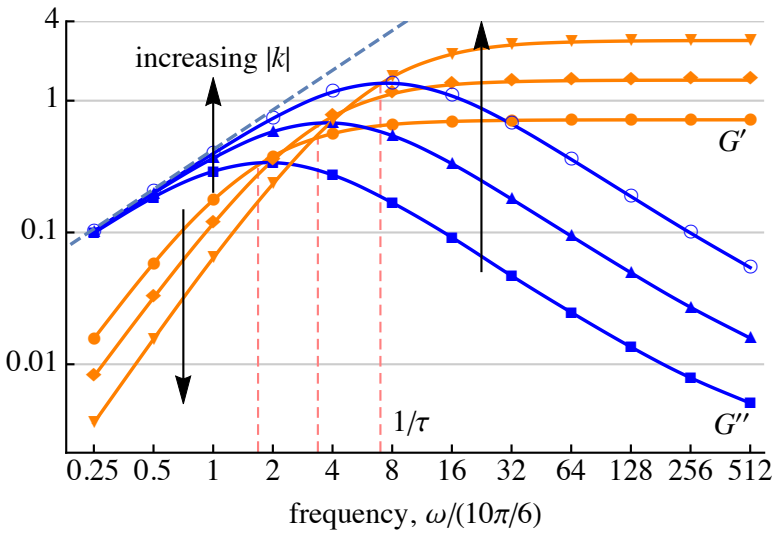

Figure 3.21: The storage and loss moduli, G' and G'', for Hookean dumbbells with spring constants $k = 1$, 2 and 4. Arrows point in the direction of increasing k. At low frequencies, G'' is independent of k, converging to $G\omega\tau$ (blue – –), and G' is inversely proportional to k; but at high frequencies, both G'' and G' are proportional to k. Note that the crossover frequency $1/\tau$ (pink – –) moves proportionally to the right as k increases.

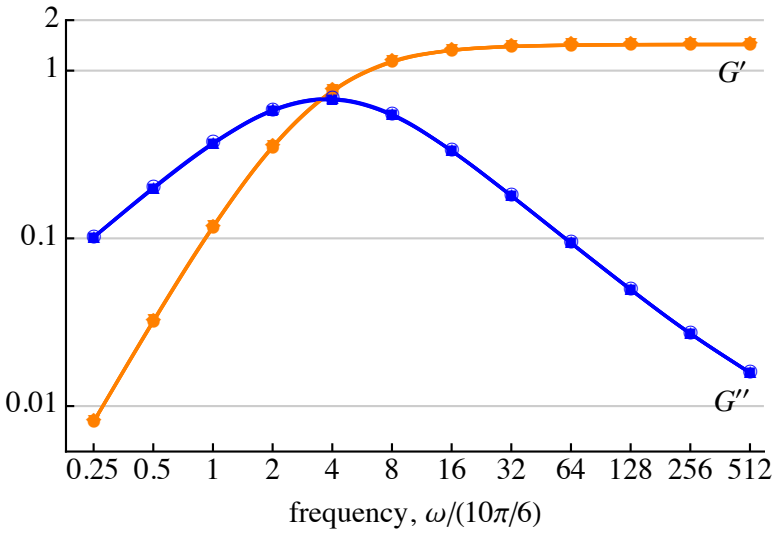

Figure 3.22: The storage and loss moduli, G' and G'', for Hookean dumbbells with oscillatory amplitudes of 0.1, 0.2 and 0.4. The measurements are indistinguishable.

to the same proportional increase in the readings for G' and G''. At lower frequencies, we see two effects: G'' converges to $G\omega\tau$ (blue dashed line), and G' shows the opposite effect to at high frequencies: increasing the spring constant leads to a proportional *decrease*. We see, as expected, that the crossover frequency (pink dashed lines) moves to the right proportionally to the increase in k.

In particular, we notice from the definitions of G' and G'' for an Oldroyd-B fluid, eq. (3.33), that since $G \sim k$ and $\tau \sim 1/k$, that for any constant c,

$$G'(c\omega, k) = cG'(\omega, k/c), \tag{3.37a}$$

$$G''(c\omega, k) = cG''(\omega, k/c). \tag{3.37b}$$

This can be seen in fig. 3.21: with the logarithmic axes, doubling the spring constant is equivalent to a shift of the curve to the right by a factor of 2 and a shift upwards by a factor of 2. In other words, the effect of changing the spring constant is reproduced (with the appropriate scaling factor) by simply changing the frequency of oscillation.

Effect of amplitude Figure 3.22 shows plots of G' and G'' for oscillation amplitudes of 0.1, 0.2 and 0.4. The moduli G' and G'' are shown to be independent of amplitude, which is what we expect from eq. (3.33). We will see in section 3.3 how we can use this as a judge of when we are in the small-amplitude regime.

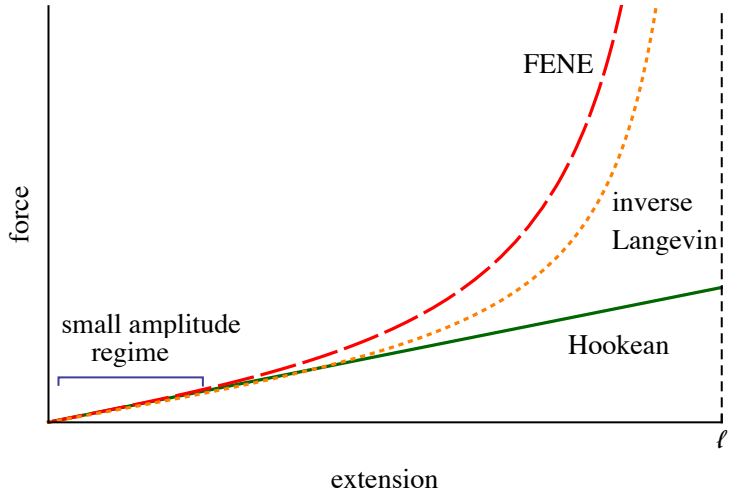

Figure 3.23: The force response to extension for Hookean, FENE and inverse Langevin (which FENE is an approximation to) dumbbells. SAOS experiments, such as we are doing here, stay in the small-amplitude regime where the difference is negligible

3.2.3 FENE dumbbells

A limitation of using Hooke's law to model polymers is that real polymers have a maximum length. Furthermore, in extensional flow, Hookean dumbbell models can predict negative viscosities at sufficiently high strain rates (O'Byrne, 2010, p. 44): a clearly unphysical result. Both these problems are often fixed by using a finitely extensible nonlinear elastic model, or *FENE* model. This force law is governed by

$$\boldsymbol{F} = \frac{-k\boldsymbol{x}}{1 - x^2/\ell^2}, \tag{3.38}$$

where ℓ is the maximum extension of the dumbbell and $x = |\boldsymbol{x}|$. More than just being a 'fix', it is a close approximation to a force law derived for polymer deformation from molecular arguments (Flory, 1953, p. 428, eq. B-4). This law, the inverse Langevin force law, has the form

$$\boldsymbol{F} = -3k\mathcal{L}^{-1}\left(\frac{x}{\ell}\right)\hat{\boldsymbol{x}}, \qquad \mathcal{L}(x) = \coth(x) - \frac{1}{x}, \tag{3.39}$$

where $\hat{\boldsymbol{x}}$ is a unit vector in the extension direction, and the factor of 3 allows us to use the same spring constant as the Hookean and FENE models (Kröger, 2005, p. 14). Figure 3.23 shows the similarity.

Although there are analytically derivable forms of G' and G'' for FENE dumbbells (Herrchen & Öttinger, 1997) in small-amplitude shear, as illustrated in fig. 3.23, FENE (and inverse Langevin) dumbbells in SAOS stay in the mostly Hookean regime. This leads, as can be seen in fig. 3.24, to indistinguishable G' and G'' readings.

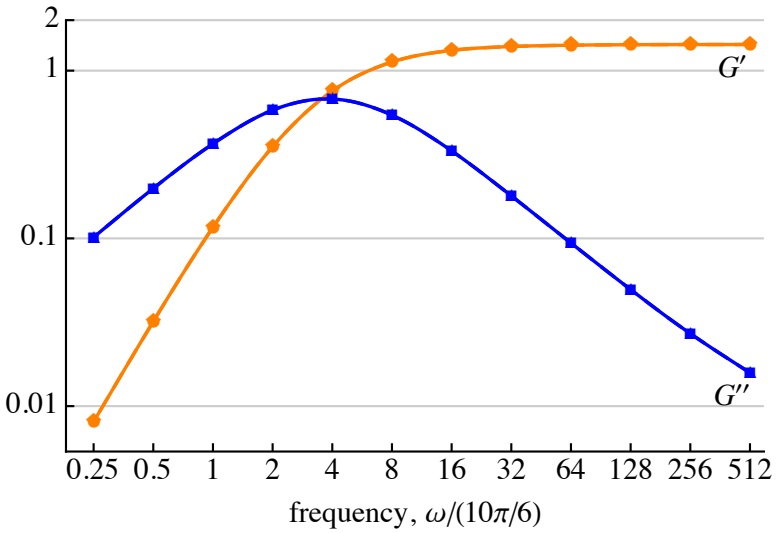

Figure 3.24: The storage and loss moduli, G' and G'' for Hookean dumbbells (– –) is indistinguishable from with FENE dumbbells (—).

3.3 Large-amplitude oscillatory shear

Since in the small-amplitude cases, many spring laws reduce to Hooke's law, we continue our investigation by performing large-amplitude oscillatory shear (LAOS) experiments. In most industrial operations, deformation of fluids is large and fast, and therefore outside the linear regime.

In a LAOS test, we once again apply an oscillatory shear,

$$\gamma(t) = \alpha \sin(\omega t), \tag{3.40}$$

but this time we find that for these large amplitudes, α, the stress response is not a pure sine function, as in eq. (3.13). Instead it is nonlinear, as in fig. 3.25(a). With small-amplitude shear, we were able to define G' and G'' as rheological properties of the fluid we were sampling. The non-sinusoidal stress response also provides a fingerprint for the fluid, giving us not just equivalents to G' and G'', but also additional information about the nonlinearity. LAOS tests can therefore be used to provide diagnostic information, allowing us to classify viscoelastic fluids (Hyun *et al.*, 2002).

There are a number of ways of measuring the nonlinear stress response of a fluid. As in SAOS, we can look at the fluid's Lissajous curves. In the linear regime, these curves, as in fig. 3.6, are elliptical, but in the nonlinear regime they are not: fig. 3.25(b) gives an example.

We can test a sample to find the extent of the linear regime—to find how large 'large' has to be in LAOS—by performing a G' and G'' sweep on the shear amplitude for a

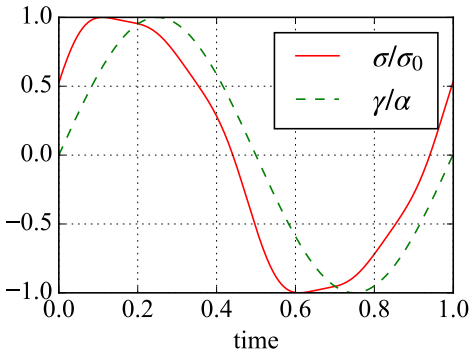

(a) A (normalised) nonlinear stress response, σ/σ_0 to oscillatory shear

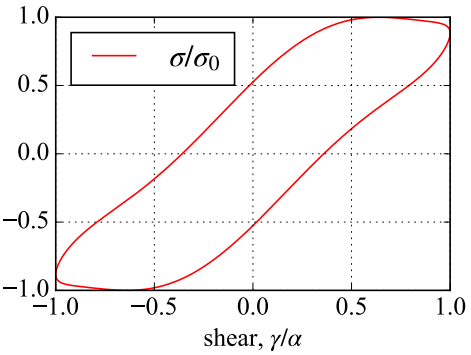

(b) The Lissajous curve for the stress response displays its nonlinearity by its non-elliptical shape.

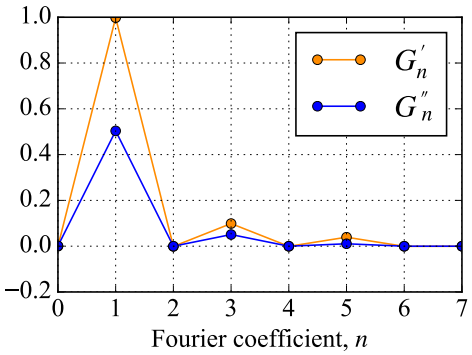

(c) Taking the Fourier transform of the stress response gives the values of the moduli G'_n and G''_n.

Figure 3.25: Two different ways of viewing the nonlinearity of the stress response to oscillatory shear in (a).

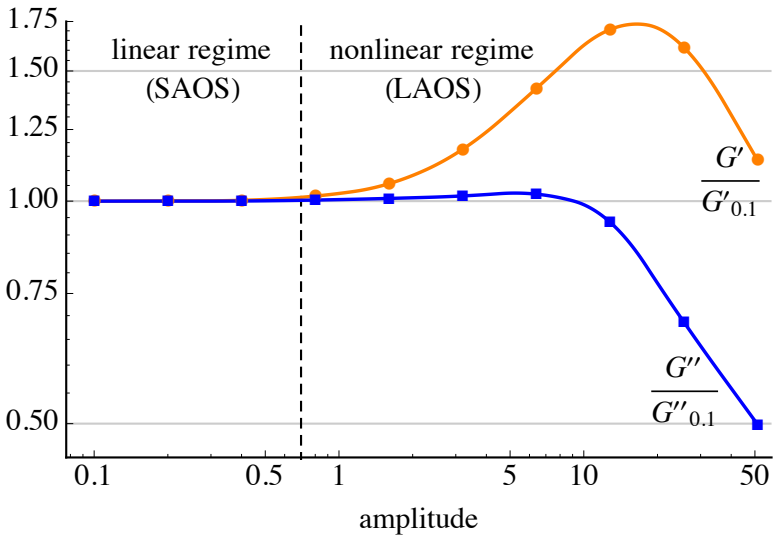

Figure 3.26: An amplitude sweep of our Hookean dumbbell solution: for a fixed frequency ($\omega/(10\pi/6) = 2$), at low amplitudes, G' and G'' (here, normalised by their values at amplitude 0.1) are independent of amplitude, but at higher amplitudes, this changes. This sweep test allows us to find the linear regime region.

fixed frequency. In the linear regime, as we saw in fig. 3.22, these moduli do not depend on the amplitude of oscillation, but at larger amplitudes, they do. Figure 3.26 confirms this for our Hookean dumbbell solution, tracking a fixed frequency over a range of amplitudes. For a more solid definition of 'large', some recent literature has defined LAOS for polymeric liquids as operating for $\alpha > 1$ (Giacomin *et al.*, 2011). In the nondimensional terms introduced in eq. (3.12), the nonlinear regime is reached when the Weissenberg number, Wi,—the ratio of relaxation time to oscillation period—is not small and when the strain amplitude, Wi/De, is also not small (Khair, 2016).

So far, however, G' and G'' have only been defined for SAOS, so we first have to find their LAOS analogues. We do this by presenting the stress response as a Fourier series (Hyun *et al.*, 2011),

$$\sigma(t) = \sum_{\substack{n=1,\\ n \text{ odd}}}^{\infty} \sigma_n \sin(n\omega t + \delta_n), \tag{3.41}$$

where the first term is exactly the response from linear viscoelasticity, eq. (3.13). Note that the summation is over odd frequencies because the imposed stress is odd. We can split up this expression for $\sigma(t)$ in the way we did before, to write

$$\sigma(t) = \alpha \sum_{\substack{n=1,\\ n \text{ odd}}}^{\infty} \left[G_n'(\omega, \alpha) \sin(n\omega t) + G_n''(\omega, \alpha) \cos(n\omega t) \right]. \tag{3.42}$$

In the literature, the first order terms G_1' and G_1'' are those which are typically given: these are the LAOS analogues of G' and G'' and are often called just that.

We can extract the G_n' and G_n'' terms from the measured stress by taking its discrete Fourier transform: a technique known as FT-rheology. For example, consider the nonlinear stress response, σ, to an applied strain in fig. 3.25. If the stress is measured at N points and placed in an array $\boldsymbol{\sigma}$, then the amplitudes of each frequency ($\alpha G_n'$ and $\alpha G_n''$ in eq. (3.42)) are given in the discrete fast Fourier transform of the stress, $\hat{\boldsymbol{\sigma}}$. The fast Fourier transform algorithm (Cooley & Tukey, 1965) arranges these amplitudes by their associated frequency in the following order:

$$0, 1, 2, 3, \ldots, \frac{N}{2} - 1, \frac{N}{2}, -\frac{N}{2} + 1, -\frac{N}{2} + 2, \ldots, -3, -2, -1. \tag{3.43}$$

In each case, the real part of each element in the array, $\hat{\boldsymbol{\sigma}}$, corresponds to the amplitude of the cosine wave, and the imaginary part to the amplitude of the sine

wave, in both cases divided by a factor. Specifically,

$$\alpha G'_n = -\frac{2}{N}\Im[\hat{\sigma}_n], \qquad \alpha G''_n = \frac{2}{N}\Re[\hat{\sigma}_n], \tag{3.44}$$

for $0 \leqslant n \leqslant N/2$. As the amplitudes for negative frequencies are redundant, we ignore amplitudes associated with negative n, i.e. the second half of the transformed array. The resultant measurements can be seen in fig. 3.25(c). The nonlinearity of the stress response is now quantified by the higher order terms of G'_n and G''_n, with those for $n = 3$ and $n = 5$ being noticeably nonzero.

Since the applied strain is odd, we expect the stress response to only have odd terms, so all G'_n and G''_n terms where n is even should be small in our measurements. G''_0, however, being the mean of the stress response, provides a useful measure of how symmetric the response is. As said, this should be small: practically, large values flag up a numerical problem during the simulation.

The FFT method is quick and produces equivalent results to the Lissajous elliptical-fitting method when tested on the SAOS experiments.

An important caveat we have so far neglected is that it is not given that the stress response to large-amplitude oscillatory shear should be periodic—sometimes described as the fluid reaching 'alternance' (Giacomin *et al.*, 2011). As collated by Khair (2016), experiments on polymer melts and colloidal gels have found stress responses to LAOS which are only quasiperiodic (Adrian & Giacomin, 1992) or indeed completely aperiodic (Hatzikiriakos & Dealy, 1991; Kim *et al.*, 2014). However, in our experiments, we do find periodic stress responses.

3.3.1 Classifying fluids with LAOS

As said at the beginning of this section, we can classify viscoelastic fluids using LAOS. Indeed, Hyun *et al.* (2002) (with further discussion in Hyun *et al.* (2011)) outline four types of behaviour for G' and G'' in a LAOS amplitude sweep, which are shown in fig. 3.27. These classes are:

- **Type I (strain thinning):** Both the elastic and viscous moduli decrease with increased amplitude. The mechanism behind this is attributed to entanglement of polymer chains. At low amplitudes, the chains remain entangled, but at high amplitudes, the chains untangle as they are stretched, aligning in the flow direction. This reduces the local drag, decreasing the viscous modulus. As the chains extend, they reach their maximum length, reducing the elastic modulus. Most polymer solutions and melts display this behaviour (Hyun

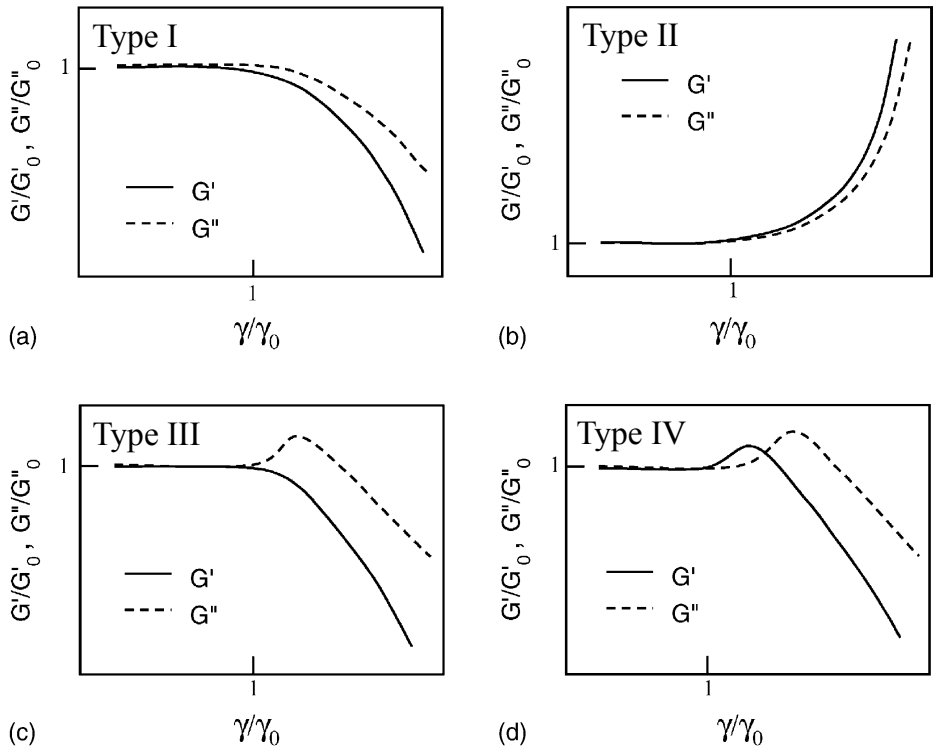

Figure 3.27: Four types of behaviour for G' and G'' in a LAOS amplitude sweep, reproduced from Hyun *et al.* (2002): Type I, strain thinning; Type II, strain hardening; Type III, weak strain overshoot; Type IV, strong strain overshoot.

et al., 2002).

- **Type II (strain hardening):** Both the elastic and viscous moduli increase with increased amplitude. The mechanism behind this is attributed to strong interactions between segments of the fluid. As the amplitude of oscillation is increased, these segments interact in a way to increase resistance to flow. For example, polymer chains crossing can form microstructure which inhibits further deformation in the flow direction. Many biological gels—Hyun *et al.* (2011) give the examples F-actin, fibrin and collagen—exhibit this behaviour, as well as PVA/Borax (polyvinyl alcohol/sodium borate) solutions (Inoue & Osaki, 1993).

- **Type III (weak strain overshoot):** Both the elastic and viscous moduli eventually decrease with increased amplitude, but the viscous modulus initially increases. The mechanism here is a combination of the previous two types: initially weak microstructure is formed which resists flow, but after a critical shear amplitude, the structure is destroyed and the chains align in the flow direction, aiding flow. This feature is common in soft, glassy materials: concentrated emulsions, suspensions and pastes among other examples (Hyun *et al.*, 2011).

- **Type IV (strong strain overshoot):** Both the elastic and viscous moduli

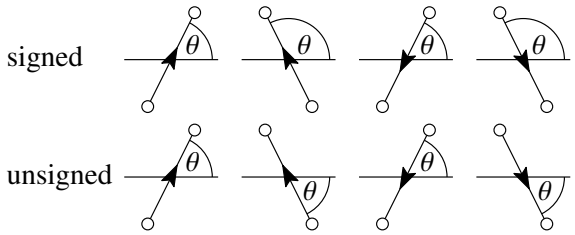

Figure 3.28: Two ways of measuring alignment for dumbbell vectors $\Delta\boldsymbol{x}$ pointing in different directions: signed, where $0^\circ \leqslant \theta < 180^\circ$, and unsigned, where $0^\circ \leqslant \theta < 90^\circ$.

eventually decrease with increased amplitude, although they both initially increase. The mechanism here is the same as Type III, but with stronger intermolecular interaction (but not as strong as in Type II). This behaviour is seen in associative polymer solutions (Tirtaatmadja *et al.*, 1997).

This classification of complex fluids looks solely at the behaviour of the first harmonic, which makes it a simple method for experimental use as it can be typically done with standard rheological equipment (using the Fourier Transform analysis above) without the need to collect full stress data. However, as we have seen, LAOS is typified by the non-sinusoidal stress response: to capture more information about the sample, other classifications exist which measure the contributions of higher harmonics.

One such test we will use here is measuring the contribution of the third harmonic relative to the first harmonic,

$$Q(\alpha) = \frac{1}{\alpha^2}\frac{\sqrt{G_3'(\alpha)^2 + G_3''(\alpha)^2}}{\sqrt{G_1'(\alpha)^2 + G_1''(\alpha)^2}}, \tag{3.45}$$

as first described by Hyun & Wilhelm (2009). (The factor of $1/\alpha^2$ at the front is due to the tendency of the nth harmonic to be proportional to the nth power of the amplitude, at small amplitudes.)

They found that the behaviour of $Q(\alpha)$ as the shear amplitude increases was different for different fluid samples: for monodisperse linear polystyrene solutions, it decreases, but for comb polystyrene solution, it increases. Concluding that Q was somehow related to polymer topology, they went no further. Nonetheless, by its definition, higher values of Q correspond to increased nonlinear effects, and thus we will find it useful as a measurement of these.

A final measurement we can take, given that we have all the particle position data, is the degree of alignment of the dumbbells in the shear direction. Alignment of dumbbells in the flow direction can affect elasticity in that direction, and we can

quantify how much by looking at the angle the dumbbells make with the shear direction: we call this the *mean dumbbell pitch*. There are two options to measure the angle from each dumbbell vector $\Delta\boldsymbol{x}$, as shown in fig. 3.28. One option is to measure dumbbells leaning into the shear as distinct from dumbbells leaning away from the shear—we call this the *signed* mean pitch,

$$\Xi^{\pm} = \text{mean}\left\{\cos^{-1}\left(\frac{\Delta\boldsymbol{x}}{|\Delta\boldsymbol{x}|}\cdot\hat{\boldsymbol{i}}\right)\text{sgn}\left(\left[\frac{\Delta\boldsymbol{x}}{|\Delta\boldsymbol{x}|}\times\hat{\boldsymbol{i}}\right]_z\right)\right\}, \tag{3.46}$$

where $\hat{\boldsymbol{i}}$ is the unit vector parallel to the shear, and this gives a pitch of $0^\circ \leqslant \theta < 180^\circ$. In a well-mixed solution, the mean signed dumbbell pitch should be 90°.

The other option is to measure pitch by how far each dumbbell is away from being horizontal—we call this the *unsigned* mean pitch,

$$\Xi = \text{mean}\left\{\cos^{-1}\left(\left|\frac{\Delta\boldsymbol{x}}{|\Delta\boldsymbol{x}|}\cdot\hat{\boldsymbol{i}}\right|\right)\right\}, \tag{3.47}$$

where taking the inverse cosine of the absolute value of the dot product gives the smallest angle between the two vectors, $0^\circ \leqslant \theta < 90^\circ$. In a well-mixed solution, the mean unsigned dumbbell pitch should be $\sim 45^\circ$.

The two measurements, signed and unsigned, show us something different: for example, if we consider two dumbbells with signed pitches of 10° and 170°, their signed mean is 90°, whereas their unsigned mean is 10°. The signed measure shows that there is no left–right bias, whereas the unsigned measure shows that the dumbbells lie almost parallel to the shear direction.

Figure 3.29 shows the mean dumbbell pitch, signed and unsigned, for Hookean dumbbells over two cycles of shear at different amplitudes. For both measurements, the suspension starts well-mixed. As the suspension is sheared, the mean pitch decreases, as to be expected; larger amplitudes lead to larger decreases. In the signed pitch figure, the measurements where the shear changes sign (multiples of π) are interesting: we see that at this neutral shear position, for higher amplitudes, the dumbbells now lean more, on average, towards the new shear direction.

The unsigned graph adds additional information. Again, as the suspension is sheared, the mean pitch decreases; but as the shear reverses, it does not return to its original measurement. The peak of the mean pitch—taking, for example, the measurement at the peak near the shear angle of 3π—decreases for increasing amplitude. In other words, larger amplitudes encourage stronger alignment of dumbbells parallel to the shear direction.

We can describe alignment as a function of shear amplitude by measuring the peaks

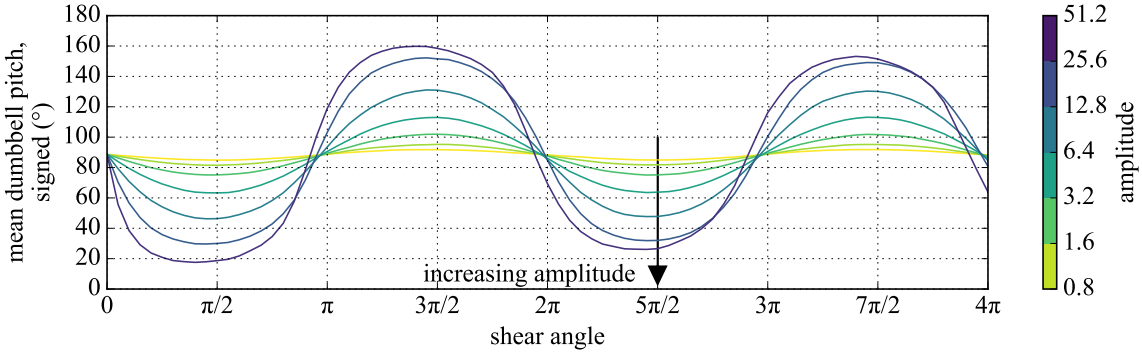

(a) Signed pitch, $0^\circ \leqslant \theta < 180^\circ$

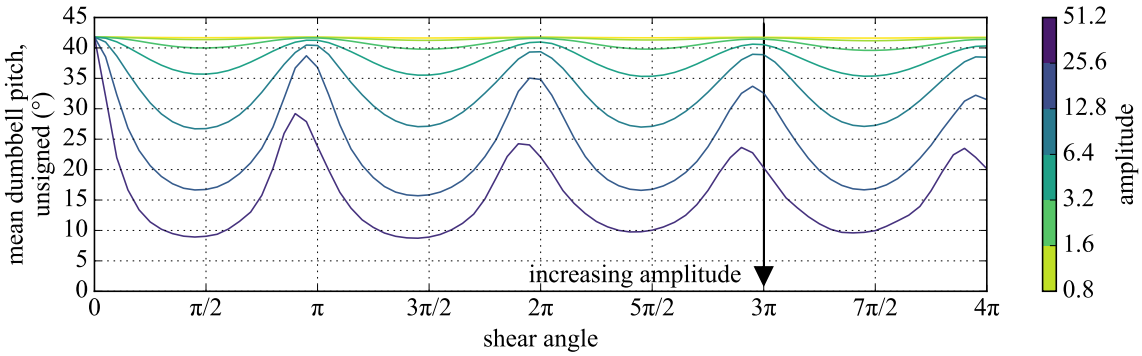

(b) Unsigned pitch, $0^\circ \leqslant \theta < 90^\circ$

Figure 3.29: Mean dumbbell pitch for Hookean dumbbells ($k = 2$, $L = 2$) over two cycles of shear at different amplitudes. The arrow points in the direction of increasing amplitude, from $\alpha = 0.8$ to 51.2, doubling each time. Note that due to edge effects (dumbbells are likely to be parallel to the edge of the box near the edges to fit inside the box) we do not have a pure well-mixed solution: the mean pitch of the unsheared solution is not exactly 45°(unsigned) or 90° (signed).

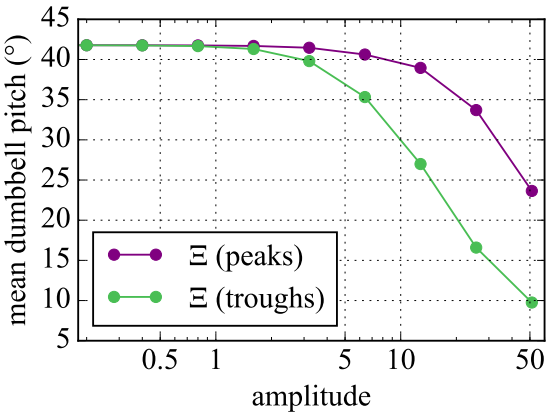

Figure 3.30: Measuring the heights of the peaks and troughs in fig. 3.29(b) across amplitudes, we can describe the alignment of the dumbbells.

or troughs of the unsigned mean dumbbell pitch, following the initial shear cycle. In fig. 3.29(b), we can use the peaks near a shear angle of 3π, when the system is sheared least, or the troughs near a shear angle of $5\pi/2$, when the system is sheared most, to give a good measure for a given amplitude: the resultant peaks/troughs graph for this figure is shown in fig. 3.30.

As seen, LAOS tests are good indicators of the microstructure of the fluid, with particular sensitivity to molecular interaction and the shape and entanglement of polymers. Here we shall see the LAOS response to our bead-and-spring suspensions for varying parameters.

3.3.2 Oldroyd-B model: Hooke's law

For our common suspension in the following tests, we shall consider a wide sample of the dumbbell suspension, with width-to-height aspect ratio $25:1$ and 10% area concentration. To stop the dumbbells contracting to zero length in an otherwise quiescent flow, the natural dumbbell length is set at $L = 2$ (recall that in these dimensionless units, the dumbbell beads have radius 0.1). We start by examining dumbbells with their extension obeying Hooke's law, eq. (3.32). We perform LAOS tests at a frequency of $\omega/(\frac{10\pi}{6}) = 2$, as we see from fig. 3.17 that at this frequency, there is only small dependence on the timestep size. From our wide sample, we only look at the central third, to remove edge effects.

A true Oldroyd-B fluid should have a linear shear stress response at both small and large amplitudes (see fig. 3.38), so what we expect to see with our LAOS tests is initially unclear: certainly we should capture small particle interactions and particle alignment.

Effect of spring constant Figure 3.31 shows the change in some rheometrical properties of our suspension after changing the spring constant. Subfigure (c) shows G' and G'', which are normalised in (a) and (b) on the smallest amplitude. Subfigure (e) shows the nonlinearity parameter Q, defined in eq. (3.45). Looking first at subfigure (e), we see that the measurement of Q for small amplitudes is not very consistent. This is strikingly different to G' and G'', which converge at this limit. However, we should not worry: the measurement of Q will always be worst here, for as we head into the linear regime, the higher harmonics contribute less, and our measurements are therefore less precise. Particularly since we divide by the amplitude squared, this can lead to measurements for $Q \lesssim 1$ which are less reliable (more discussion in section 3.3.4).

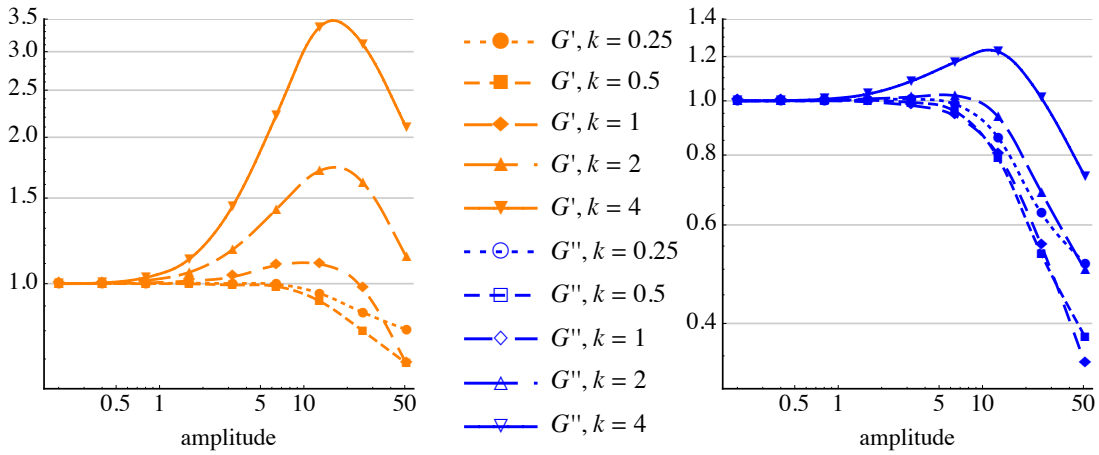

(a) G', normalised

(b) G'', normalised

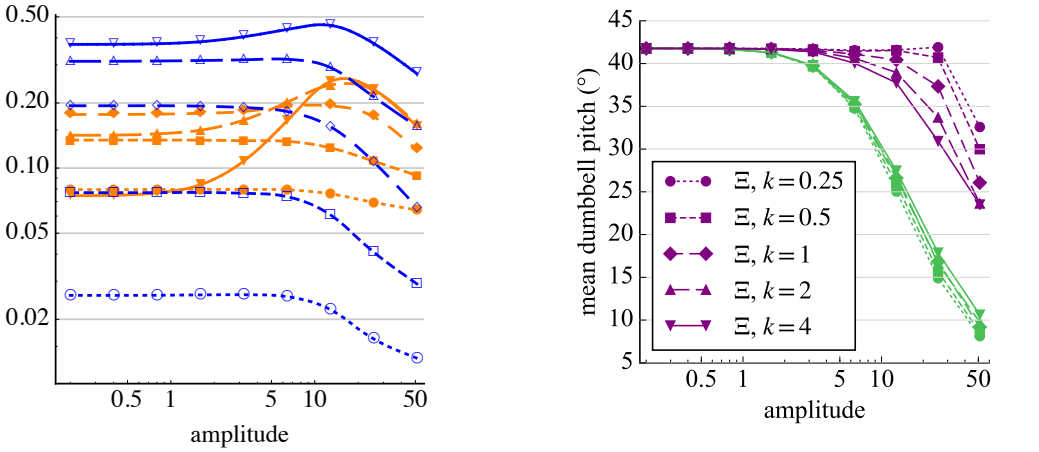

(c) G' and G''

(d) Mean dumbbell pitch, Ξ (dark purple: peaks; light green: troughs)

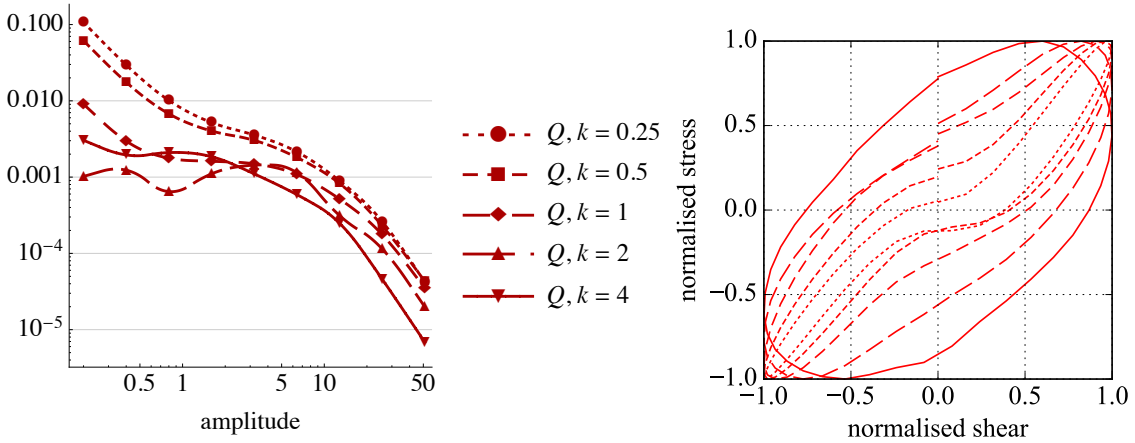

(e) Nonlinearity parameter Q

(f) Lissajous curve at $\alpha = 25.6$

Figure 3.31: An amplitude sweep of our Hookean dumbbell solution with five different spring constants at the fixed frequency of $\omega/(\frac{10\pi}{6}) = 2$.

The key observation in Q can be seen towards the right: increasing the spring constant decreases the nonlinearity. Subfigure (e) demonstrates this with a Lissajous curve for the high amplitude of $\alpha = 25.6$: the highest spring constant ($k = 4$, solid line) has an almost elliptical curve, whereas the curve for the lowest spring constant ($k = 0.25$, dotted) resembles a propeller, even being concave. This can be physically explained by considering that stronger dumbbell springs require more applied shear to deform them, and it is their deformation which causes the nonlinearity, distinguishing LAOS from (always Lissajous-elliptical) SAOS flow.

The alignment of the dumbbells is measured in subfigure (d): as expected, increasing the amplitude aligns the particles (coinciding with the decreased nonlinearity measured with Q), and increasing the spring constant leads to stronger alignment at the moments of maximum shear rate (the peaks, dark purple) across the amplitude sweep (again coinciding with decreased nonlinearity in Q). At the edges of the shear cycle (the troughs, light green), there is little difference in alignment.

Looking at the normalised values of G' and G'' in subfigures (a) and (b), we see that both moduli ultimately decrease at high amplitudes, showing strain thinning, as particles align. However, increasing the spring strength takes the suspension from a Type I, where we see mostly only strain thinning, to a Type IV, where both G' and G'' see an initial increase as the strain amplitude is increased, before eventually decreasing. That we see an initial increase in G', the elastic modulus, makes sense: as we increase the amplitude, the elastic forces in the system do more work.

We only observe a 'bump' in G' for spring forces $k \gtrsim 1$. Above this strength, the size of the bump appears to be proportional to the spring strength. Below this strength, we just see G' decreasing, although there is a turning point between $k = 0.5$ and $k = 0.25$: for passive dumbbells, with $k = 0$, we would expect flat $G'(\alpha)$ profiles, so for small enough spring constants, G' starts to decrease less. Thus the spring constant has two effects: to alter the size of the bump, and to alter the amount of strain thinning.

Interestingly, the transition stage of a bump in G' but not in G'' is not one of the four explicit types labelled by Hyun *et al.* (2002): this suggests that high spring constants may not be a good model of any real material.

The unnormalised measurements in subfigure fig. 3.31c show that the viscous modulus, G'', increases for higher spring strengths. However, at low amplitudes, the elastic modulus, G', initially shifts upwards with increasing amplitude before shifting downwards again: readings for spring constants k are close to readings for $1/k$. This is only seen at low amplitudes, though: at high amplitudes, the overshoot in G', which grows for increased spring strength, is large enough so that G' only shifts

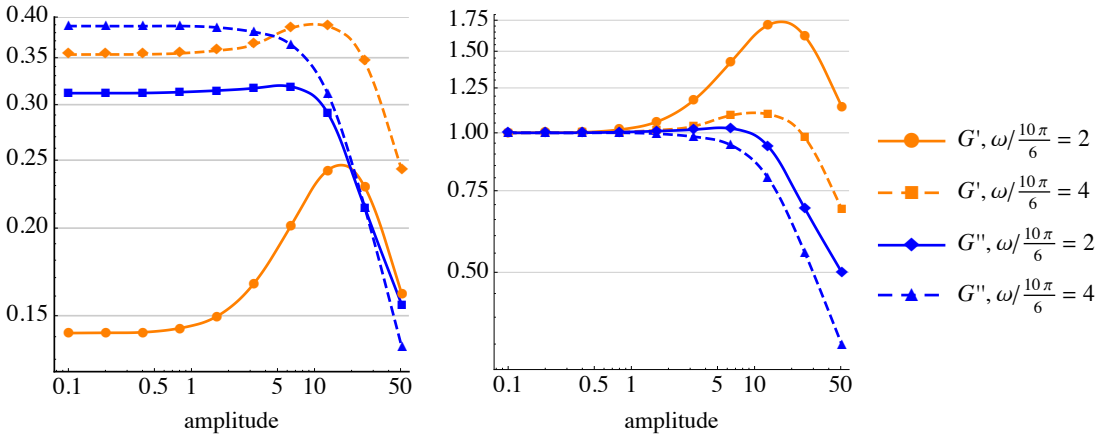

(a) G' and G'' **(b)** G' and G'', normalised

Figure 3.32: An amplitude sweep of our Hookean dumbbell solution with two different frequencies.

upwards for increased spring strength. Whether the overshoot is large enough to achieve this depends on the frequency of oscillation: fig. 3.21 shows that the chosen frequency determines the relative size of G' for different spring constants.

Effect of frequency As mentioned previously, we choose a frequency of $\omega/(\frac{10\pi}{6}) = 2$ as our base frequency for the amplitude sweeps because it shows little dependence on timestep size. For interest, in fig. 3.32, we compare the readings of G' and G'' in LAOS sweeps for this frequency and a higher frequency, $\omega/(\frac{10\pi}{6}) = 4$, which is still within the low timestep-dependence range in fig. 3.17.

As found in section 3.2.2 for SAOS, we again find that changing the frequency is equivalent to a scaling of changing the spring constant, for all harmonics:

$$G'_n(c\omega, k) = cG'_n(\omega, k/c), \tag{3.48a}$$
$$G''_n(c\omega, k) = cG''_n(\omega, k/c). \tag{3.48b}$$

Hence the values of G' and G'' for our doubled frequency of $\omega/(\frac{10\pi}{6}) = 4$ at $k = 2$ are just double the values of the usual frequency but at $k = 1$. This means that the nonlinearity parameter, Q, which is the ratio of the third harmonic to the first harmonic in the stress response, has identical values across the amplitude sweep.

Effect of natural length In fig. 3.33, we see G' and G'' for dumbbells of different natural lengths, L. Again as in SAOS, since the natural length of the dumbbell is a required physical parameter, but not part of the Oldroyd-B model, the effect of increasing it on the rheological parameters is quite complicated. If we first look at subfigure (d), though, the nonlinearity parameter Q has at least one point to make:

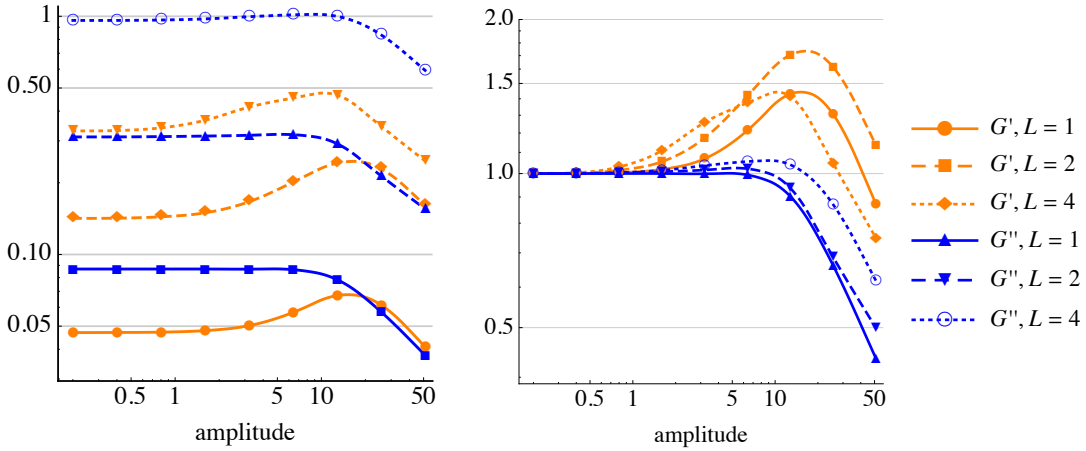

(a) G' and G''

(b) G' and G'', normalised

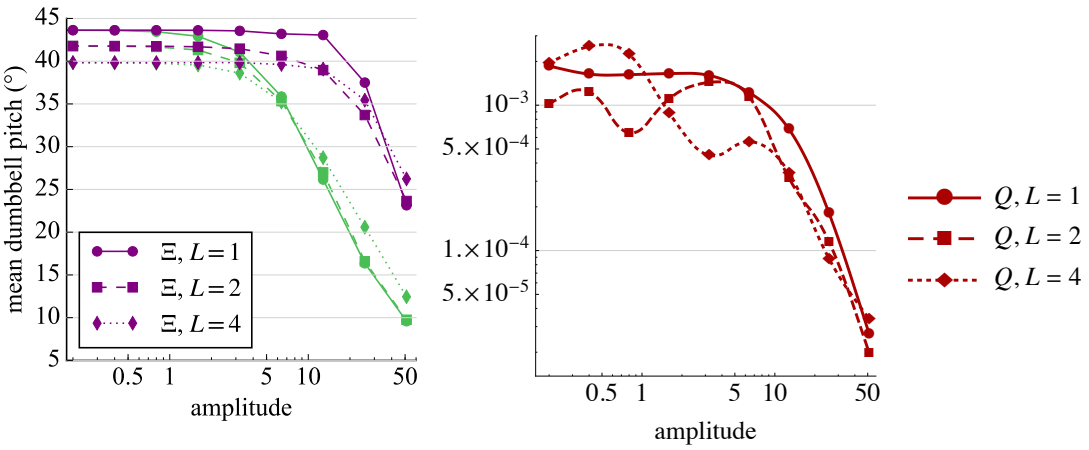

(c) Mean dumbbell pitch Ξ (dark purple: peaks; light green: troughs)

(d) Nonlinearity parameter Q

Figure 3.33: An amplitude sweep of our Hookean dumbbell solution with three different natural lengths for the dumbbells, at the fixed frequency of $\omega/(\frac{10\pi}{6}) = 2$.

at the largest amplitudes, there is not much difference between the samples. This makes sense: at the largest amplitudes, the differences between the natural lengths is comparatively small. The rest of the plot is less clear.

Looking at subfigure (a), as seen for SAOS, increasing the natural length leads to increases in the readings for G' and G''. The normalised data in (b) shows a complicated picture. The bump in both moduli kicks in earlier for higher dumbbell lengths: larger lengths have greater exposure to the shear, which could explain this. The viscous modulus, G'', throughout shows higher values for higher natural lengths. But the picture for G' is not clear, with both decreasing and increasing the natural length from 2 leading to lower readings in the elastic modulus, G', at the highest amplitude. The total dumbbell length, Δx, is given by

$$\Delta x = L + x, \tag{3.49}$$

where x is the extension of the dumbbell, and the spring force felt, ΔF, is proportional to x. However, the dumbbell stresslets (from which the total fluid stress is calculated in eq. (3.29)) are a function of $\Delta F \Delta x$: therefore, the effect of changing L on the stress and hence G' and G'' is certainly not linear and can not be expected to be clear.

Some explanation for the lack of clarity comes from subfigure (c), measuring the mean dumbbell pitch. Due to edge effects—given that the dumbbells are placed in a box, those near a wall cannot be perpendicular to it—the samples have initially different levels of alignment. At low amplitudes, the sample with small L has greater alignment than the sample with large L, but at high amplitudes this trend is reversed. However, the process involved in the trend reversal is, as yet, unexplained.

Effect of concentration We see in fig. 3.34 an amplitude sweep for concentrations of $c = 10\%$ and 20%. Large-amplitude effects begin to kick in at amplitudes of around $\alpha = 2$. Looking at subfigure (b), both suspensions again lie somewhere between Types I and IV, as we see a upward bump in G' before decreasing, yet G'' stays constant until decreasing.

As we saw in the frequency sweep, subfigure (a) shows that doubling the concentration leads to readings for G' and G'' which are, on average, twice as large. This remains true in the nonlinear regime as well, although the normalised plot, (b), shows slightly higher readings for the higher concentration. This makes some sense: although we are mostly seeing simply the sum of forces from twice as many dumbbells, there may be some extra interactions in a more concentrated solution which can increase resistance to flow. However, we should be careful: the measure of

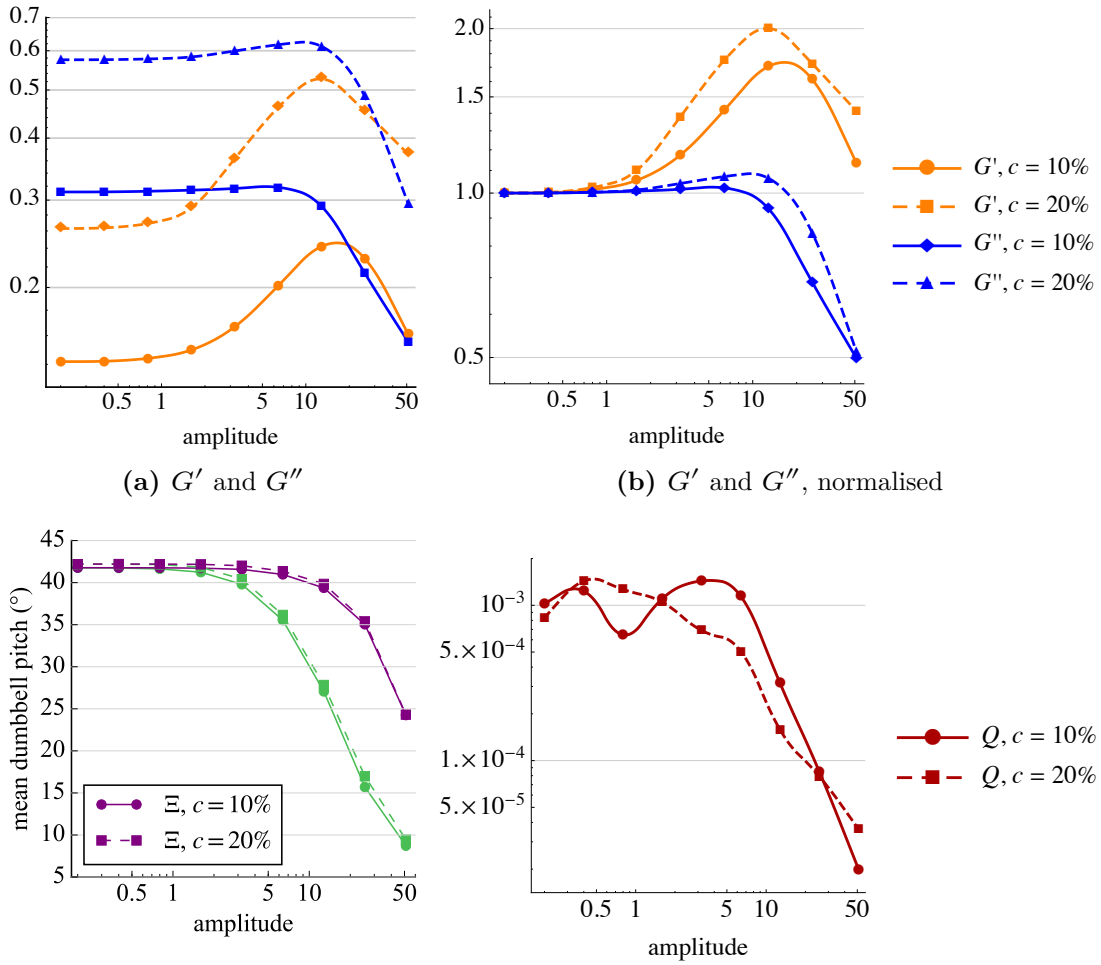

(a) G' and G''

(b) G' and G'', normalised

(c) Mean dumbbell pitch Ξ (dark purple: peaks; light green: troughs)

(d) Nonlinearity parameter Q

Figure 3.34: An amplitude sweep of our Hookean dumbbell solution at two different dumbbell concentrations, at the fixed frequency of $\omega/(\frac{10\pi}{6}) = 2$.

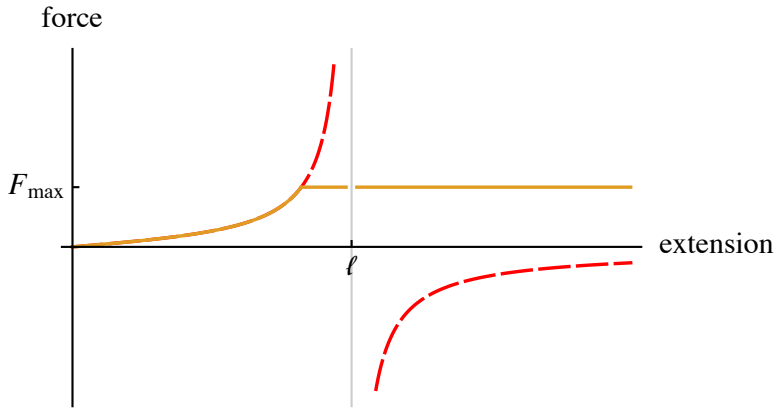

Figure 3.35: The FENE model (red, dashed) gives infinite forces at the maximum dumbbell length, ℓ, and negative forces for extensions past that. This can cause problems in the simulations, so we implement a capped version (yellow, solid).

dumbbell alignment in (c) shows very little difference between concentrations, and the nonlinearity reading in (d) also shows little difference in nonlinearity between the two solutions.

3.3.3 FENE dumbbells

In small oscillations, as we have seen in section 3.2.3, dumbbells experiencing a finitely extensible nonlinear elastic force, eq. (3.38), are indistinguishable from Hookean dumbbells, as the applied shear does not cause the spring to extend outside of its mostly linear regime.

Effect of force capping In the implementation, FENE force laws can cause numerical problems. An important feature of the model, shown in fig. 3.35, is that the spring force is infinite at the maximum dumbbell extension, ℓ, with the side effect that it is negative beyond that. Of course, physically, a dumbbell should never exceed its maximum extension, but with large oscillatory amplitudes—even with small timesteps—it is feasible that the dumbbells will temporarily extend, over a timestep, to their maximum extension or beyond. In the first case, we need to make sure that the applied contractive force is not too large as to cause too large a contraction in the following timestep, which might push it inside-out. In the second case, we need to make sure that the applied force still points in the contraction direction. We can fix both these problems by capping the force at a large threshold value, $F_{\max}$, as shown in the figure.

The choice of the cap turns out to be not very important even at large amplitudes: fig. 3.36 shows the maximum dumbbell extension over a large-amplitude shear for

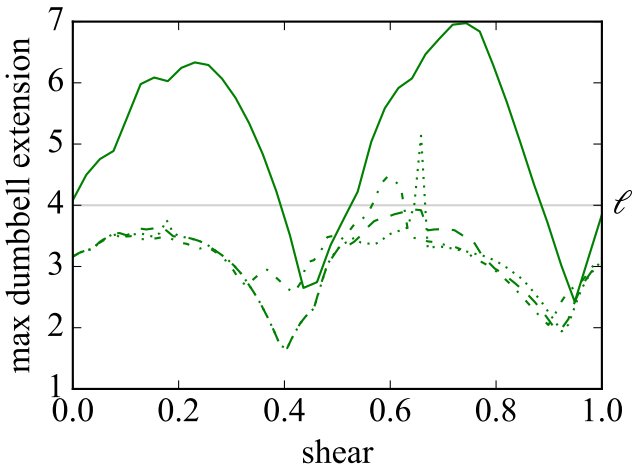

Figure 3.36: Maximum dumbbell extension over a shear cycle for capped FENE dumbbells at the large amplitude of $\alpha = 25.6$. The maximum extension is set at $\ell = 4$ (grey horizontal line) and caps correspond to $x = 3.5$ (– –), $x = 3.75$ (· — ·), $x = 3.9$ (···), all compared to Hookean dumbbells with the same spring constant (—).

three different FENE caps. Each cap, $F_{\max}$, corresponds to extensions in the FENE force law which approach the maximum extension, ℓ, and which are then compared to the maximum extension for Hookean dumbbells. As the figure shows, the three caps perform similarly, with small jumps over the maximum extension, ℓ, which are quickly recovered from. Additionally, they show that the force law works to prevent the dumbbells from extending too far (here, with only 80 timesteps per oscillation). If anything, the figure suggests that lower caps are slightly more numerically stable.

Effect of maximum extension At larger shear amplitudes, we begin to see distinctions between the different FENE models and Hookean dumbbells, although they are slight. Figure 3.37 shows the readings for G' and G'' for three samples: Hookean dumbbells (essentially FENE dumbbells with 'maximum extension' $\ell = \infty$), for FENE dumbbells with $\ell = 8$ and FENE dumbbells with $\ell = 4$. In each case, the strength, k, is the same.

Until $\alpha \gtrsim 10$, there is not a great difference. After that, we see that the shorter maximum extensions break away from the Hookean measurements, with G' decreasing for shorter maximum extensions, and G'' increasing. The nonlinearity parameter, Q, shows increased linearity with shorter maximum extensions, whereas the mean dumbbell pitch is mostly unchanged.

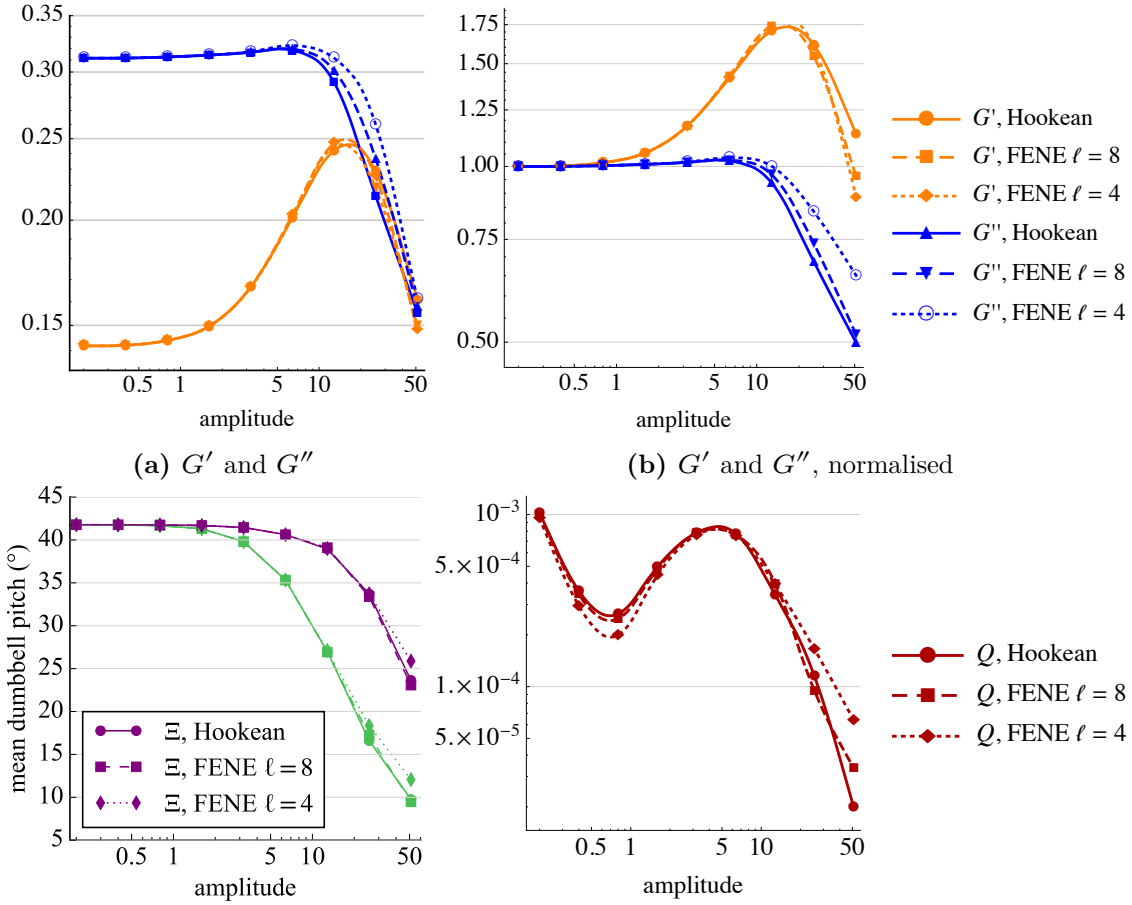

(a) G' and G''

(b) G' and G'', normalised

(c) Mean dumbbell pitch Ξ (dark purple: peaks; light green: troughs)

(d) Nonlinearity parameter Q

Figure 3.37: An amplitude sweep of Hookean dumbbells, FENE dumbbells with $\ell = 8$ and FENE dumbbells with $\ell = 4$, at the fixed frequency of $\omega/(\frac{10\pi}{6}) = 2$.

3.3.4 LAOS with fluid models

Several fluid models are derived from idealised dumbbell suspensions. We now compare the analytically-derived large-amplitude behaviour of these models with our LAOS simulations. For Hookean dumbbells, the appropriate model is the aforementioned *Oldroyd-B* model, and for FENE dumbbells we have the *FENE-P* and *FENE-CR* models.

The rheological behaviour of these models at large amplitudes can be derived from their governing equations, which for all three have the form

$$\boldsymbol{\nabla} \cdot \boldsymbol{u} = 0, \tag{3.50a}$$

$$\rho \left(\frac{\partial \boldsymbol{u}}{\partial t} + \boldsymbol{u} \cdot \boldsymbol{\nabla} \boldsymbol{u} \right) = \boldsymbol{\nabla} \cdot \boldsymbol{\sigma}, \tag{3.50b}$$

—respectively, the continuity and momentum equations, together making up the Navier–Stokes equations—and the constitutive equation,

$$\boldsymbol{\sigma} = -p\boldsymbol{I} + 2\eta \boldsymbol{E} + Gf(R)\boldsymbol{A}, \tag{3.50c}$$

where the evolution of the elastic or polymeric contribution to the stress tensor, $\boldsymbol{A}$, is given by

$$\boldsymbol{A} + \frac{\tau}{f(R)} \overset{\nabla}{\boldsymbol{A}} = g(R)\boldsymbol{I}. \tag{3.50d}$$

The parameter τ is the relaxation time of the dumbbells, as introduced in section 3.2.2, and the functions $f(R)$ and $g(R)$ depend on which model we pick. In all cases, $R^2 = \mathrm{tr}(\boldsymbol{A})$. The parameter G is proportional to the spring strength and dumbbell concentration. In the constitutive equation, $\boldsymbol{E}$ is once again the symmetric part of the velocity gradient tensor,

$$\boldsymbol{E} = \frac{1}{2} \left(\boldsymbol{\nabla} \boldsymbol{u} + (\boldsymbol{\nabla} \boldsymbol{u})^{\mathrm{T}} \right), \tag{3.51}$$

and $\boldsymbol{I}$ is the identity tensor.

It is the extra contribution to the stress from the dumbbells, the polymeric stress $\boldsymbol{\sigma}^p = Gf(R)\boldsymbol{A}$, which makes this different to the Newtonian fluid model seen back in eq. (2.4): indeed, if $f(R) = 0$, eqs. (3.50a) to (3.50c) are the governing equations for a Newtonian fluid.

The evolution of this dumbbell stress contribution is given in eq. (3.50d), where the

upper-convected time derivative of this tensor is given by

$$\overset{\nabla}{\boldsymbol{A}} = \frac{\partial \boldsymbol{A}}{\partial t} + (\boldsymbol{u}\cdot\boldsymbol{\nabla})\boldsymbol{A} - \boldsymbol{A}\cdot\boldsymbol{\nabla}\boldsymbol{u} - (\boldsymbol{\nabla}\boldsymbol{u})^{\mathrm{T}}\cdot\boldsymbol{A}. \tag{3.52}$$

Derived in Oldroyd (1950), this derivative is the rate of change of a tensor property of a fluid element, written in the coordinate system rotating and stretching with the fluid. That is to say, for a infinitesimal line element $\mathrm{d}\boldsymbol{l}$, advecting passively in the flow, the derived tensor $\mathrm{d}\boldsymbol{l}\,\mathrm{d}\boldsymbol{l}$ has

$$\overset{\nabla}{(\mathrm{d}\boldsymbol{l}\,\mathrm{d}\boldsymbol{l})} = \boldsymbol{0}. \tag{3.53}$$

The dumbbell stress contribution comes from the failure of the dumbbells to deform with the fluid elements.

The functions $f(R)$ and $g(R)$ for each model are given by (Larson, 1988)

$$\text{Newtonian:} \qquad f(R) = 0, \tag{3.54}$$

$$\text{Oldroyd-B:} \qquad f(R) = 1 \qquad g(R) = 1, \tag{3.55}$$

$$\text{FENE-P:} \qquad f(R) = \frac{1}{1 - R^2/\ell^2} \qquad g(R) = \frac{\tau}{f(R)}, \tag{3.56}$$

$$\text{FENE-CR:} \qquad f(R) = \frac{1}{1 - R^2/\ell^2} \qquad g(R) = 1, \tag{3.57}$$

where ℓ is the maximum dumbbell extension.

Suppose we now apply oscillatory xy-shear

$$\boldsymbol{u} = (\dot\gamma y, 0, 0), \quad \dot\gamma = \alpha\omega\cos(\omega t). \tag{3.58}$$

To find the rheological parameters, we need to find the xy term of the stress tensor, σ_{xy}. Written out, and neglecting the z-coordinate here for clearer notation, the stress tensor, eq. (3.50c), is

$$\begin{pmatrix} \sigma_{xx} & \sigma_{xy} \\ \sigma_{xy} & \sigma_{yy} \end{pmatrix} = \begin{pmatrix} -p & \eta\dot\gamma \\ \eta\dot\gamma & -p \end{pmatrix} + Gf(R)\begin{pmatrix} A_{xx} & A_{xy} \\ A_{xy} & A_{yy} \end{pmatrix} \tag{3.59}$$

(note that by its definition, soon coming in eq. (3.63), $\boldsymbol{A}$ is symmetric). The evolution equation, eq. (3.50d), can be rearranged and written out as

$$\begin{aligned} \frac{\partial}{\partial t}\begin{pmatrix} A_{xx} & A_{xy} \\ A_{xy} & A_{yy} \end{pmatrix} - \begin{pmatrix} \dot\gamma A_{xy} & 0 \\ \dot\gamma A_{yy} & 0 \end{pmatrix} - \begin{pmatrix} \dot\gamma A_{xy} & \dot\gamma A_{yy} \\ 0 & 0 \end{pmatrix} \\ = -\frac{f(R)}{\tau}\begin{pmatrix} A_{xx} - g(R) & A_{xy} \\ A_{xy} & A_{yy} - g(R) \end{pmatrix}. \end{aligned} \tag{3.60}$$

Since σ_{xy} depends on A_{xy} and R ($= \sqrt{A_{xx} + A_{yy}}$), we therefore have to solve the coupled system of evolution equations,

$$\frac{\partial A_{xx}}{\partial t} - 2\dot{\gamma} A_{xy} = -\frac{f(R)}{\tau}(A_{xx} - g(R)), \tag{3.61a}$$

$$\frac{\partial A_{xy}}{\partial t} - \dot{\gamma} A_{yy} = -\frac{f(R)}{\tau} A_{xy}, \tag{3.61b}$$

$$\frac{\partial A_{yy}}{\partial t} = -\frac{f(R)}{\tau}(A_{yy} - g(R)). \tag{3.61c}$$

In the Oldroyd-B case, when $f(R) = g(R) = 1$, we can solve this system explicitly (Wilson, 2006). Otherwise we can do so using a numerical ODE solver (in particular, we use Scipy's `odeint`, which in turn uses Fortran's `odepack` library).

Taking the solutions for A_{xx}, A_{xy}, A_{yy}, then, we construct the solution for σ_{xy} and pass this stress through the same process described at the beginning of this section to find G', G'', their higher harmonics and Q, for a chosen frequency, as functions of amplitude.

Oldroyd-B fluid The polymeric stress, $\boldsymbol{\sigma}^p$, is derived from the forces on the dumbbells, which in the models come from Stokes drag, Brownian motion and the spring force, $\boldsymbol{F}$. If the dumbbell length is given by $\boldsymbol{R}$, the polymeric stress is given by

$$\boldsymbol{\sigma}^p = \langle \boldsymbol{R}\boldsymbol{F} \rangle, \tag{3.62}$$

where the angle brackets $\langle \cdot \rangle$ represent some form of averaging over all the dumbbells. We can write the Hookean force law, eq. (3.32), as $\boldsymbol{F} = G\boldsymbol{R}$. Therefore the polymeric stress is given by

$$\boldsymbol{\sigma}^p = G\langle \boldsymbol{R}\boldsymbol{R} \rangle =: G\boldsymbol{A}, \tag{3.63}$$

which evolves as in eq. (3.50d) with $f(R) = g(R) = 1$.

The expressions for G' and G'' in an Oldroyd-B fluid,

$$G' = \frac{G\omega^2\tau^2}{1 + \omega^2\tau^2}, \qquad G'' = \eta\omega + \frac{G\omega\tau}{1 + \omega^2\tau^2}, \tag{3.64}$$

first introduced in eq. (3.33), are derived from explicitly solving eq. (3.61) with $f(R) = g(R) = 1$. Observe that these expressions have no dependence on amplitude: not surprising, given that Hookean dumbbells have no natural lengthscale.

For comparison with the following models, we show the trivial $G'(\alpha)$, $G''(\alpha)$ (without the viscous contribution), $Q(\alpha)$ and Lissajous plots in fig. 3.38. Note that Q should be zero throughout, given that the higher harmonics G'_3 and G''_3 are zero in the Oldroyd-B model. Instead we are just seeing a systematic numerical error, decreas-

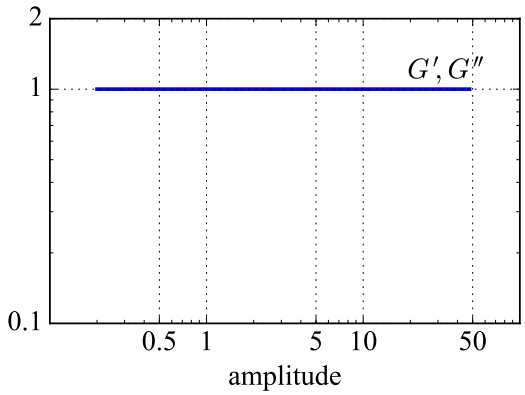

(a) Normalised G' and G''

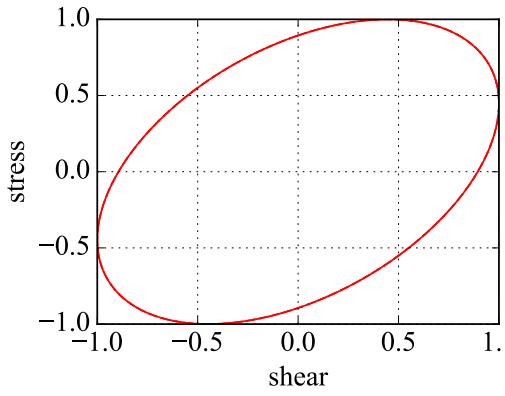

(b) Lissajous plot for all amplitudes.

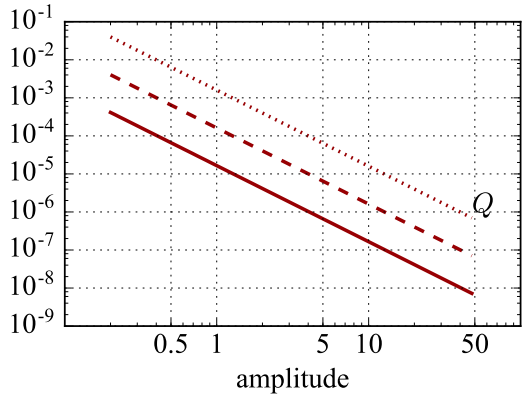

(c) Nonlinearity parameter Q at increasing resolution: 250 timesteps per oscillation (···), 2500 (– –) and 25,000 (—)

Figure 3.38: An amplitude sweep of the Oldroyd-B model, with $k = 2$ and $\omega/(\frac{10\pi}{6}) = 2$. The equations give no dependence on amplitude.

ing with smaller timesteps, which comes from the factor of α^{-2} in the definition of Q. In the following models we will not see such a distinction between resolutions at high amplitudes.

Given that our simulations with Hookean dumbbells show nontrivial rheological parameters, these must be affected by something else.

FENE-P fluid We can write the FENE force laws for the dumbbells, eq. (3.38), as

$$\boldsymbol{F} = Gf(R)\boldsymbol{R}, \qquad f(R) = \frac{1}{1 - R^2/\ell^2}. \tag{3.65}$$

The force law is no longer linear, making us unable to describe its evolution in a closed form. Approximations are therefore needed.

In the FENE-P model, developed by Bird *et al.* (1980) after inspiration from Peterlin

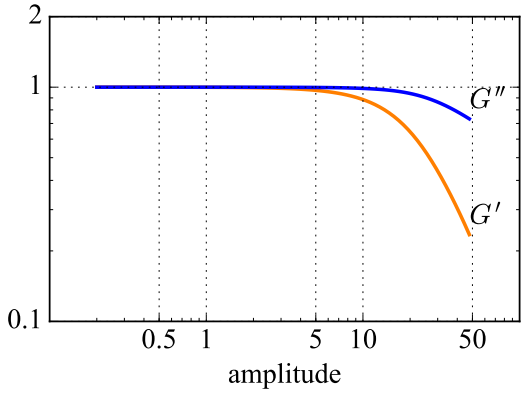

(a) Normalised G' and G''

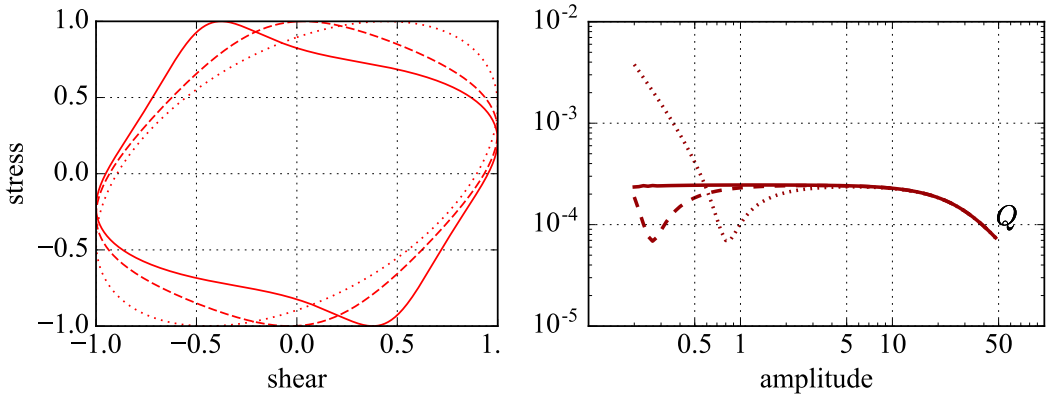

(b) Lissajous plot at amplitudes of $\alpha = 0.1$ (···), 25.6 (– –), 51.2 (—).

(c) Nonlinearity parameter Q at increasing resolution: 2500 timesteps per oscillation (···), 25,000 (– –) and 2,500,000 (—)

Figure 3.39: An amplitude sweep of the FENE-P model, with $\ell = 4$, $k = 2$ and $\omega/(\frac{10\pi}{6}) = 2$.

(1966), the force function $f(R)$ is replaced by the force due to the average dumbbell length, $f(\langle R\rangle)$. Hence the force law is linearised as

$$\boldsymbol{F} = Gf(\langle R\rangle)\boldsymbol{R}, \tag{3.66}$$

and the polymeric stress contribution becomes

$$\boldsymbol{\sigma}^p = Gf(\langle R\rangle)\langle \boldsymbol{R}\boldsymbol{R}\rangle = Gf(R)\boldsymbol{A}, \tag{3.67}$$

where $R = \mathrm{tr}(\boldsymbol{A})$. This evolves as in eq. (3.50d) with $g(R) = \tau/f(R)$, and gives a shear-thinning viscosity.

The resultant rheometric plots are seen in fig. 3.39. Subfigure (a) shows both G' and G'' decreasing, in the style of a Type I fluid. A comparison with the simulation measurements can be seen in fig. 3.40(a). The decrease in G'' matches well, similar to what we see in our simulations, but the behaviour of G' at moderate amplitudes

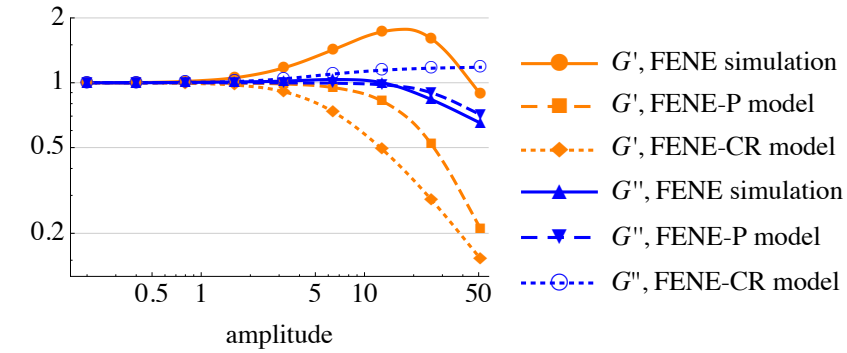

(a) Normalised G', G''

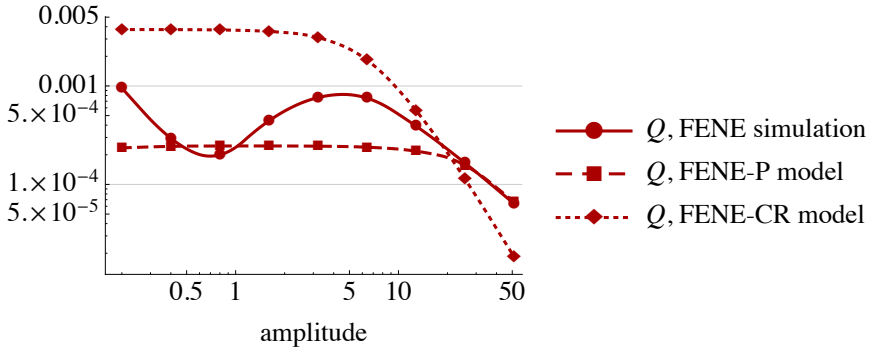

(b) Nonlinearity parameter Q

Figure 3.40: Normalised G' and G'' and the nonlinearity parameter, Q, compared for our FENE simulations and the FENE-P and FENE-CR models, all with $\ell = 4$.

is different: the model predicts no bump in this regime, although it does decrease at a similar rate following this.

The Lissajous curve in fig. 3.39(b) shows the evolution from a linear response at small amplitudes, to a flattened ellipse, to a flag-shape at the highest amplitudes.

The nonlinearity parameter, Q, in fig. 3.39(c), decreases for increased amplitude, but we can see that the results at low amplitudes are very sensitive to timestep size. These are interesting when compared to the simulation measurements in fig. 3.40(b). In the comparison figure, Q with the FENE-P model matches the simulation well at the highest amplitudes. However, the overall shape observed in the simulation, with the dip at moderate amplitudes, is similar to the overall shape for the FENE-P model at low resolutions. Increasing the resolution gives convergence to a flat profile for low amplitudes, which is what we would expect, given the convergence of G' and G'' here. This confirms that what we see for Q in the simulation at low amplitudes is noise, and nothing more substantial.

Changing the dumbbell concentration or spring law (and hence G) simply scales the stress response, in contrast to what we saw with the experiments in figs. 3.31 and 3.34. This highlights the largest difference between what we see in simulations and the FENE-P model. In the model, the dumbbell beads are assumed to not inter-

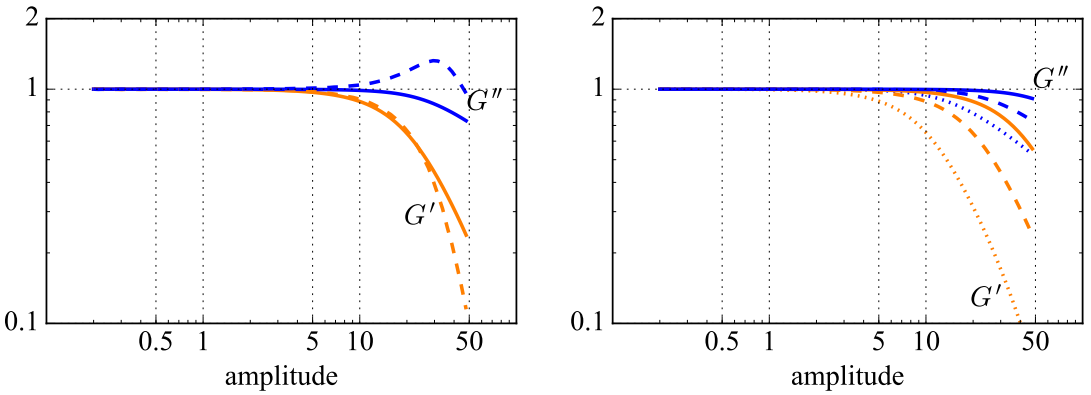

(a) Normalised G' and G'' at frequencies of $\omega/(\frac{10\pi}{6}) = 2$ (—) and 4 (– –).

(b) Normalised G' and G'' with maximum dumbbell extensions of $\ell = 2$ (···), 4 (– –) and 8 (—).

Figure 3.41: An amplitude sweep of the FENE-P model for different frequencies and maximum extensions.

act hydrodynamically, hence higher concentrations do not lead to further nonlinear effects. Instead, we see in fig. 3.34 that this leads to larger bumps in G'.

Changing the frequency or maximum extension in fig. 3.41 leads to more interesting regimes. Increasing the frequency leads to faster decreases in G' but the creation of a bump in G'': the Type III regime. This is the opposite of what we see in the simulations, fig. 3.32, where increasing the frequency reduces both G' and G''. Increasing the maximum extension makes the dumbbells more Hookean, leading to a more linear response. For G'', this agrees with our FENE suspensions, fig. 3.37, although the bump in G' remains unexplained.

FENE-CR fluid The FENE-CR model, developed by Chilcott & Rallison (1988), makes an artificial change to the evolution of $\boldsymbol{A}$, eq. (3.50d), setting $g(R) = 1$. This keeps the steady shear viscosity constant.

Figure 3.42 shows the rheometrical measurements which come from solving the governing equations. In subfigure (a), G' decreases with increased amplitude, whereas G'' rises slowly. The Lissajous plot in subfigure (b) shows the form of the nonlinear response at higher amplitudes, morphing from an ellipse to a rounded rectangle, before experiencing kinks towards the edge of shear. The nonlinearity parameter, Q, in subfigure (c) shows a familiar pattern, again decreasing at higher amplitudes.

Looking back at the comparison in fig. 3.40(a), this fits our simulation measurement worse, given that G'' does not decrease. Of course, this is to be expected: the simulations show the suspension to be shear-thinning and this model is designed explicitly to have a constant viscosity.

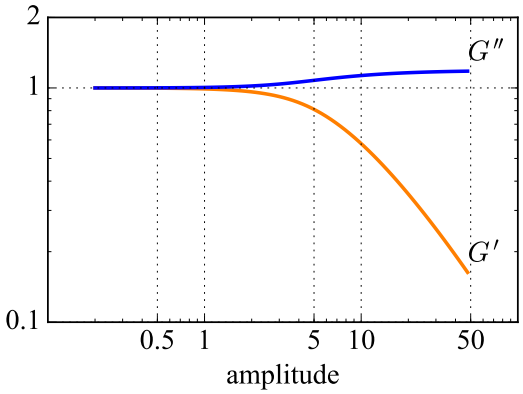

(a) Normalised G' and G''

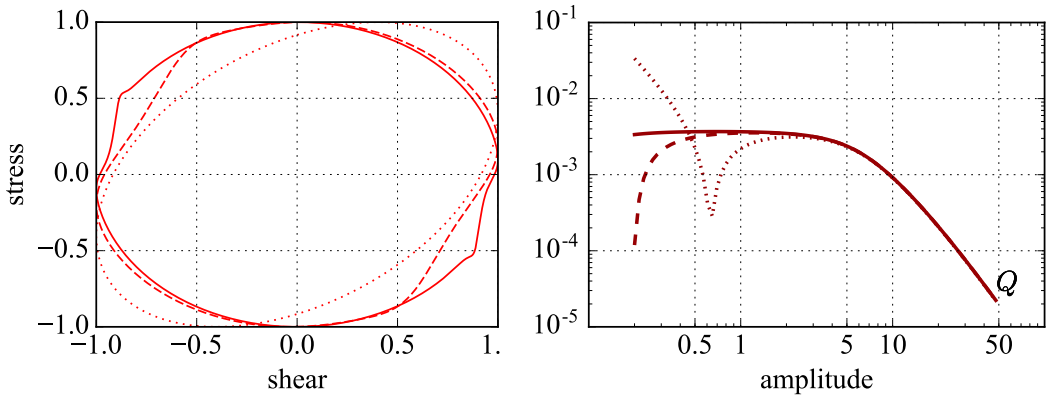

(b) Lissajous plot at amplitudes of $\alpha = 0.1$ (···), 12.8 (– –), 51.2 (—).

(c) Nonlinearity parameter Q at increasing resolution: 250 timesteps per oscillation (···), 2500 (– –) and 25,000 (—)

Figure 3.42: An amplitude sweep of the FENE-CR model, with $\ell = 4$, $k = 2$ and $\omega/(\frac{10\pi}{6}) = 2$.

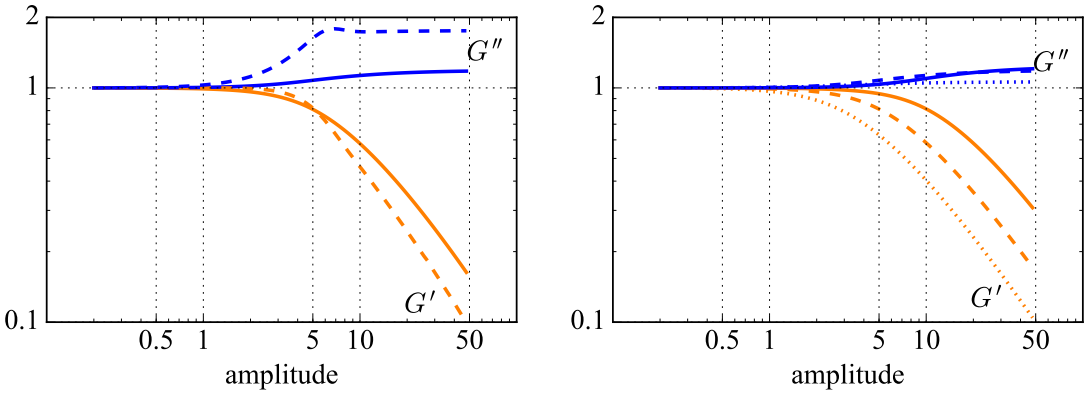

(a) Normalised G' and G'' at frequencies of $\omega/(\frac{10\pi}{6}) = 2$ (—) and 4 (– –).

(b) Normalised G' and G'' with maximum dumbbell extensions of $\ell = 2$ (···), 4 (– –) and 8 (—).

Figure 3.43: An amplitude sweep of the FENE-CR model for different frequencies and maximum extensions.

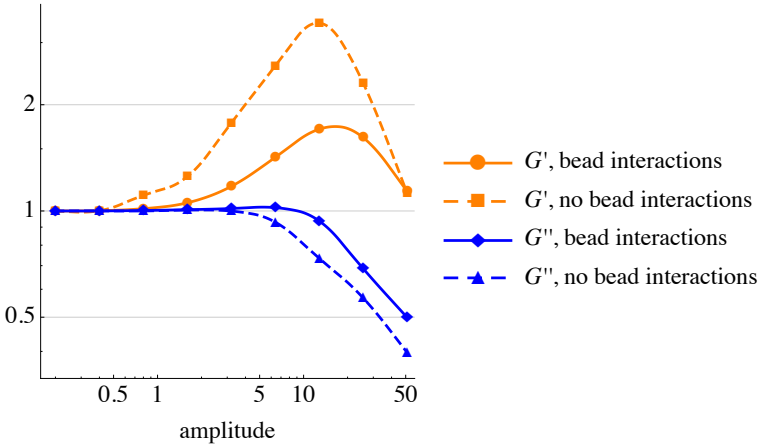

Figure 3.44: Amplitude sweep for G' and G'' for Hookean dumbbells with bead–bead interactions turned on (as they are by default) and off.

The response of the FENE-CR model to changes in spring constant, concentration, frequency and maximum dumbbell extension is mostly similar to the FENE-P model: there is still a bump in G'' at higher frequencies.

3.3.5 Comparison of simulations and fluid models

Despite tentative matching of G'' between our simulations and the FENE-P model, none of the models show the bump in G' that we see in our simulations. Given the aforementioned difference in the models with our simulations—that dumbbells are both isolated and assumed to be randomly aligned—it seems that these factors could be causing larger bumps in G'. In our simulations, dumbbells are shown to align with the flow direction at large amplitudes, an effect which is enhanced by larger spring forces (recall fig. 3.31). Both the bump and increased alignment (particularly at the edges of the shear cycle) begin at amplitudes $\alpha \gtrsim 1$, but the differences in alignment due to the spring constant are only really seen for $\alpha \gtrsim 5$. It seems unlikely that this is the only reason for the bump in G', therefore.

First, though, we only see a bump in G' in our simulations for spring forces $k \gtrsim 1$. With smaller spring forces, the behaviour of G' and G'' matches the FENE-P model much better. Simply, we may not be finding agreement with our analytical models because the spring forces we are applying may be unphysically large.

A factor not present in the model is bead interactions. Stokesian Dynamics allows us to investigate the effect of interactions by 'turning off' bead–bead interactions: in the notation of eq. (2.80), this means in the grand resistance matrix, we set $\boldsymbol{R}^{45} = \boldsymbol{R}^{54} = \boldsymbol{0}$, and only keep the diagonal terms of $\boldsymbol{R}^{44}$ and $\boldsymbol{R}^{55}$. Amplitude sweeps for Hookean dumbbells with bead interactions turned on and off are shown in fig. 3.44. However, as we can see, with interactions turned off, the bump in G' is

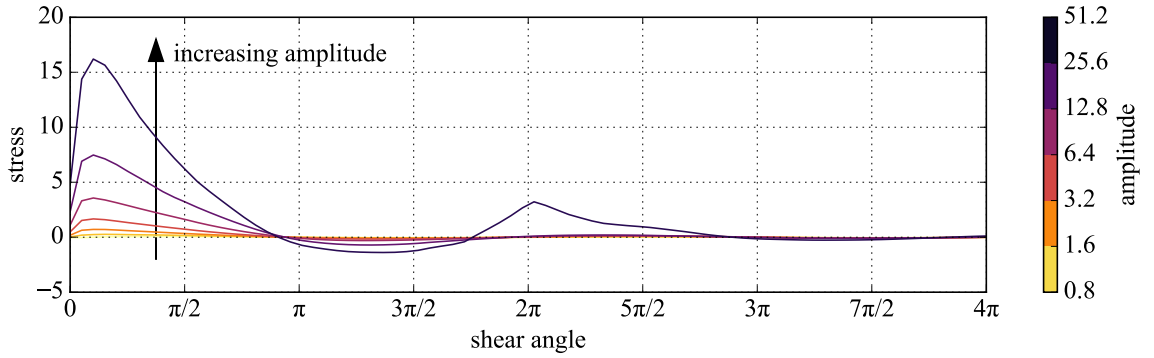

(a) Stress over two units of shear

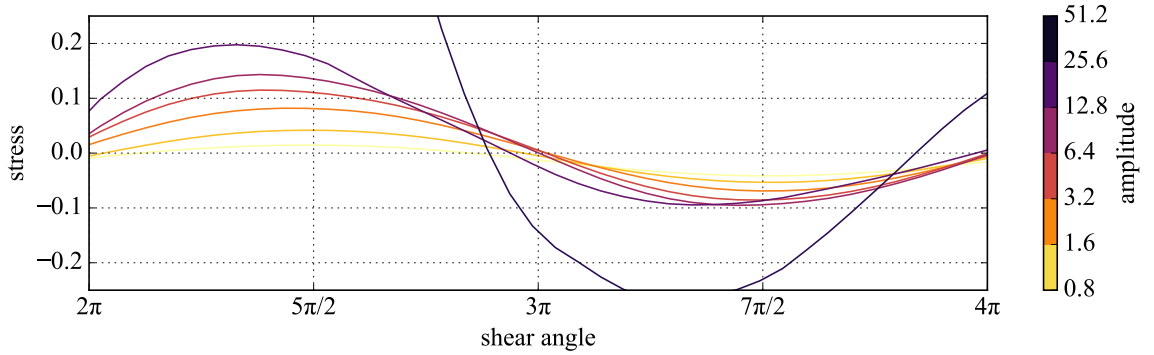

(b) Zoomed-in view of the stress over the second shear cycle. In particular, notice that the stress response is no longer periodic, even over small stresses.

Figure 3.45: Total system stress over two units of shear, where the Hookean dumbbells have zero natural length, starting with extensions of $\Delta x = 2$. Here the spring force is $k = 2$.

not only still present, but also larger: clearly, then, bead interactions are not causing the bump in G'. Qualitatively, though, both sweeps give similarly-shaped graphs: an observation which is good news, as the diagonal grand resistance matrices obtained with bead interactions turned off are extremely quick to generate and invert, making this method more viable.

A final explanation for the bump in G', and also for the Hookean dumbbells not matching the Oldroyd-B fluid, is due to the natural length we give the dumbbells. We give the dumbbells a finite natural length since otherwise they contract to zero length quickly, even in strong shear flow: fig. 3.45 shows the resultant stress in the fluid for zero-natural length dumbbells over two units of shear, where the dumbbells are placed in with extensions of $\Delta x = 2$. Even at low spring strengths, we find the same pattern: dumbbells contract quickly to zero length, reducing the stress in the fluid to almost zero. In particular, the stress response is no longer periodic, and we cannot describe it using G' and G''.

3.4 Conclusions

By placing simple bead-and-spring dumbbells, with various force laws, into a suspension, we are able to show that the resulting suspension behaves as a viscoelastic fluid. We have shown that we can tune the degree of viscoelasticity by tuning certain parameters in these force laws.

We have developed Stokesian Dynamics to allow us to include these force laws easily, and then been able to measure, using several techniques, the rheological behaviour of the simulated suspensions.

Our small-amplitude tests confirmed that the dumbbell suspension behaved as an Oldroyd-B fluid. Our large-amplitude tests showed that in the absence of any interparticle forces, other than the spring laws, the dumbbell solution behaves as a strain thinning fluid. With stronger spring constants, the solution exhibits a strong strain overshoot. Forces responsible for shear thickening and strain hardening will be discussed in chapter 5. We were also able to quantify the degree of nonlinearity in our suspension, showing that in all cases, increasing the shear amplitude led to decreased nonlinearity.

This lays good groundwork for further studies using Stokesian Dynamics, confirming that if we added larger particles, we would be able to model a suspension in a viscoelastic fluid.

Chapter 4

Sedimenting spheres in concentrated media

4.1 Introduction

Stokesian Dynamics is well-suited to simulations of particles sedimenting in a viscous fluid, which have been the focus of investigations since at least Stokes (1851). As discussed in chapter 1, the focus of investigations has moved from a single spherical particle sedimenting in a Newtonian background fluid to multiple, polydisperse particles, sedimenting through a variety of background fluids and in the presence of a variety of background flows.

Questions we can ask about these sedimenting particles include what determines their settling speed, the effective viscosity of the suspension through which they fall, and whether any structure forms in the suspension which hinders/aids this sedimentation. For example, experiments by Beiser *et al.* (2004) found that the settling speed depended on the particle material, the acidity of the suspending fluid (which influences chemical forces), as well as the suspension concentration. As we could expect, at low concentrations, sedimenting particles fell faster than at high concentrations. However, the dependence on concentration is not linear: increasing the concentration led to clusters forming, which once again increased the sedimentation rate. Finally, though, continuing to increase the concentration ultimately ended up with a system so concentrated that the overwhelming number of interactions slowed these clusters down to below the speed seen for a single particle.

At small scales, experimental work combines well with simulation work, where experiments provide observations which can then be investigated fully by simulations. Stokesian Dynamics simulations have, in the literature, found good agreement with

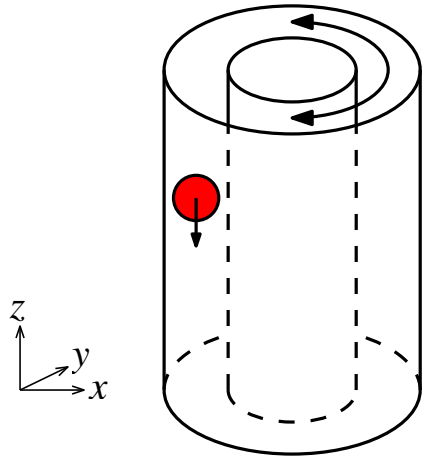

Figure 4.1: Setup of the Blanc *et al.* (2014) experiment

a number of experiments, going some way to answering some of the questions mentioned above (Feist *et al.*, 2011). Stokesian Dynamics has also been used to reproduce results from other numerical methods: those in Harlen *et al.* (1999) investigated sedimentation through a suspension of neutrally buoyant fibres, validating a dependence for the falling velocity on the fibre concentration.

Initial validation of the Stokesian Dynamics method by Dratler & Schowalter (1996) warned that impractically small timesteps would be necessary to stop particles overlapping in simulations. The solution, suggested by Bossis & Brady (1984), of treating overlapping particles as instead being very close, while keeping practically small timesteps, we find works well.

The particular sedimentation problem which concerns this chapter is inspired by the work of Blanc *et al.* (2014), with additional results from Blanc *et al.* (2015). They recently discovered that a heavy ball falling through a dense suspension of smaller particles can be made to fall at tunable speeds by applying a transverse oscillatory shear to the system, as in fig. 4.1. The mechanism, they hypothesised, is in the microstructure created in the small-particle suspension by each flow. A falling ball creates an asymmetric density disturbance, with more particles ahead of it than are found in its wake; this naturally hinders its falling. The cross-shear, on the other hand, may encourage the small particles to align in the vertical direction, making it easier for the large sphere to pass.

In the first experiment in the paper, the large ball was dropped through a resting suspension with high volume concentrations of $\phi = 0.40$ and 0.47. The mean falling velocity was found to be the same for both a non-presheared suspension and one treated to a steady preshear. Treating the suspension with an oscillatory preshear was found to make a small difference, increasing the large ball's fall speed by 5–10%.

In the second experiment, the large ball was dropped through an oscillatory cross-

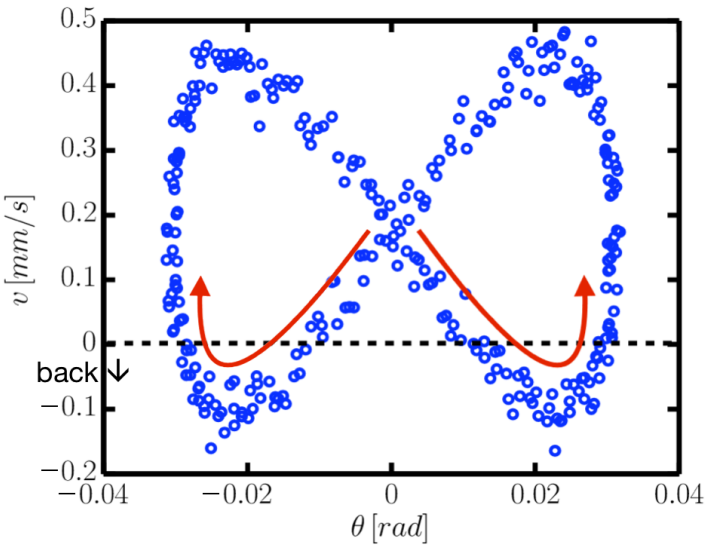

Figure 4.2: Falling ball velocity over a shear cycle, found by Blanc *et al.* (2015). Reproduced by permission.

sheared suspension. Tracking the large ball's fall speed, the mean falling speed was found to increase up to a factor of four, depending on the frequency of the oscillation. They also found (Blanc *et al.*, 2015) that for very concentrated suspensions, when they tracked the large ball's fall speed during a shear oscillation, its variation was so extreme that at some moments of the shear cycle it was actually travelling upwards (see fig. 4.2).

Here we aim to reproduce some of these observations numerically, and therefore elucidate the importance of various physical parameters on the two phenomena. Ultimately we find that we are unable to reproduce the mean velocity speed increase, although we find suspension structure which agrees with the hypothesis in Blanc *et al.* (2014); but we are able to reproduce the large velocity variance over a shear cycle, and give a mechanism for this behaviour.

In sections 4.2 to 4.4, we discuss how we set up the simulation to best mimic the experiments, taking into account particle interactions. In sections 4.5 to 4.7, we perform the simulations and detail the observed behaviour of the system as we alter parameters in the model. Finally, we offer a mechanism responsible for this behaviour in section 4.8.

4.2 Simulation setup

We implement our Stokesian Dynamics method as a bidisperse suspension: we place a large sphere into a box of small, neutrally buoyant particles (enacted by zero-force

dumbbells), where the size ratio is small enough to capture the size difference in the experiments, while not being so small as to require excessively many particles. In all cases, we apply a DLVO-type repulsive force between close pairs of particles to prevent overlap (Bossis & Brady, 1984): the role of repulsion forces is discussed in section 4.3. We use enough small particles in the simulations to not see motion at the edges of the box: this can be up to 10,000 particles and is discussed in section 4.4.

We apply shear to the suspension through the background angular velocity and shear rate, $\boldsymbol{\Omega}^\infty$ and $\boldsymbol{E}^\infty$, as discussed in chapter 2, so that

$$\tilde{\boldsymbol{u}}^\infty = (\alpha\tilde{y}\cos(2\pi\tilde{f}\tilde{t}), 0, 0), \tag{4.1}$$

in the notation of Blanc *et al.* (2014) and where tildes represent dimensional variables.

The motion the large sphere is then mostly governed by two parameters we will alter in our simulations: the interparticle repulsion strength, $\tilde{k}$, and the shear frequency, $\tilde{f}$. We nondimensionalise our lengths on the radius of the large particle, a_{large}, and our forces on the weight of the large particle, W:

$$k = \frac{\tilde{k}}{W}, \qquad \{x, y, z\} = \frac{\{\tilde{x}, \tilde{y}, \tilde{z}\}}{a_{\text{large}}}. \tag{4.2}$$

Times are scaled with the viscous timescale, T, associated with the large particle. This is defined such that imposing a unit force on the large particle, in the absence of all other particles, leads to a unit Stokes flow velocity. Therefore, the dimensionless shear frequency, f, in terms of the dimensional frequency, $\tilde{f}$, is given by

$$f = \tilde{f}T = \frac{6\pi\mu a_{\text{large}}^2\tilde{f}}{W}. \tag{4.3}$$

Thus, if we were to double the weight of the large particle, the effect in our dimensionless system would be to halve both the repulsive force, k, and the dimensionless frequency, f. The other physical parameters in the experiments are detailed in table 4.1, as well as the simulation parameters we use to represent these.

The density of the far-field mobility matrix $\mathcal{M}^\infty$ in standard Stokesian Dynamics puts limits on the box size $\widetilde{L}/a_{\text{large}}$. A 3D simulation of a large sphere sedimenting in box of smaller spheres (with size ratio $\lambda = 0.1$) at a concentration of $\phi = 0.4$ requires 14 GB of RAM for a cubic box with dimensionless side length 6. A $10 \times 10 \times 10$ box requires 360 GB for the data in $\mathcal{M}^\infty$ alone. Given that we invert $\mathcal{M}^\infty$ regularly, this quickly becomes a bottleneck with the computing resources available to us. Methods of avoiding having to fully calculate $\mathcal{M}^\infty$, such as Accelerated Stokesian Dynamics

Physical parameters		**used**	**experiment**
$\lambda = a_{\text{small}}/a_{\text{large}}$	particle size ratio	1/10	1/33
α	shear amplitude	1/3	various, greatest effects at $\sim 1/3$
$f = \tilde{f}T$	dimensionless frequency	free	
c	2D area concentration	0.6	
ϕ	3D volume concentration	0.40	0.40, 0.47
Simulation parameters		**used**	**ideal**
N	number of small particles	∼10,000	large
N_p	pre-shear oscillations	2	large
N_{osc}	main oscillations	2	large
$\Delta t/T$	timestep	$2\pi/250f$	small
$(\tau a_{\text{large}})^{-1}$	repulsion decay length	1/20	
$k = \tilde{k}/W$	strength of DLVO force	free	

Table 4.1: Physical parameters used in the experiments by Blanc *et al.* (2014), and the values we use in our simulations.

(Sierou & Brady, 2001) or Fast Lubrication Dynamics (Kumar, 2010) are discussed in chapter 2. Our systems are not periodic, as it is not clear how the suspension bulk would be affected by the unwanted reproductions of the heavy sphere above and below the box.

In the experiments, the suspension is housed in a Couette cell and is subjected to Couette shear. We reproduce the suspension as a cube of small particles, randomly distributed using the Lubachevsky–Stillinger algorithm, as described in appendix A.2.10. Into this suspension we place a large sphere with its weight force set in the z-direction. This cube is then subjected to background shear in the xy-plane.

In our oscillatory shear tests, we choose the timestep size, Δt, such that there are 250 timesteps per oscillation period, T_s, regardless of the chosen frequency,

$$\Delta t = \frac{T_s}{250} = \frac{2\pi}{250f}. \tag{4.4}$$

This allows us to maintain the same resolution over a shear cycle. A parameter connected to the timestep which also requires consideration is how often we generate the inverted far-field mobility matrix $(\mathcal{M}^{\infty})^{-1}$. As discussed in chapter 2, we choose to perform this computationally intensive task every 10 timesteps as this is seen to give reasonable results. In some circumstances, some computation time can be saved, while maintaining accuracy, by decreasing the number of frames per oscillation (i.e., increasing the size of the timestep) but increasing how often the inverted mobility matrix is calculated to compensate: fig. 4.3 gives the overall run time for one of the oscillatory simulations in this chapter, altering these parameters. However, how well accuracy is maintained depends heavily on the concentration and strength of the forces in the simulation. Where results in this chapter appear ‘choppy’, it is

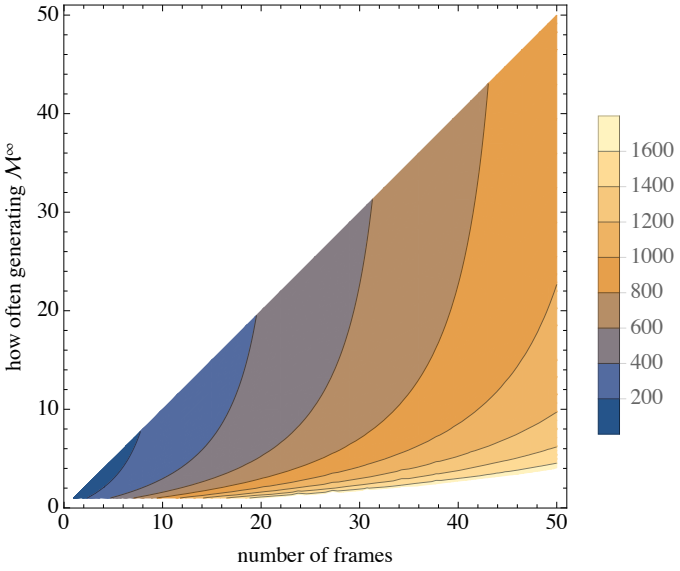

Figure 4.3: Overall run time for one of the oscillatory simulations in this chapter, in minutes, for a given number of frames per oscillation and choosing to generate the inverted far-field mobility matrix $(\mathcal{M}^\infty)^{-1}$ every y timesteps. This does not take into account the quality of the output.

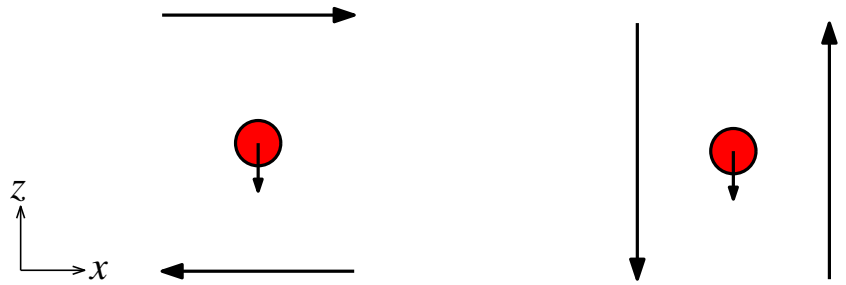

(a) Sedimenting in the velocity gradient direction **(b)** Sedimenting in the shear direction

Figure 4.4: In the experiments, the ball falls in the vorticity direction of the oscillating shear flow. We also consider two other shear directions.

normally because of sensitivity to how often this matrix is generated.

Since simulations are such a flexible tool, we have also considered the two other possible orientations of the shearing flow relative to the fall direction, as illustrated in fig. 4.4. In these cases, the direction out of the plane of shear is essentially neutral and we can make a reasonable approximation by considering a single layer of spheres (in which we parametrise the small-particle suspension in terms of its area concentration rather than the volume fraction).

The experiments in Blanc *et al.* (2014) that we attempt to mimic are set up, with parameters in table 4.1, thus:

1. Monodisperse small particles are dispersed in a density-matched Newtonian fluid, which is placed into a Couette cell.

2. The system may be oscillatory presheared (experiments done both with and

without).

3. A large heavy sphere is placed in the cell, towards the top.

4. The heavy sphere is dropped along the centreline of the gap, while the cell has oscillatory shear applied to it.

5. The velocity of the falling ball is measured over the following oscillations.

Our simulations, unless otherwise specified, are set up in a similar way:

1. The small particles are randomly distributed in a given box.

2. The large particle is placed inside the suspension, with any overlapping small particles deleted. No weight force is applied to the large particle yet.

3. The simulation is run for 25 timesteps with no background flow and with only the repulsion force turned on. This allows the particles to equilibrate.

4. The system is presheared for two oscillations, with only the repulsion force turned on. This allows the system to form shear-related structure.

5. Gravity is activated on the large sphere, and it falls through the box for one oscillation, allowing structure to form under and around the ball.

6. With all expected structure formed, the velocity of the ball is now measured over the following oscillations.

4.3 The role of repulsion forces

In simulating concentrated suspensions, we have to be careful of particles overlapping. Lubrication interactions in the Stokesian Dynamics method slow down approaching particles, but without a globally sufficiently small timestep, particles can still sometimes overlap (Dratler & Schowalter, 1996; Ekiel-Jeżewska *et al.*, 2008). To counter this, a repulsion model is commonly included. A common choice is the pairwise DLVO repulsion model for the force, $\boldsymbol{F}$, between two spherical particles of radius a and b, with their surfaces separated by a distance h and unit vector displacement $\boldsymbol{d}$,

$$\boldsymbol{F} = \frac{2ab}{(a+b)}\tilde{k}\mathrm{e}^{-\tau h}\boldsymbol{d}, \tag{4.5}$$

as in Mari *et al.* (2014). The strength of repulsion, $\tilde{k}$, is a parameter we can vary. The repulsion decay length, $(\tau a_{\text{large}})^{-1}$, however, we fix, setting $\tau = 20/a_{\text{large}}$, as in table 4.1.

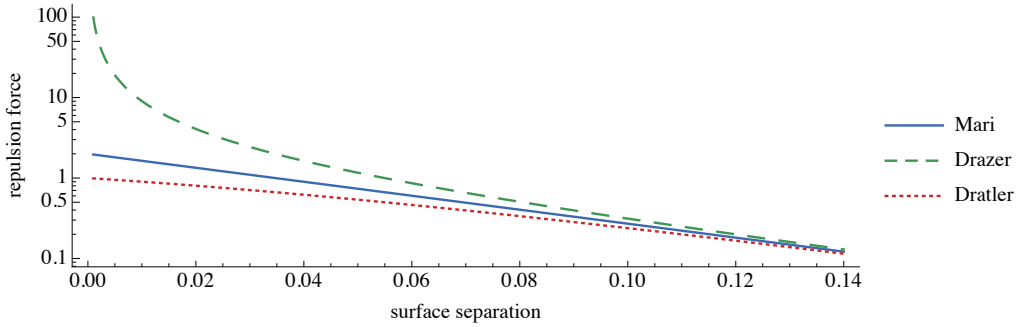

Figure 4.5: Three repulsion forces used with close-packed particles, from Mari *et al.* (2014) (eq. (4.5)), Drazer *et al.* (2002) (eq. (4.6)), and Dratler & Schowalter (1996) (eq. (4.7)). Each model has been set with equivalent constants $\tilde{k} = 2$, $\tau = 20/a_{\text{large}}$.

Other repulsive force models exist, for example,

$$\boldsymbol{F} = \tilde{k}\frac{\mathrm{e}^{-\tau h}}{1-\mathrm{e}^{-\tau h}}\boldsymbol{d}, \tag{4.6}$$

(Drazer *et al.*, 2002), or,

$$\boldsymbol{F} = \tilde{k}\frac{\mathrm{e}^{-\tau h}}{1+\mathrm{e}^{-\tau h}}\boldsymbol{d}, \tag{4.7}$$

(Dratler & Schowalter, 1996), shown here for equally-sized particles. Typically, as shown in fig. 4.5, these models all decay exponentially.

The choice of $\tau = 20/a_{\text{large}}$ comes from Mari *et al.* (2014). The values of repulsion force strength, k, we choose, come from parameter trials. As pairs of particles approach, the required level of force to produce velocities bringing the pair closer together increases. This is due to lubrication, encoded in the resistance matrix $\mathcal{R}^{\text{2B,exact}}$, and is reversible: the force required to repel the particles also increases. When pairs of particles overlap, we want the repulsion force between them to be sufficient to stop them overlapping over the next few timesteps. However, as has already been said, SD does not allow overlapping particles, as the resistance becomes asymptotically large as the pairs approach. Overlapping particle pairs are therefore given repulsion forces equal to those given to pairs which are as close as we have computed resistance scalars for. This force has to be large enough to stop overlapping, but must not be too large as to make the particles repel so much that they overlap with other particles on the next timestep. Therefore the choice of repulsion force strength, and indeed the repulsion decay length, have to be selected so that they balance the timestep, the smallest separation distance computed, and the concentration.

Without a mild repulsion force, a concentrated system can quickly jam, with the sedimenting sphere unable to pass through. Figure 4.6 shows the falling speed of a large particle through such a 2D, unsheared and initially unrepelled suspension (i.e.

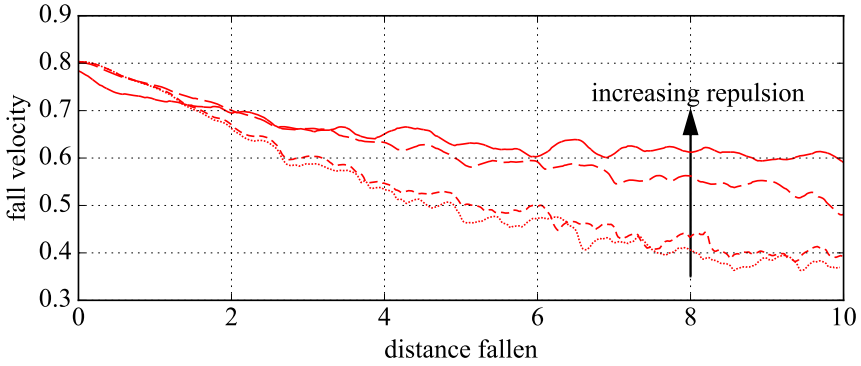

Figure 4.6: Fall velocity of a large particle sedimenting through an unsheared 2D suspension of area concentration $c = 0.6$, with increasing levels of repulsion. Without repulsion, the suspensions jams quickly, causing the falling sphere to decelerate greatly. The repulsion model used here is eq. (4.5) with $\tilde{k} = 0$, 0.02, 0.2 and 2; $\tau = 20/a_{\text{large}}$, as in the following sections.

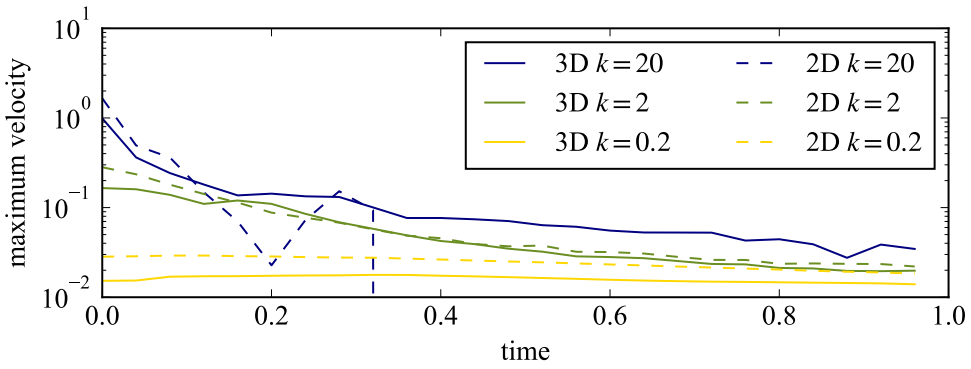

Figure 4.7: Maximum velocity of all particles after enabling repulsion in a randomly distributed cell. After 25 timesteps (corresponding to 1 time unit here), all repulsion strengths lead to, at most, small 'jiggling' of particles.

no steps 3 or 4 above), without and with increasing levels of subsequently-applied repulsion. The difference is dramatic: where in the unrepelled system (dotted, bottom line), the falling particle decelerates throughout to less than half of its starting speed as it falls through, and continues to decelerate, in the highest—but still moderate—repelled system (solid, top line), the particle reaches an approximately steady falling velocity of around 75% of its initial speed quite quickly.

We apply repulsion to a randomly distributed cell of particles for a time unit (25 timesteps) to allow the particles to equilibrate before we shear the suspension. Figure 4.7 shows the maximum particle velocity over this time frame. Higher repulsive strengths lead to initially larger velocities, but for both 2D and 3D suspensions, after a time unit, the largest velocities are reduced to a fairly constant 'jiggling', which is a property of the timestep.

It is convenient to quantify the structure of the suspension by looking at the particle

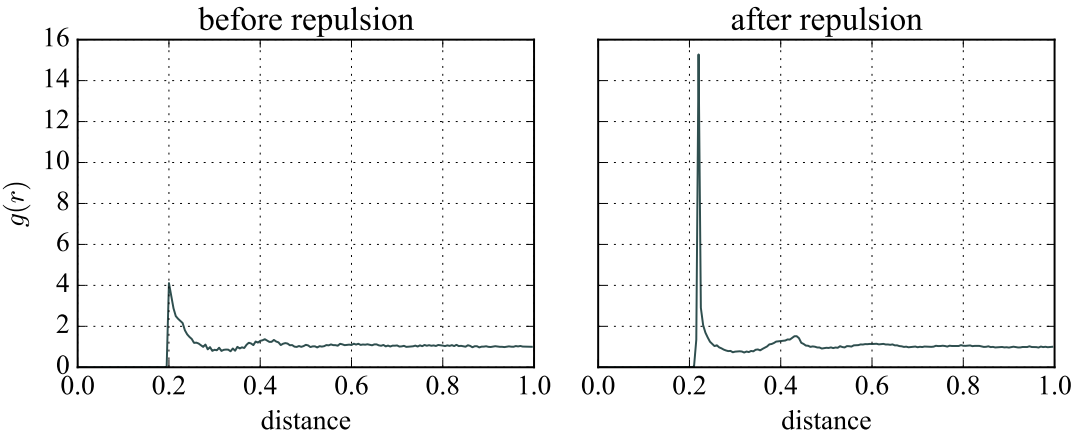

Figure 4.8: Particle density functions of the small sphere suspension before and after a strong repulsion force is added. This sample is with the strongest repulsion magnitude we use, $k = 20$. A wide peak two small particle radii out (0.2 units) before repulsion becomes a tall, narrow peak after repulsion. The same thing, to a lesser degree, is seen at 0.4 units. The particle density function is normalised so that $g(r) \to 1$ as $r \to \infty$.

density function (PDF, or pair distribution function, or percolation function) (Bossis & Brady, 1984; Drazer *et al.*, 2002). This function, commonly notated $g(r)$, counts the number of particles a distance r from a reference particle at a given time, averaged over a set of reference particles. Figure 4.8 shows, on the left, the PDF for a randomly generated 3D field of small particles. No particles can be closer than two particle radii away (otherwise they would overlap), and we see a peak in the number of particles at this closest value of 0.2, with a fairly wide tail. There is a smaller shallow peak at the next band, 0.4. The right-hand figure shows the PDF after 25 frames of strong repulsion: the first peak is now much taller and narrower, as the bands are now better defined, but otherwise the repulsion does not have an effect on the structure of the suspension. Weaker repulsion has a less pronounced effect.

In our simulations, the repulsion force is the only non-hydrodynamic force applied to the small particles in the system, which are otherwise passive. We find this to be sufficient to reproduce some of the features seen in experiment. However, other pairwise forces can be added and have interesting consequences. Although not relevant to the problem here, the addition of attractive forces, for example, has been shown to encourage shear-banding (Ovarlez *et al.*, 2009).

Recent work suggests that frictional contact forces are important in reproducing other features, for example, shear thickening (Mari *et al.*, 2014). Several models exist to describe these frictional contacts, typically consisting of one force normal to the line of contact between two particles, and one tangential. This has been tested in experiments with suspensions of rough spheres: Gallier *et al.* (2014*b*) were able to distinguish the separate contributions to the viscosity from contact and from

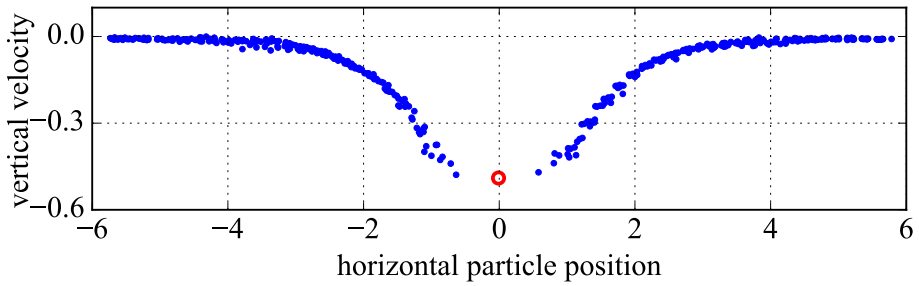

(a) through a monolayer suspension

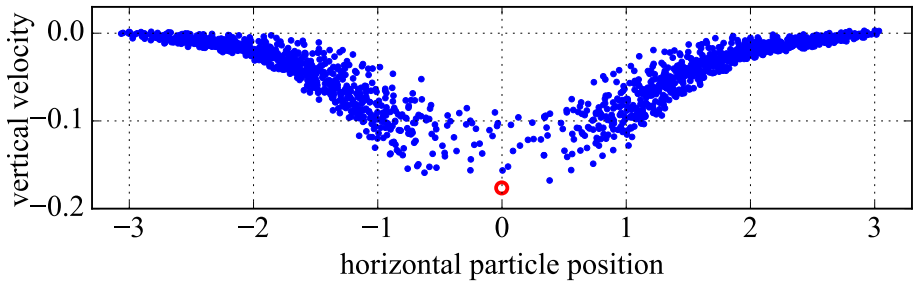

(b) through a fully 3D suspension, without walls at the sides

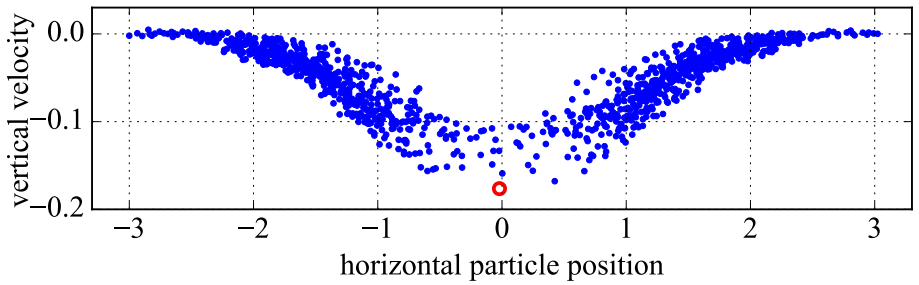

(c) through a fully 3D suspension, with walls at the sides

Figure 4.9: Vertical velocities of small particles at the same depth as the sedimenting large particle (with a centre-to-centre height difference of up to a_{large}) at a representative depth. The velocity of the large particle is marked on (◦) for reference. The horizontal measurements are nondimensionalised on of a_{large}.

hydrodynamics. Their result that at least a third of the viscosity comes from contact argues for the importance of contact in suspension rheology. More interestingly, this suggests that you can tune the viscosity of the suspension by changing the surface properties of the particles. Frictional contact forces are discussed in chapter 5.

4.4 Setting the size of the box

Our large particle sediments through a box of smaller particles. This box is not periodic, as it is not clear how the suspension bulk would be affected by the unwanted reproductions of the heavy sphere above and below the box. In order to balance the requirement for a large box size with the availability of computational resources, we set the box size so that as the large sphere sediments, we see no vertical motion at the edges of the box.

We confirm this in fig. 4.9. Here, we have plotted the vertical velocities of the small particles at the same approximate depth as the sedimenting particle through a monolayer and through fully 3D suspensions, with and without walls at the sides. The velocities were captured when the sedimenting particle was approximately halfway through the sample, but the profile is similar at all depths, repulsion strengths and shear rates. At the edges of the box, the vertical velocities of the particles are almost zero, as we desire. This effect is only slightly emphasised in the presence of walls. In a three-dimensional simulation, a box width of $6a_{\text{large}}$, as in subfigures (b) and (c), requires around 10,000 small particles.

4.5 Sedimentation in unsheared suspension

To quantify the effect of an applied shear, we first perform some simulations of the large ball falling in an unsheared suspension.

4.5.1 2D monolayer unsheared suspension

As we later examine a sphere sedimenting in a sheared monolayer, a reasonable approximation for the shear directions shown in fig. 4.4, we start by letting a sphere fall through a monolayer of randomly assembled smaller beads. We plot in fig. 4.10 the transient fall speed of the large sphere (normalised by its Stokes velocity in pure solvent) as it sediments through this suspension. We find that for three well-differentiated repulsion strengths, the falling ball decelerates before achieving a mean falling velocity which has only a weak dependence on the repulsion magnitude, k.

The deceleration is caused by the build-up of concentration beneath the ball, which is also quantified in fig. 4.10. With the local area concentration starting at $c \approx 0.55$, we see that below the particle (upper line), the concentration increases until it finds an equilibrium level: from $c \approx 0.63$ at the highest repulsion to $c \approx 0.72$ at the lowest. In the lowest repulsion sample, the area concentration is still comfortably below the maximum circle packing fraction of 0.91 with hexagonal packing, but is approximately the square packing fraction of $\pi/4 \approx 0.79$. The concentration behind (lower line) initially decreases, as the falling ball creates a wake, before increasing again as the wake enters the more concentrated zone created by the falling ball. The wake, as seen in fig. 4.11, is unexpected normally in reversible Stokes flow, but is due to the repulsive force, which is inherently irreversible.

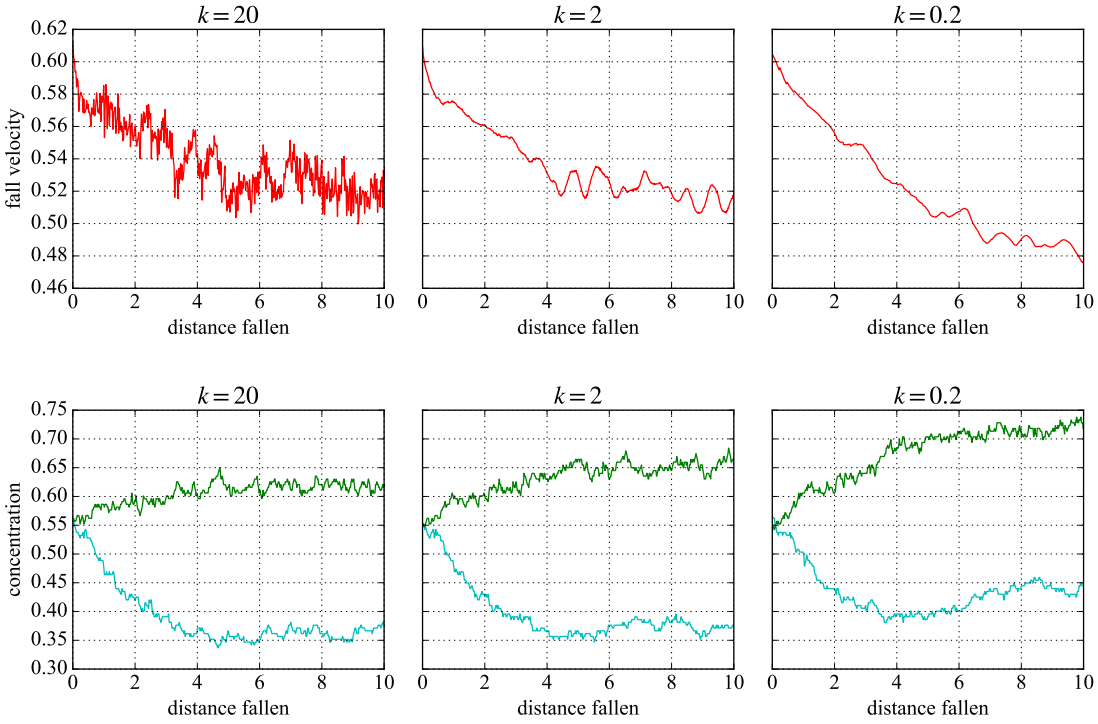

Figure 4.10: **Top:** A large ball sedimenting through a 2D unsheared suspension, at different repulsion strengths, slows down as it falls. In contrast to fig. 4.6, here we having given the suspension some time to equilibrate after applying the repulsion force, before activating gravity on the large ball. **Bottom:** The concentration of small particles behind (lower line) and ahead of (upper line) the falling ball as it falls. The concentration is measured in a box the width of the particle and of dimensionless height 8, centred on the falling ball.

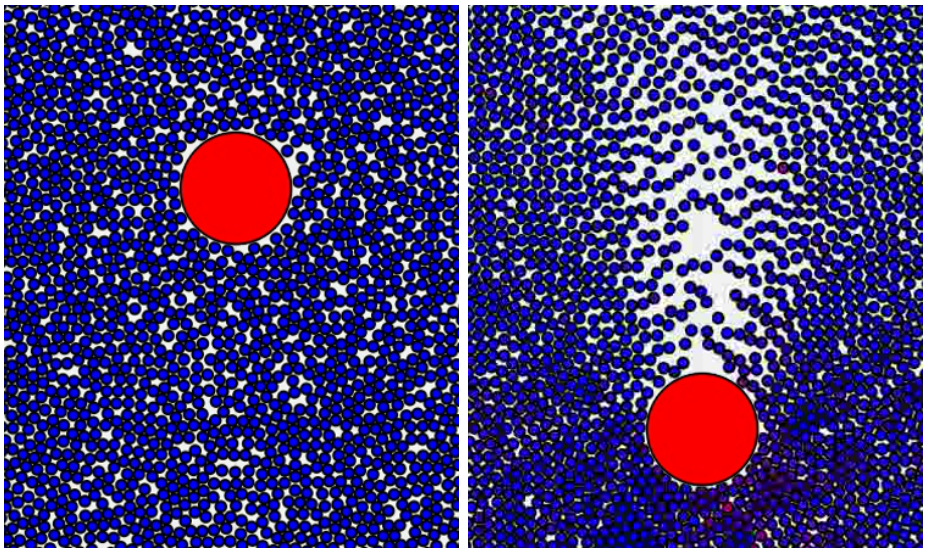

Figure 4.11: As the heavy ball falls through the (2D) suspension, it leaves a wake behind it.

4.5.2 3D unsheared suspension

We perform the same shear on a cube of small particles containing the sedimenting sphere. In contrast to the 2D monolayer simulation, the falling velocity and concentration in fig. 4.12 stabilise much more quickly. We see a quick deceleration for all three repulsion strengths before reaching a fairly constant velocity. The mean falling velocity is shown to have a stronger dependence on the repulsion strength, k, than in 2D, and in fact suggests the opposite dependence: weaker strengths lead to faster mean velocities. In 3D, the number of neighbouring particles—the 'kissing number'—is much higher than in 2D, and the slower falling speeds with a higher repulsion force can be explained by higher (upwards) repulsion from the large number of smaller particles beneath the falling ball.

The concentration build-up beneath the ball is also shown in the same figure. As expected, behind the ball (lower line) we see a reduction from the starting volume concentration of $\phi \approx 0.33$ to $\phi \approx 0.30$. Unlike in the 2D simulations, however, the concentration in front of the ball (upper line) shows very little change. This can again be rationalised by the larger number of neighbours beneath the ball in 3D giving stronger resistance to compression, as well as the extra available space for them to move into in 3D.

4.6 Oscillatory preshear

In the experiments from Blanc *et al.* (2015), it was found that a large ball, sedimenting in a oscillatory sheared suspension, can sometimes slow so much as to travel upwards over the course of a shear cycle. Given that the hypothesised mechanism is in the structure created by the shear, we set out here to investigate the form of this structure in our simulations. In line with the experiments, we preshear the suspension with two oscillations. This also allows us to observe the effect this shear has on a neutrally buoyant large sphere.

We place the large sphere towards the top of the cube of smaller particles, ready for release, but for now make it neutrally buoyant. We have conducted tests with our 3D simulations where walls of particles have been added along the neutral planes, but we have found that this makes only a small difference to the behaviour of the large sphere. A slice through the 3D sample is shown in fig. 4.13, showing the neutrally-buoyant sphere in the centre of the cube.

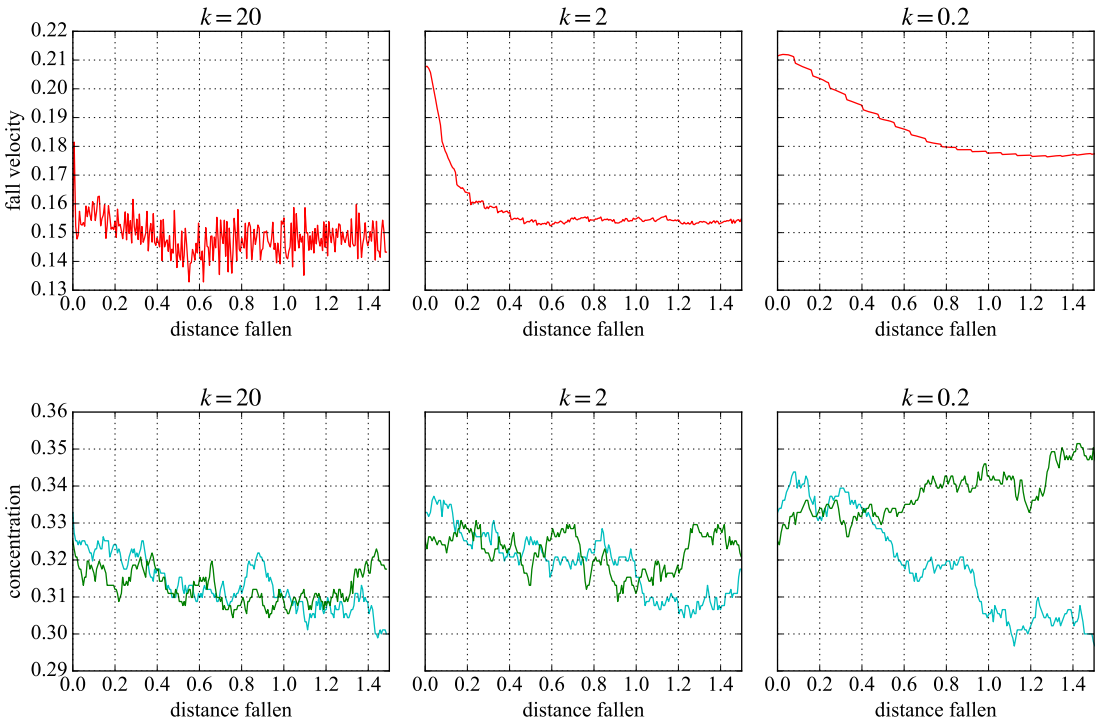

Figure 4.12: **Top:** A large ball sedimenting through a 3D unsheared suspension, at different repulsion strengths, slows down as it falls. Weaker repulsions lead to faster falling speeds. **Bottom:** The concentration of small particles behind (lighter, predominantly lower line) and ahead of (darker, predominantly upper line) the falling ball over time. The concentration is measured in a cube the width and depth of the particle, with dimensionless height 3, centred on the falling ball.

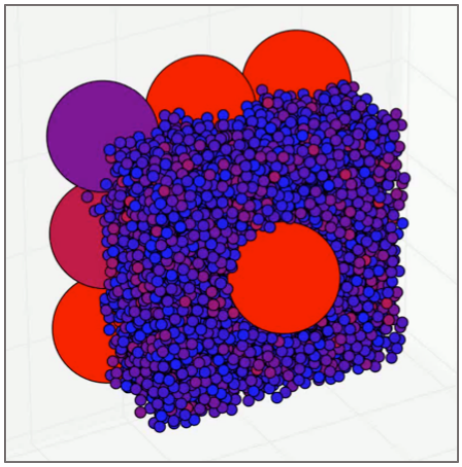

Figure 4.13: A slice through the 3D sample of the large ball in shear

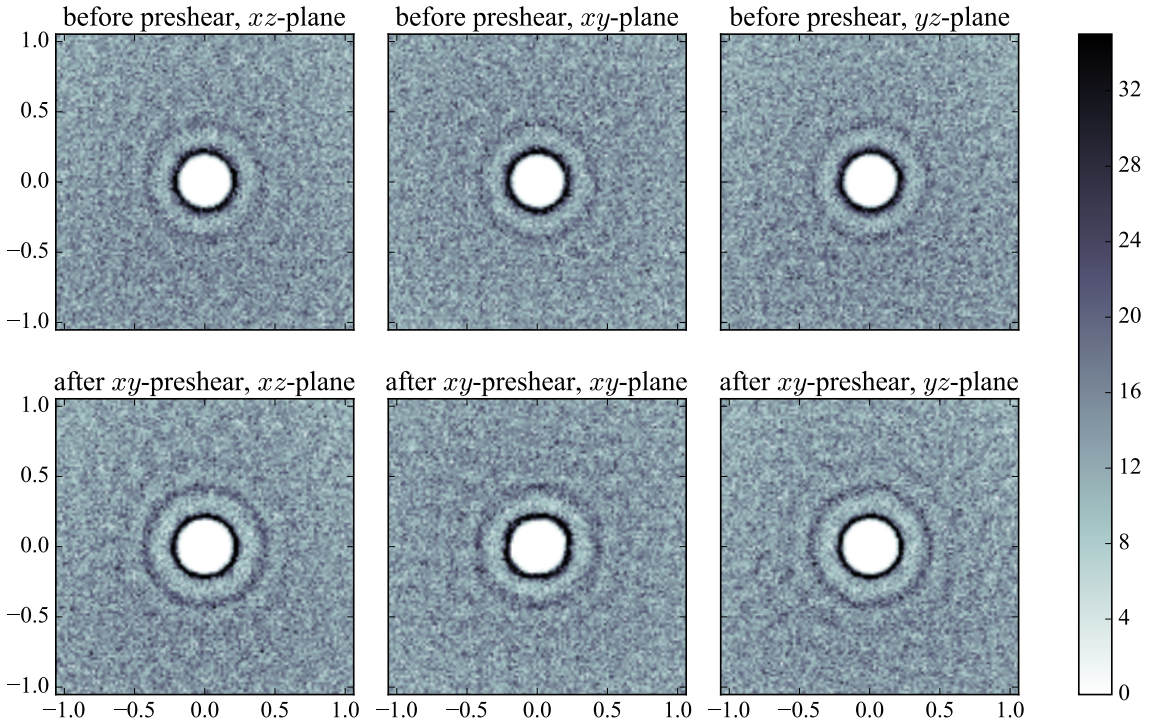

Figure 4.14: 3D oscillatory preshear: Particle density function plots in three planes before and after two oscillations of xy-preshear. At this moderate repulsion and frequency choice ($k = 2$, $f = 1$), we see that preshear emphasises the circular structure in the neutral planes, but again forms square packing in the shear plane. The slices in the plane have depth of 2 small particle radii.

4.6.1 Effect of shear direction

We place the large sphere towards the top of the cube of smaller particles, ready for release, but for now make it neutrally buoyant. We perform one simulation for each of the three shear directions shown in figs. 4.1 and 4.4, respectively,

$$\text{xy-shear, fig. 4.1:} \quad \dot{\gamma} = \alpha\omega\cos(\omega t), \quad \boldsymbol{\Omega}^\infty = \frac{\dot{\gamma}}{2}\begin{pmatrix}0\\0\\-1\end{pmatrix}, \quad \boldsymbol{E}^\infty = \frac{\dot{\gamma}}{2}\begin{pmatrix}0&1&0\\1&0&0\\0&0&0\end{pmatrix}, \tag{4.8a}$$

$$\text{xz-shear, fig. 4.4(a):} \quad \dot{\gamma} = \alpha\omega\cos(\omega t), \quad \boldsymbol{\Omega}^\infty = \frac{\dot{\gamma}}{2}\begin{pmatrix}0\\1\\0\end{pmatrix}, \quad \boldsymbol{E}^\infty = \frac{\dot{\gamma}}{2}\begin{pmatrix}0&0&1\\0&0&0\\1&0&0\end{pmatrix}, \tag{4.8b}$$

$$\text{zx-shear, fig. 4.4(b):} \quad \dot{\gamma} = \alpha\omega\cos(\omega t), \quad \boldsymbol{\Omega}^\infty = \frac{\dot{\gamma}}{2}\begin{pmatrix}0\\-1\\0\end{pmatrix}, \quad \boldsymbol{E}^\infty = \frac{\dot{\gamma}}{2}\begin{pmatrix}0&0&1\\0&0&0\\1&0&0\end{pmatrix}, \tag{4.8c}$$

recalling that the large sphere sediments in the z-direction.

Applying two cycles of shear in each simulation, we find that the oscillatory preshear creates structure in the suspension bulk. Figure 4.14 shows the particle density func-

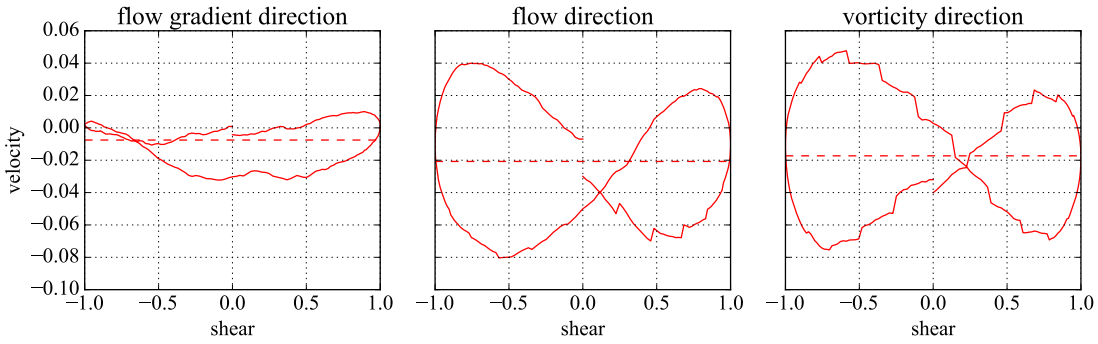

Figure 4.15: Velocity profiles of the neutrally buoyant large sphere in oscillatory shear in a 3D suspension. Here we see the velocities in the (negative) z-direction for each of the three simulations corresponding the geometries in figs. 4.1 and 4.4. That is to say, the shear is applied so that the z-direction corresponds to the flow gradient direction, the flow direction, and the vorticity direction respectively. All three profiles are for the moderate parameters $f = 1$, $k = 2$. The horizontal dashed line shows the mean velocity.

tions of slices in each plane through a 3D suspension before and after an oscillatory shear in the xy plane (corresponding to fig. 4.1). We see that the preshear slightly emphasises the circular structure near the centre of the plots in the neutral planes, but that in the shear plane, we see distinctive alignment of particles parallel and perpendicular to the shear direction: square packing.

The observation of square packing agrees with the hypothesis in Blanc *et al.* (2014): that particles align in the vertical direction under oscillatory shear. However, as we shall see, in our simulations this does not lead to faster sedimentation.

The velocity profiles of the large sphere, in a cube of smaller particles, under all three directions of shear are shown in fig. 4.15. In each, the velocity of the large sphere is plotted against the system shear for the second oscillation, and the horizontal dashed line marks the mean velocity. The oscillation begins with motion to the right, and we plot *falling* velocity as positive. We find that in all cases the mean velocity over a shear oscillation is negative. That is to say, the ball, when neutrally buoyant, travels upwards over the course of the shear. This is purely an effect of our asymmetric geometry: the large ball is placed near the top of the region occupied by particles, so it is driven upwards by the excess of particles below it. Furthermore, in all cases, the ball translates vertically, mostly in a figure-of-eight shape, although in the flow gradient direction, where the variation in velocity is smaller, this is less clear. Interestingly, we observe that the shear in the vorticity direction leads to the profile traversing the figure of eight in the opposite direction to the shear in the flow direction. We will discuss this observation further in section 4.8. We also find that the velocity change is of similar magnitude in the flow and vorticity directions, but opposite in sign.

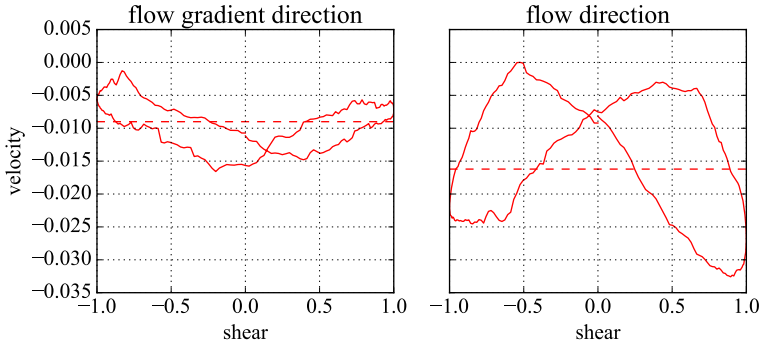

Figure 4.16: Velocity profiles of the neutrally buoyant large sphere in oscillatory shear in a 2D suspension. Here we see the velocities in the (negative) z-direction for the two simulations corresponding the geometries in fig. 4.4. That is to say, the shear is applied so that the z-direction corresponds to the flow gradient direction and flow direction respectively. Both profiles are for the moderate parameters $f = 1$, $k = 2$. The horizontal dashed line shows the mean velocity.

The velocity profiles of the large sphere in an equivalent monolayer of smaller particles, under the two possible directions of shear, are similar to the 3D results, as can be seen in fig. 4.16. Again the mean velocity is negative, indicating that the neutrally buoyant ball travels upwards over the course of a shear. Compared to their 3D counterparts, the 2D plots are less 'neat': this is to be expected, as the larger number of neighbours in 3D offers more stability. Similarly to the 3D results, the variation in the flow gradient plot is less than in the flow direction plot. In both plots, the variation in velocity appears less than in 3D, but as we do not expect sedimentation velocities in 2D and 3D to match, we should not expect the variation over a shear cycle to match either. These plots give us confidence that for oscillations in the shear directions in fig. 4.4, simulations of sedimentation through monolayers provide qualitatively reasonable representations of sedimentations through fully 3D samples, while saving considerable computation time.

4.6.2 Effect of shear frequency and repulsion

We examine the importance of the shear frequency and repulsion strength on both a 2D monolayer and a fully 3D sample. The respective particle density function plots in the shear plane are shown in figs. 4.17 and 4.18. Each shows PDFs for nine parameter combinations: simulations with different repulsion strengths, k, and different oscillation frequencies, f. We see that in the shear plane, the imposed oscillatory shear creates a square-packing structure in the suspension bulk. At low repulsions and high frequencies, there is little difference from the circular structures seen prior to shearing (see fig. 4.8), but the effect is clearer for increasing repulsion strength and decreasing frequency. We can quantify the degree of square packing in

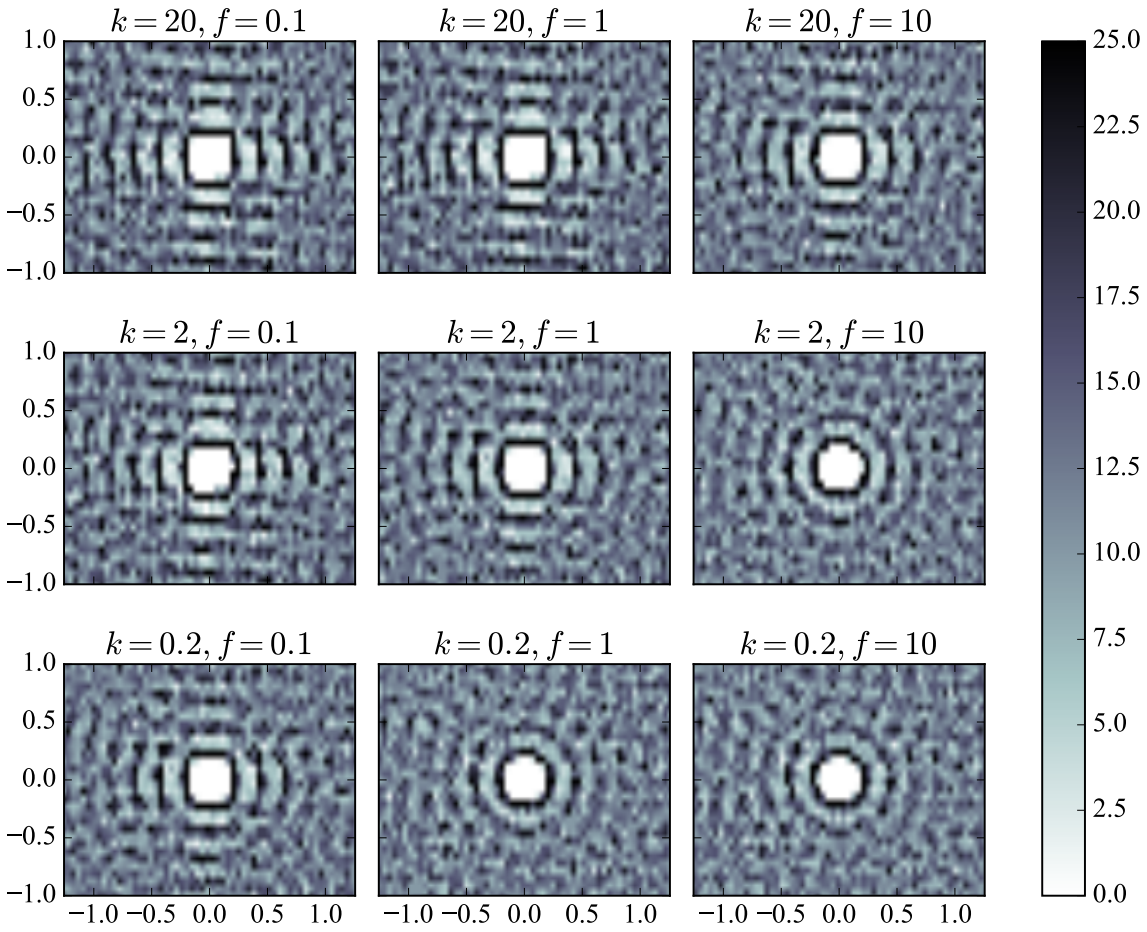

Figure 4.17: 2D oscillatory preshear: Particle density function plots for oscillatory preshear after two oscillations. High frequency, low repulsion plots show little difference to their initial state (see fig. 4.8), but for lower frequencies and higher repulsions, we see distinctive square packing.

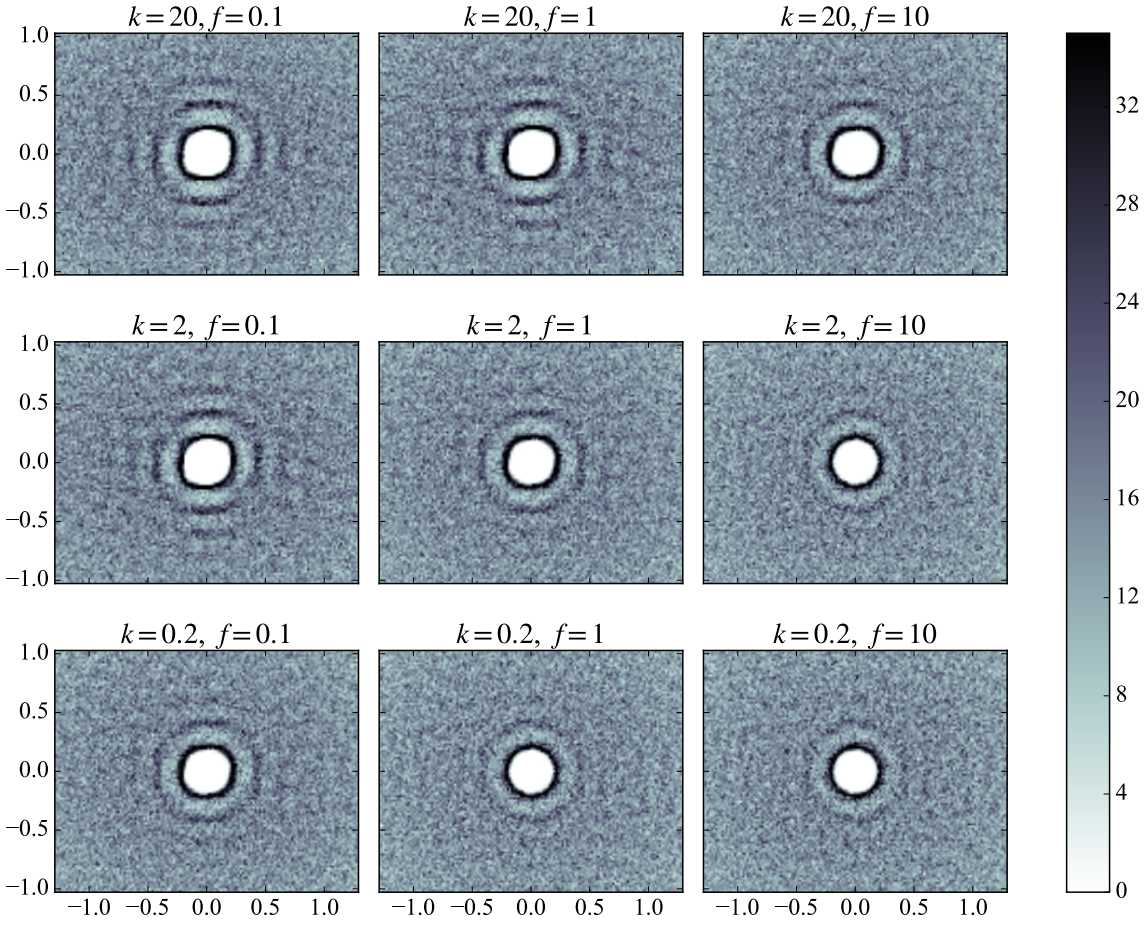

Figure 4.18: 3D oscillatory preshear: Particle density function plots for oscillatory preshear after two oscillations. As with the monolayer, high frequency, low repulsion plots show little difference to their initial state (see fig. 4.8), but for lower frequencies and higher repulsions, we see distinctive square packing. The slices in the plane have depth of 2 small particle radii.

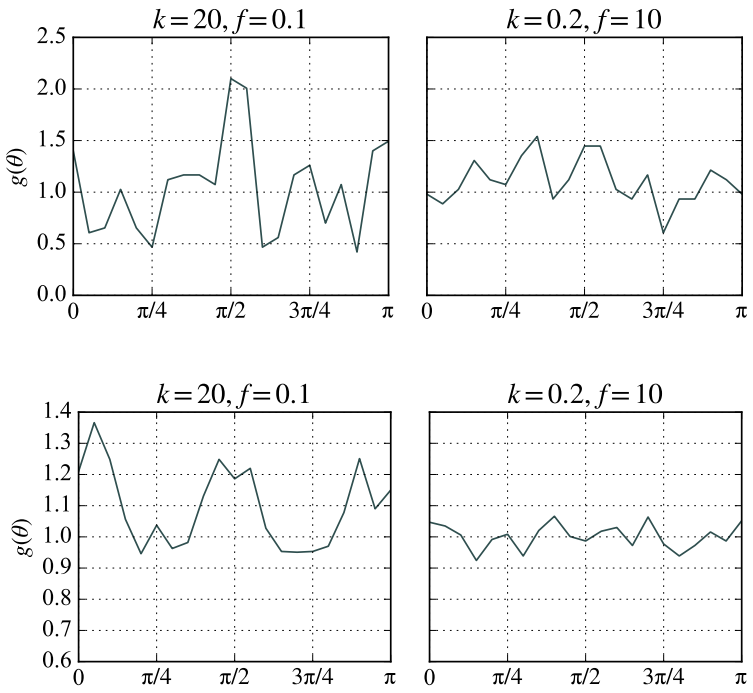

Figure 4.19: **Top:** 2D oscillatory preshear. **Bottom:** 3D oscillatory preshear. Two particle density function plots as a function of angle at a constant radius band corresponding to the second dark band in fig. 4.17. By the symmetry expected, we only plot from $\theta = 0$ (the positive x-axis in the PDF plots in fig. 4.17) to $\theta = \pi$. The low-frequency, high-repulsion cases on the left show peaks at 0, $\pi/2$ and π which are taller than in the right-hand plot, corresponding to the observed square packing. The particle density function is normalised so that the means of the right-hand plots are 1.

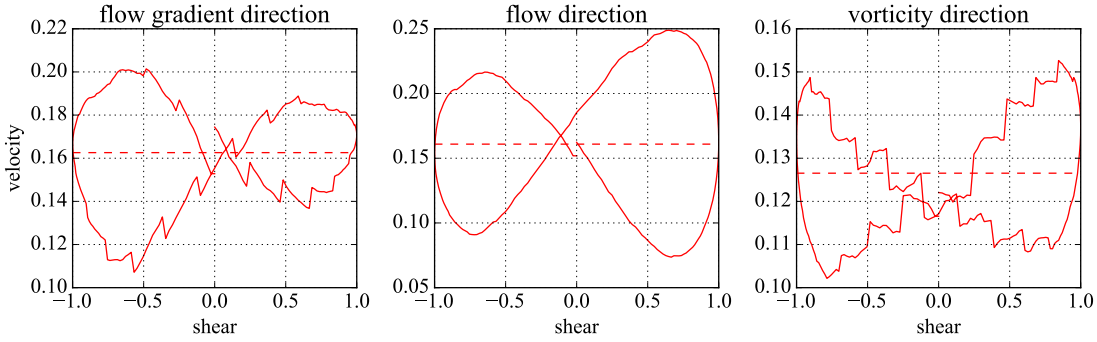

Figure 4.20: Velocity profile of the sedimenting heavy sphere in oscillatory shear. Here we see the velocities in the (negative) z-direction for each of the three simulations corresponding the geometries in figs. 4.1 and 4.4. That is to say, the shear is applied so that the z-direction corresponds to the flow gradient direction, the flow direction, and the vorticity direction respectively. All three profiles are for the moderate parameters $f = 1$, $k = 2$. The horizontal dashed line shows the mean velocity over the shear.

the particle density function plots as a function of angle round the second dark band, $g(\theta)$. Figure 4.19 shows two extreme cases in 2D and 3D. The right-hand plots—the high-frequency, low-repulsion cases—show a mostly constant concentration of particles around the band, but the left-hand plots—the low-frequency, high-repulsion cases—show peaks at $\theta = 0$, $\pi/2$ and π, corresponding to the observed square packing. Once again, with the advantage of more particles in the system, the 3D plots are less erratic.

4.7 Sedimentation in oscillatory shear

We now apply a weight force to the large sphere while continuing to shear the suspension.

4.7.1 Effect of shear direction

The velocity profile of the falling sphere in the system, sheared in each of the three directions, is shown in fig. 4.20. In all three shear directions, the fall velocity of the ball oscillates over a shear cycle. Note that shear in the flow gradient and flow directions leads to figures of eight which are traversed in the opposite direction to the vorticity direction: in the first two cases, the ball slows down over a shear, whereas in the latter case, it speeds up. We describe a mechanism for this behaviour in section 4.8. The third figure in fig. 4.20 therefore reproduces the figure-of-eight shape observed in experiment, but traversed in the opposite direction. The periodic ‘jumps’ in the plot are a sensitivity to a detail of the Stokesian Dynamics

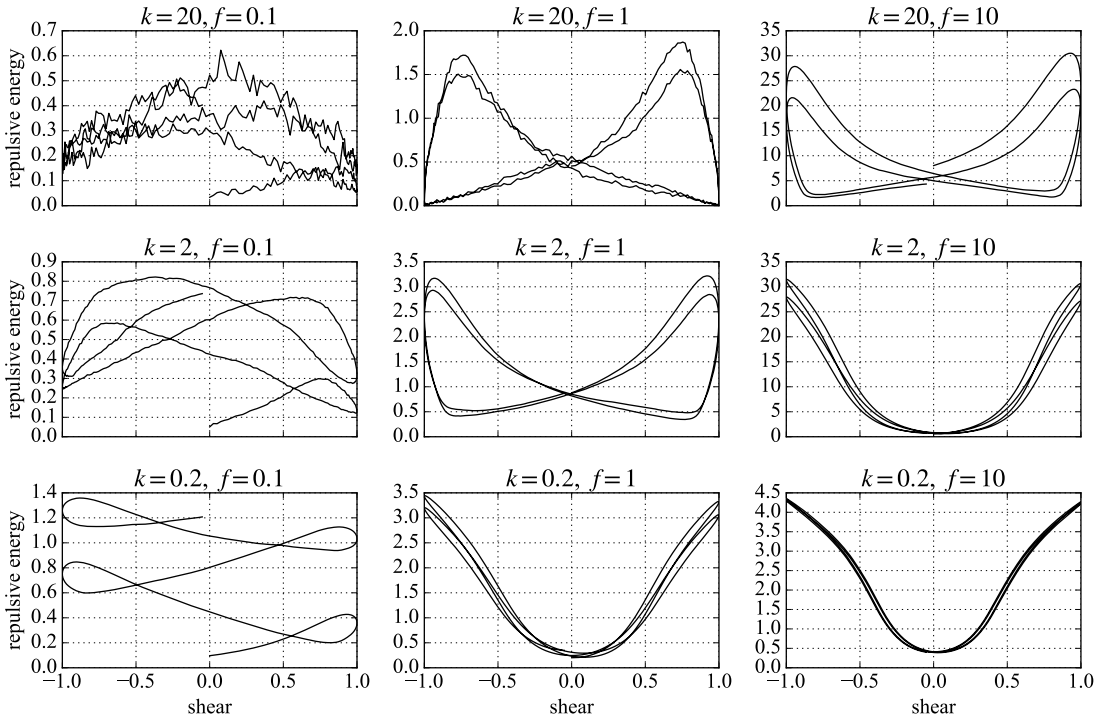

Figure 4.21: Two-dimensional simulations of a ball falling in the flow-gradient direction. We plot the total energy in the system against state of shear. In each plot, the oscillation begins with motion to the right.

method—specifically, how often we calculate the long-range mobility matrix $\mathcal{M}^{\infty}$. The velocity profiles appear to be a sum of the unsheared falling speed, fig. 4.12, and the oscillatory behaviour from the shear, fig. 4.15. We do not observe significant changes in the mean velocity from the unsheared case.

4.7.2 Effect of frequency and repulsion strength

We now look at the effect of changing the frequency and repulsion strength. Some elucidation of the effects at work here is provided by examining the repulsive energy in the system over time. This may be calculated from the magnitudes of the repulsive forces in the system, for the exponential force we are using (eq. (4.5)): the repulsive energy, E, for a pair of particles i and j with surface separation h_{ij} is the work done against the repulsive force in bringing them to that position, starting from far apart:

$$E(i,j) = \int_{h_{ij}}^{\infty} \boldsymbol{F} \cdot \mathrm{d}\boldsymbol{r} = \frac{1}{\tau}|\boldsymbol{F}(h_{ij})|, \tag{4.9}$$

recalling that τ is related to the repulsion decay length. This is then summed over all pairs of particles in the system.

Figure 4.21 measures the repulsive energy in a 2D system over two oscillations of

shear in the velocity gradient direction (fig. 4.4(a)) for different parameter values. We see broadly three regimes. The first, in the bottom-right of the figure, is a U-shape: the high-frequency, low-repulsion regime. Starting from the centre of the plot and moving to the right, the repulsion energy increases as the system is sheared and compressed, and then reverses mostly symmetrically as the system is unsheared and uncompressed. In this limit, the oscillation is too fast for the repulsion to act: the hydrodynamic forces associated with the shear dominate over the weight and repulsion forces, essentially making the particles passive. At high frequencies and low repulsions, the energy plot is therefore reversible. We begin to see hysteresis above and to the left of this plot, as decreasing the frequency gives the repulsion time to act, and increasing the repulsion forces no longer leaves the shear forces dominant.

These hysteresis loops are emphasised in the central plot in the figure—with intermediate parameter values—where we have a figure of eight. Again starting from the centre of the plot and moving rightwards, the system is compressed as it is sheared, building up structure and repulsion energy. At the end of the shear, though, the repulsion force has time to act, whereas it did not in the previous regime. The particles repel each other, the structure is destroyed, and the system relaxes. Then, as the system is sheared in the opposite direction, the particles are compressed again and the structure and energy increases. This alternating between construction and destruction generates the figure of eight.

Finally, the bottom-left plot of the same figure—low repulsion, low frequency—shows ascending loops. This regime is just a slower version of the aforementioned one: the system has time to relax when the shear direction changes, but as shears take longer with low frequencies, the concentration builds up more beneath the falling ball over a shear and thus the system repulsion energy increases over time.

These different regimes loosely match with the velocity profiles shown in fig. 4.22, measured over a single oscillation of the shear flow for the same nine different parameter combinations. We show the second falling oscillation here. Again, the oscillation begins with motion to the right, and we plot falling velocity as positive.

Starting in the bottom-left, the low-repulsion, low-frequency case, we see the velocity decrease over time as the concentration builds up beneath the ball, agreeing with the loops in the repulsive energy plot. In the central plots we see figures of eight, as the particle slows down under the increased repulsion from the structured, compressed suspension. As the system relaxes and the structure is lost—the small particles 'space out' under repulsion—the large particle is able to fall with less hindrance, and its speed increases until the reverse shear increases the local concentration and

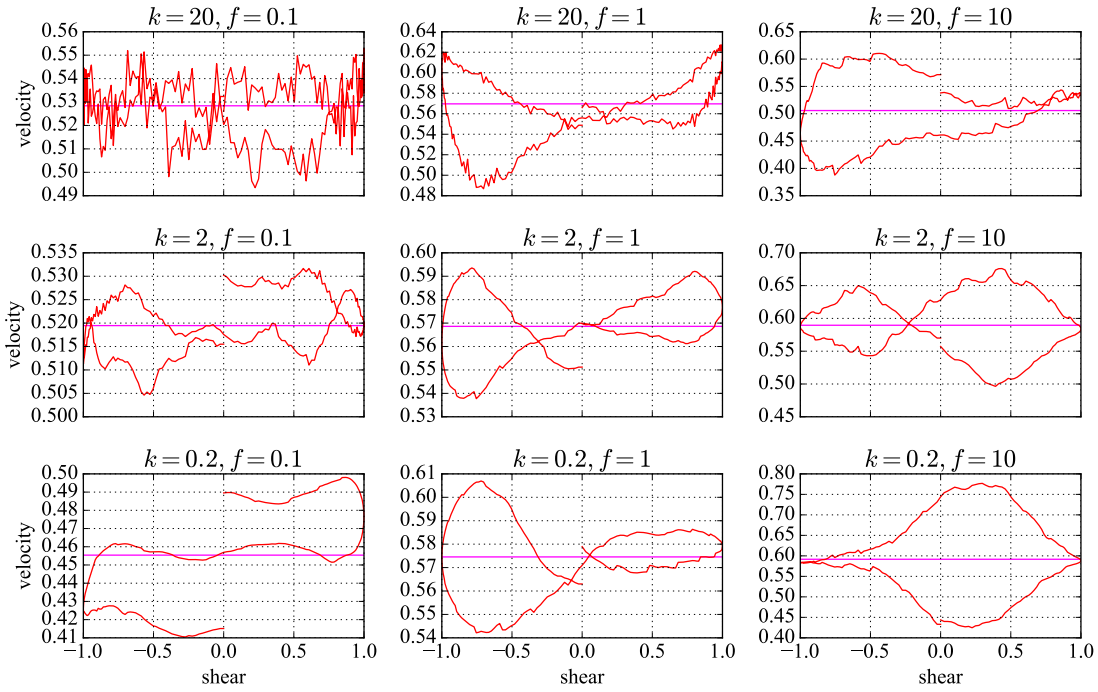

Figure 4.22: Two-dimensional simulations of a ball falling in the flow-gradient direction. We plot the instantaneous fall speed against state of shear. In each plot, the oscillation begins with motion to the right. The magenta horizontal line marks the mean falling speed over the shear.

repulsion forces again.

Still in fig. 4.22, in the bottom-right case (low repulsion and high frequency) we see behaviour that appears counterintuitive: when the shear is moving to the right the ball accelerates, but when the shear is moving to the left it decelerates, which would appear to break the intrinsic symmetries of the system. However, with both repulsive forces and the weight of the ball being very small in this limit compared with the hydrodynamic forces associated with the external shear flow, all the particles are essentially passive, and simply move with the shear flow, hindered by each other's presence in a purely hydrodynamic way. The falling ball is pushed primarily horizontally, with small perturbations in the vertical direction. One of these is caused by the presence of the small particles, which happen (for this simulation) to be arranged in such a way that the perturbation is upwards when the motion is to the left and (by reversibility) downwards when the motion is to the right. The other is caused by the particle's weight, which always drives it downwards. Because we have made velocities dimensionless using the Stokes velocity of the large sphere in the absence of small particles, these velocities both appear order 1 in our plots.

Looking from left to right across the same figure, we can see that increasing the frequency increases the velocity difference over the shear: speeding up the oscillation by a factor of 10 leads to an approximate doubling of the percentage velocity gain. This

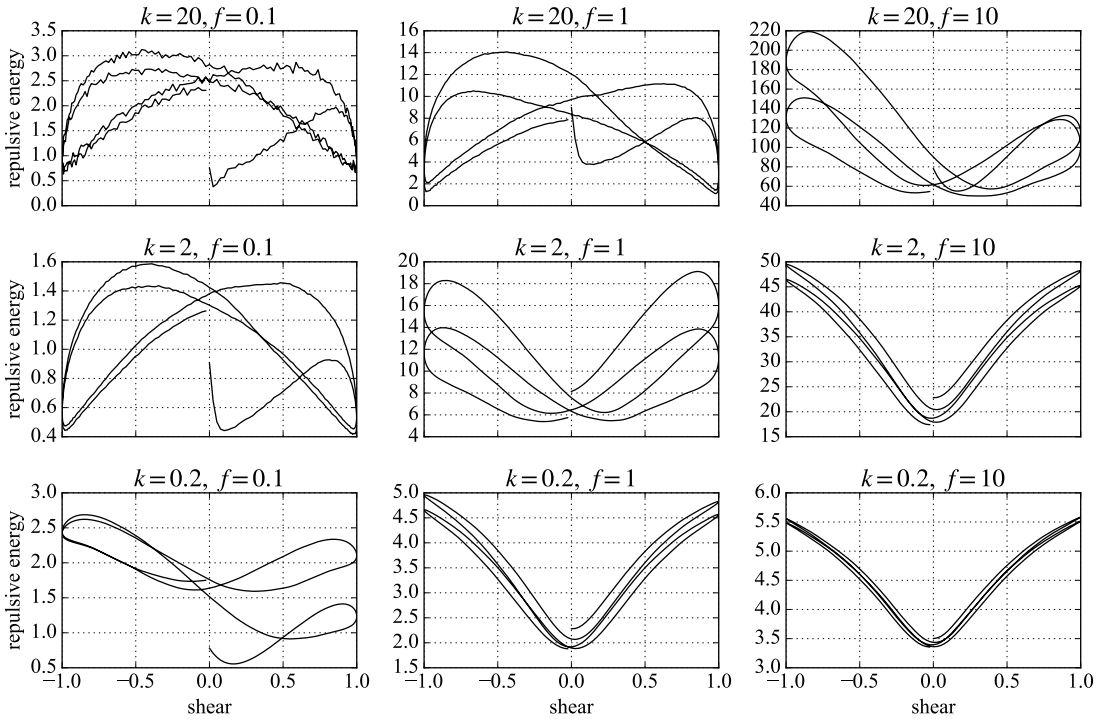

Figure 4.23: Three-dimensional simulations of a ball falling in the vorticity direction. We plot the total energy in the system against state of shear. In each plot, the oscillation begins with motion to the right.

suggests that increasing the frequency of oscillation further, or reducing the weight of the falling ball, should lead to greater velocity differences, allowing the particle to rise over parts of the shear. This would mimic the behaviour seen experimentally. These results are all for sedimentation in a monolayer sheared with xz-shear. It is not until we shear a 3D cell in the xy-plane, simulating the experiments, that we see the ball travel upwards.

Figures 4.23 and 4.24 show the repulsive energy and velocity profiles for the falling sphere in a cube of smaller particles, undergoing xy-shear. The repulsive energy is of a similar magnitude to in 2D, but the loops retain a stronger U-shape in the moderate parameter values. The velocity profiles are generally smoother than their 2D counterparts, generating clean figures of eight in the central and right-hand column. This is not surprising, given that the increased number of neighbours in 3D suspensions offers more consistent resistance to the movement of the large sphere. As mentioned when looking at preshear, the velocity plots are traversed in the opposite direction to the two-dimensional simulations. In this geometry, the build-up of structure corresponds to the ball speeding up, which is lost when the structure is destroyed. The mechanism is discussed fully in section 4.8.

Some observations are the same as in 2D: increasing the frequency by a factor of 10 leads to a similar proportional increase in the velocity difference over the shear

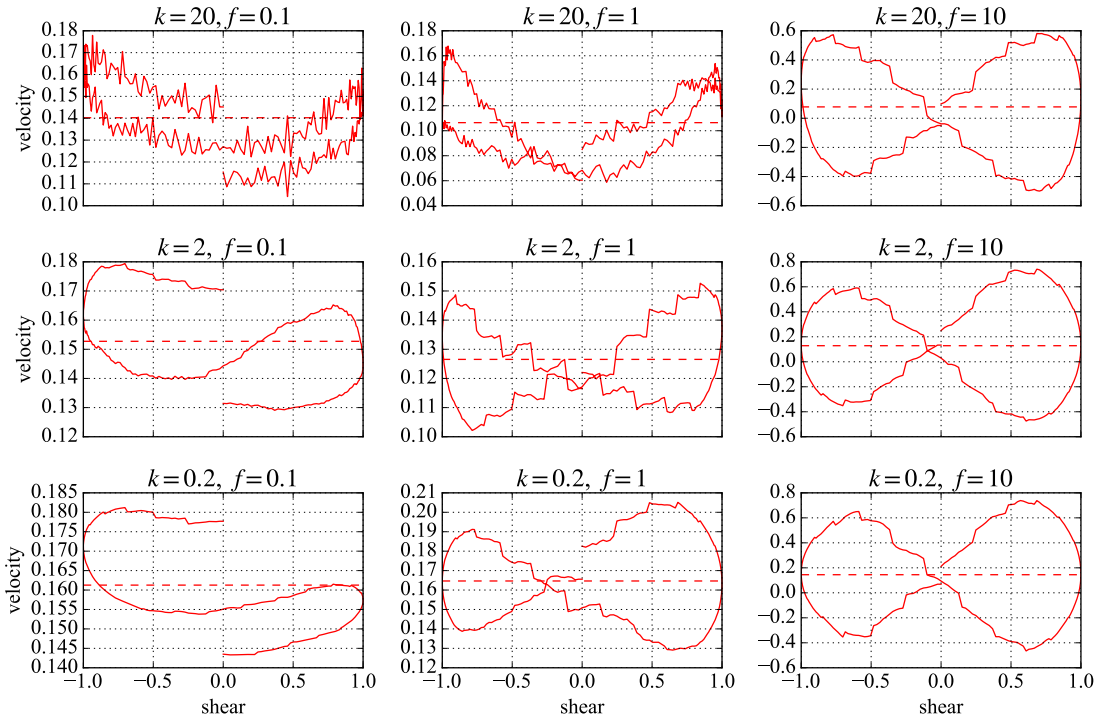

Figure 4.24: Three-dimensional simulations of a ball falling in the vorticity direction. We plot the instantaneous fall speed against state of shear. In each plot, the oscillation begins with motion to the right. The dashed horizontal line marks the mean falling speed over the shear.

cycle. In our high frequency cases, this leads to the ball traversing upwards over the course of the cycle: the same behaviour seen in the experiments, although with the profile again traversed in the opposite direction. Changing the repulsion strength does not seem to lead to significant changes in the profiles.

4.7.3 Effect of concentration and amplitude

The concentration of the suspension is varied in fig. 4.25 to $\phi = 0.1$ and 0.2, as well as the existing $\phi = 0.4$ which we use for the rest of the study. Here we look at xy-shear, so the ball is falling in the vorticity direction, with the moderate frequency and repulsion parameters $f = 1$, $k = 2$. We see that, as expected, decreasing the concentration increases the mean fall velocity. However, it does not appear to dramatically change the variation in velocity over the shear, which remains at approximately ± 0.05.

The amplitude of the shear is varied for the same moderate parameters in fig. 4.26. We see that the mean shear velocity is mostly unchanged from the unsheared suspension, but the variation in velocity across the shear is increased by increasing the shear amplitude proportionally. This makes sense: increasing the amplitude

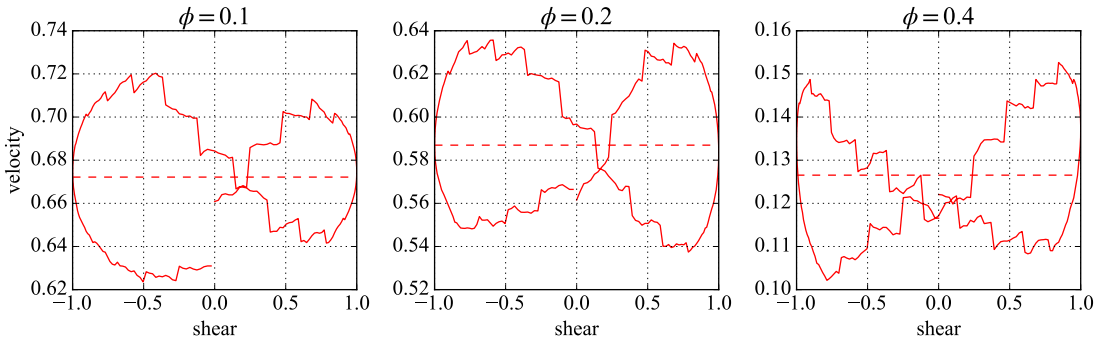

Figure 4.25: Velocity profile of the sedimenting heavy sphere in oscillatory shear. Here we see the velocities in the (negative) z-direction for a heavy ball sedimenting in xy-shear. The volume concentrations are $\phi = 0.1$, 0.2 and 0.4 (used in the rest of the study). All three profiles are for the moderate parameters $f = 1$, $k = 2$. The horizontal dashed line shows the mean velocity over the shear.

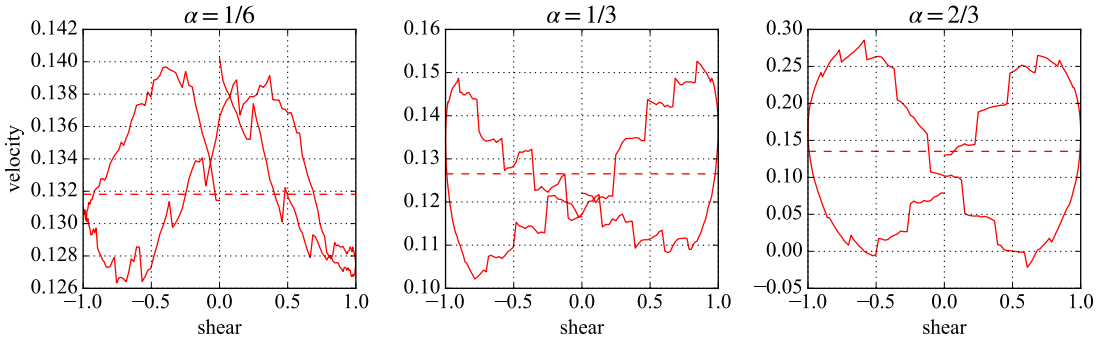

Figure 4.26: Velocity profile of the sedimenting heavy sphere in oscillatory shear. Here we see the velocities in the (negative) z-direction for a heavy ball sedimenting in xy-shear. The amplitude of the oscillatory oscillation is $\alpha = 1/6$, $1/3$ (as in the rest of the study), and $2/3$. All three profiles are for the moderate parameters $f = 1$, $k = 2$. The horizontal dashed line shows the mean velocity over the shear.

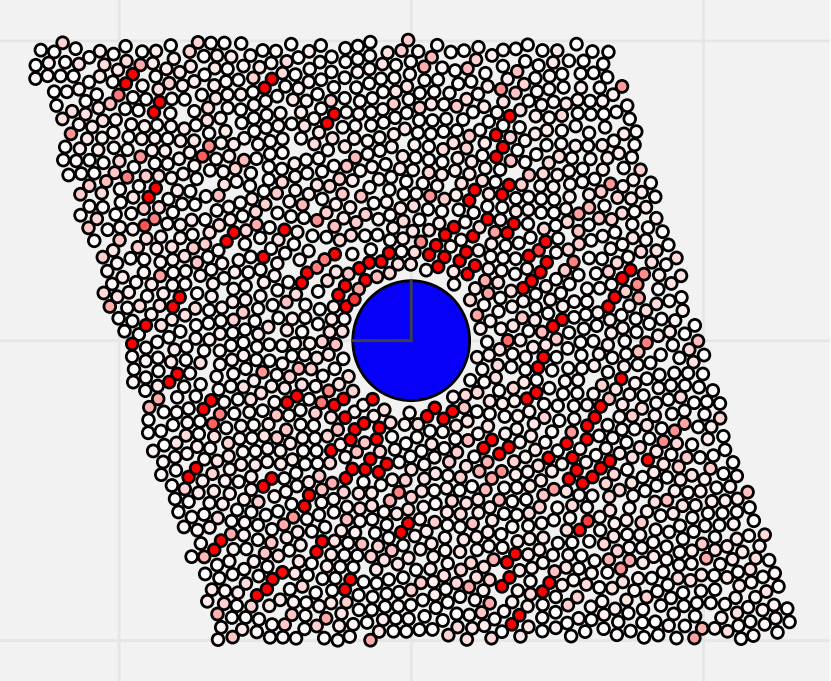

Figure 4.27: Under shear alone, chains of particles experiencing high forces (marked in red) form parallel to the compression axis. We have faded out small particles not in the chains.

increases the energy put into the system.

4.8 Mechanism behind velocity profiles

For a sphere sedimenting in the flow gradient and flow directions, we see the ball slowing over a shear and speeding up at the extremes. For a sphere sedimenting in the vorticity direction, we see the ball speeding up over a shear and slowing down at the extremes.

It is tempting to argue on energy lines, that the slowing falling velocity, and hence the height gain in Blanc *et al.* (2015), must come from a release of the elastic energy associated with the repulsive forces. However, as we see in the central case in figs. 4.21 and 4.22, this is not the case. Here, the maximal rate of release of elastic energy actually coincides with downwards acceleration of the large sphere, where the relaxing system allows the ball to fall with less hindrance. There is no paradox here: the imposed shear flow is an energy source which adapts instantaneously to the energy being dissipated by viscous forces.

Instead, we break the oscillatory shear, and hence the velocity profile, into two periods: a structure-creating period, as the system is sheared; and a destruction period, as the shear direction changes, when the system is allowed to relax. Whether

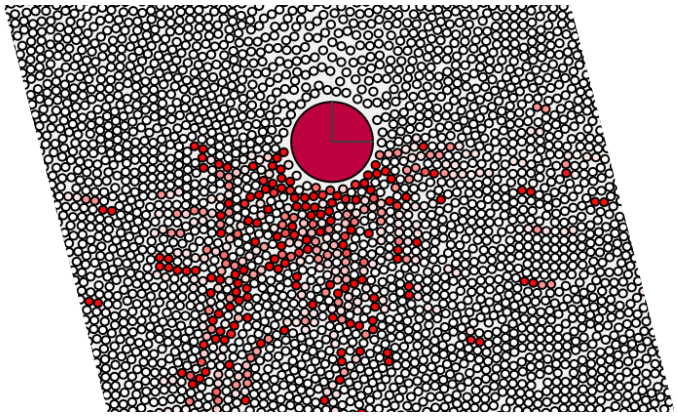

Figure 4.28: As the large sphere falls, the concentration beneath the ball increases, so the repulsion chains induced by the shear form beneath and to the side of the ball, adding upward force.

this causes the falling sphere to accelerate or decelerate depends on the direction of the shear, and to a lesser extent, the amplitude of shear.

We have already seen in section 4.6.1 that as the system is sheared, it forms a square-packing structure in the shear plane. In the same plane, we also see the formation of 'chains of repulsion'. Figure 4.27 shows this effect in xz-preshear: small particles lying parallel to the compression axis experience high repulsion forces (marked in red). Since in our systems, the ball is placed near the top of the system, there are more small particles beneath the ball than above it, giving us longer, stronger chains. The net effect of these chains is to push the ball to areas of less concentration (which lie above it).

For sedimentation in the shear plane, we see, as in fig. 4.28, that as the particle falls, it builds up concentration beneath it. Simultaneously, shearing the suspension causes these chains of repulsion to form. As chains form in more concentrated areas, there are more chains in front of the falling particle than behind it, and there are more along the compression axis than in the uncompressed axis. The heavy ball is pushed by these chains of repulsion towards less concentrated areas (which again lie above it), which is why it slows down—and, given long enough chains of repulsion, can make it move upwards.

In both preshear and sedimentation in the xy-direction (corresponding to sedimentation perpendicular to the shear plane), we see a figure of eight in the velocity plots of a similar magnitude but traversed in the opposite direction. Again, chains of repulsion are formed, but these have a reduced effect, as they lie predominantly in the shear plane. Instead, the square-packing structure is responsible for the acceleration over the shear. As seen in fig. 4.29, the shear causes vertical chains to form parallel to the sedimentation direction. In sedimentation, this makes it easier for the ball to fall through, relative to the unsheared suspension. When the shear direction

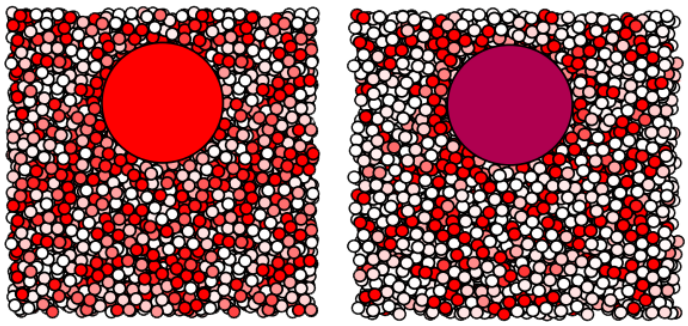

Figure 4.29: A vertical slice through a cube of small particles, with a neutrally buoyant large particle in xy-preshear. Particle experiencing high forces are marked in red. **Left:** before shear. **Right:** during shear, when vertical chains form.

changes, the structure is destroyed and the ball slows down again, in places being pushed upwards by the repelling particles. In preshear, the net force on the large sphere from the small particles is upwards (seen by the mean upwards velocity in fig. 4.15), provided by the larger number of particles beneath the large sphere. Over the shear, structure forms which reduces this net effect, causing the ball to slow down over shear. As the shear direction changes, the structure is again destroyed and the net upwards force accelerates the ball upwards.

We see in fig. 4.26 that the velocity profiles are dependent on the amplitude of shear. We have already observed that increasing the amplitude of oscillation increases the energy put into the system, which explains the increases velocity differences at higher amplitudes. But at the smallest amplitude ($\alpha = 1/6$), the velocity difference over a the shear cycle is small—only $\pm 6\%$ of the mean falling speed—and the profile is erratic, appearing to traverse the figure of eight in the opposite direction to the higher amplitudes. This we attribute to structure: at reduced amplitudes we expect to see less structure build up, and so the playoff between structure creation and destruction is less clear.

Furthermore, that in fig. 4.25 we saw little difference to the velocity difference for different concentrations is initially surprising, given the mechanism described above depends on structure, which should be enhanced by concentration. But with reduced concentration, the mean velocity is higher (so proportionally the velocity difference is reduced), so the falling ball meets more particles over a shear cycle, producing a similar effect to an increased concentration.

4.9 Conclusions

The experiments by Blanc *et al.* (2014) posed multiple questions about the behaviour of the microstructure in an oscillatory sheared suspension. Our Stokesian Dynamics

simulations offer explanations for some of their observations. In particular, we are able to qualitatively recreate the figure-of-eight velocity profiles, although traversed in the opposite direction in the shear geometry most closely matching the experiments. We also have a feasible mechanism—repulsion chains in the plane in 2D, breakdown of vertical chains in 3D—for which the upward motion in the shear, observed in the experiments, is possible. We have also shown that the behaviour over a shear cycle is strongly affected by the imposed frequency and repulsion strength, giving different regimes for the velocity profiles. That we have not seen the increased fall velocity in the heavy sphere suggests that another mechanism is responsible for this, or at least that it requires more than just repulsion between particles. The distances travelled by the ball in experiments are up to 20 times larger than the box size in our simulations, and the number of shear cycles experienced by the falling ball far higher, so it is feasible that observing this increased fall velocity requires additional particles with higher build-ups of structure.

Chapter 5

Shear thickening and friction

5.1 Introduction

5.1.1 Shear thickening

A long-standing classification of fluids is how their viscosities change under an applied shear rate. The simplest fluids—water, air—have viscosities that, in ordinary conditions and contexts, are unaffected by shear rate changes. These are *Newtonian* fluids: see fig. 5.1. Most common suspensions, on the other hand, have viscosities, η, which decrease with shear rate, $\dot{\gamma}$: they thin. The class of *shear-thinning* fluids includes tomato ketchup, mayonnaise, paint, lava and—everyone's favourite—chocolate (Townsend & Wilson, 2016). This is often a desirable property: when painting, for example, you want the paint to be thin enough to apply it to walls easily and evenly, but when you stop shearing the paint with the roller, you want the paint to not drip down the wall.

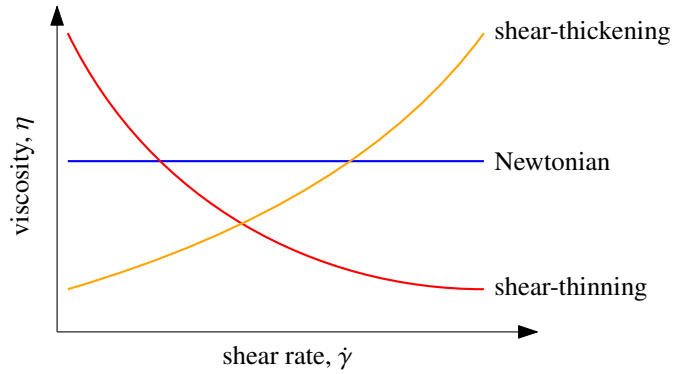

Figure 5.1: Fluids' viscosities may increase, decrease, or stay the same as an applied shear rate is changed. We use the response of the fluid to this change to classify fluids as shear-thickening, shear-thinning, or Newtonian.

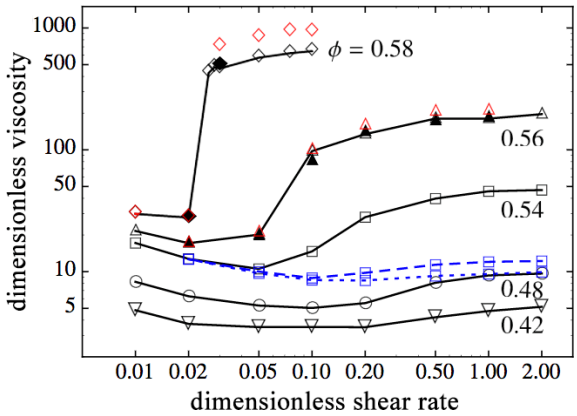

Figure 5.2: Continuous and discontinuous shear thickening is observed here at varying volume concentrations (ϕ). Reproduced from Seto *et al.* (2013).

The opposite, *shear thickening*, is the more exciting behaviour. The classic kitchen experiment of cornflour ('corn starch' in the US) and water is probably the best-known example. Mixed together into a paste, it forms a thick liquid under relaxation, but when struck it becomes almost solid. Given sufficient mixing, it is possible to run across the top of swimming pools full of this mixture.

Which physical property it is, exactly, of cornflour suspensions that makes it shear thicken is, surprisingly, still not clear. Starch is a long polymer, and, as discussed in chapter 3, polymer solutions tend to shear thin: shearing unravels the long molecules, which end up lying flat and parallel to each other, aiding the flow. The behaviour of different starches in solution under shear also varies (Dintzis *et al.*, 1996). A suspension of cornstarch was shown in fig. 1.2, where the polymer has formed into particles.

A good overview of our current understanding of shear thickening is given in Wyart & Cates (2014), and here we give the relevant observations. Shear thickening appears to occur in two forms. In the first case, the viscosity may increase smoothly with shear rate, in so-called continuous shear thickening (CST). This is observed experimentally at medium volume fractions. In the second case, at higher volume fractions, the viscosity of solutions has been observed to suddenly increase, in so-called discontinuous shear thickening (DST). An example from the literature is shown in fig. 5.2, where the discontinuous increase is by an order of magnitude.

For either CST or DST, particle interactions have been established as being important: shear thickening is not typically seen in attractive particle solutions, for example (Brown & Jaeger, 2014). Up until recently, explanations for shear thickening have included the flow-induced formation of particle clusters (Brady & Bossis, 1988) or the tendency of granular materials to expand under flow (Barnes, 1989). Both of these explanations, however, are problematic in the face of DST. The former fails to predict viscosity jumps of the required magnitude (among other problems)

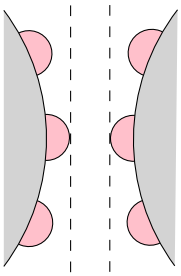

Figure 5.3: The recent trend in simulation is to give the particles a roughness height, represented by the pink bumps here, which stops the particles from approaching when their surface separation is less than this height.

(Brown & Jaeger, 2014), while the latter incorrectly predicts DST for smooth, hard particles (Wyart & Cates, 2014).

Indeed, simulations of smooth, hard particles are unable, mostly, to reproduce shear thickening behaviour. The current consensus, therefore, is that discontinuous shear thickening arises from *frictional contact* between particles (Seto *et al.*, 2013). At a certain shear rate and for high enough concentrations, lubrication is overridden by friction forces as *rough* particles come into contact.

Following this consensus, the recent trend in simulation is to mimic the roughness of particles by taking smooth particles and imposing that when two approaching particles are some small distance away—mimicking a 'roughness height'—that a contact force and a friction force act to oppose their motion. Figure 5.3 sketches the idea. The friction model is imposed additionally to lubrication forces, which continue to act.

5.1.2 Frictional contact

As we have stated, when particles approach, they interact in the presence of hydrodynamic lubrication forces. This feature is baked into the Stokesian Dynamics method, which, as we first saw in chapter 2, considers particles to interact under long-range hydrodynamic forces and near-field lubrication forces. Up to this point, however, we have always assumed in our model that the particles in our suspension are smooth. Under lubrication forces, smooth particles under finite forces can never come into contact. However, experiments (Arp & Mason, 1977; Zeng *et al.*, 1996) show quite clearly that although particles may appear smooth, microscopic roughness of particles—tiny surface asperities—can lead to particle contact.

This contact has been shown to be responsible for a number of observations in suspension mechanics, not just shear-thickening. In particular, it breaks the reversibility of interactions, a key feature of Stokes flow, and one that will be illustrated

in section 5.3. Instead of particles passing each other symmetrically, we see a wake behind each particle, as the passing particles are slightly deflected by the roughness. Simulations in the literature (Da Cunha & Hinch, 1996) have shown that this roughness does not have to be large: the minimum surface separation during collision can be less than 10^{-4} of the particle radius, and so roughness heights of this order can be sufficient. Indeed, a typical roughness height for particles used in suspension experiments is 5×10^{-3} of the particle radius (Smart & Leighton, 1989; Blanc *et al.*, 2011).

This fore–aft asymmetry can also be seen in oscillatory shear experiments. Returning to the particle density function plots in chapter 4, experiments by Blanc *et al.* (2011) show 'downstream depletion zones' where only a small number of particles are found after a series of oscillatory shear cycles. This depletion again suggests deflection on the particle scale, which can be explained by particle roughness. Indeed, the paper aims to measure the particle roughness indirectly by examining the size of these depletion zones.

We now try to pin down the contribution to viscosity from rough particles in a suspension. We established in chapter 1 that the presence of particles contributes to the *effective viscosity*, η, of the solution—the viscosity of the Newtonian fluid which gives the same stress at the same shear rate. Recall the effective viscosity formula for a dilute suspension of spheres by Einstein (1906):

$$\eta = \left(1 + \frac{5}{2}\phi\right)\mu, \tag{5.1}$$

for a concentration ϕ and a suspending medium of viscosity μ. For dilute suspensions, rough or smooth (so long as the roughness height is not unreasonable large), the viscosity of the suspension behaves in this way. Continuing this expansion in the volume fraction, ϕ, the ϕ^2 term is much harder to calculate, for the viscosity at this point depends on more than than just the concentration. Wilson & Davis (2000) give the nice example of two particles in shear flow which rotate endlessly around each other, giving a viscosity which is *time*-periodic. It is at this order as well that particle interactions matter, and so the roughness of the particles needs to be considered.

A number of experimental and simulation measurements of the effective viscosity of a suspension at different concentrations and friction coefficients are compiled in Gallier *et al.* (2014*b*, fig. 9). With a given roughness height, both experiments (with unknown friction coefficients) and simulations (with a variety of friction coefficients) show increases in viscosity with concentration. This, at least, was expected from eq. (5.1). Interestingly, however, they found that frictionless simulations systemat-

ically underestimate the viscosity at higher concentrations, up to about a factor of two. Increasing the friction coefficient up to $\nu = 0.5$ (we use the notation ν here, rather than the more conventional μ, to avoid confusion with viscosity) shows a substantial increase in viscosity, giving good agreement with experiments. Of course, it is worth noting that the underestimation of viscosity in the frictionless case is only apparent at high concentrations, when particles are in sufficient contact.

To examine the role of friction further in suspension viscosity, the paper (Gallier *et al.*, 2014*b*, fig. 10) also considers the *origin* of the viscosity at different concentrations. The contribution to viscosity from hydrodynamics and from contact are plotted together. At low concentrations, the viscosity is almost entirely derived from hydrodynamics, but as concentration increases, the contact contribution also increases. Increasing the friction coefficient was found to make no difference to the hydrodynamic contribution to viscosity. But, at the highest friction coefficient ($\nu = 0.5$), the contact contribution was shown to have increased to 70% of the total relative viscosity: a powerful argument for the importance of contact in suspension rheology. From a practical perspective, this also suggests that you can *tune* the viscosity of the suspension by changing the surface properties of the particles.

In this chapter, we will introduce an effective frictional model, show how we can integrate it into Stokesian Dynamics using a new, more accurate and efficient method, and then demonstrate that it captures some of the required behaviour. We will, interestingly, also show that improving the accuracy of the frictional model leads to us *not* seeing some of the experimentally observed behaviour, suggesting that the approximations used so far in the literature capture an important feature of the particle roughness.

5.2 Friction model and implementation

We start by implementing a particle friction model. A number of models have been used in the literature: e.g. hard-sphere repulsion (Da Cunha & Hinch, 1996), stick–rotate (Davis, 1992), stick–slide (Mari *et al.*, 2014) and roll–slip (Wilson & Davis, 2000). The level of sophistication differs: the hard-sphere repulsion model applies normal forces only, similar to that in chapter 4, whereas the others also apply tangential forces, improving the match to experiment (Zeng *et al.*, 1996).

We implement interparticle friction using a refinement of the roll–slip model. In the roll–slip model, we say that as two particles approach, once their surface separation is sufficiently small and below some critical value, they are ‘in contact’. At this point, their approach is stopped by small deformations on the surface on the particle, as

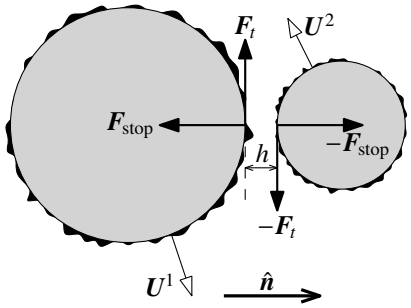

Figure 5.4: The normal contact force, $\boldsymbol{F}_{\text{stop}}$, and tangential friction force, $\boldsymbol{F}_t$, oppose the motion of the approaching particles. These forces are added to any existing forces already acting on the particles.

illustrated in fig. 5.3. The particles then remain in contact at this distance while the net hydrodynamic force on each particle continues to compress the pair together. As soon as these hydrodynamic forces no longer push the two particles together, contact is broken: there are no more frictional forces on the particles and the particles move freely.

While the particles are in contact, contact forces are placed on each particle in the pair. This is done in a way that the net force on the pair is unchanged, and is illustrated in fig. 5.4. In the normal direction (parallel to the line of centres), the force applied to each particle, $\boldsymbol{F}_{\text{stop}}$, is exactly that to stop the particles approaching any further. As far as we are aware, this is the first implementation to use the exact stopping value. This is, therefore, an important distinction from the existing literature which typically uses one, or a combination, of the following approximations to $\boldsymbol{F}_{\text{stop}}$:

- a linear spring contact force,

$$\boldsymbol{F} = -k|h|\hat{\boldsymbol{n}}, \tag{5.2}$$

  activated when h, the particle surface separation shown in fig. 5.4, is negative (Seto *et al.*, 2013; Mari *et al.*, 2014; Ness & Sun, 2016; Trulsson *et al.*, 2017),

- a Hertz contact force,

$$\boldsymbol{F} = -k|h|^{3/2}\hat{\boldsymbol{n}}, \tag{5.3}$$

  activated when h is negative (Gallier *et al.*, 2014*b*),

- a dashpot force,

$$\boldsymbol{F} = -k(\boldsymbol{U} \cdot \hat{\boldsymbol{n}})\hat{\boldsymbol{n}}, \tag{5.4}$$

  proportional to the normal approach velocity (Mari *et al.*, 2014),

- a short-range repulsion force,

$$\boldsymbol{F} = -k\mathrm{e}^{-\tau h}\hat{\boldsymbol{n}} \qquad \text{or} \qquad \boldsymbol{F} = \frac{-k\mathrm{e}^{-\tau h}}{1-\mathrm{e}^{-\tau h}}\hat{\boldsymbol{n}}, \tag{5.5}$$

  such as that we used in chapter 4 (Seto *et al.*, 2013; Vázquez-Quesada *et al.*, 2016).

Although these force laws repel close particles, particles are still able to approach under sufficiently large shear. This has the effect of 'softening' roughness under large shear. Closer particles lead to increased viscosity due to dissipation through increased lubrication forces. As we implement a true stopping force, we are able to measure how much shear thickening relies on 'soft' roughness.

In the tangent direction (i.e. tangent to the contacting surfaces), a frictional contact force is applied which opposes the tangential motion. This frictional contact force depends on a frictional coefficient, ν. If the normal force, $\boldsymbol{F}_{\text{stop}}$, is large, then the frictional contact force is allowed to increase so that it balances the tangential hydrodynamic force at the contact point: the particles therefore roll around each other. However, if the normal force is small, then the frictional force can only increase to have magnitude $|\nu\boldsymbol{F}_{\text{stop}}|$ and although it still opposes the tangential motion, the particles slip around each other.

This model has three parameters: the critical separation distance, which has typical values (Smart & Leighton, 1989)

$$10^{-3} \leqslant \frac{h}{(a_1+a_2)/2} \leqslant 10^{-2}, \tag{5.6}$$

the coefficient of friction, which has typical values (Zeng *et al.*, 1996)

$$0.1 \leqslant \nu \leqslant 0.4, \tag{5.7}$$

and the critical load, F_{crit}, which is used to set a timescale

$$T_{\text{crit}} = \frac{6\pi\mu a^2}{F_{\text{crit}}} \tag{5.8}$$

against which the shear rate will be made dimensionless.

Our implementation of this model is a refinement of that used in Wilson & Davis (2002, sec. 3.1.1), and works in the following way. An overview of the method is given in fig. 5.7.

Step 1. Find new approaching pairs of particles which are less than some critical radius apart.

Step 2. Find the normal forces $\boldsymbol{F}_{\text{stop}}$ required to stop each pair approaching. We do this in the following way, illustrated in fig. 5.4. In the case of two particles, labelled 1 and 2, the normal stopping force on particle 1 can be written

$$\boldsymbol{F}_{\text{stop}} = -F^{12}_{\text{stop}}\hat{\boldsymbol{n}}^{12}, \tag{5.9}$$

where $\hat{\boldsymbol{n}}^{12}$ is the unit normal between the particles at positions $\boldsymbol{r}^1$ and $\boldsymbol{r}^2$,

$$\hat{\boldsymbol{n}}^{12} = \frac{\boldsymbol{r}^2 - \boldsymbol{r}^1}{|\boldsymbol{r}^2 - \boldsymbol{r}^1|}. \tag{5.10}$$

An equal and opposite force, $-\boldsymbol{F}_{\text{stop}}$, is placed on particle 2. Furthermore, the criterion for stopping this pair approaching is that

$$(\boldsymbol{U}^2 - \boldsymbol{U}^1) \cdot \hat{\boldsymbol{n}}^{12} = 0. \tag{5.11}$$

We can then write the resistance formulation of this system as

$$\begin{pmatrix} \boldsymbol{F}^1 - F^{12}_{\text{stop}}\hat{\boldsymbol{n}}^{12} \\ \boldsymbol{F}^2 + F^{12}_{\text{stop}}\hat{\boldsymbol{n}}^{12} \\ \boldsymbol{T}^1 \\ \boldsymbol{T}^2 \\ \boldsymbol{S}^1 \\ \boldsymbol{S}^2 \end{pmatrix} = \mathcal{R} \begin{pmatrix} \boldsymbol{U}^1 - \boldsymbol{u}^\infty(\boldsymbol{x}^1) \\ \boldsymbol{U}^2 - \boldsymbol{u}^\infty(\boldsymbol{x}^2) \\ \boldsymbol{\Omega}^1 - \boldsymbol{\Omega}^\infty \\ \boldsymbol{\Omega}^2 - \boldsymbol{\Omega}^\infty \\ -\boldsymbol{E}^\infty \\ -\boldsymbol{E}^\infty \end{pmatrix}, \tag{5.12}$$

where $\boldsymbol{F}^1$ and $\boldsymbol{F}^2$ are other, non-frictional forces acting on the particles, and $\boldsymbol{u}^\infty(\boldsymbol{x})$ is the background velocity at each particle position,

$$\boldsymbol{u}^\infty(\boldsymbol{x}) = \boldsymbol{U}^\infty + \boldsymbol{\Omega}^\infty \times \boldsymbol{x} + \boldsymbol{E}^\infty \cdot \boldsymbol{x}. \tag{5.13}$$

Here, $\mathcal{R}$ is the normal Stokesian Dynamics grand resistance matrix, which includes the usual far-field and lubrication hydrodynamics, and so this equation is simply posing a typical Stokesian Dynamics problem.

We can combine eqs. (5.11) and (5.12) into one matrix equation:

$$\left(\begin{array}{c} \boldsymbol{F}^1 \\ \boldsymbol{F}^2 \\ \hline \hat{\boldsymbol{n}}^{12} \cdot [\boldsymbol{u}^\infty(\boldsymbol{x}^2) - \boldsymbol{u}^\infty(\boldsymbol{x}^1)] \end{array}\right) = \left(\begin{array}{cc|c} & & \hat{\boldsymbol{n}}^{12} \\ \multicolumn{2}{c|}{\mathcal{R}} & -\hat{\boldsymbol{n}}^{12} \\ \hline \hat{\boldsymbol{n}}^{12} & -\hat{\boldsymbol{n}}^{12} & 0 \end{array}\right) \left(\begin{array}{c} \boldsymbol{U}^1 - \boldsymbol{u}^\infty(\boldsymbol{x}^1) \\ \boldsymbol{U}^2 - \boldsymbol{u}^\infty(\boldsymbol{x}^2) \\ \hline F^{12}_{\text{stop}} \end{array}\right), \tag{5.14}$$

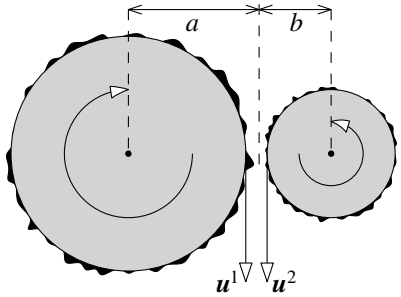

Figure 5.5: When particles roll past each other, the velocities at the contact point are equal.

where, for clarity, the torque and stresslet terms are omitted. An extra row and column is added to the resistance matrix for every near pair. For example, for three particles, where only 1–2 and 2–3 are close, we have

$$\left(\begin{array}{c} \boldsymbol{F}^1 \\ \boldsymbol{F}^2 \\ \boldsymbol{F}^3 \\ \hline \hat{\boldsymbol{n}}^{12}\cdot[\boldsymbol{u}^\infty(\boldsymbol{x}^2)-\boldsymbol{u}^\infty(\boldsymbol{x}^1)] \\ \hat{\boldsymbol{n}}^{23}\cdot[\boldsymbol{u}^\infty(\boldsymbol{x}^3)-\boldsymbol{u}^\infty(\boldsymbol{x}^2)] \end{array}\right) = \left(\begin{array}{ccc|cc} & \mathcal{R} & & \hat{\boldsymbol{n}}^{12} & \boldsymbol{0} \\ & & & -\hat{\boldsymbol{n}}^{12} & \hat{\boldsymbol{n}}^{23} \\ & & & \boldsymbol{0} & -\hat{\boldsymbol{n}}^{23} \\ \hline \hat{\boldsymbol{n}}^{12} & -\hat{\boldsymbol{n}}^{12} & \boldsymbol{0} & \multicolumn{2}{c}{\multirow{2}{*}{0}} \\ \boldsymbol{0} & \hat{\boldsymbol{n}}^{23} & -\hat{\boldsymbol{n}}^{23} & & \end{array}\right) \left(\begin{array}{c} \boldsymbol{U}^1-\boldsymbol{u}^\infty(\boldsymbol{x}^1) \\ \boldsymbol{U}^2-\boldsymbol{u}^\infty(\boldsymbol{x}^2) \\ \boldsymbol{U}^3-\boldsymbol{u}^\infty(\boldsymbol{x}^3) \\ \hline F^{12}_{\text{stop}} \\ F^{23}_{\text{stop}} \end{array}\right). \tag{5.15}$$

(Note that vectors in the top-right segment of the resistance matrix are column vectors, and those in the bottom-left segment are row vectors.)

Solving this in the usual Stokesian Dynamics way allows us to find the exact normal forces required to stop approaching particles.

Step 3. Check that the magnitudes of the stopping forces, F_{stop}, are all positive: those that come out negative represent pairs that are not actually approaching, and so can be removed from the list of approaching close particles. No force is added to these particles.

Step 4. For each remaining close pair of particles, apply the normal force, $\boldsymbol{F}_{\text{stop}}$, to stop the spheres approaching. Then test whether the normal stopping force exceeds a critical load value, $F_{\text{stop}} > F_{\text{crit}}$. In the style of Mari *et al.* (2014, sec. II.B.2), we stipulate that the normal force has to exceed this value for (tangential) friction to be activated. If the normal force is below this threshold, we add no (tangential) friction force and particles act under the normal force only, behaving as frictionless hard spheres as they slide past each other.

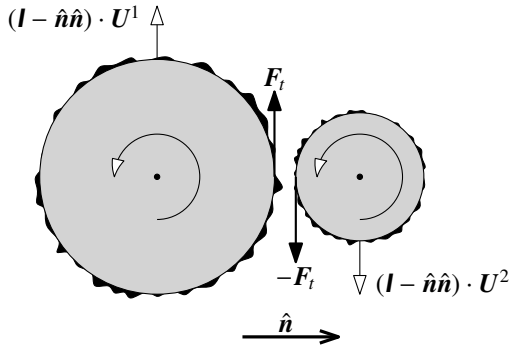

Figure 5.6: We can determine the tangential force required to set the contact velocity difference to zero by considering this small test case.

Step 5. For each remaining close pair of particles, where $F_{\text{stop}} > F_{\text{crit}}$, we will have both a normal contact force and a tangential friction force. We now need to determine whether the particles roll over or slip past each other. In this step we determine which tangential forces need applying to allow the particles to roll over each other. In the next step, we compare it with the normal force to determine which behaviour applies. Note that in the absence of friction, the presence of lubrication forces means that the motion will look fairly roll-dominated: this is demonstrated shortly.

Rolling occurs when the tangential velocities of the particles, at the point of contact, are equal to each other (see fig. 5.5). For spheres where the centre-to-contact distances are a and b, the tangential velocities on the surface are

$$\boldsymbol{u}^1 = (\boldsymbol{I} - \hat{\boldsymbol{n}}\hat{\boldsymbol{n}}) \cdot \boldsymbol{U}^1 + \boldsymbol{\Omega}^1 \times a\hat{\boldsymbol{n}}, \tag{5.16}$$

$$\boldsymbol{u}^2 = (\boldsymbol{I} - \hat{\boldsymbol{n}}\hat{\boldsymbol{n}}) \cdot \boldsymbol{U}^2 + \boldsymbol{\Omega}^2 \times (-b\hat{\boldsymbol{n}}). \tag{5.17}$$

Given that we want the particles to roll over each other, we need to exert a tangential force at the contact point to make these velocities equal. The current tangential velocity difference is

$$(\boldsymbol{I} - \hat{\boldsymbol{n}}\hat{\boldsymbol{n}}) \cdot (\boldsymbol{U}^2 - \boldsymbol{U}^1) - (a\boldsymbol{\Omega}^1 + b\boldsymbol{\Omega}^2) \times \hat{\boldsymbol{n}}. \tag{5.18}$$

By finding the tangential forces and torques associated with this velocity, we can apply these forces and torques in the opposite direction, thus making the velocities equal and letting the particles roll over each other.

We can calculate an approximation to this force by creating the mobility matrix for

the small test case shown in fig. 5.6. In particular, we want to solve

$$\begin{pmatrix} (\boldsymbol{I}-\hat{\boldsymbol{n}}\hat{\boldsymbol{n}})\cdot\boldsymbol{U}^1 \\ (\boldsymbol{I}-\hat{\boldsymbol{n}}\hat{\boldsymbol{n}})\cdot\boldsymbol{U}^2 \\ \boldsymbol{\Omega}^1 \\ \boldsymbol{\Omega}^2 \end{pmatrix} = \mathcal{M}\begin{pmatrix} \boldsymbol{F}_t \\ -\boldsymbol{F}_t \\ \hat{\boldsymbol{n}}a\times\boldsymbol{F}_t \\ \hat{\boldsymbol{n}}b\times\boldsymbol{F}_t \end{pmatrix}. \tag{5.19}$$

to find $\boldsymbol{F}_t$ in terms of eq. (5.18). Explicitly, excusing the abuse of notation, this equation is

$$\begin{pmatrix} (\boldsymbol{I}-\hat{\boldsymbol{n}}\hat{\boldsymbol{n}})\cdot\boldsymbol{U}^1 \\ (\boldsymbol{I}-\hat{\boldsymbol{n}}\hat{\boldsymbol{n}})\cdot\boldsymbol{U}^2 \\ \boldsymbol{\Omega}^1 \\ \boldsymbol{\Omega}^2 \end{pmatrix} = \begin{pmatrix} y_a^{11} & y_a^{12} & y_b^{11}\hat{\boldsymbol{n}}\times & -y_b^{21}\hat{\boldsymbol{n}}\times \\ y_a^{21} & y_a^{22} & y_b^{12}\hat{\boldsymbol{n}}\times & -y_b^{22}\hat{\boldsymbol{n}}\times \\ -y_b^{11}\hat{\boldsymbol{n}}\times & -y_b^{12}\hat{\boldsymbol{n}}\times & y_c^{11} & y_c^{12} \\ y_b^{21}\hat{\boldsymbol{n}}\times & y_b^{22}\hat{\boldsymbol{n}}\times & y_c^{21} & y_c^{22} \end{pmatrix}\begin{pmatrix} \boldsymbol{F}_t \\ -\boldsymbol{F}_t \\ \hat{\boldsymbol{n}}a\times\boldsymbol{F}_t \\ \hat{\boldsymbol{n}}b\times\boldsymbol{F}_t \end{pmatrix}, \tag{5.20}$$

where y_a^{11}, etc., are the mobility scalars introduced in chapter 2. Noting that $\hat{\boldsymbol{n}}\times(\hat{\boldsymbol{n}}\times\boldsymbol{F}_t) = -\boldsymbol{F}_t$, we can combine the four simultaneous equations in the matrix to show that

$$\begin{aligned}(\boldsymbol{I}-\hat{\boldsymbol{n}}\hat{\boldsymbol{n}})\cdot(\boldsymbol{U}^2-\boldsymbol{U}^1) - (a\boldsymbol{\Omega}^1+b\boldsymbol{\Omega}^2)\times\hat{\boldsymbol{n}} = \big[&-(y_a^{11}-y_a^{12}-y_a^{21}+y_a^{22}) \\ &+2(ay_b^{11}-ay_b^{12}+by_b^{21}-by_b^{22}) \\ &-(a^2y_c^{11}+aby_c^{12}+aby_c^{21}+b^2y_c^{22})\big]\,\boldsymbol{F}_t.\end{aligned} \tag{5.21}$$

This gives us the tangential component of the contact force acting on sphere 1: $\boldsymbol{F}_t$. For close spheres, these mobility scalars can be written in terms of the sphere surface separation distance, $\xi = 2r/(a+b)-2$ (Kim & Karrila, 2005, tables 11.17 and 11.21). In particular, for equal-sized spheres, $a = b$, this reduces the above equation to

$$\boldsymbol{F}_t = \frac{\pi\mu a(\ln\xi - 6.04 + 6.33/\ln\xi)}{1-4.69/\ln\xi}\left[(\boldsymbol{I}-\hat{\boldsymbol{n}}\hat{\boldsymbol{n}})\cdot(\boldsymbol{U}^2-\boldsymbol{U}^1) - a(\boldsymbol{\Omega}^1+\boldsymbol{\Omega}^2)\times\hat{\boldsymbol{n}}\right], \tag{5.22}$$

which matches Wilson & Davis (2002, eq. 3.2).

Step 6. Finally, we set the friction force to have magnitude

$$\min(F_t, \nu F_{\text{stop}}) \tag{5.23}$$

and to act in the tangential direction opposing the motion, i.e. parallel to $\boldsymbol{F}_t$.

As already mentioned, this algorithm is summarised in fig. 5.7.

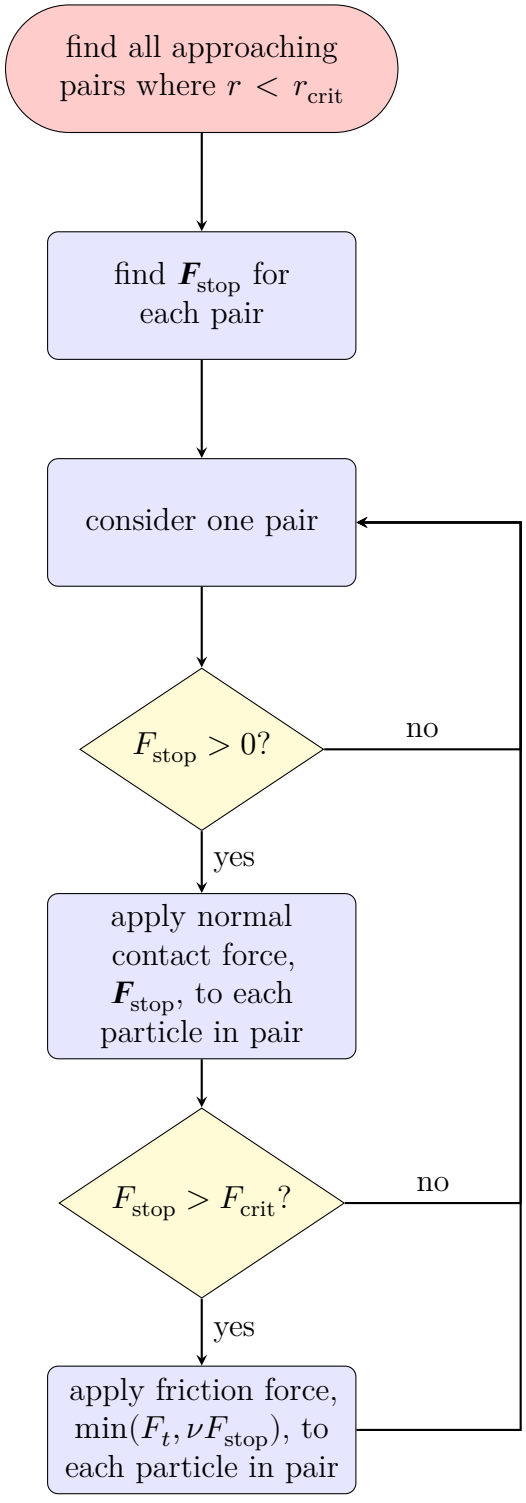

Figure 5.7: Overview of the friction algorithm

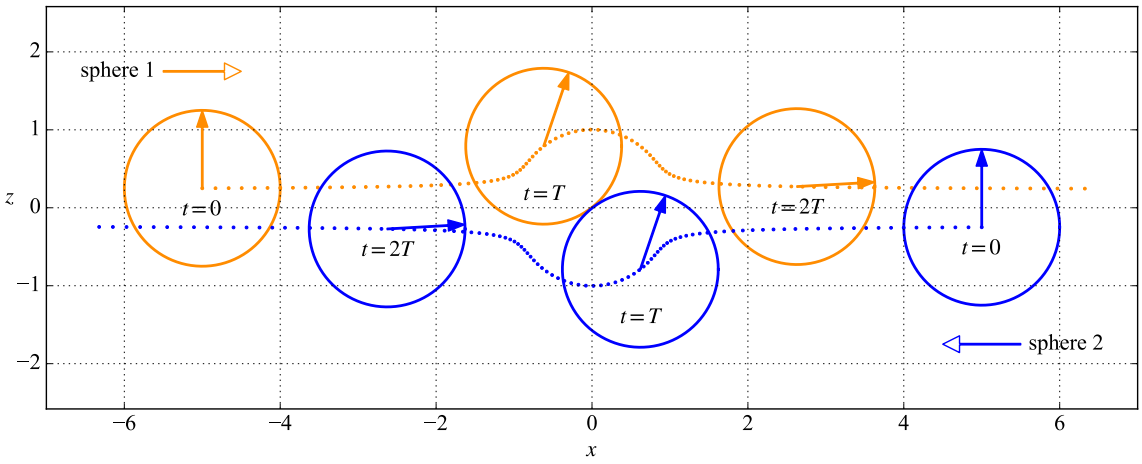

Figure 5.8: Passing equal-sized spheres interacting in the absence of contact. Note the symmetric behaviour. The circles indicate the position of the particle at three different times, $t = 0, T, 2T$. The arrows in the circles indicate the orientation of the particles, which always start upright. The dotted lines indicate the path of the particle centres and the dots are spaced at regular time intervals. Sphere 1 starts from the top-left and sphere 2 starts from the bottom-right.

5.3 Test cases

5.3.1 Two passing spheres, forced past each other

We now consider the motion of two passing spheres. Firstly, we consider particles with imposed external forces upon them, acting in quiescent fluid.

Two equal-sized spheres are set up as shown in fig. 5.8 ($t = 0$), at initial positions $(-5a, 0.25a)$ and $(5a, -0.25a)$, and are given horizontal forces $\hat{\boldsymbol{\imath}}$ and $-\hat{\boldsymbol{\imath}}$ so that they are set to collide. The paths of the particles are then marked in the figure by dotted lines (evenly spaced in time), and occasional drawings of the spheres with internal arrows mark the orientation of the particle at that point. The symmetry of the original configuration means that they meet at the origin in our coordinate system.

It is first worth noting the behaviour of the approaching particles in the absence of contact forces entirely, shown in fig. 5.8. Some notable features here are the symmetry of the particle paths—to be expected from reversible Stokes flow—and the almost 90° rotation of the particles following their interaction.

Contact is added in fig. 5.9, which we implement once particles are a small distance apart. In subfigure (b), the coefficient of friction is small at $\nu = 0.1$, so although a normal force keeps the particles that small distance apart, the tangential frictional force is small and we expect mostly slipping behaviour. Two key observations here are the lack of fore–aft symmetry in the particle paths—a feature strongly observed in experiments—and the reduced rotation—about 60°—of the particles after their

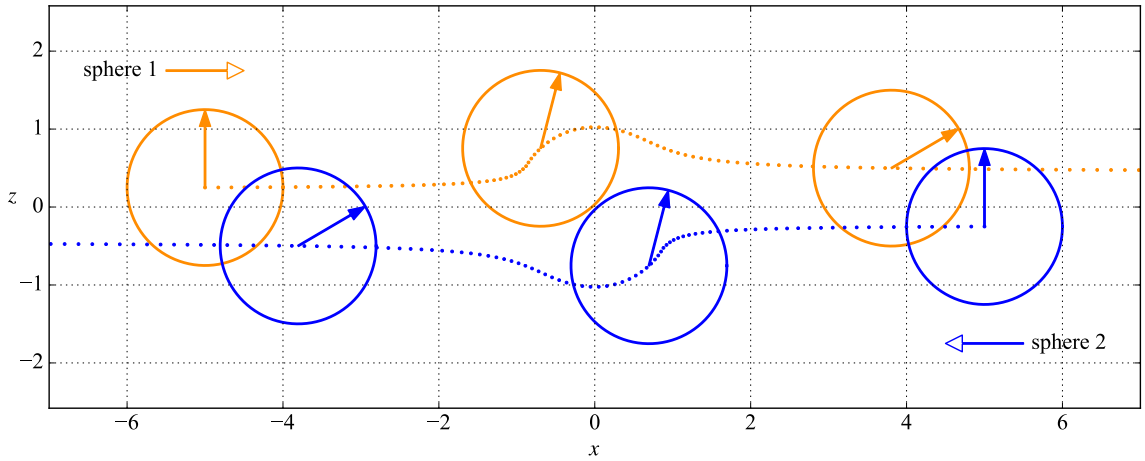

(a) Passing equal-sized spheres with only the normal contact force applied.

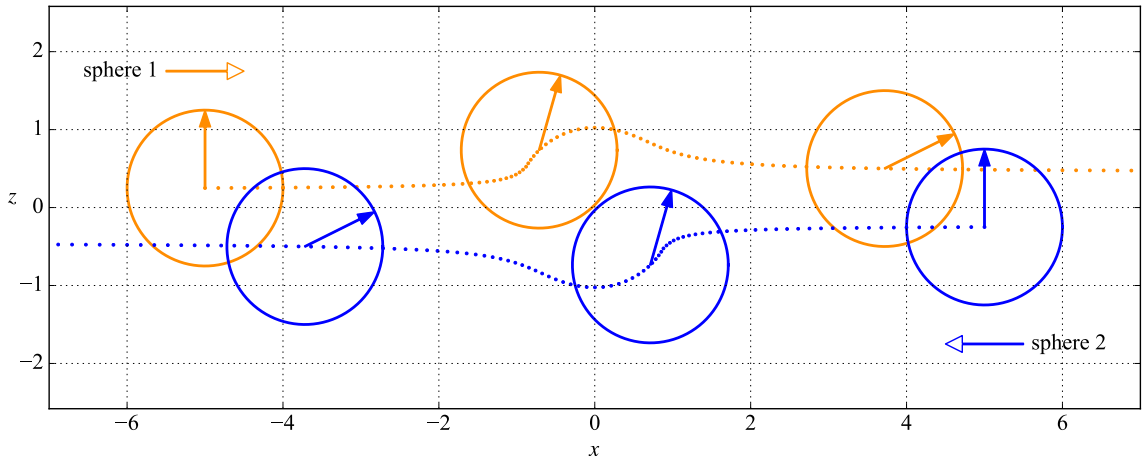

(b) Passing equal-sized spheres with a small coefficient of friction, leading to slipping.

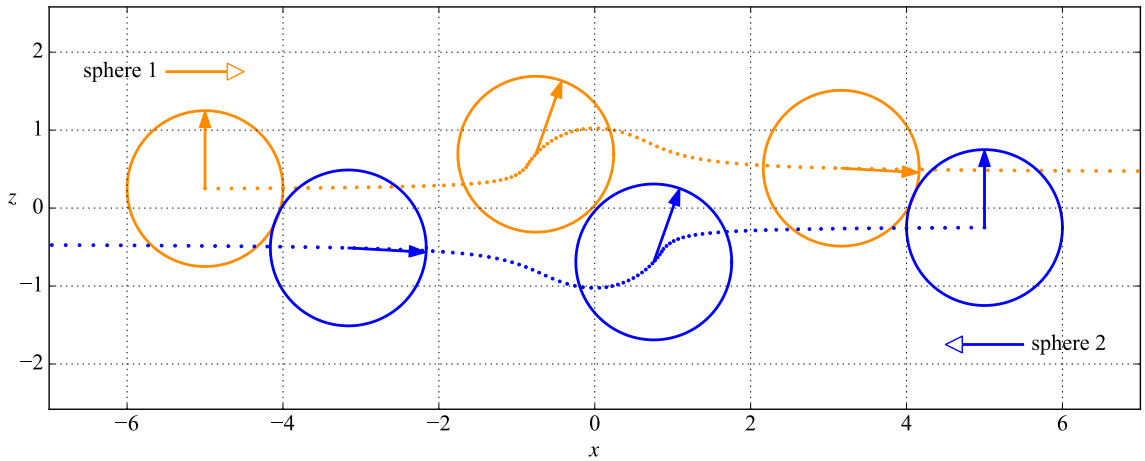

(c) Passing equal-sized spheres with a high coefficient of friction, leading to rolling.

Figure 5.9: Equal-sized spheres pass each other under different friction laws. The circles indicating the position of the particle at three different times are placed at the same time in all three cases and in fig. 5.8. Friction is set to act when the centre-to-centre distance is less than $2.05a$ (an exaggerated value here for effect).

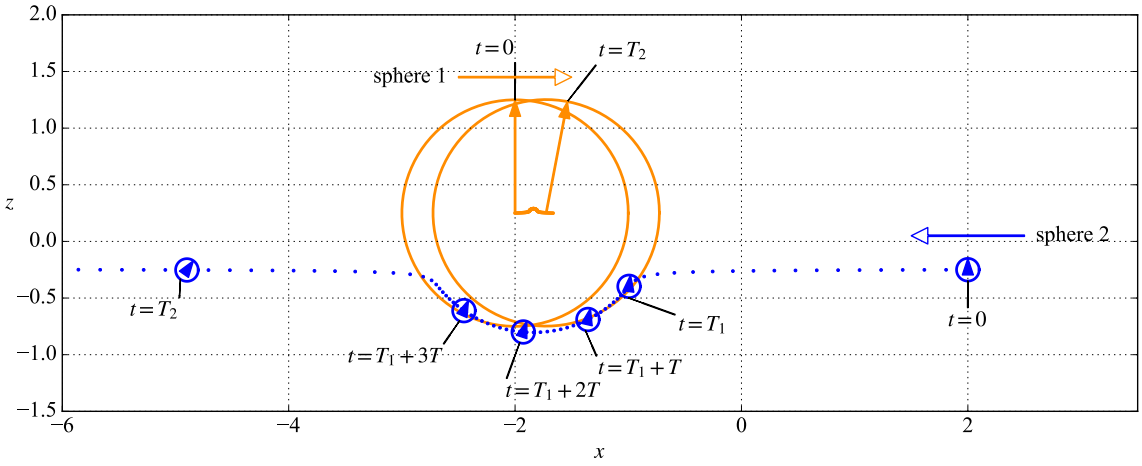

Figure 5.10: One large sphere and one small sphere (size ratio 1 : 10) pass each other in the absence of friction. Note the symmetric behaviour. The circles indicate the position of the particle at different times.

interaction. Indeed, comparison with subfigure (a), in which only the normal contact force is applied, demonstrates that the motion of the particles in the slip case is almost entirely dependent on this normal force. In particular, the reduced rotation when compared to the non-contact case is due to the roughness height: particles which are further apart experience reduced lubrication forces. We also see that the particles travel further in fig. 5.9(a) than they do without contact forces in fig. 5.8.

Subfigure (c) shows the rolling regime when there is a high coefficient of friction ($\nu = 0.5$) between the particles. Again we see the asymmetry in the fore–aft particle paths, but we also see a 90° rotation of the particle: the same rotation as seen in the non-contact case, which has this time not been reduced by the particle roughness height.

As mentioned at the beginning of the chapter, experimental solutions are rarely completely monodisperse, so we also examine polydisperse solutions. We show the behaviour of two very differently sized particles passing each other under various friction regimes in figs. 5.10 and 5.11. First, fig. 5.10 shows the non-contact regime. One large ($a = 1$) and one small ($a = 0.1$) particle are placed as shown in the figure ($t = 0$), with initial positions $(-2, 0.25)$ and $(2, -0.25)$, and are given horizontal external forces $\hat{\boldsymbol{\imath}}$ and $-\hat{\boldsymbol{\imath}}$ respectively, so that they are set to collide. As we saw in the equisized non-contact case, the trajectories of the particles are fore–aft symmetric.

The three different frictional cases are again considered in fig. 5.11. Subfigure (a) again shows the trajectories of the particles with only the normal contact force applied, which breaks the fore–aft symmetry. Subfigure (b) adds the tangential friction force but with a small coefficient of friction, leading to slipping, and subfigure (c) does the same but with a high coefficient of friction, leading to a clear rolling regime.

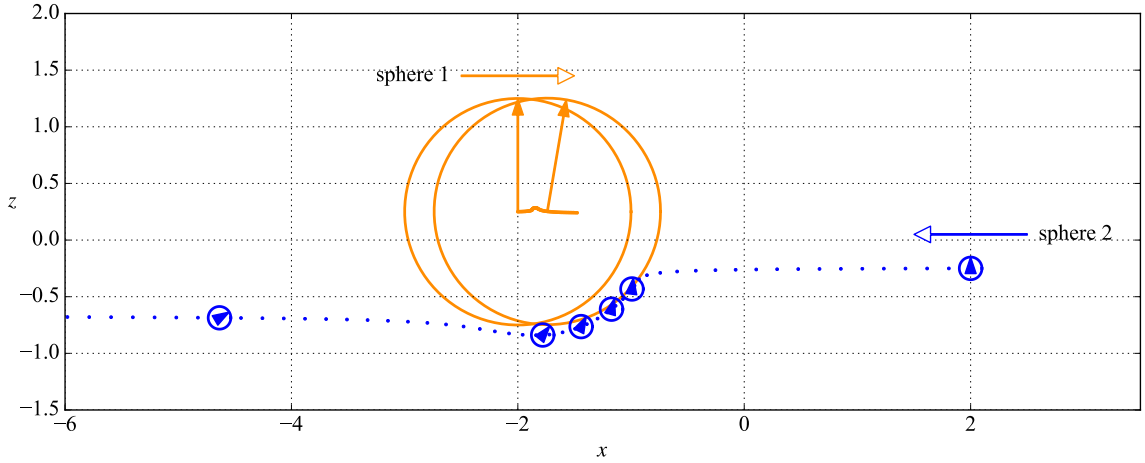

(a) Passing differently-sized spheres with only the normal contact force applied.

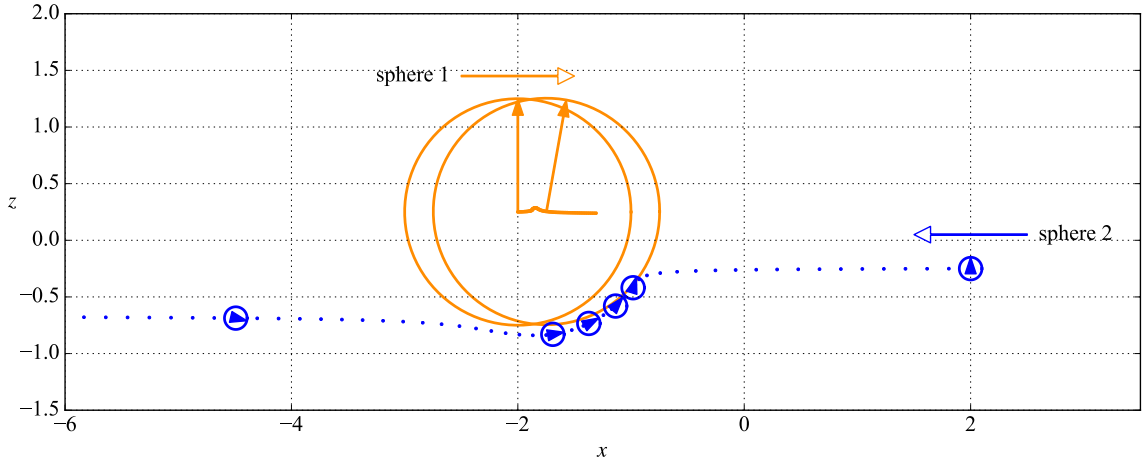

(b) Passing differently-sized spheres with a small coefficient of friction, leading to slipping.

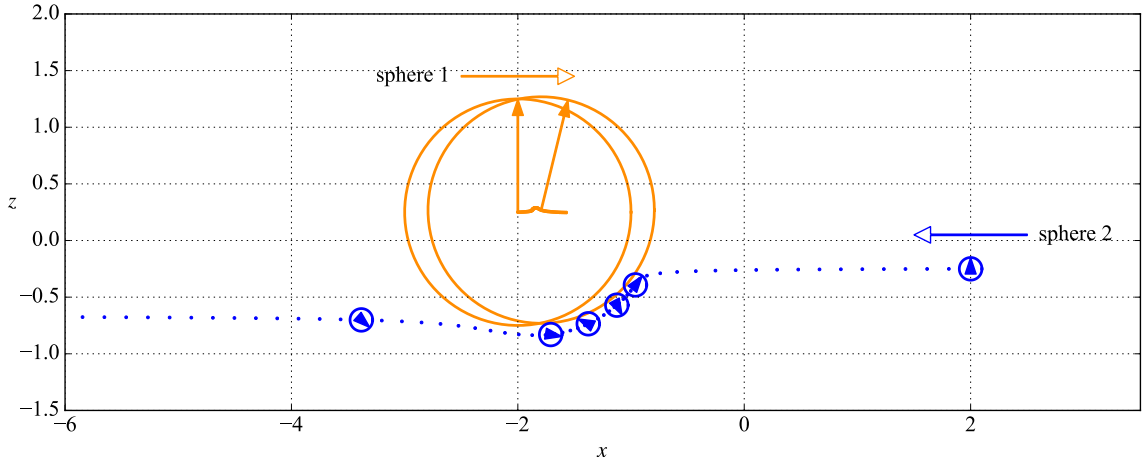

(c) Passing differently-sized spheres with a high coefficient of friction, leading to rolling.

Figure 5.11: Differently-sized spheres with size ratio $1:10$ pass each other under different friction laws. Friction is set to act when the centre-to-centre distance is less than $2.05\overline{a}$ (an exaggerated value here for effect), where $\overline{a}$ is the average particle size.

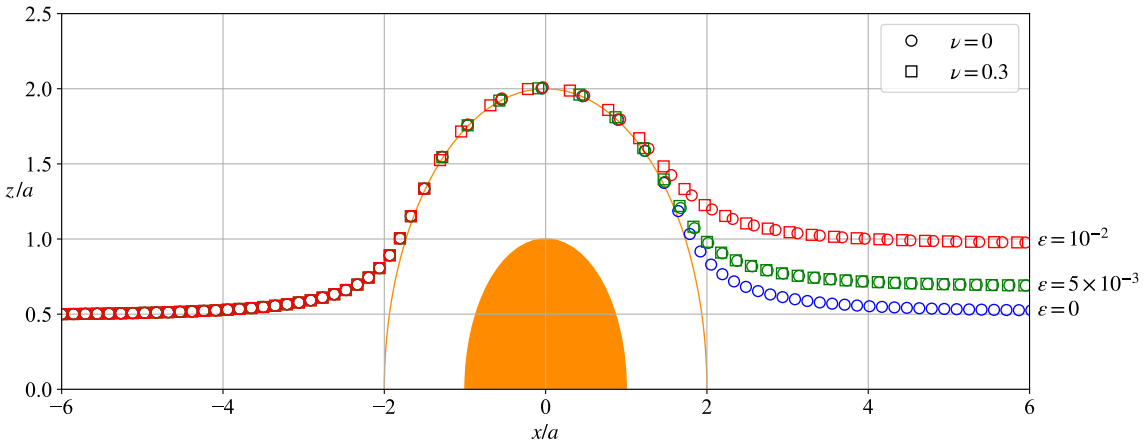

Figure 5.12: Relative trajectories of two equal-sized spheres passing each other under shear flow. Cases are considered where the particles have different dimensionless roughness heights, $\varepsilon = 0$, 5×10^{-3} and 10^{-2} and different coefficients of friction, $\nu = 0$ and 0.3. The z-axis is stretched for clarity and the simulations use a timestep $\Delta t = 10^{-3}/\dot{\gamma}$.

5.3.2 Two passing spheres in shear flow

We also consider the subtly different case of two spheres passing each other due to an imposed shear flow. This test case is inspired by Gallier *et al.* (2014*b*, fig. 3). As in section 5.3.1, two particles are freely suspended diagonally across from each other, centred at the origin and this time separated by a vector distance $(-6a, 0.5a)$. An xz-shear flow is then applied with shear rate $\dot{\gamma}$ about the origin, moving the particles towards each other so that they interact.

The relative trajectories of the particles in the shear plane are shown in fig. 5.12. The reference particle is shaded at the origin, and the outer orange circle shows the nearest possible approach of two particles of radius a. The figure shows the trajectories for particles with different dimensionless roughness, $\varepsilon = h/a$, for different coefficients of friction, ν.

The smooth case, $\varepsilon = 0$, corresponds again to smooth spheres, and as already discussed, we see the symmetric trajectory expected from Stokes flow. Increasing the roughness height reduces the closest approach of the passing particles, but only when the particles are approaching. The normal contact force acts to break this symmetry, leading to the same fore–aft asymmetry we have already seen. Given that it only acts tangentially, the addition of friction (squares vs circles) does not change the particle trajectory, although we can see in the largest roughness height that the interaction with friction is a little slower.

This figure shows qualitatively very good agreement with Gallier *et al.* (2014*b*, fig. 3), but note that since they use a different contact model ('DEM-like', from granular particle theory (Pöschel & Schwager, 2005)), we do not expect exact matching.

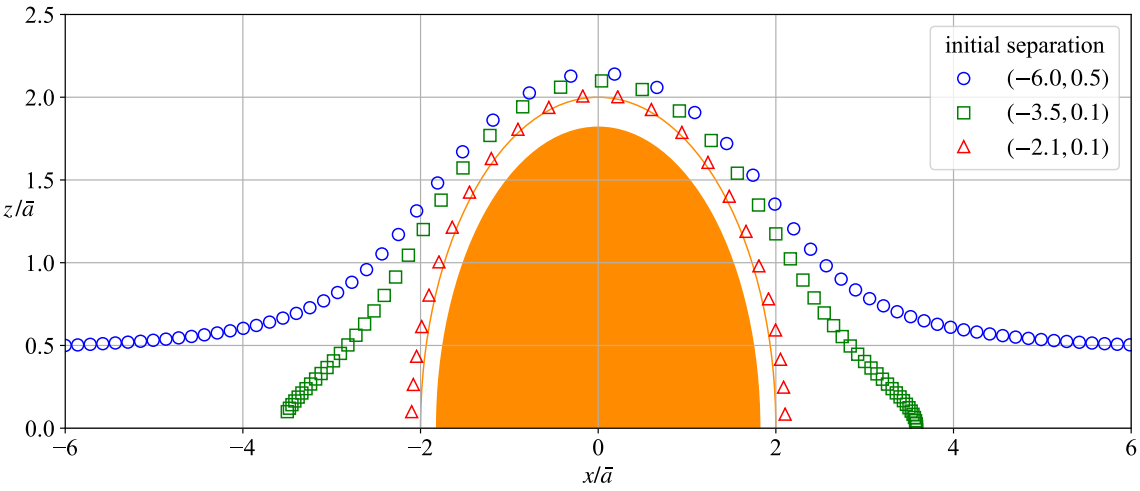

Figure 5.13: Relative trajectories of two spheres with size ratio $1:10$ passing each other under shear flow. Dimensions are scaled on the average particle size, $\overline{a} = (a_1 + a_2)/2$. None of these trajectories lead to contact, as the rotation of the large sphere in the shear flow deflects the small particle at all but the smallest separations. The z-axis is stretched for clarity and the simulations use a timestep $\Delta t = 10^{-3}/\dot{\gamma}$.

We run a similar test with unequal spheres, although with a size ratio of $1:10$, we find that the spheres do not come into contact unless initially they are almost touching. Figure 5.13 shows the relative trajectories of two unequal spheres, starting at different scaled separations, $(-6\overline{a}, 0.5\overline{a})$, $(-3.5\overline{a}, 0.1\overline{a})$ and $(-2.1\overline{a}, 0.1\overline{a})$, where $\overline{a}$ is the average particle size. In this figure, the large particle is the reference particle in solid orange and once again the outer orange ring represents the nearest possible approach. Essentially, the rotation of the large particle in the shear flow deflects the small particle at all but the smallest separation. For this reason, we do not consider this test case any further.

5.4 Measuring shear-thickening in suspension

The following sections concern the viscosity of monolayers of spheres. We measure the stress contribution from the particles in the system in the same manner as in eq. (3.27). That is to say, the stress contribution per unit monolayer volume is

$$\sigma_{ij} = \frac{1}{V} \sum_{\alpha} S_{ij}^{\alpha}, \tag{5.24}$$

where $\boldsymbol{S}^{\alpha}$ are the stresslets of the particles, α, and the volume of the (monolayer) sample box is V.

The stresslets are linear in the background viscosity, μ, so any change to the background viscosity—for example, time dependence or temperature—leads to a propor-

tional change in the stress contribution.

As shown in fig. 5.1, we observe shear-thickening when the effective viscosity, η, of a suspension increases as the shear rate, $\dot{\gamma}$, is increased. Since the effective viscosity is defined in shear flow as $\eta = \sigma/\dot{\gamma}$, we can observe whether the system shear-thickens by plotting the dimensionless mean viscosity against the dimensionless shear rate,

$$\frac{\eta}{\mu} = \frac{\sigma}{\mu\dot{\gamma}} \qquad \text{against} \qquad \dot{\Gamma} = \dot{\gamma}T_{\text{crit}} = \frac{6\pi\mu\dot{\gamma}a^2}{F_{\text{crit}}}. \tag{5.25}$$

Here, μ is the viscosity of the suspending medium. The dimensionless shear rate, notated $\dot{\Gamma}$ to match the literature, is analogous to the Péclet number, which measures the ratio of the rate of advection by the flow to to the rate of diffusion. Shear thickening has been seen to occur for $\dot{\Gamma}$ above 10^{-1} (Gallier *et al.*, 2014*b*). Here we consider shear rates in the region $10^0 < \dot{\Gamma} < 10^2$.

A lower bound for the dimensionless effective viscosity is given by the dilute limit of $1 + 5c/3$, where c is the particle area concentration. To see this, note, as mentioned after eq. (3.27), that for a monolayer of N identical spheres (i.e. with depth $2a$), the area concentration is given by

$$c = \frac{2\pi a^3 N}{V}. \tag{5.26}$$

Then if we consider the spheres to be sufficiently far apart so as to be essentially isolated, we know from Faxén's third law, eq. (2.45c), that for one isolated sphere,

$$S_{ij} = -\frac{20}{3}\pi\mu a^3 E^{\infty}_{ij}. \tag{5.27}$$

Setting a continuous shear, $E_{12} = E_{21} = -\dot{\gamma}/2$, the stress contribution from this isolated particle in the shear plane, $\sigma = \sigma_{12}$, is therefore

$$\sigma = \frac{1}{V}S_{12} = \frac{c}{2\pi a^3 N}\left(\frac{10}{3}\pi\mu a^3\dot{\gamma}\right) = \frac{\mu\dot{\gamma}}{N}\left(\frac{5c}{3}\right). \tag{5.28}$$

For N such spheres we therefore have the dimensionless viscosity contribution

$$\frac{\eta}{\mu} = \frac{\sigma}{\mu\dot{\gamma}} = \frac{5c}{3}. \tag{5.29}$$

This is the monolayer analogue of the dilute viscosity contribution given by Einstein (1906) and in eq. (5.1), where in full 3D this term is instead $5c/2$.

We now perform some SD simulations for various parameters. In each case, we shear the suspension for five shear units, which we will see is sufficient for the system to equilibrate. We then take the final three shear units and average the viscosity measurement. This is done for either two or three different initial conditions, and

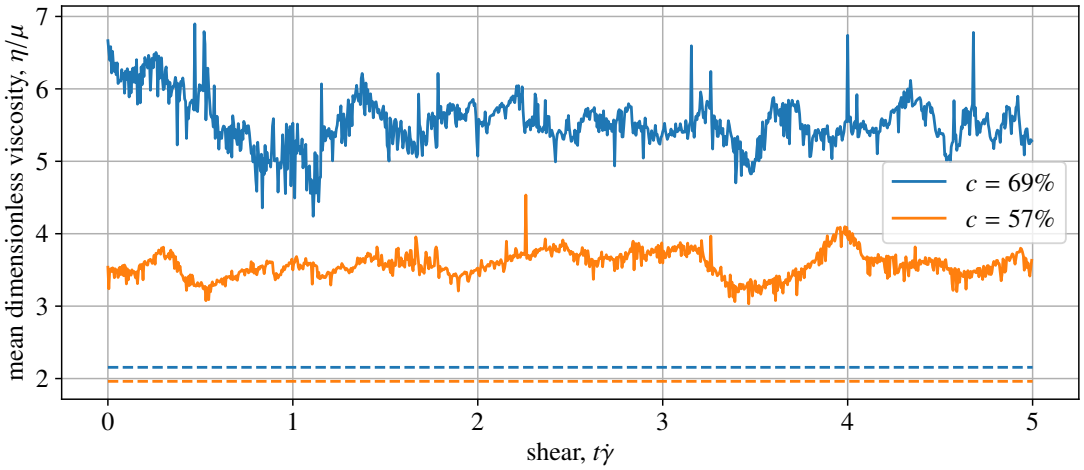

Figure 5.14: Dimensionless viscosity for the monodisperse system with two different concentrations at a given shear rate, measured over five shear units. The mean value over the final three shear units is used as the single data point in the next graph. Here the friction coefficient is $\nu = 0.3$, roughness height $h = 0.01a$, timestep $\Delta t = 5 \times 10^{-3}\dot{\gamma}^{-1}$ and the dimensionless shear rate is $\dot{\Gamma} = 6\pi$. The dashed lines represent the dilute viscosity limit for each concentration, $1 + 5c/3$.

the measurements averaged. This gives us one data point on the viscosity–shear rate graph for a particular set of parameters.

These tests are all performed under continuous shear. The requirement of the first two shear units to allow the system to equilibrate means that oscillatory shear tests, where the amplitudes are typically much smaller than two shear units, produce mostly noise.

Effect of concentration To illustrate the measurement of the viscosity in the system for a given shear rate, fig. 5.14 shows the dimensionless viscosity for two different concentrations of suspension at a given shear rate over five shear units. Initially, as the system equilibrates, there is considerable movement in the measurement, particularly at higher concentrations. After the first one or two shear units, the measurements are relatively stable, and so we can take the mean value of the viscosity as representative of that set of parameters.

These data points are collected in fig. 5.15, which measures the mean dimensionless viscosity for monolayer suspensions with increasing particle concentration. For all but the highest concentration, the system is formed of 90 identical particles in a square periodic domain; the highest concentration uses 420. (This is discussed shortly, under 'Effect of periodic cell size'.) The friction coefficient is set at the reasonable value of $\nu = 0.3$ and the timestep is $\Delta t = 5 \times 10^{-3}/\dot{\gamma}$.

At low-to-medium concentrations, we see almost no change in the viscosity. At

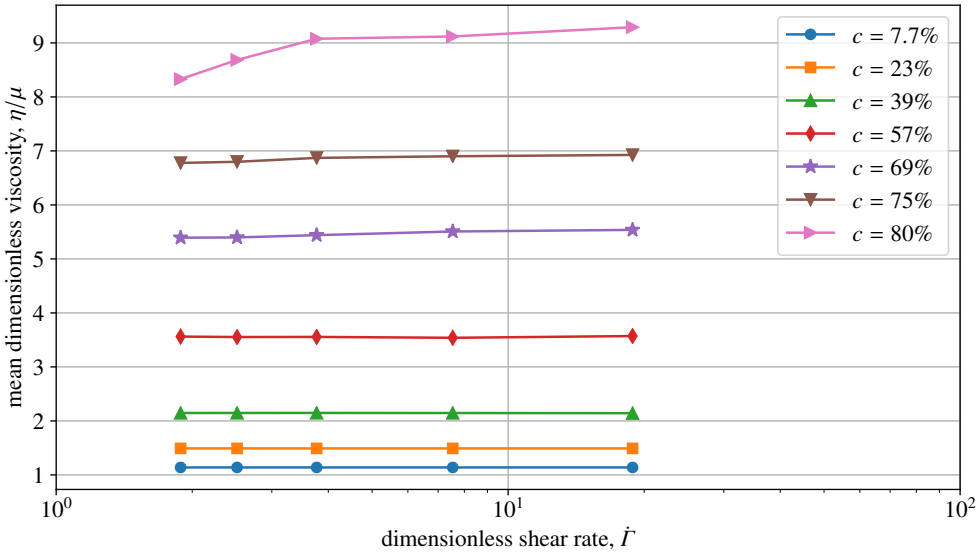

Figure 5.15: Dependence of the dimensionless viscosity on dimensionless shear rate at different values of the area fraction, c. At concentrations up to 69% we use full Stokesian Dynamics with 90 particles; at 75% we use 98 particles; and at the highest concentration we use the '$\mathcal{M}^{\infty}$-off' approximation to allow us to use more particles. The model parameters are $h = 0.01a$ and $\nu = 0.3$.

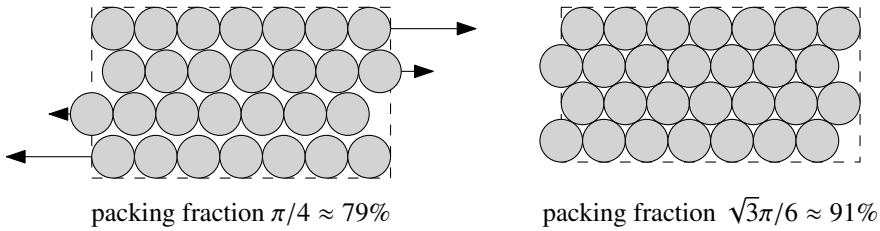

Figure 5.16: Packing fractions below 79% allow for particles to shear past each other without bumping. When packing fractions approach 91%, the system jams completely.

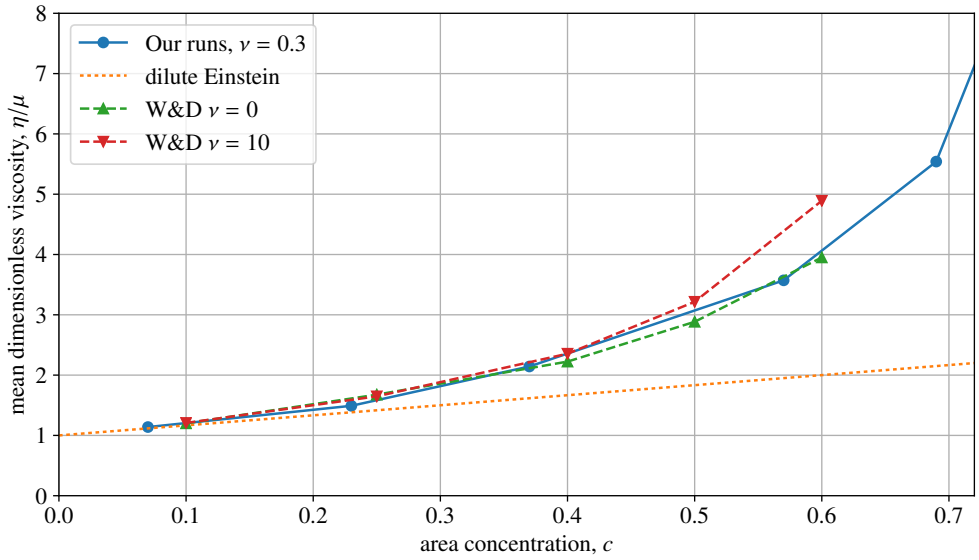

Figure 5.17: Dimensionless viscosity for the monodisperse system for different concentrations, c. We compare our measurements at at a shear rate of $\dot{\Gamma} = 0.6\pi$ and model parameters $\nu = 0.3$ and $h = 0.01a$ with the measurements from Wilson & Davis (2002) (marked 'W&D') and the dilute Einstein limit of $1 + 5c/3$. Note that the W&D results are indicated as compromised by a coding error as described in Wilson & Davis (2017), but the corrigendum reports that the effect on the viscosity is minor.

69% concentration we see a 3% increase, but at 80%, we see a 20% increase in additional viscosity over our range of shear rates. This highest area concentration is just above the square-packing fraction for circles, $\pi/4 \approx 79\%$. Square-packing—see fig. 5.16—marks the highest concentration where particles can slide past each other (in rows) without having to bump past each other. Systems with higher concentrations necessarily, then, see some form of jamming: the phenomenon where particles lock together and act together as a single object. This may be global, where the whole system locks into place, or it may be local, where certain bands of particles jam (perhaps at the edges) but leave a freely-flowing channel. Stokesian Dynamics is not particularly well-suited to modelling jammed systems, so we only consider concentrations as high as seen here.

For validation, we compare our viscosity readings in fig. 5.17 with existing results in the literature. We find good agreement, although our results are slightly lower. This is what we expect, given the increased particle separation in our model.

Effect of 'turning off' $\mathcal{M}^\infty$ As discussed in section 2.8, in concentrated monodisperse systems, it is common to neglect the far-field or many-body effects by 'turning off' the far-field mobility matrix $\mathcal{M}^\infty$. It is replaced by a diagonal self-term-only matrix which contains only the leading terms of the pair hydrodynamic interactions. This speeds up calculation significantly, but can have an effect on ac-

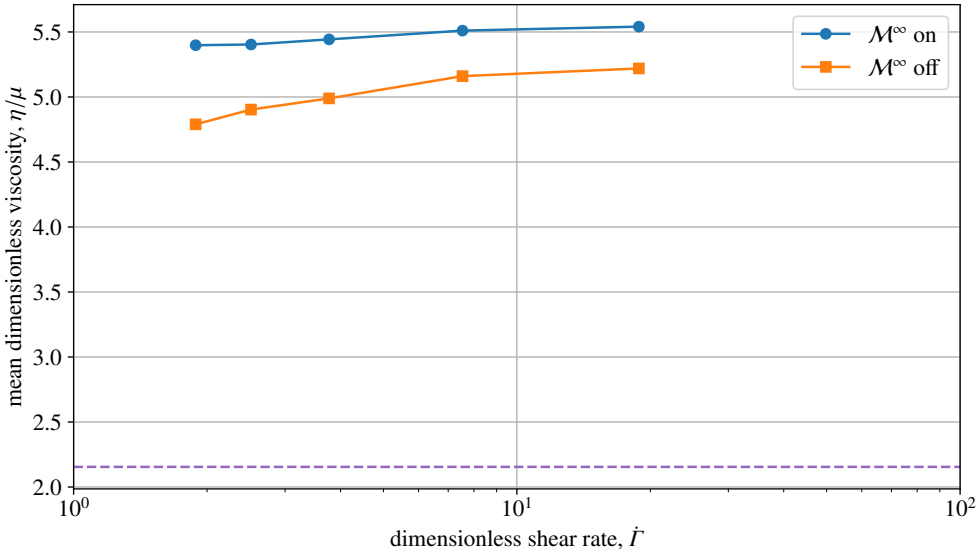

Figure 5.18: Comparison of the viscosity calculated with the full far-field mobility matrix $\mathcal{M}^\infty$ ('on') and with a diagonal approximation ('off'). Simulations of 90 spheres at $\nu = 0.3$, $h = 0.01a$ and $c = 69.3\%$. The dashed line represents the dilute viscosity limit, $1 + 5c/3$

curacy (Ball & Melrose, 1997). The tests in this section use the full $\mathcal{M}^\infty$ for systems up to 100 particles, and the approximation for larger systems. The discrepancy in readings between an 'on' and 'off' simulation for 90 spheres is shown in fig. 5.18.

The readings with $\mathcal{M}^\infty$ 'on' are 5–15% higher than with this matrix 'turned off', but the readings are qualitatively similar. Both exhibit shear thickening, although the effect is weaker in the more accurate 'on' readings. Given the popularity of this approximation, as discussed in section 2.8, it is useful to know that viscosity readings from this method will be qualitatively similar, but slightly underestimated.

Effect of periodic cell size In the concentration test, for concentrations up to 69%, we used a system of 90 particles with a full $\mathcal{M}^\infty$ simulation. For the most concentrated test at 80%, we used a larger system of 420 particles, with the $\mathcal{M}^\infty$ approximation. We now explain these choices.

Figure 5.19 shows viscosity readings, with the $\mathcal{M}^\infty$ approximation turned on for the sake of computation speed, for larger periodic systems, while maintaining the concentration. As we saw from the concentration sweep that all but the highest two concentrations give a mostly flat viscosity profile, we check the effect of changing the size of the periodic cell for the higher two concentrations: $c = 69\%$ and 80%. For both concentrations, the results are roughly equivalent and all cases see shear thickening.

At the lower of the two concentrations, the smaller system is clearly sufficient, with

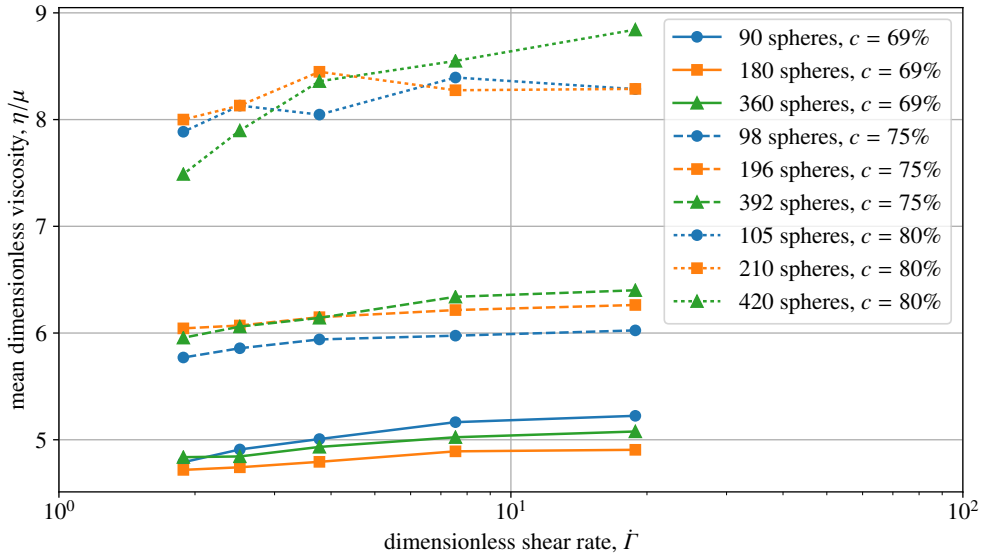

Figure 5.19: The effect of system size. Model parameters $\nu = 0.3$, $h = 0.01a$, and we are using the '$\mathcal{M}^\infty$-off' approximation to save computation time. At the highest concentration, box size effects are important; at $c = 69\%$, 90 particles will suffice and at $c = 75\%$, we use 98 particles.

discrepancies coming from the local behaviour of the particles but otherwise presenting a similar profile to the larger systems. However, at the extreme concentration of 80%, the measurements are unreliable in small systems. Larger numbers of particles are required to measure the viscosity sufficiently. For this reason, in tests in this section, concentrations of 80% are represented by larger periodic cells.

Effect of friction coefficient Figure 5.20 shows the viscosity profiles for four reasonable friction coefficients, $\nu = 0.1$, 0.2, 0.3, 0.4, and for no friction. The concentration is set at $c = 69.3\%$ and we use a periodic cell of 90 particles. At low shear rates, the viscosity readings are similar, and past the lowest shear rates, all frictional systems see shear thickening as the shear rate increases. Increasing the friction coefficient leads to greater shear thickening but the increase is small—only 3% in the greatest case.

Effect of timestep All our measurements use a standard timestep resolution of $\Delta t = 0.005/\dot{\gamma}$, i.e. 200 timesteps per shear unit. Figure 5.21 shows the effect on our measurements of changing the timestep. The larger timestep of $0.025/\dot{\gamma}$ under RK4 timestepping is not sufficiently small to capture any shear-thickening effects. We find by decreasing the timestep to $0.001/\dot{\gamma}$ that our timestep choice of $0.005/\dot{\gamma}$ systematically overestimates the viscosity by about 5%, although there is otherwise good agreement on the shape of the graph. This compromise is deemed acceptable, given the computation time saved.

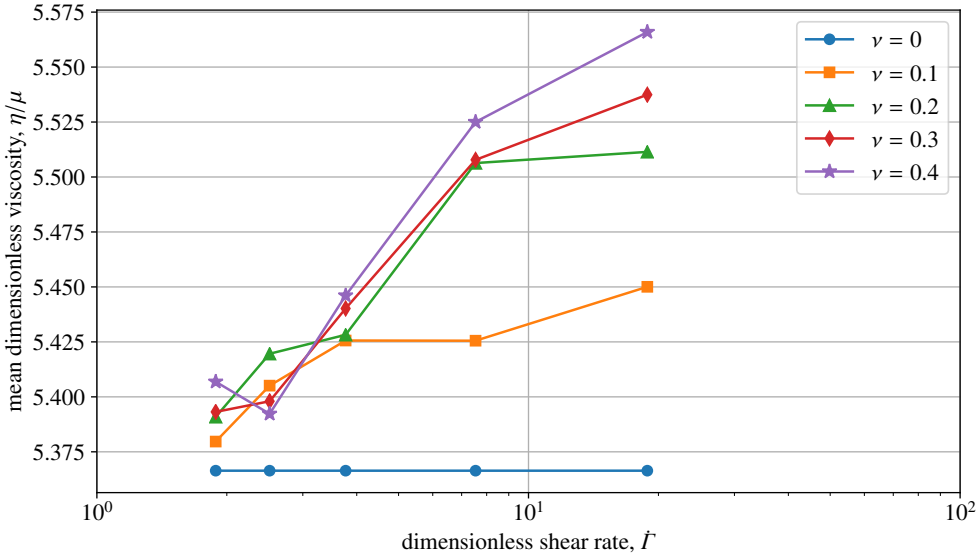

Figure 5.20: The effect of varying the friction coefficient, ν. Plot of the mean steady viscosity for the monodisperse system where the concentration is set at $c = 69.3\%$, the roughness height is $h = 0.01a$, and we use a periodic cell of 90 particles.

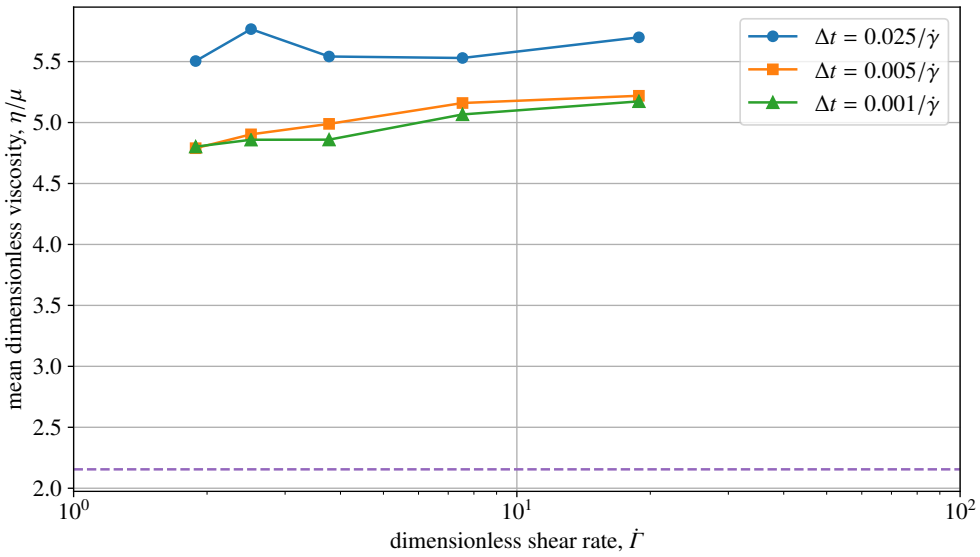

Figure 5.21: The effect of varying the timestep, Δt. Plot of the mean steady viscosity with model parameters $\nu = 0.3$, $h = 0.01a$, and a periodic box containing 90 spheres at an area fraction of 69.3%. A timestep $\Delta t = 0.025\dot{\gamma}^{-1}$ is too large to make meaningful predictions; but the marginal gain in accuracy by reducing from $\Delta t = 0.005\dot{\gamma}^{-1}$ to $\Delta t = 0.001\dot{\gamma}^{-1}$ does not merit the extra computational effort involved. The dashed line again shows the dilute limit.

5.5 Conclusions

For the first time, we have implemented here an accurate model for frictional contact: one where particles truly stop approaching after reaching a critical separation value, instead of simply being repelled by a spring-type repulsion force. We have shown that, at high enough particle concentrations, this frictional contact model can lead to shear-thickening behaviour in suspensions. We have also confirmed that increasing the frictional coefficient leads to increased shear thickening, but only by small amounts.

We have also tested the parameters of the simulation method. In particular, we have seen that only a few units of shear are required in monolayer suspensions for the particles to equilibrate before we can take viscosity readings. We have tested the number of particles required to ensure reliable measurements, and we have quantified the efficacy of neglecting the far-field mobility matrix in the Stokesian Dynamics formulation.

Of notice was how this implementation of a true stopping force leads to only continuous shear thickening, instead of the dramatic viscosity jumps seen in discontinuous shear thickening. We are therefore led to conclude that *compressive* particle roughness, modelled by the repulsion forces in the literature, is an important part of the discontinuous shear thickening model. This seems to be a likely source of the energy dissipation which is reflected in discontinuous shear thickening: that under high shear, particles approach closer than the roughness height, and experience high repulsion forces. These particles require more energy from the imposed shear in order to pass each other, and this is reflected in the viscosity measurements taken of the suspension.

This is not the only possible mechanism at the particle scale. Under sufficiently high pressures, the particle asperities may melt. The contacting particles would then maintain contact until they overcome a critical force to separate. This critical force would be considerably larger than those used in our current model, and particles would remain in contact for longer periods as they are fused together.

A similar pressure-based argument involves cavitation bubbles (Yu *et al.*, 1995). Under sufficiently low pressures at contact, voids may form in the background fluid. These cavitation bubbles that form could cause suction behind particles which also would require a critical force to separate.

Both of these mechanisms involve much larger irreversible actions than in our current model, but could explain the dissipation required for discontinuous shear thickening. A contact model could be developed for the melting mechanism using the Stokesian

Dynamics framework we have developed; the cavitation bubble mechanism requiring a more sophisticated technique.

Chapter 6

Conclusions and further work

This thesis introduced the numerical simulation technique of Stokesian Dynamics for modelling the behaviour of particle systems. It gave a full description of the method, and then extended it to include non-Newtonian effects. It then conducted three studies using this method: one validating our extension, one investigating an interesting experimental result, and one on the currently very active research area of shear thickening.

In chapter 2, *Stokesian Dynamics*, we gave a complete and thorough recipe for implementing SD on both finite and periodic domains. All the results in the thesis came from our own implementation of SD, written mostly in Python, which uses the derivations in this chapter. This provided an independent implementation of the method from the few existing pieces of software in the community. Having shown that our implementation matches existing results, we extended SD to include differently-sized spheres. Before we used this extension, we gave a warning for the use of a common approximation in SD which can fail with large sphere size differences.

Natural further work in the implementation of SD would be to incorporate parallelisation, an important technique for scientific computing, having come up against natural restrictions on processor speeds. As discussed in chapter 2, we have avoided doing so in this thesis because the main bottleneck in SD is solving a dense matrix equation: an operation which is not parallelisable. However, there are places where it could be useful: filling the dense matrix, for example. Perhaps the natural next step, to gain the greatest time saving, would be to integrate parallel processing into the timestepping scheme, even with a conventional scheme such as RK4, by computing intermediate steps mostly simultaneously. Making greater use of Cython subroutines would also give speed increases in this area. Although we found that it did not give us time savings, combining the aforementioned with an accelerated SD scheme as discussed in this chapter, therefore avoiding the bottleneck, could also

help.

Having extended SD to include differently-sized spheres, we incorporated a simple model of viscoelasticity by using small spheres as 'beads' in bead–spring dumbbells. We started chapter 3, *Oscillatory rheometry*, by testing various methods of performing rheometry on our suspension. We found that the most effective method was to apply a background shear and measure the resulting stress in the system through the sum of the stresslets in the fluid. We then tested different spring laws in shear, showing the ease of doing so using our method, and compared their rheological behaviour to continuum constitutive models. We demonstrated that the addition of the dumbbells produced viscoelastic results; in particular, that Oldroyd-B behaviour was observed under small-amplitude shear. Under large-amplitude shear, we found that our dumbbell suspension exhibited strain-thinning behaviour. We established measures for the nonlinearity of the suspension, and were able to show that the degree of nonlinearity increased with shear amplitude. In all cases, we showed how tuning the parameters in the dumbbell model affected the viscoelasticity.

Having confirmed how the addition of dumbbells produces viscoelastic effects, a natural next step for further work is to add large particles into the suspension. We could then apply various standard rheometrical tests and observe the behaviour of the large particles. For example: under oscillatory shear, does any structure form from the large particles? Under continuous shear, what conditions are required for particles to form chains? Under funnelling flow, when do we see waves in the particle concentration travel through the suspension (so-called arching)? And in all three cases, how does viscoelasticity change that?

In chapter 4, *Sedimenting spheres in concentrated media*, we simulated a large spherical particle sedimenting through a suspension of many smaller particles that was undergoing oscillatory shear. This simulation was based on a recent experimental paper where, at some parts of the shear, the large particle was found to fall 'upwards'. In our simulations, we were able to examine the structure of the small particles and in doing so, were able to offer explanations for some of the experimental observations. We were able to qualitatively recreate the figure-of-eight velocity profiles for the falling ball, including upward motion, and offered a feasible mechanism for this: repulsion chains in 2D, and breakdown of vertical chains in 3D. We demonstrated the effect of changing the imposed frequency or the interparticle repulsion strength on the behaviour of the falling ball.

We were not able to capture the increased fall velocity observed in the experiments under certain strength shears, and this lays the path for further work. In particular, the interparticle repulsion force may not be sufficient to capture all the required physics. Contact forces, as discussed in chapter 5 and which we saw to be important

in determining the viscosity of highly concentrated suspensions, may be required to fully simulate this experiment. Furthermore, our large ball falls through a box 20 times shallower than in the experiment, and it may be that larger fall times are required to build up more structure. Both of these are possible to simulate with SD: the details of the first are in chapter 5, and for the latter, deeper boxes can be created by removing particles from the top of the box and randomly placing them at the bottom, to keep computational cost down.

The experiments are performed with two different sizes of spherical particle, with a size ratio of 1/33. Our simulations use a size ratio of 1/10. A question that can be explored is the effect of changing this size ratio: do we expect reducing the small particle size to make a difference to the behaviour of the large sphere? If we increase the small particle size, at what size ratio do we begin to see significant changes to the velocity profile of the falling ball? Unaddressed by the experiments, but something we can examine in simulation, is examining how sensitive the experiments might be to polydispersity in the small particle sizes. This could be implemented in a simulation with one large particle, and two classes of small particle, with varying small size ratios.

In chapter 5, *Shear thickening and friction*, we properly implemented interparticle frictional contact to model shear thickening, a feature seen—but only recently beginning to be understood—in some suspensions. This is an active area of current research and in the literature, friction is usually implemented in an ad hoc way. This new method allowed us to investigate contact models accurately and efficiently. We showed that frictional contact can lead to shear thickening at sufficiently high concentrations, and we demonstrated how parameters in the model change the amount of shear thickening expected. Our results were then compared to existing literature. In particular, we noted that an exact stopping force, implemented in our accurate model when close particles approach, leads to only continuous shear thickening, and not the dramatic jumps seen in discontinuous shear thickening. This led us to conclude that an important condition of particle roughness must be compressibility.

As mentioned, frictional contact as a mechanism for shear thickening is an extremely active current research area, and much work is currently being done in this area across the community. There is some natural further work from our results: quantifying the degree of compressibility required, for example. We could also ask the effect of different shear profiles.

An alternative mechanism at the roughness level which could be investigated, is that under sufficiently high pressures, asperities melt. This would lead to maintaining contact longer—a much larger irreversible action than in our current model—and the particles having to overcome a critical force to separate. A contact model could

be developed for this mechanism and the effects on shear-thickening investigated.

Another alternative is the formation of cavitation bubbles—voids formed in extreme low pressure regions—which cause suction in the contact regions between particles. These would also require a significant critical force to be overcome, and would also cause irreversibility. This would be harder to set up in the Stokesian Dynamics formalism, however.

Both these alternative explanations depend on temperature: melting in the first instance, and essentially boiling to form the bubbles in the second. We have seen in chapter 5 that if the background fluid viscosity depends on temperature, then the suspension effective viscosity depends on temperature in the same way. This would no longer be the case if either of these mechanisms were implemented, and this could form an interesting study, comparing to experimental work looking for temperature dependence on effective viscosity. This would be of particular interest in cryopreservation research, a current area looking to apply shear-thickening fluids in order to protect supercooled biological tissue from destructive ice formation.

Overall, the mechanics of suspensions continues to be an interesting and active research area. The challenges of predicting macroscale behaviour from what we know on the microscale continue to be met by rheologists working theoretically, experimentally and with simulations. One such simulation method, Stokesian Dynamics, that we use here, continues to be flexible and efficient in the face of new demands from researchers. Working together, we are continually learning more about the behaviour of suspensions: some of the most interesting and abundant materials found in our lives.

Appendix A

Derivations, notes and calculations

A.1 Relations between the resistance and mobility tensors

A.1.1 Symmetric formulation

In the symmetric formulation of a spheres-only Stokesian Dynamics simulation, the resistance and mobility problems are solving

$$\begin{pmatrix} \boldsymbol{F} \\ \boldsymbol{T} \\ \boldsymbol{S} \end{pmatrix} = \mathcal{R} \begin{pmatrix} \boldsymbol{U} - \boldsymbol{u}^{\infty}(\boldsymbol{x}) \\ \boldsymbol{\Omega} - \boldsymbol{\Omega}^{\infty} \\ -\boldsymbol{E}^{\infty} \end{pmatrix} \qquad \text{and} \qquad \begin{pmatrix} \boldsymbol{U} - \boldsymbol{u}^{\infty}(\boldsymbol{x}) \\ \boldsymbol{\Omega} - \boldsymbol{\Omega}^{\infty} \\ -\boldsymbol{E}^{\infty} \end{pmatrix} = \mathcal{M} \begin{pmatrix} \boldsymbol{F} \\ \boldsymbol{T} \\ \boldsymbol{S} \end{pmatrix} \tag{A.1}$$

respectively. The mobility matrix is the inverse of the resistance matrix, $\mathcal{M} = \mathcal{R}^{-1}$, and in particular for one particle we have

$$\begin{pmatrix} \boldsymbol{a} & \tilde{\boldsymbol{b}} & \tilde{\boldsymbol{g}} \\ \boldsymbol{b} & \boldsymbol{c} & \tilde{\boldsymbol{h}} \\ \boldsymbol{g} & \boldsymbol{h} & \boldsymbol{m} \end{pmatrix} = \begin{pmatrix} \boldsymbol{A} & \widetilde{\boldsymbol{B}} & \widetilde{\boldsymbol{G}} \\ \boldsymbol{B} & \boldsymbol{C} & \widetilde{\boldsymbol{H}} \\ \boldsymbol{G} & \boldsymbol{H} & \boldsymbol{M} \end{pmatrix}^{-1} \tag{A.2}$$

or more specifically,

$$\begin{pmatrix} \boldsymbol{a} & \tilde{\boldsymbol{b}} & \tilde{\boldsymbol{g}} \\ \boldsymbol{b} & \boldsymbol{c} & \tilde{\boldsymbol{h}} \\ \boldsymbol{g} & \boldsymbol{h} & \boldsymbol{m} \end{pmatrix} \begin{pmatrix} \boldsymbol{A} & \widetilde{\boldsymbol{B}} & \widetilde{\boldsymbol{G}} \\ \boldsymbol{B} & \boldsymbol{C} & \widetilde{\boldsymbol{H}} \\ \boldsymbol{G} & \boldsymbol{H} & \boldsymbol{M} \end{pmatrix} = \begin{pmatrix} \boldsymbol{I}^2 & 0 & 0 \\ 0 & \boldsymbol{I}^2 & 0 \\ 0 & 0 & \boldsymbol{I}^4 \end{pmatrix}, \tag{A.3}$$

where $\boldsymbol{I}^2_{ij} = \delta_{ij}$, the normal identity tensor, and

$$\boldsymbol{I}^4_{ijk\ell} = \frac{1}{2}\left(\delta_{ik}\delta_{j\ell} + \delta_{i\ell}\delta_{jk} - \frac{2}{3}\delta_{ij}\delta_{k\ell}\right). \tag{A.4}$$

Here $\boldsymbol{I}^4$ is the fourth-rank deviatoric (traceless) unit tensor. The first term in its expression is the fourth-rank identity tensor. Adding the second term gives you the symmetric unit tensor, i.e. multiplication by it gives you a symmetric tensor. Including the third term makes it traceless. Since the $\boldsymbol{S}$ and $\boldsymbol{E}$ terms with which the product $\boldsymbol{mM} = \boldsymbol{I}^4$ is affiliated are both symmetric and traceless, this is the form of the unit tensor we expect to find. Observe that it contracts under eq. (2.79) to the second-rank identity tensor $\boldsymbol{I}^2$, which is what we would hope to find when writing eq. (A.3) in purely matrix form.

Breaking the tensors into their component scalars (see table A.1, removing the $(\alpha\tilde{\alpha})$ sub- and superscripts), we can show by calculation the following relations to hold:

$$x^c X^C = 1, \tag{A.7a}$$

$$\begin{pmatrix} x^a & \sqrt{\frac{2}{3}}x^g \\ \sqrt{\frac{2}{3}}x^g & x^m \end{pmatrix}\begin{pmatrix} X^A & \sqrt{\frac{2}{3}}X^G \\ \sqrt{\frac{2}{3}}X^G & X^M \end{pmatrix} = \begin{pmatrix} 1 & 0 \\ 0 & 1 \end{pmatrix}, \tag{A.7b}$$

$$\begin{pmatrix} y^a & -y^b & \sqrt{2}y^g \\ -y^b & y^c & \sqrt{2}y^h \\ \sqrt{2}y^g & \sqrt{2}y^h & y^m \end{pmatrix}\begin{pmatrix} Y^A & -Y^B & \sqrt{2}Y^G \\ -Y^B & Y^C & \sqrt{2}Y^H \\ \sqrt{2}Y^G & \sqrt{2}Y^H & Y^M \end{pmatrix} = \begin{pmatrix} 1 & 0 & 0 \\ 0 & 1 & 0 \\ 0 & 0 & 1 \end{pmatrix}, \tag{A.7c}$$

$$z^m Z^M = 1. \tag{A.7d}$$

For two particles, we have

$$\begin{pmatrix} \boldsymbol{a}_{11} & \boldsymbol{a}_{12} & \tilde{\boldsymbol{b}}_{11} & \tilde{\boldsymbol{b}}_{12} & \tilde{\boldsymbol{g}}_{11} & \tilde{\boldsymbol{g}}_{12} \\ \boldsymbol{a}_{21} & \boldsymbol{a}_{22} & \tilde{\boldsymbol{b}}_{21} & \tilde{\boldsymbol{b}}_{22} & \tilde{\boldsymbol{g}}_{21} & \tilde{\boldsymbol{g}}_{22} \\ \boldsymbol{b}_{11} & \boldsymbol{b}_{12} & \boldsymbol{c}_{11} & \boldsymbol{c}_{12} & \tilde{\boldsymbol{h}}_{11} & \tilde{\boldsymbol{h}}_{12} \\ \boldsymbol{b}_{21} & \boldsymbol{b}_{22} & \boldsymbol{c}_{21} & \boldsymbol{c}_{22} & \tilde{\boldsymbol{h}}_{21} & \tilde{\boldsymbol{h}}_{22} \\ \boldsymbol{g}_{11} & \boldsymbol{g}_{12} & \boldsymbol{h}_{11} & \boldsymbol{h}_{12} & \boldsymbol{m}_{11} & \boldsymbol{m}_{12} \\ \boldsymbol{g}_{21} & \boldsymbol{g}_{22} & \boldsymbol{h}_{21} & \boldsymbol{h}_{22} & \boldsymbol{m}_{21} & \boldsymbol{m}_{22} \end{pmatrix}\begin{pmatrix} \boldsymbol{A}_{11} & \boldsymbol{A}_{12} & \widetilde{\boldsymbol{B}}_{11} & \widetilde{\boldsymbol{B}}_{12} & \widetilde{\boldsymbol{G}}_{11} & \widetilde{\boldsymbol{G}}_{12} \\ \boldsymbol{A}_{21} & \boldsymbol{A}_{22} & \widetilde{\boldsymbol{B}}_{21} & \widetilde{\boldsymbol{B}}_{22} & \widetilde{\boldsymbol{G}}_{21} & \widetilde{\boldsymbol{G}}_{22} \\ \boldsymbol{B}_{11} & \boldsymbol{B}_{12} & \boldsymbol{C}_{11} & \boldsymbol{C}_{12} & \widetilde{\boldsymbol{H}}_{11} & \widetilde{\boldsymbol{H}}_{12} \\ \boldsymbol{B}_{21} & \boldsymbol{B}_{22} & \boldsymbol{C}_{21} & \boldsymbol{C}_{22} & \widetilde{\boldsymbol{H}}_{21} & \widetilde{\boldsymbol{H}}_{22} \\ \boldsymbol{G}_{11} & \boldsymbol{G}_{12} & \boldsymbol{H}_{11} & \boldsymbol{H}_{12} & \boldsymbol{M}_{11} & \boldsymbol{M}_{12} \\ \boldsymbol{G}_{21} & \boldsymbol{G}_{22} & \boldsymbol{H}_{21} & \boldsymbol{H}_{22} & \boldsymbol{M}_{21} & \boldsymbol{M}_{22} \end{pmatrix}$$

$$= \begin{pmatrix} \boldsymbol{I}^2 & 0 & 0 & 0 & 0 & 0 \\ 0 & \boldsymbol{I}^2 & 0 & 0 & 0 & 0 \\ 0 & 0 & \boldsymbol{I}^2 & 0 & 0 & 0 \\ 0 & 0 & 0 & \boldsymbol{I}^2 & 0 & 0 \\ 0 & 0 & 0 & 0 & \boldsymbol{I}^4 & 0 \\ 0 & 0 & 0 & 0 & 0 & \boldsymbol{I}^4 \end{pmatrix}. \tag{A.8}$$

Breaking these tensors into their component scalars (see table A.1), further calcula-

Resistance tensors:

$$A_{ij}^{(\alpha\widetilde{\alpha})} = X_{\alpha\widetilde{\alpha}}^{A} L_{ij}^{1} + Y_{\alpha\widetilde{\alpha}}^{A} L_{ij}^{2} \tag{A.5a}$$

$$B_{ij}^{(\alpha\widetilde{\alpha})} = Y_{\alpha\widetilde{\alpha}}^{B} L_{ij}^{3} \tag{A.5b}$$

$$C_{ij}^{(\alpha\widetilde{\alpha})} = X_{\alpha\widetilde{\alpha}}^{C} L_{ij}^{1} + Y_{\alpha\widetilde{\alpha}}^{C} L_{ij}^{2} \tag{A.5c}$$

$$G_{ijk}^{(\alpha\widetilde{\alpha})} = X_{\alpha\widetilde{\alpha}}^{G} L_{ijk}^{4} + Y_{\alpha\widetilde{\alpha}}^{G} L_{ijk}^{5} \tag{A.5d}$$

$$H_{ijk}^{(\alpha\widetilde{\alpha})} = Y_{\alpha\widetilde{\alpha}}^{H} L_{ijk}^{6} \tag{A.5e}$$

$$M_{ijk\ell}^{(\alpha\widetilde{\alpha})} = X_{\alpha\widetilde{\alpha}}^{M} L_{ijk\ell}^{7} + Y_{\alpha\widetilde{\alpha}}^{M} L_{ijk\ell}^{8} + Z_{\alpha\widetilde{\alpha}}^{M} L_{ijk\ell}^{9} \tag{A.5f}$$

(A.5g)

Mobility tensors:

$$a_{ij}^{(\alpha\widetilde{\alpha})} = x_{\alpha\widetilde{\alpha}}^{a} L_{ij}^{1} + y_{\alpha\widetilde{\alpha}}^{a} L_{ij}^{2} \tag{A.6a}$$

$$b_{ij}^{(\alpha\widetilde{\alpha})} = y_{\alpha\widetilde{\alpha}}^{b} L_{ij}^{3} \tag{A.6b}$$

$$c_{ij}^{(\alpha\widetilde{\alpha})} = x_{\alpha\widetilde{\alpha}}^{c} L_{ij}^{1} + y_{\alpha\widetilde{\alpha}}^{c} L_{ij}^{2} \tag{A.6c}$$

$$g_{ijk}^{(\alpha\widetilde{\alpha})} = x_{\alpha\widetilde{\alpha}}^{g} L_{ijk}^{4} + y_{\alpha\widetilde{\alpha}}^{g} L_{ijk}^{5} \tag{A.6d}$$

$$h_{ijk}^{(\alpha\widetilde{\alpha})} = y_{\alpha\widetilde{\alpha}}^{h} L_{ijk}^{6} \tag{A.6e}$$

In symmetric formulation (appendix A.1.1):

$$m_{ijk\ell}^{(\alpha\widetilde{\alpha})} = x_{\alpha\widetilde{\alpha}}^{m} L_{ijk\ell}^{7} + y_{\alpha\widetilde{\alpha}}^{m} L_{ijk\ell}^{8} + z_{\alpha\widetilde{\alpha}}^{m} L_{ijk\ell}^{9} \tag{A.6f}$$

In Kim formulation (appendix A.1.2):

$$m_{ijk\ell}^{(\alpha)} = x_{\alpha}^{m} L_{ijk\ell}^{7} + y_{\alpha}^{m} L_{ijk\ell}^{8} + z_{\alpha}^{m} L_{ijk\ell}^{9} \tag{A.6g}$$

Table A.1: Component scalars of the resistance and mobility tensors for two spheres. Unit displacement tensors $\boldsymbol{L}^{i}$ are given by eq. (2.70). Source: Kim & Karrila (2005, p. 182, table 7.1)

tion shows the following relations to hold:

$$\begin{pmatrix} x_{11}^c & x_{12}^c \\ x_{21}^c & x_{22}^c \end{pmatrix} = \begin{pmatrix} X_{11}^C & X_{12}^C \\ X_{21}^C & X_{22}^C \end{pmatrix}^{-1}, \tag{A.9a}$$

$$\begin{pmatrix} x_{11}^a & x_{12}^a & \sqrt{\frac{2}{3}}x_{11}^g & \sqrt{\frac{2}{3}}x_{21}^g \\ x_{21}^a & x_{22}^a & \sqrt{\frac{2}{3}}x_{12}^g & \sqrt{\frac{2}{3}}x_{22}^g \\ \sqrt{\frac{2}{3}}x_{11}^g & \sqrt{\frac{2}{3}}x_{12}^g & x_{11}^m & -x_{12}^m \\ \sqrt{\frac{2}{3}}x_{21}^g & \sqrt{\frac{2}{3}}x_{22}^g & -x_{21}^m & x_{22}^m \end{pmatrix} = \begin{pmatrix} X_{11}^A & X_{12}^A & \sqrt{\frac{2}{3}}X_{11}^G & \sqrt{\frac{2}{3}}X_{21}^G \\ X_{21}^A & X_{22}^A & \sqrt{\frac{2}{3}}X_{12}^G & \sqrt{\frac{2}{3}}X_{22}^G \\ \sqrt{\frac{2}{3}}X_{11}^G & \sqrt{\frac{2}{3}}X_{12}^G & X_{11}^M & -X_{12}^M \\ \sqrt{\frac{2}{3}}X_{21}^G & \sqrt{\frac{2}{3}}X_{22}^G & -X_{21}^M & X_{22}^M \end{pmatrix}^{-1}, \tag{A.9b}$$

$$\begin{pmatrix} y_{11}^a & y_{12}^a & y_{11}^b & y_{21}^b & \sqrt{2}y_{11}^g & \sqrt{2}y_{21}^g \\ y_{21}^a & y_{22}^a & y_{12}^b & y_{22}^b & \sqrt{2}y_{12}^g & \sqrt{2}y_{22}^g \\ y_{11}^b & y_{12}^b & y_{11}^c & -y_{12}^c & -\sqrt{2}y_{11}^h & \sqrt{2}y_{21}^h \\ y_{21}^b & y_{22}^b & -y_{21}^c & y_{22}^c & \sqrt{2}y_{12}^h & -\sqrt{2}y_{22}^h \\ \sqrt{2}y_{11}^g & \sqrt{2}y_{12}^g & -\sqrt{2}y_{11}^h & \sqrt{2}y_{12}^h & y_{11}^m & -y_{12}^m \\ \sqrt{2}y_{21}^g & \sqrt{2}y_{22}^g & \sqrt{2}y_{21}^h & -\sqrt{2}y_{22}^h & -y_{21}^m & y_{22}^m \end{pmatrix}$$

$$= \begin{pmatrix} Y_{11}^A & Y_{12}^A & Y_{11}^B & Y_{21}^B & \sqrt{2}Y_{11}^G & \sqrt{2}Y_{21}^G \\ Y_{21}^A & Y_{22}^A & Y_{12}^B & Y_{22}^B & \sqrt{2}Y_{12}^G & \sqrt{2}Y_{22}^G \\ Y_{11}^B & Y_{12}^B & Y_{11}^C & -Y_{12}^C & -\sqrt{2}Y_{11}^H & \sqrt{2}Y_{21}^H \\ Y_{21}^B & Y_{22}^B & -Y_{21}^C & Y_{22}^C & \sqrt{2}Y_{12}^H & -\sqrt{2}Y_{22}^H \\ \sqrt{2}Y_{11}^G & \sqrt{2}Y_{12}^G & -\sqrt{2}Y_{11}^H & \sqrt{2}Y_{12}^H & Y_{11}^M & -Y_{12}^M \\ \sqrt{2}Y_{21}^G & \sqrt{2}Y_{22}^G & \sqrt{2}Y_{21}^H & -\sqrt{2}Y_{22}^H & -Y_{21}^M & Y_{22}^M \end{pmatrix}^{-1}, \tag{A.9c}$$

$$\begin{pmatrix} z_{11}^m & z_{12}^m \\ z_{21}^m & z_{22}^m \end{pmatrix} = \begin{pmatrix} Z_{11}^M & Z_{12}^M \\ Z_{21}^M & Z_{22}^M \end{pmatrix}^{-1}. \tag{A.9d}$$

A.1.2 Kim formulation

In the formulation of Kim (Kim & Karrila, 2005, sec. 7.2), for a spheres-only Stokesian Dynamics simulation, the resistance and mobility problems are solving

$$\begin{pmatrix} \boldsymbol{F} \\ \boldsymbol{T} \\ \boldsymbol{S} \end{pmatrix} = \mathcal{R} \begin{pmatrix} \boldsymbol{U} - \boldsymbol{u}^\infty(\boldsymbol{x}) \\ \boldsymbol{\Omega} - \boldsymbol{\Omega}^\infty \\ -\boldsymbol{E}^\infty \end{pmatrix} \quad \text{and} \quad \begin{pmatrix} \boldsymbol{U} - \boldsymbol{u}^\infty(\boldsymbol{x}) \\ \boldsymbol{\Omega} - \boldsymbol{\Omega}^\infty \\ \boldsymbol{S} \end{pmatrix} = \mathcal{M}_{\text{Kim}} \begin{pmatrix} \boldsymbol{F} \\ \boldsymbol{T} \\ -\boldsymbol{E}^\infty \end{pmatrix} \tag{A.10}$$

respectively. In this formulation, the resistance and mobility matrices are not their respective inverses. The resistance matrix is of the same form as in the symmetric formulation in appendix A.1.1, but the mobility matrix, denoted $\mathcal{M}_{\text{Kim}}$ here to emphasise this, is not.

For two spheres, the mobility problem has the form

$$\begin{pmatrix} \boldsymbol{U}^1 - \boldsymbol{u}^\infty(\boldsymbol{x}^1) \\ \boldsymbol{U}^2 - \boldsymbol{u}^\infty(\boldsymbol{x}^2) \\ \boldsymbol{\Omega}^1 - \boldsymbol{\Omega}^\infty \\ \boldsymbol{\Omega}^2 - \boldsymbol{\Omega}^\infty \\ \boldsymbol{S}^1 \\ \boldsymbol{S}^2 \end{pmatrix} = \begin{pmatrix} \boldsymbol{a}_{11} & \boldsymbol{a}_{12} & \tilde{\boldsymbol{b}}_{11} & \tilde{\boldsymbol{b}}_{12} & \tilde{\boldsymbol{g}}_1 \\ \boldsymbol{a}_{21} & \boldsymbol{a}_{22} & \tilde{\boldsymbol{b}}_{21} & \tilde{\boldsymbol{b}}_{22} & \tilde{\boldsymbol{g}}_2 \\ \boldsymbol{b}_{11} & \boldsymbol{b}_{12} & \boldsymbol{c}_{11} & \boldsymbol{c}_{12} & \tilde{\boldsymbol{h}}_1 \\ \boldsymbol{b}_{21} & \boldsymbol{b}_{22} & \boldsymbol{c}_{21} & \boldsymbol{c}_{22} & \tilde{\boldsymbol{h}}_2 \\ \boldsymbol{g}_{11} & \boldsymbol{g}_{12} & \boldsymbol{h}_{11} & \boldsymbol{h}_{12} & \boldsymbol{m}_1 \\ \boldsymbol{g}_{21} & \boldsymbol{g}_{22} & \boldsymbol{h}_{21} & \boldsymbol{h}_{22} & \boldsymbol{m}_2 \end{pmatrix} \begin{pmatrix} \boldsymbol{F}^1 \\ \boldsymbol{F}^2 \\ \boldsymbol{T}^1 \\ \boldsymbol{T}^2 \\ -\boldsymbol{E}^\infty \end{pmatrix}, \tag{A.11}$$

with symmetry relations calculated similarly to in section 2.4.5 given by

$$a_{ij}^{(\alpha\widetilde{\alpha})} = a_{ji}^{(\widetilde{\alpha}\alpha)}, \tag{A.12a}$$
$$c_{ij}^{(\alpha\widetilde{\alpha})} = c_{ji}^{(\widetilde{\alpha}\alpha)}, \tag{A.12b}$$
$$b_{ij}^{(\alpha\widetilde{\alpha})} = \tilde{b}_{ji}^{(\widetilde{\alpha}\alpha)}, \tag{A.12c}$$
$$g_{ijk}^{(1\alpha)} + g_{ijk}^{(2\alpha)} = -\tilde{g}_{kij}^{(\alpha)}, \tag{A.12d}$$
$$h_{ijk}^{(1\alpha)} + h_{ijk}^{(2\alpha)} = -\tilde{h}_{kij}^{(\alpha)}, \tag{A.12e}$$
$$m_{ijk\ell}^{(1)} + m_{ijk\ell}^{(2)} = m_{k\ell ij}^{(1)} + m_{k\ell ij}^{(2)}. \tag{A.12f}$$

Breaking the tensors into their component mobility and resistance scalars (see table A.1), written in the two-sphere literature notation (see differences with ours in section 2.4.2), calculation shows the following relations to hold:

$$\begin{pmatrix} x_{11}^a & x_{12}^a \\ x_{12}^a & x_{22}^a \end{pmatrix} = \begin{pmatrix} X_{11}^A & X_{12}^A \\ X_{12}^A & X_{22}^A \end{pmatrix}^{-1}, \tag{A.13a}$$
$$\begin{pmatrix} x_{11}^c & x_{12}^c \\ x_{12}^c & x_{22}^c \end{pmatrix} = \begin{pmatrix} X_{11}^C & X_{12}^C \\ X_{12}^C & X_{22}^C \end{pmatrix}^{-1}, \tag{A.13b}$$
$$\begin{pmatrix} x_{11}^g & x_{12}^g \\ x_{21}^g & x_{22}^g \end{pmatrix} = \begin{pmatrix} X_{11}^G & X_{12}^G \\ X_{21}^G & X_{22}^G \end{pmatrix} \begin{pmatrix} x_{11}^a & x_{12}^a \\ x_{12}^a & x_{22}^a \end{pmatrix}, \tag{A.13c}$$
$$\begin{pmatrix} y_{11}^a & y_{12}^a & y_{11}^b & y_{21}^b \\ y_{12}^a & y_{22}^a & y_{12}^b & y_{22}^b \\ y_{11}^b & y_{12}^b & y_{11}^c & y_{12}^c \\ y_{21}^b & y_{22}^b & y_{12}^c & y_{22}^c \end{pmatrix} = \begin{pmatrix} Y_{11}^A & Y_{12}^A & Y_{11}^B & Y_{21}^B \\ Y_{12}^A & Y_{22}^A & Y_{12}^B & Y_{22}^B \\ Y_{11}^B & Y_{12}^B & Y_{11}^C & Y_{12}^C \\ Y_{21}^B & Y_{22}^B & Y_{12}^C & Y_{22}^C \end{pmatrix}^{-1}, \tag{A.13d}$$
$$\begin{pmatrix} y_{11}^g & y_{21}^g \\ y_{12}^g & y_{22}^g \\ -y_{11}^h & -y_{21}^h \\ -y_{12}^h & -y_{22}^h \end{pmatrix} = \begin{pmatrix} y_{11}^a & y_{12}^a & y_{11}^b & y_{21}^b \\ y_{12}^a & y_{22}^a & y_{12}^b & y_{22}^b \\ y_{11}^b & y_{12}^b & y_{11}^c & y_{12}^c \\ y_{21}^b & y_{22}^b & y_{12}^c & y_{22}^c \end{pmatrix} \begin{pmatrix} Y_{11}^G & Y_{21}^G \\ Y_{12}^G & Y_{22}^G \\ -Y_{11}^H & -Y_{21}^H \\ -Y_{12}^H & -Y_{22}^H \end{pmatrix}, \tag{A.13e}$$

$$x_\alpha^m = X_{\alpha1}^M + X_{\alpha2}^M - \frac{2}{3}\left[X_{\alpha1}^G(x_{11}^g + x_{21}^g) + X_{\alpha2}^G(x_{12}^g + x_{22}^g)\right], \tag{A.14a}$$

$$y_\alpha^m = Y_{\alpha1}^M + Y_{\alpha2}^M - 2\left[Y_{\alpha1}^G(y_{11}^g + y_{21}^g) + Y_{\alpha2}^G(y_{12}^g + y_{22}^g) + Y_{\alpha1}^H(y_{11}^h + y_{21}^h) + Y_{\alpha2}^H(y_{12}^h + y_{22}^h)\right], \tag{A.14b}$$

$$z_\alpha^m = Z_{\alpha1}^M + Z_{\alpha2}^M. \tag{A.14c}$$

Observe that the resistance scalar functions X^M, Y^M and Z^M cannot be uniquely defined from the mobility functions in this formulation. Rather, we can only find $X_{\alpha1}^M + X_{\alpha2}^M$, etc., in terms of x_α^m. Inversely, the generation of the mobility scalar function from the resistance scalars is uniquely defined. Since we are generating the mobility scalars in our code and then converting them to resistance scalars, we choose to adapt this formulation, as shown in appendix A.1.3.

A.1.3 Adapted Kim formulation

We can adapt the Kim formulation to make the mobility matrix $\mathcal{M}_{\text{Kim}}$ into a square matrix $\mathcal{M}_{\text{aKim}}$ by introducing an extra $\boldsymbol{E}$ in the force vector. For two spheres, the mobility problem has the form

$$\begin{pmatrix} \boldsymbol{U}^1 - \boldsymbol{u}^\infty(\boldsymbol{x}^1) \\ \boldsymbol{U}^2 - \boldsymbol{u}^\infty(\boldsymbol{x}^2) \\ \boldsymbol{\Omega}^1 - \boldsymbol{\Omega}^\infty \\ \boldsymbol{\Omega}^2 - \boldsymbol{\Omega}^\infty \\ \boldsymbol{S}^1 \\ \boldsymbol{S}^2 \end{pmatrix} = \begin{pmatrix} \boldsymbol{a}_{11} & \boldsymbol{a}_{12} & \tilde{\boldsymbol{b}}_{11} & \tilde{\boldsymbol{b}}_{12} & \tilde{\boldsymbol{g}}_{11} & \tilde{\boldsymbol{g}}_{12} \\ \boldsymbol{a}_{21} & \boldsymbol{a}_{22} & \tilde{\boldsymbol{b}}_{21} & \tilde{\boldsymbol{b}}_{22} & \tilde{\boldsymbol{g}}_{21} & \tilde{\boldsymbol{g}}_{21} \\ \boldsymbol{b}_{11} & \boldsymbol{b}_{12} & \boldsymbol{c}_{11} & \boldsymbol{c}_{12} & \tilde{\boldsymbol{h}}_{11} & \tilde{\boldsymbol{h}}_{12} \\ \boldsymbol{b}_{21} & \boldsymbol{b}_{22} & \boldsymbol{c}_{21} & \boldsymbol{c}_{22} & \tilde{\boldsymbol{h}}_{21} & \tilde{\boldsymbol{h}}_{22} \\ \boldsymbol{g}_{11} & \boldsymbol{g}_{12} & \boldsymbol{h}_{11} & \boldsymbol{h}_{12} & \boldsymbol{m}_{11} & \boldsymbol{m}_{12} \\ \boldsymbol{g}_{21} & \boldsymbol{g}_{22} & \boldsymbol{h}_{21} & \boldsymbol{h}_{22} & \boldsymbol{m}_{21} & \boldsymbol{m}_{22} \end{pmatrix} \begin{pmatrix} \boldsymbol{F}^1 \\ \boldsymbol{F}^2 \\ \boldsymbol{T}^1 \\ \boldsymbol{T}^2 \\ \boldsymbol{E}^1 \\ \boldsymbol{E}^2 \end{pmatrix}, \tag{A.15}$$

where $\boldsymbol{E}^1 = \boldsymbol{E}^2 = -\boldsymbol{E}^\infty$ for any realistic simulation. But we can relax this constraint to generate the resistance scalar functions from our mobility code.

In the adapted Kim formulation, the inverses in eq. (A.13) hold, with the addition of

$$\begin{pmatrix} x_{11}^m & x_{12}^m \\ x_{21}^m & x_{22}^m \end{pmatrix} = \begin{pmatrix} X_{11}^M & X_{12}^M \\ X_{21}^M & X_{22}^M \end{pmatrix} - \frac{2}{3}\begin{pmatrix} X_{11}^G & X_{12}^G \\ X_{21}^G & X_{22}^G \end{pmatrix}\begin{pmatrix} x_{11}^g & x_{21}^g \\ x_{12}^g & x_{22}^g \end{pmatrix}, \tag{A.16a}$$

$$\begin{pmatrix} y_{11}^m & y_{12}^m \\ y_{21}^m & y_{22}^m \end{pmatrix} = \begin{pmatrix} Y_{11}^M & Y_{12}^M \\ Y_{21}^M & Y_{22}^M \end{pmatrix} - 2\left[\begin{pmatrix} Y_{11}^G & Y_{12}^G \\ Y_{21}^G & Y_{22}^G \end{pmatrix}\begin{pmatrix} y_{11}^g & y_{21}^g \\ y_{12}^g & y_{22}^g \end{pmatrix} + \begin{pmatrix} Y_{11}^H & Y_{12}^H \\ Y_{21}^H & Y_{22}^H \end{pmatrix}\begin{pmatrix} y_{11}^h & y_{21}^h \\ y_{12}^h & y_{22}^h \end{pmatrix}\right], \tag{A.16b}$$

$$\begin{pmatrix} z_{11}^m & z_{12}^m \\ z_{21}^m & z_{22}^m \end{pmatrix} = \begin{pmatrix} Z_{11}^M & Z_{12}^M \\ Z_{21}^M & Z_{22}^M \end{pmatrix}. \tag{A.16c}$$

The relationship between $\mathcal{M}_{\text{aKim}}$ and $\mathcal{M}$ is found by rearranging, effectively switching the $-\boldsymbol{E}_{[\,]}^{\infty}$ and $\boldsymbol{S}_{[\,]}^{\alpha}$ terms in the mobility formulation with $\mathcal{M}$,

$$\begin{pmatrix} \boldsymbol{U}^{\alpha} - \boldsymbol{u}^{\infty}(\boldsymbol{x}^{\alpha}) \\ \boldsymbol{\Omega}^{\alpha} - \boldsymbol{\Omega}^{\infty} \\ -\boldsymbol{E}_{[\,]}^{\infty} \\ \boldsymbol{U}^{\beta} - \boldsymbol{u}^{\infty}(\overline{\boldsymbol{x}}^{\beta}) \\ \frac{1}{2}\left[\Delta\boldsymbol{U}^{\beta} - \Delta\boldsymbol{u}^{\infty}(\overline{\boldsymbol{x}}^{\beta}; \Delta\boldsymbol{x}^{\beta}\cdot)\right] \end{pmatrix} = \begin{pmatrix} \boldsymbol{a} & \tilde{\boldsymbol{b}} & \tilde{\boldsymbol{g}} & \boldsymbol{m}^{14} & \boldsymbol{m}^{15} \\ \boldsymbol{b} & \boldsymbol{c} & \tilde{\boldsymbol{h}} & \boldsymbol{m}^{24} & \boldsymbol{m}^{25} \\ \boldsymbol{g} & \boldsymbol{h} & \boldsymbol{m} & \boldsymbol{m}^{34} & \boldsymbol{m}^{35} \\ \boldsymbol{m}^{41} & \boldsymbol{m}^{42} & \boldsymbol{m}^{43} & \boldsymbol{m}^{44} & \boldsymbol{m}^{45} \\ \boldsymbol{m}^{51} & \boldsymbol{m}^{52} & \boldsymbol{m}^{53} & \boldsymbol{m}^{54} & \boldsymbol{m}^{55} \end{pmatrix} \begin{pmatrix} \boldsymbol{F}^{\alpha} \\ \boldsymbol{T}^{\alpha} \\ \boldsymbol{S}_{[\,]}^{\alpha} \\ \boldsymbol{F}^{\beta} \\ \Delta\boldsymbol{F}^{\beta} \end{pmatrix}, \tag{A.17}$$

or in short,

$$\mathcal{U} = \mathcal{M}\mathcal{F}. \tag{A.18}$$

To do this, consider the row-picking matrices

$$\mathcal{D} = \operatorname{diag}(\boldsymbol{0}, \boldsymbol{0}, \boldsymbol{I}, \boldsymbol{0}, \boldsymbol{0}), \qquad \mathcal{D}^* = \boldsymbol{I} - \mathcal{D}. \tag{A.19}$$

Then the velocity moment and force vectors we want are

$$\mathcal{U}_{\text{aKim}} = \mathcal{D}^*\mathcal{U} + \mathcal{D}\mathcal{F}, \qquad \mathcal{F}_{\text{aKim}} = \mathcal{D}^*\mathcal{F} + \mathcal{D}\mathcal{U}. \tag{A.20}$$

Substituting and rearranging, we arrive at

$$\mathcal{M}_{\text{aKim}} = (\mathcal{D}^* - \mathcal{M}\mathcal{D})^{-1}(\mathcal{M}\mathcal{D}^* - \mathcal{D}). \tag{A.21}$$

Explicitly, this looks like, notating $\boldsymbol{t} = \boldsymbol{m}^{-1}$,

$$\begin{pmatrix} \boldsymbol{a} & \tilde{\boldsymbol{b}} & \tilde{\boldsymbol{g}} & \boldsymbol{m}^{14} & \boldsymbol{m}^{15} \\ \boldsymbol{b} & \boldsymbol{c} & \tilde{\boldsymbol{h}} & \boldsymbol{m}^{24} & \boldsymbol{m}^{25} \\ \boldsymbol{g} & \boldsymbol{h} & \boldsymbol{m} & \boldsymbol{m}^{34} & \boldsymbol{m}^{35} \\ \boldsymbol{m}^{41} & \boldsymbol{m}^{42} & \boldsymbol{m}^{43} & \boldsymbol{m}^{44} & \boldsymbol{m}^{45} \\ \boldsymbol{m}^{51} & \boldsymbol{m}^{52} & \boldsymbol{m}^{53} & \boldsymbol{m}^{54} & \boldsymbol{m}^{55} \end{pmatrix}_{\text{aKim}} =$$

$$\begin{pmatrix} \boldsymbol{a} - \tilde{\boldsymbol{g}}\boldsymbol{t}\boldsymbol{g} & \tilde{\boldsymbol{b}} - \tilde{\boldsymbol{g}}\boldsymbol{t}\boldsymbol{h} & \tilde{\boldsymbol{g}}\boldsymbol{t} & \boldsymbol{m}^{14} - \tilde{\boldsymbol{g}}\boldsymbol{t}\boldsymbol{m}^{34} & \boldsymbol{m}^{15} - \tilde{\boldsymbol{g}}\boldsymbol{t}\boldsymbol{m}^{35} \\ \boldsymbol{b} - \tilde{\boldsymbol{h}}\boldsymbol{t}\boldsymbol{g} & \boldsymbol{c} - \tilde{\boldsymbol{h}}\boldsymbol{t}\boldsymbol{h} & \tilde{\boldsymbol{h}}\boldsymbol{t} & \boldsymbol{m}^{24} - \tilde{\boldsymbol{h}}\boldsymbol{t}\boldsymbol{m}^{34} & \boldsymbol{m}^{25} - \tilde{\boldsymbol{h}}\boldsymbol{t}\boldsymbol{m}^{35} \\ -\boldsymbol{t}\boldsymbol{g} & -\boldsymbol{t}\boldsymbol{h} & \boldsymbol{t} & -\boldsymbol{t}\boldsymbol{m}^{34} & -\boldsymbol{t}\boldsymbol{m}^{35} \\ \boldsymbol{m}^{41} - \boldsymbol{m}^{43}\boldsymbol{t}\boldsymbol{g} & \boldsymbol{m}^{42} - \boldsymbol{m}^{43}\boldsymbol{t}\boldsymbol{h} & \boldsymbol{m}^{43}\boldsymbol{t} & \boldsymbol{m}^{44} - \boldsymbol{m}^{43}\boldsymbol{t}\boldsymbol{m}^{34} & \boldsymbol{m}^{45} - \boldsymbol{m}^{43}\boldsymbol{t}\boldsymbol{m}^{35} \\ \boldsymbol{m}^{51} - \boldsymbol{m}^{53}\boldsymbol{t}\boldsymbol{g} & \boldsymbol{m}^{52} - \boldsymbol{m}^{53}\boldsymbol{t}\boldsymbol{h} & \boldsymbol{m}^{53}\boldsymbol{t} & \boldsymbol{m}^{54} - \boldsymbol{m}^{53}\boldsymbol{t}\boldsymbol{m}^{34} & \boldsymbol{m}^{55} - \boldsymbol{m}^{53}\boldsymbol{t}\boldsymbol{m}^{35} \end{pmatrix}. \tag{A.22}$$

[Thanks to Michael 'Dalston Junction' Dallaston and Jonathan Ramalheira-Tsu for

helpful discussions on this operation.]

A.2 Other useful things

A.2.1 Note on resistance scalar function notation

In the literature, the scalar functions are typically written for two identical particles $1, 2$ in the form $W^P_{\alpha\tilde{\alpha}}$, for $W \in \{X, Y, Z\}$ and $\alpha, \tilde{\alpha} \in \{1, 2\}$. The unit displacement tensors $\boldsymbol{L}^E$ are written in terms of the unit displacement vector $\boldsymbol{d} = (\boldsymbol{x}^2 - \boldsymbol{x}^1)/s$.

In our notation, for two particles, the the unit displacement tensors L^E are written in terms of the unit displacement vector $\boldsymbol{d} = (\boldsymbol{x}^2 - \boldsymbol{x}^1)/s$ or $\boldsymbol{d} = (\boldsymbol{x}^1 - \boldsymbol{x}^2)/s$, depending on whether we are considering the effect of particle 1 on particle 2, or the effect of particle 2 on particle 1. For $\boldsymbol{L}^E$ tensors with an even product of $\boldsymbol{d}$s, this gives no change, but for those with an odd product (those in $\boldsymbol{B}$ and $\boldsymbol{G}$), we will get a sign difference. This sign difference is absorbed into the scalar function W.

If $\lambda = a_2/a_1$ and s' is the scaled particle separation, $s' = 2s/(a_1+a_2)$, the conversion from literature notation to ours is as follows:

$$\begin{aligned} &W^P_{11} \to W^P_1(s', \lambda), && W^P_{12} \to W^P_2(s', \lambda), \\ &W^P_{21} \to \kappa W^P_2(s', 1/\lambda), && W^P_{22} \to \kappa W^P_1(s', 1/\lambda), \end{aligned} \tag{A.23}$$

where $\kappa = -1$ for $P \in \{B, G\}$ for the reasons stated above, and $\kappa = 1$ otherwise.

The literature notation approach is favoured for the 'sum over all two-particle matrices' formation of eq. (2.65), since every matrix generated only involves two identical particles. For our more direct approach, dealing directly with N^α non-identical particles, we need to be more precise about the definitions of these functions.

A.2.2 Near-field asymptotic forms of the scalar resistance functions

The scalar resistance functions $X^P_\gamma(s', \lambda)$, $Y^P_\gamma(s', \lambda)$, $Z^P_\gamma(s', \lambda)$, introduced in section 2.4.3, where $\boldsymbol{P}$ is the relevant component tensor, are found numerically using 2-sphere code from Wilson (2013). For $s' \ll 1$ and $s' \ll \lambda$ there are asymptotic forms from Jeffrey & Onishi (1984) and Jeffrey (1992). In the notation of Jeffrey & Onishi (1984), $\xi = s' - 2$.

Since these papers were published, a number of errors have been found, as well as omissions of formulae required to generate these expressions (and therefore the value of these functions) independently. A partial list of errata has been published by Kengo Ichiki (`http://ryuon.sourceforge.net/twobody/errata.html`), and some of these errors appear to have been noticed by authors using this paper in their extensions.

This short section, then, aims to be a comprehensive description of how to fully generate, from scratch, expressions for these functions. Omissions have been unomitted and errors have been fixed. Throughout, the relevant equations will be referenced, with corrections where necessary. Equations from Jeffrey & Onishi (1984) are labelled (JO 1.1), those from Jeffrey (1992) are labelled (J 1), and those from the helpful Ichiki *et al.* (2013) are labelled (I 1).

After finding the relevant terms, to match the far-field forms, the terms

$$X^A, Y^A, Y^B, X^C, Y^C, X^G, Y^G, Y^H, X^M, Y^M, Z^M \tag{A.24}$$

are scaled by multiplying respectively by

$$1,\ 1,\ -\frac{2}{3},\ \frac{4}{3},\ \frac{4}{3},\ -\frac{2}{3},\ -\frac{2}{3},\ \frac{4}{3},\ \frac{10}{9},\ \frac{10}{9},\ \frac{10}{9}. \tag{A.25}$$

X^A terms

Here the X^A formulae are given in full, with changes from the source material when noted. The same directions for alteration, when required, will be given for the other terms in later sections.

Set up the recurrence relations

$$P_{n00} = \delta_{1n}, \tag{A.26}$$

$$V_{n00} = \delta_{1n}, \tag{A.27}$$

$$V_{npq} = P_{npq} - \frac{2n}{(n+1)(2n+3)} \sum_{s=1}^{q} \binom{n+s}{n} P_{s(q-s)(p-n-1)}, \tag{A.28}$$

$$\begin{aligned} P_{npq} = \sum_{s=1}^{q} \binom{n+s}{n} \Bigg(& \frac{n(2n+1)(2ns-n-s+2)}{2(n+1)(2s-1)(n+s)} P_{s(q-s)(p-n+1)} \\ & - \frac{n(2n-1)}{2(n+1)} P_{s(q-s)(p-n-1)} - \frac{n\left(4n^2-1\right)}{2(n+1)(2s+1)} V_{s(q-s-2)(p-n+1)} \Bigg), \end{aligned} \tag{A.29}$$

(JO 3.6–3.9). Then define the formulae

$$f_k(\lambda) = 2^k \sum_{q=0}^{k} P_{1(k-q)q} \lambda^q, \tag{A.30}$$

$$g_1(\lambda) = 2\lambda^2(1+\lambda)^{-3}, \tag{A.31}$$

$$g_2(\lambda) = \frac{1}{5}\lambda(1+7\lambda+\lambda^2)(1+\lambda)^{-3}, \tag{A.32}$$

$$g_3(\lambda) = \frac{1}{42}(1+18\lambda-29\lambda^2+18\lambda^3+\lambda^4)(1+\lambda)^{-3}, \tag{A.33}$$

$$m_1(m) = -2\delta_{m2} + (m-2)(1-\delta_{m2}), \tag{A.34}$$

(JO 3.15, 3.19); and

$$A_{11}^X = 1 - \frac{1}{4}g_1 + \sum_{\substack{m=2 \\ m \text{ even}}}^{\infty} \left[2^{-m}(1+\lambda)^{-m} f_m - g_1 - 2m^{-1}g_2 + 4m^{-1}m_1^{-1}g_3\right], \tag{A.35}$$

$$-\frac{1}{2}(1+\lambda)A_{12}^X = \frac{1}{4}g_1 + 2g_2\log 2 - 2g_3 + \sum_{\substack{m=1 \\ m \text{ odd}}}^{\infty} \left[2^{-m}(1+\lambda)^{-m} f_m - g_1 - 2m^{-1}g_2 + 4m^{-1}m_1^{-1}g_3\right], \tag{A.36}$$

(JO 3.22–3.23). Then the resistance scalars are given by

$$X_{11}^A = g_1\xi^{-1} + g_2\log(\xi^{-1}) + A_{11}^X + g_3\xi\log(\xi^{-1}), \tag{A.37}$$

$$-X_{12}^A = g_1\xi^{-1} + g_2\log(\xi^{-1}) - \frac{1}{2}(1+\lambda)A_{12}^X + g_3\xi\log(\xi^{-1}), \tag{A.38}$$

from (JO 3.17–3.18) up to $O(\xi\log(\xi^{-1}))$: note the different factor on X_{12}^A.

Y^A terms

The recurrence relations are (JO 4.6–4.11), but with V_{npq} corrected to

$$V_{npq} = P_{npq} + \frac{2n}{(n+1)(2n+3)} \sum_{s=1}^{q} \binom{n+s}{n+1} P_{s(q-s)(p-n-1)}, \tag{A.39}$$

noticing the sign change on the 1 in the last subscript.

The required intermediate formulae for the f, g and m functions are eq. (A.30), (JO 4.16–4.17), and eq. (A.34), respectively.

Then the A^Y terms are given by (JO-4.17–4.18), leaving us with the resistance scalar

formulae,

$$Y_{11}^A = g_2 \log(\xi^{-1}) + A_{11}^Y + g_3 \xi \log(\xi^{-1}), \tag{A.40}$$

$$-Y_{12}^A = g_2 \log(\xi^{-1}) - \frac{1}{2}(1+\lambda) A_{12}^Y + g_3 \xi \log(\xi^{-1}), \tag{A.41}$$

from (JO 4.15–4.16), with a different factor on Y_{12}^A.

Y^B terms

The recurrence relations are the same as those for the Y^A terms. The required intermediate formulae for the f, g and m functions are

$$f_k(\lambda) = 2^{k+1} \sum_{q=0}^{k} Q_{1(k-q)q} \lambda^q, \tag{A.42}$$

(JO between 5.6 and 5.7), and eq. (A.34), respectively.

The B^Y terms are given by

$$B_{11}^Y = 2g_2 \log 2 - 2g_3 + \sum_{\substack{m=1 \\ m \text{ odd}}}^{\infty} \left[2^{-m} (1+\lambda)^{-m} f_m - 2m^{-1} g_2 + 4m^{-1} m_1^{-1} g_3 \right], \tag{A.43}$$

$$-\frac{1}{4}(1+\lambda)^2 B_{12}^Y = -g_3 \; + \sum_{\substack{m=2 \\ m \text{ even}}}^{\infty} \left[2^{-m} (1+\lambda)^{-m} f_m - 2m^{-1} g_2 + 4m^{-1} m_1^{-1} g_3 \right], \tag{A.44}$$

having been corrected from (JO 5.7–5.8).

Then the resistance scalars are given by

$$Y_{11}^B = g_2 \log(\xi^{-1}) + \frac{2}{3} B_{11}^Y + g_3 \xi \log(\xi^{-1}), \tag{A.45}$$

$$-Y_{12}^B = g_2 \log(\xi^{-1}) - \frac{1}{4}(1+\lambda)^2 B_{12}^Y + g_3 \xi \log(\xi^{-1}), \tag{A.46}$$

from (JO 5.5–5.6), with a different factor on Y_{12}^B, and noting a correction to the B_{11}^Y term.

X^C terms

Expressions for the resistance scalars can be expressed directly as

$$X_{11}^C = \frac{\lambda^3}{(1+\lambda)^3}\zeta\left(3, \frac{\lambda}{1+\lambda}\right) - \frac{\lambda^2}{4(1+\lambda)}\xi\log(\xi^{-1}), \tag{A.47}$$

$$X_{12}^C = -\frac{\lambda^3}{(1+\lambda)^3}\zeta(3,1) + \frac{\lambda^2}{4(1+\lambda)}\xi\log(\xi^{-1}), \tag{A.48}$$

(JO 6.9–6.10), where X_{12}^C has been divided by $8/(1+\lambda)^3$, and where $\zeta(z,a)$ is the Hurwitz zeta function,

$$\zeta(z,a) = \sum_{k=0}^{\infty}\frac{1}{(k+a)^z}. \tag{A.49}$$

Y^C terms

The recurrence relations are the same as those for the Y^A terms except the initial conditions are replaced by (JO 7.3–7.5).

The intermediate formula for the f function is

$$f_k(\lambda) = 2^k\sum_{q=0}^{k} Q_{1(k-q)q}\lambda^{q+(k \bmod 2)}, \tag{A.50}$$

with the g formula given by (JO between 7.10 and 7.11), with the correction to g_5 of

$$g_5(\lambda) = \frac{2}{125}\lambda(43 - 24\lambda + 43\lambda^2)(1+\lambda)^{-4}. \tag{A.51}$$

The m function is again given by eq. (A.34).

Then the C^Y terms are

$$C_{11}^Y = 1 - g_3 + \sum_{\substack{m=2\\ m \text{ even}}}^{\infty}\left[2^{-m}(1+\lambda)^{-m}f_m - 2m^{-1}g_2 + 4m^{-1}m_1^{-1}g_3\right], \tag{A.52}$$

$$C_{12}^Y = 2g_4\log 2 - 2g_5 \; + \sum_{\substack{m=1\\ m \text{ odd}}}^{\infty}\left[2^{3-m}(1+\lambda)^{3-m}f_m - 2m^{-1}g_4 + 4m^{-1}m_1^{-1}g_5\right], \tag{A.53}$$

noting the corrections to both of (JO 7.11-7.12).

The resistance scalars are finally

$$Y_{11}^C = g_2 \log(\xi^{-1}) + C_{11}^Y + g_3 \xi \log(\xi^{-1}), \tag{A.54}$$

$$\frac{8}{(1+\lambda)^3} Y_{12}^C = g_4 \log(\xi^{-1}) + C_{12}^Y + g_5 \xi \log(\xi^{-1}), \tag{A.55}$$

noting the different factor on Y_{12}^C from (JO 7.9–7.10).

X^G terms

The recurrence relations are the same as those for X^A, and the f and g functions are (I 94) and (J between 19b and 20a). The G^X terms are given by (J 21), noting that in their notation, $\tilde{f}(\lambda) = 2^{-m} f(\lambda)$. This gives us expressions for X^G of

$$X_{11}^G = g_1 \xi^{-1} + g_2 \log(\xi^{-1}) + G_{11}^X + g_3 \xi \log(\xi^{-1}), \tag{A.56}$$

$$X_{12}^G = -g_1 \xi^{-1} - g_2 \log(\xi^{-1}) + \frac{1}{4}(1+\lambda)^2 G_{12}^X - g_3 \xi \log(\xi^{-1}), \tag{A.57}$$

from (J 19) with a different factor on the X_{12}^G.

Y^G terms

The recurrence relations are the same as those for Y^A, and the f and g functions are (I 115) and (J between 27b and 28a). The G^Y terms are given by (J 29), giving us expressions for Y^G of

$$Y_{11}^G = g_2 \log(\xi^{-1}) + G_{11}^Y + g_3 \xi \log(\xi^{-1}), \tag{A.58}$$

$$Y_{12}^G = -g_2 \log(\xi^{-1}) + \frac{1}{4}(1+\lambda)^2 G_{12}^Y - g_3 \xi \log(\xi^{-1}), \tag{A.59}$$

from (J 27) with a different factor on the Y_{12}^G.

Y^H terms

The recurrence relations are the same as those for Y^C, and the f and g functions are (I 120) and (J between 35b and 36a). The G^Y terms are given by (J 37), giving us expressions for Y^H of

$$Y_{11}^H = g_2 \log(\xi^{-1}) + H_{11}^Y + g_3 \xi \log(\xi^{-1}), \tag{A.60}$$

$$Y_{12}^H = g_5 \log(\xi^{-1}) + \frac{1}{8}(1+\lambda)^3 H_{12}^Y + g_6 \xi \log(\xi^{-1}), \tag{A.61}$$

from (J 35) with a different factor on the Y_{12}^H.

X^M terms

The recurrence relations are the same as those for X^A, but with the different initial conditions (J 44). The f and g functions are given by (I 105) and (J between 48b and 49a). The M^X terms are given by (J 50), giving us expressions for X^M of

$$X_{11}^M = g_1\xi^{-1} + g_2\log(\xi^{-1}) + M_{11}^X + g_3\xi\log(\xi^{-1}), \tag{A.62}$$

$$X_{12}^M = g_4\xi^{-1} + g_5\log(\xi^{-1}) + \frac{1}{8}(1+\lambda)^3 M_{12}^X + g_6\xi\log(\xi^{-1}), \tag{A.63}$$

from (J 48) with a different factor on the X_{12}^M.

Y^M terms

The recurrence relations are the same as those for Y^A, but with the different initial conditions (J 58). The f and g functions are given by (I 125) and (J between 64b and 65a). The M^Y terms are given by (J 66), giving us expressions for Y^M of

$$Y_{11}^M = g_2\log(\xi^{-1}) + M_{11}^Y + g_3\xi\log(\xi^{-1}), \tag{A.64}$$

$$Y_{12}^M = g_5\log(\xi^{-1}) + \frac{1}{8}(1+\lambda)^3 M_{12}^Y + g_6\xi\log(\xi^{-1}), \tag{A.65}$$

from (J 64) with a different factor on the Y_{12}^M.

Z^M terms

The recurrence relations are (J 73–76). The f and g functions are given by (I 131) and (J between 79b and 80a). The M^Z terms are given by (J 81), giving us expressions for Z^M of

$$Z_{11}^M = M_{11}^Z + g_3\xi\log(\xi^{-1}), \tag{A.66}$$

$$Z_{12}^M = \frac{1}{8}(1+\lambda)^3 M_{12}^Z - g_3\xi\log(\xi^{-1}), \tag{A.67}$$

from (J 79) with a different factor on the Z_{12}^M.

A.2.3 Derivatives of the Oseen tensor

Recall that

$$J_{ij}(\boldsymbol{r}) = \frac{\delta_{ij}}{r} + \frac{r_i r_j}{r^3}, \tag{A.68}$$

$$R_{ij}(\boldsymbol{r}) = -\frac{1}{2}\varepsilon_{jk\ell}\nabla_k J_{i\ell}(\boldsymbol{r}), \tag{A.69}$$

$$K_{ijk}(\boldsymbol{r}) = \frac{1}{2}\left(\nabla_k J_{ij}(\boldsymbol{r}) + \nabla_j J_{ik}(\boldsymbol{r})\right). \tag{A.70}$$

Then

$$\nabla_\ell r = \frac{r_\ell}{r}, \tag{A.71}$$

$$\nabla^2 r = \frac{2}{r}, \tag{A.72}$$

$$\nabla_\ell J_{ij}(\boldsymbol{r}) = \frac{1}{r^3}\left(-\delta_{ij}r_\ell + \delta_{i\ell}r_j + \delta_{j\ell}r_i\right) - \frac{3}{r^5}r_i r_j r_\ell, \tag{A.73}$$

$$\begin{aligned}\nabla_m\nabla_\ell J_{ij}(\boldsymbol{r}) = {}& \frac{1}{r^3}\left(-\delta_{ij}\delta_{\ell m} + \delta_{i\ell}\delta_{jm} + \delta_{j\ell}\delta_{im}\right) + \frac{15}{r^7}r_i r_j r_\ell r_m \\ & - \frac{3}{r^5}\left(-\delta_{ij}r_\ell r_m + \delta_{i\ell}r_j r_m + \delta_{j\ell}r_i r_m + \delta_{im}r_j r_\ell + r_i\delta_{jm}r_\ell + r_i r_j\delta_{\ell m}\right),\end{aligned} \tag{A.74}$$

$$\nabla_\ell R_{ij}(\boldsymbol{r}) = -\frac{1}{2}\varepsilon_{jmn}\nabla_\ell\nabla_m J_{in}(\boldsymbol{r}), \tag{A.75}$$

$$\nabla_\ell K_{ijk}(\boldsymbol{r}) = \frac{1}{2}\left(\nabla_\ell\nabla_k J_{ij}(\boldsymbol{r}) + \nabla_\ell\nabla_j J_{ik}(\boldsymbol{r})\right), \tag{A.76}$$

$$\nabla^2 J_{ij}(\boldsymbol{r}) = \frac{2\delta_{ij}}{r^3} - \frac{6r_i r_j}{r^5}, \tag{A.77}$$

$$\nabla_k\nabla^2 J_{ij}(\boldsymbol{r}) = -\frac{6}{r^5}\left(\delta_{ij}r_k + \delta_{ik}r_j + \delta_{jk}r_i\right) + \frac{30}{r^7}r_i r_j r_k, \tag{A.78}$$

$$\nabla^2 R_{ij}(\boldsymbol{r}) = -\frac{1}{2}\varepsilon_{jk\ell}\nabla_k\nabla^2 J_{i\ell}(\boldsymbol{r}), \tag{A.79}$$

$$\nabla^2 K_{ijk}(\boldsymbol{r}) = \nabla_k\nabla^2 J_{ij}(\boldsymbol{r}), \tag{A.80}$$

$$\nabla_\ell\nabla^2 K_{ijk}(\boldsymbol{r}) = \nabla_\ell\nabla_k\nabla^2 J_{ij}(\boldsymbol{r}) \tag{A.81}$$

$$= -\frac{6}{r^5}\left(\delta_{ij}\delta_{k\ell} + \delta_{ik}\delta_{j\ell} + \delta_{jk}\delta_{i\ell}\right) - \frac{210}{r^9}r_i r_j r_k r_\ell \tag{A.82}$$

$$+ \frac{30}{r^7}\left(\delta_{ij}r_k r_\ell + \delta_{ik}r_j r_\ell + \delta_{jk}r_i r_\ell + \delta_{i\ell}r_j r_k + \delta_{j\ell}r_i r_k + \delta_{k\ell}r_i r_j\right),$$

$$\nabla^4 J_{ij}(\boldsymbol{r}) = 0. \tag{A.83}$$

A.2.4 Derivatives of the realspace periodic Oseen tensor, $\boldsymbol{J}^r$

Recall that the non-periodic Oseen tensor can be written

$$J_{ij}(\boldsymbol{r}) = [\delta_{ij}\nabla^2 - \nabla_i\nabla_j]r. \tag{A.84}$$

The realspace periodic Oseen tensor is then written as

$$J^r_{ij}(\boldsymbol{r}) = [\delta_{ij}\nabla^2 - \nabla_i\nabla_j](r\operatorname{erfc}\lambda r), \tag{A.85}$$

where $\operatorname{erfc} x = 1 - \operatorname{erf} x$, the complementary error function.

The derivatives of this function are then simply

$$\nabla_\ell J^r_{ij}(\boldsymbol{r}) = [\delta_{ij}\nabla_\ell\nabla^2 - \nabla_\ell\nabla_i\nabla_j](r\operatorname{erfc}\lambda r), \tag{A.86}$$
$$\nabla_m\nabla_\ell J^r_{ij}(\boldsymbol{r}) = [\delta_{ij}\nabla_m\nabla_\ell\nabla^2 - \nabla_m\nabla_\ell\nabla_i\nabla_j](r\operatorname{erfc}\lambda r), \tag{A.87}$$
$$\nabla^2 J^r_{ij}(\boldsymbol{r}) = [\delta_{ij}\nabla^4 - \nabla_i\nabla_j\nabla^2](r\operatorname{erfc}\lambda r), \tag{A.88}$$
$$\nabla_k\nabla^2 J^r_{ij}(\boldsymbol{r}) = [\delta_{ij}\nabla_k\nabla^4 - \nabla_k\nabla_i\nabla_j\nabla^2](r\operatorname{erfc}\lambda r), \tag{A.89}$$
$$\nabla_\ell\nabla_k\nabla^2 J^r_{ij}(\boldsymbol{r}) = [\delta_{ij}\nabla_\ell\nabla_k\nabla^4 - \nabla_\ell\nabla_k\nabla_i\nabla_j\nabla^2](r\operatorname{erfc}\lambda r). \tag{A.90}$$

The derivatives of $r\operatorname{erfc}\lambda r$ are computed in appendix A.2.5. The tensors $\boldsymbol{R}^r$, $\boldsymbol{K}^r$, and their derivatives, are mostly the same as in the non-periodic case but with $\boldsymbol{J}$ replaced with $\boldsymbol{J}^r$:

$$R^r_{ij}(\boldsymbol{r}) = -\frac{1}{2}\varepsilon_{jk\ell}\nabla_k J^r_{i\ell}(\boldsymbol{r}), \tag{A.91}$$
$$K^r_{ijk}(\boldsymbol{r}) = \frac{1}{2}\left[\nabla_k J^r_{ij}(\boldsymbol{r}) + \nabla_j J^r_{ik}(\boldsymbol{r})\right], \tag{A.92}$$
$$\nabla_\ell R^r_{ij}(\boldsymbol{r}) = -\frac{1}{2}\varepsilon_{jmn}\nabla_\ell\nabla_m J^r_{in}(\boldsymbol{r}), \tag{A.93}$$
$$\nabla_\ell K^r_{ijk}(\boldsymbol{r}) = \frac{1}{2}\left[\nabla_\ell\nabla_k J^r_{ij}(\boldsymbol{r}) + \nabla_\ell\nabla_j J^r_{ik}(\boldsymbol{r})\right], \tag{A.94}$$
$$\nabla^2 R^r_{ij}(\boldsymbol{r}) = -\frac{1}{2}\varepsilon_{jk\ell}\nabla_k\nabla^2 J^r_{i\ell}(\boldsymbol{r}), \tag{A.95}$$
$$\nabla^2 K^r_{ijk}(\boldsymbol{r}) = \frac{1}{2}\left[\nabla_k\nabla^2 J^r_{ij}(\boldsymbol{r}) + \nabla_j\nabla^2 J^r_{ik}(\boldsymbol{r})\right], \tag{A.96}$$
$$\nabla_\ell\nabla^2 K^r_{ijk}(\boldsymbol{r}) = \frac{1}{2}\left[\nabla_\ell\nabla_k\nabla^2 J^r_{ij}(\boldsymbol{r}) + \nabla_\ell\nabla_j\nabla^2 J^r_{ik}(\boldsymbol{r})\right]. \tag{A.97}$$

(Note that the definition of $\boldsymbol{K}^r$ is not the same as the non-periodic version, as the same symmetries are not present here.)

A.2.5 Derivatives of $r\operatorname{erfc}\lambda r$

The derivatives of $r\operatorname{erfc}\lambda r$ can be written in terms of derivatives of $\operatorname{erfc}\lambda r$ (see appendix A.2.6), as follows. First, we define

$$\kappa_{ij\ell} = \delta_{ij}r_\ell + \delta_{i\ell}r_j + \delta_{j\ell}r_i, \tag{A.98}$$
$$\kappa_{ij\ell m} = \delta_{ij}r_\ell r_m + \delta_{i\ell}r_j r_m + \delta_{j\ell}r_i r_m + \delta_{im}r_j r_\ell + \delta_{jm}r_i r_\ell + \delta_{\ell m}r_i r_j, \tag{A.99}$$

$$\delta_{ij\ell m} = \delta_{ij}\delta_{\ell m} + \delta_{j\ell}\delta_{im} + \delta_{i\ell}\delta_{jm}, \tag{A.100}$$

$$r_{ij\ell} = r_i r_j r_\ell, \tag{A.101}$$

$$r_{ij\ell m} = r_i r_j r_\ell r_m. \tag{A.102}$$

Then,

$$\nabla_j(r\operatorname{erfc}\lambda r) = \frac{r_j}{r}\operatorname{erfc}(\lambda r) + r_j\operatorname{erfc}^{(1)}(\lambda r), \tag{A.103}$$

$$\begin{aligned}\nabla_i\nabla_j(r\operatorname{erfc}\lambda r) = &\left[\frac{\delta_{ij}}{r} - \frac{r_i r_j}{r^3}\right]\operatorname{erfc}(\lambda r)\\ &+ \left[\delta_{ij} + \frac{r_i r_j}{r^2}\right]\operatorname{erfc}^{(1)}(\lambda r)\\ &+ \frac{r_i r_j}{r}\operatorname{erfc}^{(2)}(\lambda r),\end{aligned} \tag{A.104}$$

$$\begin{aligned}\nabla_i\nabla_j\nabla_\ell(r\operatorname{erfc}\lambda r) = &\left[-\frac{\kappa_{ij\ell}}{r^3} + \frac{3r_{ij\ell}}{r^5}\right]\operatorname{erfc}(\lambda r)\\ &- \left[-\frac{\kappa_{ij\ell}}{r^2} + \frac{3r_{ij\ell}}{r^4}\right]\operatorname{erfc}^{(1)}(\lambda r)\\ &+ \frac{\kappa_{ij\ell}}{r}\operatorname{erfc}^{(2)}(\lambda r)\\ &+ \frac{r_i r_j r_\ell}{r^2}\operatorname{erfc}^{(3)}(\lambda r),\end{aligned} \tag{A.105}$$

$$\begin{aligned}\nabla_i\nabla_j\nabla_\ell\nabla_m(r\operatorname{erfc}\lambda r) = &\left[-\frac{\delta_{ij\ell m}}{r^3} + \frac{3\kappa_{ij\ell m}}{r^5} - \frac{15r_{ij\ell m}}{r^7}\right]\operatorname{erfc}(\lambda r)\\ &- \left[-\frac{\delta_{ij\ell m}}{r^2} + \frac{3\kappa_{ij\ell m}}{r^4} - \frac{15r_{ij\ell m}}{r^6}\right]\operatorname{erfc}^{(1)}(\lambda r)\\ &+ \left[\frac{\delta_{ij\ell m}}{r} - \frac{3r_{ij\ell m}}{r^5}\right]\operatorname{erfc}^{(2)}(\lambda r)\\ &+ \left[\frac{\kappa_{ij\ell m}}{r^2} - \frac{2r_{ij\ell m}}{r^4}\right]\operatorname{erfc}^{(3)}(\lambda r)\\ &+ \frac{r_{ij\ell m}}{r^3}\operatorname{erfc}^{(4)}(\lambda r),\end{aligned} \tag{A.106}$$

$$\nabla^2(r\operatorname{erfc}\lambda r) = \frac{2}{r}\operatorname{erfc}(\lambda r) + 4\operatorname{erfc}^{(1)}(\lambda r) + r\operatorname{erfc}^{(2)}(\lambda r), \tag{A.107}$$

$$\begin{aligned}\nabla_\ell\nabla^2(r\operatorname{erfc}\lambda r) = &-\frac{2r_\ell}{r^3}\operatorname{erfc}(\lambda r) + \frac{2r_\ell}{r^2}\operatorname{erfc}^{(1)}(\lambda r)\\ &+ \frac{5r_\ell}{r}\operatorname{erfc}^{(2)}(\lambda r) + r_\ell\operatorname{erfc}^{(3)}(\lambda r),\end{aligned} \tag{A.108}$$

$$\begin{aligned}\nabla_\ell\nabla_m\nabla^2(r\operatorname{erfc}\lambda r) = &\left[\frac{-2\delta_{\ell m}}{r^3} + \frac{6r_\ell r_m}{r^5}\right]\operatorname{erfc}(\lambda r)\\ &- \left[\frac{-2\delta_{\ell m}}{r^2} + \frac{6r_\ell r_m}{r^4}\right]\operatorname{erfc}^{(1)}(\lambda r)\\ &+ \left[\frac{5\delta_{\ell m}}{r} - \frac{3r_\ell r_m}{r^3}\right]\operatorname{erfc}^{(2)}(\lambda r)\\ &+ \left[\delta_{\ell m} + \frac{5r_\ell r_m}{r^2}\right]\operatorname{erfc}^{(3)}(\lambda r)\end{aligned}$$

$$+\frac{r_\ell r_m}{r}\operatorname{erfc}^{(4)}(\lambda r), \tag{A.109}$$

$$\begin{aligned}\nabla_i\nabla_j\nabla_k\nabla^2(r\operatorname{erfc}\lambda r) =& \left[\frac{6\kappa_{ijk}}{r^5}-\frac{30r_{ijk}}{r^7}\right]\operatorname{erfc}(\lambda r)\\ &-\left[\frac{6\kappa_{ijk}}{r^4}-\frac{30r_{ijk}}{r^6}\right]\operatorname{erfc}^{(1)}(\lambda r)\\ &+\left[\frac{-3\kappa_{ijk}}{r^3}+\frac{3r_{ijk}}{r^5}\right]\operatorname{erfc}^{(2)}(\lambda r)\\ &+\left[\frac{5\kappa_{ijk}}{r^2}-\frac{13r_{ijk}}{r^4}\right]\operatorname{erfc}^{(3)}(\lambda r)\\ &+\left[\frac{\kappa_{ijk}}{r}+\frac{4r_{ijk}}{r^3}\right]\operatorname{erfc}^{(4)}(\lambda r)\\ &+\frac{r_{ijk}}{r^2}\operatorname{erfc}^{(5)}(\lambda r),\end{aligned} \tag{A.110}$$

$$\begin{aligned}\nabla_i\nabla_j\nabla_k\nabla_\ell\nabla^2(r\operatorname{erfc}\lambda r) =& \left[\frac{6\delta_{ijk\ell}}{r^5}-\frac{30\kappa_{ijk\ell}}{r^7}+\frac{210r_{ijk\ell}}{r^9}\right]\operatorname{erfc}(\lambda r)\\ &-\left[\frac{6\delta_{ijk\ell}}{r^4}-\frac{30\kappa_{ijk\ell}}{r^6}+\frac{210r_{ijk\ell}}{r^8}\right]\operatorname{erfc}^{(1)}(\lambda r)\\ &+\left[\frac{-3\delta_{ijk\ell}}{r^3}+\frac{3\kappa_{ijk\ell}}{r^5}+\frac{15r_{ijk\ell}}{r^7}\right]\operatorname{erfc}^{(2)}(\lambda r)\\ &+\left[\frac{5\delta_{ijk\ell}}{r^2}-\frac{13\kappa_{ijk\ell}}{r^4}+\frac{55r_{ijk\ell}}{r^6}\right]\operatorname{erfc}^{(3)}(\lambda r)\\ &+\left[\frac{\delta_{ijk\ell}}{r}+\frac{4\kappa_{ijk\ell}}{r^3}-\frac{25r_{ijk\ell}}{r^5}\right]\operatorname{erfc}^{(4)}(\lambda r)\\ &+\left[\frac{\kappa_{ijk\ell}}{r^2}+\frac{2r_{ijk\ell}}{r^4}\right]\operatorname{erfc}^{(5)}(\lambda r)\\ &+\frac{r_{ijk\ell}}{r^3}\operatorname{erfc}^{(6)}(\lambda r),\end{aligned} \tag{A.111}$$

$$\nabla^4(r\operatorname{erfc}\lambda r) = \frac{12}{r}\operatorname{erfc}^{(2)}(\lambda r)+8\operatorname{erfc}^{(3)}(\lambda r)+r\operatorname{erfc}^{(4)}(\lambda r), \tag{A.112}$$

$$\begin{aligned}\nabla_\ell\nabla^4(r\operatorname{erfc}\lambda r) =& -\frac{12r_\ell}{r^3}\operatorname{erfc}^{(2)}(\lambda r)+\frac{12r_\ell}{r^2}\operatorname{erfc}^{(3)}(\lambda r)\\ &+\frac{9r_\ell}{r}\operatorname{erfc}^{(4)}(\lambda r)+r_\ell\operatorname{erfc}^{(5)}(\lambda r),\end{aligned} \tag{A.113}$$

$$\begin{aligned}\nabla_\ell\nabla_m\nabla^4(r\operatorname{erfc}\lambda r) =& \left[\frac{-12\delta_{\ell m}}{r^3}+\frac{36r_\ell r_m}{r^5}\right]\operatorname{erfc}^{(2)}(\lambda r)\\ &-\left[\frac{-12\delta_{\ell m}}{r^2}+\frac{36r_\ell r_m}{r^4}\right]\operatorname{erfc}^{(3)}(\lambda r)\\ &+\left[\frac{9\delta_{\ell m}}{r}+\frac{3r_\ell r_m}{r^3}\right]\operatorname{erfc}^{(4)}(\lambda r)\\ &+\left[\delta_{\ell m}+\frac{9r_\ell r_m}{r^2}\right]\operatorname{erfc}^{(5)}(\lambda r)\\ &+\frac{r_\ell r_m}{r}\operatorname{erfc}^{(6)}(\lambda r).\end{aligned} \tag{A.114}$$

A.2.6 Derivatives of $\operatorname{erfc}\lambda r$

Defining

$$E = \frac{2}{\sqrt{\pi}}\lambda \exp(-s^2\lambda^2), \tag{A.115}$$

then the derivatives of $\operatorname{erfc}\lambda r$ are given by

$$\operatorname{erfc}^{(1)}(\lambda r) = -E, \tag{A.116}$$
$$\operatorname{erfc}^{(2)}(\lambda r) = 2\lambda^2 r E, \tag{A.117}$$
$$\operatorname{erfc}^{(3)}(\lambda r) = -2\lambda^2 E(2\lambda^2 r^2 - 1), \tag{A.118}$$
$$\operatorname{erfc}^{(4)}(\lambda r) = 4\lambda^4 r E(2\lambda^2 r^2 - 3), \tag{A.119}$$
$$\operatorname{erfc}^{(5)}(\lambda r) = -4\lambda^4 E(4\lambda^4 r^4 - 12\lambda^2 r^2 + 3), \tag{A.120}$$
$$\operatorname{erfc}^{(6)}(\lambda r) = 8\lambda^6 r E(4\lambda^4 r^4 - 20\lambda^2 r^2 + 15). \tag{A.121}$$

A.2.7 Fourier-transformed derivatives of the wavespace periodic Oseen tensor, $\widehat{\boldsymbol{J}^k}$

The wavespace periodic Oseen tensor is given by

$$J^k_{ij}(\boldsymbol{r}) = [\delta_{ij}\nabla^2 - \nabla_i\nabla_j](r \operatorname{erf}\lambda r). \tag{A.122}$$

This tensor decays slowly in realspace (r), but we find that if we Fourier transform it, that it decays quickly in wavespace (k). There are equivalent definitions of the Fourier transform, but following Beenakker (1986), with the conversion to wavespace as in eq. (2.148), we give the Fourier transform of a function $f(\boldsymbol{r})$ as

$$\hat{f}(\boldsymbol{r}) = \int f(\boldsymbol{r}) \exp(\mathrm{i}\boldsymbol{k}\cdot\boldsymbol{r})\,\mathrm{d}\boldsymbol{r}. \tag{A.123}$$

Recalling the useful property of Fourier transforms that

$$\widehat{\nabla_j f}(\boldsymbol{r}) = \mathrm{i}k_j\hat{f}(\boldsymbol{k}), \tag{A.124}$$

the Fourier transform of $\boldsymbol{J}^k$ is therefore

$$\widehat{J^k_{ij}}(\boldsymbol{k}) = \mathscr{F}[J^k_{ij}](\boldsymbol{k}) = -(\delta_{ij}k^2 - k_ik_j)\int r \operatorname{erf}(\lambda r)\exp(\mathrm{i}\boldsymbol{k}\cdot\boldsymbol{r})\,\mathrm{d}\boldsymbol{r} \tag{A.125}$$
$$= (\delta_{ij}k^2 - k_ik_j)\frac{8\pi}{k^4}\left(1 + \frac{k^2}{4\lambda^2} + \frac{k^4}{8\lambda^4}\right)\exp\left(-\frac{k^2}{4\lambda^2}\right), \tag{A.126}$$

with the final integral evaluated by Beenakker (1986) (note the disappearance of the minus sign). The required tensors are then

$$\mathscr{F}[\nabla_m \nabla_\ell J^k_{ij}](\boldsymbol{k}) = -k_m k_\ell \mathscr{F}[J^k_{ij}](\boldsymbol{k}), \tag{A.127}$$

$$\mathscr{F}[\nabla_\ell R^k_{ij}](\boldsymbol{k}) = -\frac{1}{2}\varepsilon_{jmn}\mathscr{F}[\nabla_\ell \nabla_m J^k_{in}](\boldsymbol{k}), \tag{A.128}$$

$$\mathscr{F}[\nabla_\ell K^k_{ijk}](\boldsymbol{k}) = \frac{1}{2}\left(\mathscr{F}[\nabla_\ell \nabla_k J^k_{ij}](\boldsymbol{k}) + \mathscr{F}[\nabla_\ell \nabla_j J^k_{ik}](\boldsymbol{k})\right), \tag{A.129}$$

$$\mathscr{F}[\nabla^2 J^k_{ij}](\boldsymbol{k}) = -k^2 \mathscr{F}[J^k_{ij}](\boldsymbol{k}), \tag{A.130}$$

$$\mathscr{F}[\nabla_\ell \nabla^2 K^k_{ijk}](\boldsymbol{k}) = k_k k_\ell k^2 \mathscr{F}[J^k_{ij}](\boldsymbol{k}). \tag{A.131}$$

A.2.8 Wavespace periodic mobility tensors evaluated at 0 ($\boldsymbol{a}^k(\boldsymbol{0})$, etc.)

The definitions of the tensors $\boldsymbol{a}^k(\boldsymbol{r})$, etc., are the same as their non-periodic forms in table 2.1, but with $\boldsymbol{J}(\boldsymbol{r})$ replaced with $\boldsymbol{J}^k(\boldsymbol{r})$. The derived tensors $\boldsymbol{R}^k$ and $\boldsymbol{K}^k$, and their derivatives, are listed in eqs. (A.91) to (A.97), if $\boldsymbol{J}^r$ is replaced by $\boldsymbol{J}^k$. Then, the derivatives of $\boldsymbol{J}^k(\boldsymbol{r})$ are evaluated at $\boldsymbol{r} = \boldsymbol{0}$, from appendix A.2.9.

$$a^k_{ij}(\boldsymbol{0}) = \frac{1}{8\pi\mu}\left[\frac{8\lambda}{\sqrt{\pi}} - \frac{a_1^2 + a_2^2}{6}\cdot\frac{160\lambda^3}{3\sqrt{\pi}}\right]\delta_{ij}, \tag{A.132}$$

$$b^k_{ij}(\boldsymbol{0}) = 0, \tag{A.133}$$

$$c^k_{ij}(\boldsymbol{0}) = 0, \tag{A.134}$$

$$g^k_{ijk}(\boldsymbol{0}) = 0, \tag{A.135}$$

$$h^k_{ijk}(\boldsymbol{0}) = 0, \tag{A.136}$$

$$m^k_{ijk\ell}(\boldsymbol{0}) = \frac{1}{8\pi\mu}\left[-\frac{8\lambda^3}{3\sqrt{\pi}} + \frac{a_1^2 + a_2^2}{10}\cdot\frac{168\lambda^5}{5\sqrt{\pi}}\right](2\delta_{ij}\delta_{k\ell} - 3\delta_{ik}\delta_{j\ell} - 3\delta_{i\ell}\delta_{jk}). \tag{A.137}$$

A.2.9 Derivatives of the wavespace periodic Oseen tensor evaluated at 0, $\boldsymbol{J}^k(\boldsymbol{0})$

The wavespace periodic Oseen tensor is given by

$$J^k_{ij}(\boldsymbol{r}) = [\delta_{ij}\nabla^2 - \nabla_i\nabla_j](r \operatorname{erf} \lambda r). \tag{A.138}$$

Evaluated at $\boldsymbol{r} = \boldsymbol{0}$, we find explicitly that

$$J^k_{ij}(\boldsymbol{0}) = \frac{8\lambda}{\sqrt{\pi}}\delta_{ij}, \tag{A.139}$$

$$\nabla_\ell J^k_{ij}(\boldsymbol{0}) = 0, \tag{A.140}$$

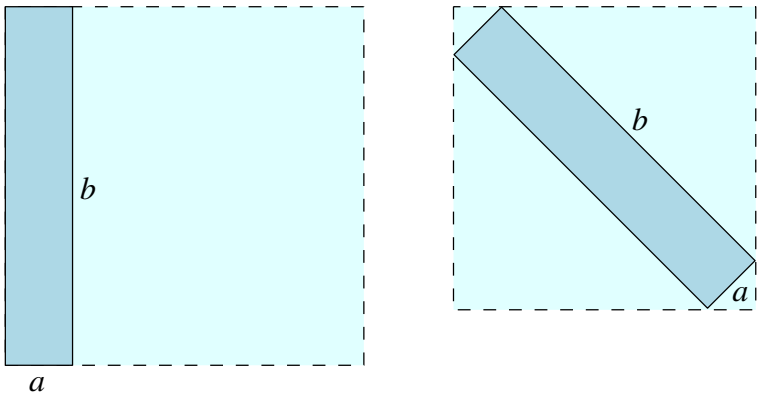

Figure A.1: For a rectangle where $a < (\sqrt{2}-1)b$, it is more efficient to lie it diagonally at 45° across a square than to simply place it in a square with side length equal to b.

$$\nabla_m \nabla_\ell J^k_{ij}(\mathbf{0}) = -\frac{16\lambda^3}{3\sqrt{\pi}}(4\delta_{ij}\delta_{\ell m} - \delta_{i\ell}\delta_{jm} - \delta_{im}\delta_{j\ell}), \tag{A.141}$$

$$\nabla^2 J^k_{ij}(\mathbf{0}) = -\frac{160\lambda^3}{3\sqrt{\pi}}\delta_{ij}, \tag{A.142}$$

$$\nabla_\ell \nabla^2 J^k_{ij}(\mathbf{0}) = 0, \tag{A.143}$$

$$\nabla_m \nabla_\ell \nabla^2 J^k_{ij}(\mathbf{0}) = \frac{336\lambda^5}{5\sqrt{\pi}}(4\delta_{ij}\delta_{\ell m} - \delta_{i\ell}\delta_{jm} - \delta_{im}\delta_{j\ell}). \tag{A.144}$$

A.2.10 Random distribution of particles

In chapter 4, particles are randomly distributed in a cell of a given size. We do this, in both 2D and 3D, using an adaptation of code from John Brady's group at Caltech. This code works using the Lubachevsky–Stillinger algorithm (Lubachevsky & Stillinger, 1990). Points corresponding to the number of required particles are randomly distributed through the cell, then are given random velocities. As the points move, they increase in size to become particles, colliding where appropriate, until they are the required size.

The particles are distributed in a periodic cubic (or square) cell. If we are not looking to use the full periodic cube, typically we choose the side length of the cube to be that of the largest side of the desired box. For narrow boxes, however, it is sometimes more efficient to lay the box diagonally across the cube. Specifically, in 2D and as shown in fig. A.1, it is more efficient to lie a rectangle with side lengths $a < b$ at 45° across a square, if $a < (\sqrt{2}-1)b$.

A.3 List of symbols

The typography in this thesis adheres to the following convention:

a, B, γ	scalars, sets,
$\boldsymbol{a}, \boldsymbol{B}, \boldsymbol{\gamma}$	vectors,
$\mathsf{a}, \mathsf{B}, \boldsymbol{\gamma}$	tensors, matrices,
$\mathcal{M}, \mathcal{R}$	mobility and resistance matrices.

This also extends to zero, so $\mathbf{0}$ and $\mathsf{0}$ are respectively the zero vector and the zero matrix or tensor,

$$\mathbf{0} = (0, 0, \dots, 0), \tag{A.145}$$

$$\mathsf{0} = \begin{pmatrix} 0 & 0 & \cdots & 0 \\ 0 & 0 & \cdots & 0 \\ \vdots & \vdots & \ddots & \vdots \\ 0 & 0 & \cdots & 0 \end{pmatrix}. \tag{A.146}$$

A list of common symbols found in the thesis and an internal reference for more information now follows.

Latin		**see**
A	force–velocity element of the resistance matrix	eq. (2.10)
	polymeric contribution to stress tensor	eq. (3.50c)
a	velocity–force element of the mobility matrix	eq. (2.10)
a	particle radius	
$\mathcal{B}$	basis for periodic domain, $\mathcal{B} = \{\boldsymbol{b}_1, \boldsymbol{b}_2, \boldsymbol{b}_3\}$	section 2.5
c	particle concentration in 2D (cf. ϕ, the 3D version)	eq. (5.26)
$\boldsymbol{d}$	unit displacement vector between two particles, $\boldsymbol{d} = \boldsymbol{r}/r$	section 4.3
E	rate of strain	eq. (2.4)
$\mathcal{E}$	contraction tensor	eq. (2.54)
$\mathcal{F}$	force moment vector, $\mathcal{F} = (\boldsymbol{F}, \boldsymbol{T}, \boldsymbol{S})$	section 2.4.3
$\mathscr{F}$	Fourier transform, $\mathscr{F}[f](k) = \hat{f}(k)$	eq. (A.125)
$\boldsymbol{F}$	force	
f	oscillation frequency (cf. ω, $\omega = 2\pi f$)	eq. (4.1)
G	relaxation modulus of fluid	eq. (3.3)
G'	storage modulus of fluid, representing elasticity	eq. (3.11)
G''	loss modulus of fluid, representing viscosity	eq. (3.11)
h	particle surface separation	figs. 2.19 and 5.4
$\Im$	imaginary part of a complex number	
I, I^i	identity tensor (of rank i)	eq. (A.4)
J	Oseen tensor, the Green's function for Stokes flow	eq. (2.14)
K	derivative of the Oseen tensor related to the stresslet	eq. (2.25)
$\boldsymbol{k}$	position in wavespace	eq. (2.148)

k	spring constant	eq. (3.32)
	repulsion force strength	eq. (4.5)
L	natural length of spring	section 3.2
$\boldsymbol{L}^i$	unit displacement tensors, $i \in \{1, \ldots, 9\}$	eq. (2.70)
ℓ	maximum length of spring	section 3.2
$\mathcal{M}$	mobility matrix, made from $\boldsymbol{a}$, $\boldsymbol{b}$, $\boldsymbol{c}$, $\boldsymbol{g}$, $\boldsymbol{h}$, $\boldsymbol{m}$	eq. (2.6)
$\mathcal{M}^\infty$	far-field mobility matrix	section 2.3
N^α, N^β	number of spheres or dumbbells (respectively) in our system	
$\boldsymbol{n}$, $\hat{\boldsymbol{n}}$	unit normal	eq. (5.10)
Q	contribution of third harmonic relative to first harmonic in large-amplitude oscillatory shear	eq. (3.45)
$\mathfrak{R}$	real part of a complex number	
$\mathcal{R}$	(grand) resistance matrix, made from $\boldsymbol{A}$, $\boldsymbol{B}$, $\boldsymbol{C}$, $\boldsymbol{G}$, $\boldsymbol{H}$, $\boldsymbol{M}$	eqs. (2.5) and (2.13)
$\mathcal{R}^{\mathrm{2B,exact}}$	two-body resistance matrix due to lubrication	section 2.3
$\mathcal{R}^{\mathrm{2B},\infty}$	two-body far-field resistance matrix	section 2.6.1
$\boldsymbol{R}$	rotlet	eq. (2.24)
$\boldsymbol{R}^{ij}$	ijth submatrix of $\mathcal{R}$	eq. (2.10)
Re	Reynolds number	section 2.2
$\boldsymbol{r}$	position	
r	distance, normally between two particles	
r^*	critical distance for which particles closer than this feel lubrication effects	eq. (2.12)
$\boldsymbol{S}$	stresslet	eq. (2.27) and fig. 2.3
S, S^α, S^β	surface of particle, or specifically surface of sphere or dumbbell	eq. (2.17) and section 2.4.5
s	separation distance of particles	section 2.4.2
s'	separation distance of particles, scaled on average particle size	section 2.4.2
$\boldsymbol{T}$	torque on particle	eq. (2.26) and fig. 2.3
$\mathcal{U}$	velocity moment vector, $\mathcal{U} = (\boldsymbol{U}, \boldsymbol{\Omega}, \boldsymbol{E})$	section 2.4.3
$\boldsymbol{U}$	particle velocity	
$\boldsymbol{u}$	fluid velocity	
$\boldsymbol{x}$	position	
X, Y, Z	resistance scalars	eq. (2.69) and appendix A.1
x, y, z	mobility scalars	appendix A.1

Greek		**see**
α	sphere	
	amplitude of oscillation	eq. (3.5)
β	dumbbell, composed of two beads a distance apart	
$\dot{\Gamma}$	dimensionless shear rate	eq. (5.25)
γ	shear	
$\dot{\gamma}$	shear rate	fig. 3.1
δ	Kronecker delta	eq. (2.14)
	phase difference between maximum shear and maximum amplitude in small-amplitude oscillatory shear	fig. 3.6
ε	Levi-Civita symbol	eq. (2.24)
η	effective viscosity of fluid	chapter 1

λ	size ratio of particles	section 2.4.2
	radius to switch between realspace and wavespace in periodic domains	eq. (2.143)
μ	viscosity of (background) fluid	eq. (1.1)
ν	coefficient of friction	section 5.1.2
Ξ, $\Xi^{\pm}$	mean dumbbell pitch	eq. (3.46)
$\boldsymbol{\sigma}$	stress tensor	eq. (2.4)
σ_0	maximum stress response to small-amplitude oscillatory shear	eq. (3.13)
τ	relaxation time of fluid	section 3.1.1
	parameter of repulsion decay length, $(\tau a)^{-1}$	eq. (4.5)
ϕ	particle concentration in 3D (cf. c, the 2D version)	eq. (1.2)
$\boldsymbol{\Omega}$	angular velocity	
ω	oscillation frequency (cf. f, $\omega = 2\pi f$)	eq. (3.5)

Bibliography

Adrian, D. W. & Giacomin, A. J. 1992 The quasi-periodic nature of a polyurethane melt in oscillatory shear. *Journal of Rheology* **36** (7), 1227–1243.

Ando, T., Chow, E. & Skolnick, J. 2013 Dynamic simulation of concentrated macromolecular solutions with screened long-range hydrodynamic interactions: Algorithm and limitations. *The Journal of Chemical Physics* **139** (12), 121922.

Arp, P. A. & Mason, S. G. 1977 The kinetics of flowing dispersions. *Journal of Colloid and Interface Science* **61** (1), 44–61.

Ball, R. C. & Melrose, J. R. 1997 A simulation technique for many spheres in quasi-static motion under frame-invariant pair drag and Brownian forces. *Physica A: Statistical Mechanics and its Applications* **247** (1), 444–472.

Banchio, A. J. & Brady, J. F. 2003 Accelerated Stokesian Dynamics: Brownian motion. *The Journal of Chemical Physics* **118** (22), 10323–10332.

Barnes, H. A. 1989 Shear-Thickening ("Dilatancy") in Suspensions of Nonaggregating Solid Particles Dispersed in Newtonian Liquids. *Journal of Rheology* **33** (2), 329–366.

Batchelor, G. K. 1970 The stress system in a suspension of force-free particles. *Journal of Fluid Mechanics* **41** (03), 545–570.

Batchelor, G. K. 1972 Sedimentation in a dilute dispersion of spheres. *Journal of Fluid Mechanics* **52** (02), 245–268.

Beenakker, C. W. J. 1984 The effective viscosity of a concentrated suspension of spheres (and its relation to diffusion). *Physica A: Statistical Mechanics and its Applications* **128** (1–2), 48–81.

Beenakker, C. W. J. 1986 Ewald sum of the Rotne–Prager tensor. *The Journal of Chemical Physics* **85** (3), 1581–1582.

Beiser, M., Bickert, G. & Scharfer, P. 2004 Comparison of sedimentation behavior and structure analysis with regard to destabilization processes in suspensions. *Chemical Engineering & Technology* **27** (10), 1084–1088.

Binous, H. & Phillips, R. J. 1999 Dynamic simulation of one and two particles sedimenting in viscoelastic suspensions of FENE dumbbells. *Journal of Non-Newtonian Fluid Mechanics* **83** (1–2), 93–130.

Bird, R. B., Dotson, P. J. & Johnson, N. L. 1980 Polymer solution rheology based on a finitely extensible bead–spring chain model. *Journal of Non-Newtonian Fluid Mechanics* **7** (2), 213–235.

Bird, R. B. & Hassager, O. 1987 *Dynamics of Polymeric Liquids, Volume I: Fluid Mechanics*. Wiley-Interscience, New York.

Blanc, F., Lemaire, E. & Peters, F. 2014 Tunable fall velocity of a dense ball in oscillatory cross-sheared concentrated suspensions. *Journal of Fluid Mechanics* **746**.

Blanc, F., Lemaire, E., Peters, F. & Lobry, L. 2015 Fall velocity of a dense ball in cross-sheared concentrated suspensions: Oscillatory and step-shear flows. In *Annual European Rheology Conference 2015*. Nantes, France. CS20.

Blanc, F., Peters, F. & Lemaire, E. 2011 Experimental signature of the pair trajectories of rough spheres in the shear-induced microstructure in noncolloidal suspensions. *Physical Review Letters* **107** (20), 208302.

Bossis, G. & Brady, J. F. 1984 Dynamic simulation of sheared suspensions. I. General method. *The Journal of Chemical Physics* **80** (10), 5141–5154.

Bossis, G. & Brady, J. F. 1987 Self-diffusion of Brownian particles in concentrated suspensions under shear. *The Journal of Chemical Physics* **87** (9), 5437–5448.

Brady, J. F. & Bossis, G. 1988 Stokesian Dynamics. *Annual Review of Fluid Mechanics* **20** (1), 111–157.

Brady, J. F., Phillips, R. J., Lester, J. C. & Bossis, G. 1988 Dynamic simulation of hydrodynamically interacting suspensions. *Journal of Fluid Mechanics* **195**, 257–280.

Brenner, H. & O'Neill, M. E. 1972 On the Stokes resistance of multiparticle systems in a linear shear field. *Chemical Engineering Science* **27** (7), 1421–1439.

Brown, E. & Jaeger, H. M. 2014 Shear thickening in concentrated suspensions: Phenomenology, mechanisms, and relations to jamming. *Reports on Progress in Physics* **77** (4), 046602.

Bybee, M. D. 2009 *Hydrodynamic simulations of colloidal gels: Microstructure, dynamics, and rheology*. PhD Thesis, University of Illinois at Urbana–Champaign.

Chhabra, R. P. 2006 *Bubbles, Drops, and Particles in Non-Newtonian Fluids*, 2nd edn. CRC Press.

Chilcott, M. D. & Rallison, J. M. 1988 Creeping flow of dilute polymer solutions past cylinders and spheres. *Journal of Non-Newtonian Fluid Mechanics* **29**, 381–432.

Chong, J. S., Christiansen, E. B. & Baer, A. D. 1971 Rheology of concentrated suspensions. *Journal of Applied Polymer Science* **15** (8), 2007–2021.

Cooley, J. W. & Tukey, J. W. 1965 An algorithm for the machine calculation of complex Fourier series. *Mathematics of Computation* **19** (90), 297–301.

Da Cunha, F. R. & Hinch, E. J. 1996 Shear-induced dispersion in a dilute suspension of rough spheres. *Journal of Fluid Mechanics* **309**, 211–223.

Davis, R. H. 1992 Effects of surface roughness on a sphere sedimenting through a dilute suspension of neutrally buoyant spheres. *Physics of Fluids A: Fluid Dynamics* **4** (12), 2607–2619.

Davis, R. H. & Acrivos, A. 1985 Sedimentation of noncolloidal particles at low Reynolds numbers. *Annual Review of Fluid Mechanics* **17** (1), 91–118.

De Gennes, P. G. 1976 Dynamics of Entangled Polymer Solutions. II. Inclusion of Hydrodynamic Interactions. *Macromolecules* **9** (4), 594–598.

Dintzis, F. R., Berhow, M. A., Bagley, E. B., Wu, Y. V. & Felker, F. C. 1996 Shear-thickening behavior and shear-induced structure in gently solubilized starches. *Cereal Chemistry* **73** (5), 638–643.

Dörr, A., Sadiki, A. & Mehdizadeh, A. 2013 A discrete model for the apparent viscosity of polydisperse suspensions including maximum packing fraction. *Journal of Rheology* **57** (3), 743–765.

Dratler, D. I. & Schowalter, W. R. 1996 Dynamic simulation of suspensions of non-Brownian hard spheres. *Journal of Fluid Mechanics* **325**, 53–77.

Drazer, G., Koplik, J., Khusid, B. & Acrivos, A. 2002 Deterministic and stochastic behaviour of non-Brownian spheres in sheared suspensions. *Journal of Fluid Mechanics* **460**, 307–335.

Durlofsky, L., Brady, J. F. & Bossis, G. 1987 Dynamic simulation of hydrodynamically interacting particles. *Journal of Fluid Mechanics* **180**, 21–49.

Einstein, A. 1906 Eine neue Bestimmung der Moleküldimensionen. *Annalen der Physik* **324** (2), 289–306.

Ekiel-Jeżewska, M. L., Gubiec, T. & Szymczak, P. 2008 Stokesian dynamics of close particles. *Physics of Fluids* **20** (6), 063102.

Ewald, P. P. 1921 Die Berechnung optischer und elektrostatischer Gitterpotentiale. *Annalen der Physik* **369** (3), 253–287.

Ewoldt, R. H., Hosoi, A. E. & McKinley, G. H. 2009 Nonlinear viscoelastic biomaterials: Meaningful characterization and engineering inspiration. *Integrative and Comparative Biology* **49** (1), 40–50.

Feist, M., Keller, F., Nirschl, H. & Dörfler, W. 2011 Stokesian dynamics and the settling behaviour of particle–fibre-mixtures. *The Canadian Journal of Chemical Engineering* **89** (4), 682–690.

Flory, P. J. 1953 *Principles of Polymer Chemistry*. Cornell University Press.

Gallier, S., Lemaire, E., Lobry, L. & Peters, F. 2014*a* A fictitious domain approach for the simulation of dense suspensions. *Journal of Computational Physics* **256**, 367–387.

Gallier, S., Lemaire, E., Peters, F. & Lobry, L. 2014*b* Rheology of sheared suspensions of rough frictional particles. *Journal of Fluid Mechanics* **757**, 514–549.

Giacomin, A. J., Bird, R. B., Johnson, L. M. & Mix, A. W. 2011 Large-amplitude oscillatory shear flow from the corotational Maxwell model. *Journal of Non-Newtonian Fluid Mechanics* **166** (19–20), 1081–1099.

Golub, G. H. & Van Loan, C. F. 2012 *Matrix Computations*, 3rd edn. JHU Press.

Hafid, H., Ovarlez, G., Toussaint, F., Jézequel, P.-H. & Roussel, N. 2010 Estimating measurement artifacts in concrete rheometers from MRI measurement on model materials. In *Design, Production and Placement of Self-Consolidating Concrete*, pp. 127–137. Springer.

Harlen, O. G., Sundararajakumar, R. R. & Koch, D. L. 1999 Numerical simulations of a sphere settling through a suspension of neutrally buoyant fibres. *Journal of Fluid Mechanics* **388**, 355–388.

Hatzikiriakos, S. G. & Dealy, J. M. 1991 Wall slip of molten high density polyethylene. I. Sliding plate rheometer studies. *Journal of Rheology* **35** (4), 497–523.

Herrchen, M. & Öttinger, H. C. 1997 A detailed comparison of various FENE dumbbell models. *Journal of Non-Newtonian Fluid Mechanics* **68** (1), 17–42.

Hinch, E. J. 1972 Note on the symmetries of certain material tensors for a particle in Stokes flow. *Journal of Fluid Mechanics* **54** (03), 423–425.

Hyun, K., Kim, S. H., Ahn, K. H. & Lee, S. J. 2002 Large amplitude oscillatory shear as a way to classify the complex fluids. *Journal of Non-Newtonian Fluid Mechanics* **107** (1–3), 51–65.

Hyun, K. & Wilhelm, M. 2009 Establishing a new mechanical nonlinear coefficient Q from FT-rheology: First investigation of entangled linear and comb polymer model systems. *Macromolecules* **42** (1), 411–422.

Hyun, K., Wilhelm, M., Klein, C. O., Cho, K. S., Nam, J. G., Ahn, K. H., Lee, S. J., Ewoldt, R. H. & McKinley, G. H. 2011 A review of nonlinear oscillatory shear tests: Analysis and application of large amplitude oscillatory shear (LAOS). *Progress in Polymer Science* **36** (12), 1697–1753.

Ichiki, K., Kobryn, A. E. & Kovalenko, A. 2013 Resistance functions for two unequal spheres in linear flow at low Reynolds number with the Navier slip boundary condition. *arXiv:1302.0461 [cond-mat, physics:physics]* .

Inoue, T. & Osaki, K. 1993 Rheological properties of poly(vinyl alcohol)/sodium borate aqueous solutions. *Rheologica Acta* **32** (6), 550–555.

Jánosi, I. M., Tél, T., Wolf, D. E. & Gallas, J. A. 1997 Chaotic particle dynamics in viscous flows: The three-particle Stokeslet problem. *Physical Review E* **56** (3), 2858.

Jeffrey, D. J. 1992 The calculation of the low Reynolds number resistance functions for two unequal spheres. *Physics of Fluids A: Fluid Dynamics* **4** (1), 16–29.

Jeffrey, D. J. & Onishi, Y. 1984 Calculation of the resistance and mobility functions for two unequal rigid spheres in low-Reynolds-number flow. *Journal of Fluid Mechanics* **139**, 261–290.

Khair, A. S. 2016 Large amplitude oscillatory shear of the Giesekus model. *Journal of Rheology* **60** (2), 257–266.

Kim, J., Merger, D., Wilhelm, M. & Helgeson, M. E. 2014 Microstructure and nonlinear signatures of yielding in a heterogeneous colloidal gel under large amplitude oscillatory shear. *Journal of Rheology* **58** (5), 1359–1390.

Kim, S. & Karrila, S. J. 2005 *Microhydrodynamics: Principles and Selected Applications*. Dover Publications, Mineola, NY, USA.

Krieger, I. M. & Dougherty, T. J. 1959 A mechanism for non-Newtonian flow in suspensions of rigid spheres. *Transactions of The Society of Rheology* **3** (1), 137–152.

Kröger, M. 2005 *Models for Polymeric and Anisotropic Liquids*. Springer Science & Business Media.

Kumar, A. 2010 *Microscale dynamics in suspensions of non-spherical particles*. PhD Thesis, University of Illinois at Urbana–Champaign.

Ladd, A. J. C. 1990 Hydrodynamic transport coefficients of random dispersions of hard spheres. *The Journal of Chemical Physics* **93** (5), 3484–3494.

Ladyzhenskaya, O. A. 1964 *The Mathematical Theory of Viscous Incompressible Flow*, revised English edn. Gordon and Breach.

Lamb, H. 1932 *Hydrodynamics*. Cambridge University Press.

Larson, R. G. 1988 *Constitutive Equations for Polymer Melts and Solutions. Butterworths Series in Chemical Engineering* 2. Butterworth–Heinemann.

Lewis, T. B. & Nielsen, L. E. 1968 Viscosity of dispersed and aggregated suspensions of spheres. *Transactions of The Society of Rheology* **12** (3), 421–443.

Lorentz, H. A. 1896 Eene algemeene stelling omtrent de beweging eener vloeistof met wrijving en eenige daaruit afgeleide gevolgen (A general theorem concerning the motion of a viscous fluid and a few consequences derived from it). *Amsterdam, Zittingsverlag Akademie van Wetenschappen* **5**, 168–175.

Lubachevsky, B. D. & Stillinger, F. H. 1990 Geometric properties of random disk packings. *Journal of Statistical Physics* **60** (5–6), 561–583.

Mari, R., Seto, R., Morris, J. F. & Denn, M. M. 2014 Shear thickening, frictionless and frictional rheologies in non-Brownian suspensions. *Journal of Rheology* **58** (6), 1693–1724.

Mooney, M. 1951 The viscosity of a concentrated suspension of spherical particles. *Journal of Colloid Science* **6** (2), 162–170.

Mwasame, P. M., Wagner, N. J. & Beris, A. N. 2016 Modeling the effects of polydispersity on the viscosity of noncolloidal hard sphere suspensions. *Journal of Rheology* **60** (2), 225–240.

Ness, C. & Sun, J. 2016 Two-scale evolution during shear reversal in dense suspensions. *Physical Review E* **93** (1), 012604.

Nott, P. R. & Brady, J. F. 1994 Pressure-driven flow of suspensions: Simulation and theory. *Journal of Fluid Mechanics* **275**, 157–199.

Oberbeck, A. 1876 Ueber stationäre Flüssigkeitsbewegungen mit Berücksichtigung der inneren Reibung. *Journal für die reine und angewandte Mathematik* **81**, 62–80.

O'Byrne, A. T. 2010 *Re-entrant corner flows of Oldroyd-B fluids*. PhD thesis, University of Bath.

Oldroyd, J. G. 1950 On the formulation of rheological equations of state. *Proceedings of the Royal Society of London A: Mathematical, Physical and Engineering Sciences* **200**, 523–541.

Ovarlez, G., Rodts, S., Chateau, X. & Coussot, P. 2009 Phenomenology and physical origin of shear localization and shear banding in complex fluids. *Rheologica Acta* **48** (8), 831–844.

Peterlin, A. 1966 Hydrodynamics of macromolecules in a velocity field with longitudinal gradient. *Journal of Polymer Science Part B: Polymer Letters* **4** (4), 287–291.

Peters, I. R., Majumdar, S. & Jaeger, H. M. 2016 Direct observation of dynamic shear jamming in dense suspensions. *Nature* **532** (7598), 214–217.

Pöschel, T. & Schwager, T. 2005 *Computational Granular Dynamics: Models and Algorithms*. Springer Science & Business Media.

Rallison, J. M. 2014 Appendix A: Stokes flows. Unpublished manuscript.

Sami, S. 1996 *Stokesian Dynamics simulations of Brownian suspensions in extensional flow*. MS thesis, California Institute of Technology.

Seto, R., Mari, R., Morris, J. F. & Denn, M. M. 2013 Discontinuous shear thickening of frictional hard-sphere suspensions. *Physical Review Letters* **111** (21), 218301.

Sierou, A. & Brady, J. F. 2001 Accelerated Stokesian Dynamics simulations. *Journal of Fluid Mechanics* **448**, 115–146.

Smart, J. R. & Leighton, D. T. 1989 Measurement of the hydrodynamic surface roughness of noncolloidal spheres. *Physics of Fluids A: Fluid Dynamics* **1** (1), 52–60.

Stokes, G. G. 1851 On the effect of the internal friction of fluids on the motion of pendulums. *Transactions of the Cambridge Philosophical Society* **9**, 8–106.

TA Instruments 2000 AR 500/1000 rheometers user manual. *Tech. Rep.* PN 500017.002.

Tirtaatmadja, V., Tam, K. C. & Jenkins, R. D. 1997 Rheological properties of model alkali-soluble associative (HASE) polymers: Effect of varying hydrophobe chain length. *Macromolecules* **30** (11), 3271–3282.

Torres, F. & Gilbert, J. 1996 Large-scale Stokesian Dynamics simulations of non-Brownian suspensions. *Tech. Rep.* C9600004. Xerox Research Centre of Canada.

Townsend, A. K. & Wilson, H. J. 2016 The fluid dynamics of the chocolate fountain. *European Journal of Physics* **37** (1), 015803.

Trulsson, M., DeGiuli, E. & Wyart, M. 2017 Effect of friction on dense suspension flows of hard particles. *Physical Review E* **95** (1), 012605.

Vázquez-Quesada, A., Tanner, R. I. & Ellero, M. 2016 Shear thinning of noncolloidal suspensions. *Physical Review Letters* **117** (10), 108001.

Wilson, H. J. 2006 Lecture notes on linear viscoelasticity. `ucl.ac.uk/~ucahhwi/GM05/`.

Wilson, H. J. 2013 Stokes flow past three spheres. *Journal of Computational Physics* **245**, 302–316.

Wilson, H. J. & Davis, R. H. 2000 The viscosity of a dilute suspension of rough spheres. *Journal of Fluid Mechanics* **421**, 339–367.

Wilson, H. J. & Davis, R. H. 2002 Shear stress of a monolayer of rough spheres. *Journal of Fluid Mechanics* **452**, 425–441.

Wilson, H. J. & Davis, R. H. 2017 Shear stress of a monolayer of rough spheres—corrigendum. *Journal of Fluid Mechanics* **814**, 614–617.

Wyart, M. & Cates, M. E. 2014 Discontinuous shear thickening without inertia in dense non-Brownian suspensions. *Physical Review Letters* **112** (9), 098302.

Yeo, K. & Maxey, M. R. 2010 Simulation of concentrated suspensions using the force-coupling method. *Journal of Computational Physics* **229** (6), 2401–2421.

Yu, P.-W., Ceccio, S. L. & Tryggvason, G. 1995 The collapse of a cavitation bubble in shear flows—A numerical study. *Physics of Fluids* **7** (11), 2608–2616.

Zapryanov, Z. & Tabakova, S. 1998 *Dynamics of Bubbles, Drops and Rigid Particles*. Springer Science & Business Media.

Zeng, S., Kerns, E. T. & Davis, R. H. 1996 The nature of particle contacts in sedimentation. *Physics of Fluids* **8** (6), 1389–1396.